

**METATHESIS OF 1-HEXENE OVER A WO_3/SiO_2
CATALYST IN A GAS-PHASE FIXED BED REACTOR**

David Lokhat

[B.Sc.(Eng)]

July, 2008

Metathesis of 1-hexene over a WO_3/SiO_2 catalyst in a gas-phase fixed bed reactor

David Lokhat

A dissertation submitted in the
School of Chemical Engineering
University of KwaZulu-Natal
Durban

In fulfilment of the requirements of the degree of
Master of Science in Engineering

July, 2008

DECLARATION

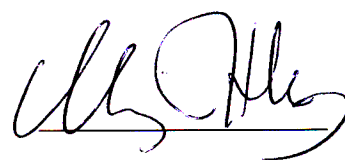
The work presented in this dissertation was performed at the University of KwaZulu-Natal, Durban and at the Technical University of Łódź, Poland from January 2007 to April 2008. The work was supervised by Professor M. Starzak.

This dissertation is presented as the full requirement for the degree of Master of Science in Chemical Engineering. All the work presented in this dissertation is original unless otherwise stated and has not (in whole or in part) been submitted previously to any tertiary institution as part of a degree.

A handwritten signature in black ink, consisting of a stylized 'D' and 'L' followed by a horizontal line.

David Lokhat

I hereby certify that I find this work to be suitable for submission for the degree of Master of Science in Chemical Engineering

A handwritten signature in black ink, featuring a large, stylized 'M' and 'S'.

Professor M. Starzak

Acknowledgements

I would like to thank my supervisor, Professor Mathew Starzak, for his guidance and assistance. I also want to thank Dr. Marek Stelmachowski and the Department of Process and Environmental Engineering of the Technical University of Łódź, Poland, for allowing me to conduct a portion of the experimental work at their research facility as part of a scientific collaboration between South Africa and Poland. I would like to express my sincere appreciation to Sharon Eggers, from the Electron Microscope Unit of the University of KwaZulu-Natal, Faiza Khan, from the School of Pure and Applied Chemistry and Dr. Axel Hofmann, from the School of Geological Sciences for assisting me in the various catalyst characterization procedures used in this investigation. I am very thankful to Brett Parel for conducting the G.C.M.S. analyses of the product samples. I would like to express my deepest gratitude to the undergraduate students Sudeshen Thevan, Yashveer Maharajh, Revandan Bisetty and Neantha Seebran for their help during the commissioning of the experimental equipment. I would like to thank the staff of the Chemical Engineering workshop, Les Henwood, Ken Jack, Kelly Robertson and Danny Singh, for all their help in the design and commissioning of the experimental equipment.

I would like to thank my postgraduate colleagues, Rinay Bownath, Shalendra Subramoney, Suren Moodley, Carl McCawley, Simon Kretzschmar and Bruce Moller for their help and advice. Lastly, I would like to thank my sister, Sarah, my mother and aunt for their support and encouragement.

Abstract

The performance of a WO_3/SiO_2 catalyst has been investigated for the metathesis of 1-hexene in an isothermal, gas-phase fixed bed tubular reactor between 420-500°C and at 1atm. The reactor was fabricated from stainless steel and was placed in an electric tube furnace. The study focused on the effect of operating conditions (reaction temperature, feed gas composition and space time) on the yield of heavy olefins ($\text{C}_7 - \text{C}_{16}$) and the primary product, decene, using a full factorial experimental design. The objective was to determine the optimum operating conditions for the production of decene. Compositions of condensed liquid and vapour product streams were determined via gas-liquid chromatography. Oxidative and reductive pre-treatments of the catalyst were compared to a conventional pre-treatment under nitrogen in terms of their effect on conversion and product distribution. Experimental tests for the existence of external and internal mass transfer resistances were also conducted.

An improved yield of decene was obtained after oxidative pre-treatment of the catalyst. The conversion of 1-hexene, selectivity and yield of decene dropped after pre-treatment under hydrogen and nitrogen only. This may be due to over-reduction of the tungsten centres and the formation of an inactive non-stoichiometric surface phase.

The best yield of decene obtained from the experimental design was 2.19% at 420°C, 51% feed composition and 661g.min.mol^{-1} . The yield of decene decreased by 0.11% when the reaction temperature was raised by 40°C, and by 0.17% when the feed gas composition was raised by 17.5% and increased by 0.21% when the space time was increased by 223g.min.mol^{-1} . The large amount of ethylene and propylene produced as well as the formation of polynuclear aromatics suggest significant cracking of 1-hexene. For the size range and flow-rates that were employed, the reaction does not suffer from intraparticle and external mass transfer resistance effects.

It was concluded that a combination of lower temperature, lower feed gas composition and higher space time should be used to maximize the yield of decene. A final experiment was conducted to test this conclusion. At 380°C, 55% feed composition and $2875\text{g.min.mol}^{-1}$, the yield of decene was 12.80%, which represented a significant improvement.

Table of contents

List of figures	x
List of tables	xvii
List of symbols	xx
Chapter 1 Preliminaries	1
1.1 Introduction	1
1.2 Olefin metathesis and the development of well defined catalysts	3
1.3 Industrial applications of olefin metathesis	9
1.3.1. Production of normal olefins	9
1.3.1.1 Production of propene	9
1.3.1.1(a) The Phillips triolefin process	9
1.3.1.1(b) The Meta-4 process	10
1.3.1.2 Production of 1-hexene	11
1.3.1.3 Production of neohexene	11
1.3.1.4 The Shell higher olefins process (SHOP)	12
1.3.1.5 Production of α -olefins	13
1.3.2 Production of polymers	13
1.3.2.1 Polyoctenamer	13
1.3.2.2 Polynorbornene	14
1.3.2.3 Polydicyclopentadiene	14
1.3.2.4 Hydrogenated polymers	15
1.3.3 Other applications	15
1.4 Research objectives	16
1.5 Outline of the dissertation	17
Chapter 2 Literature review	19
2.1 The WO_3/SiO_2 metathesis catalyst	19
2.2 The mechanism of the olefin metathesis reaction	23
2.3 Alkene metathesis over WO_3/SiO_2	25
2.3.1 Mechanism	25

2.3.2 Reaction kinetics	34
2.4 Isomerization of alkenes over WO_3/SiO_2	39
2.5 Catalyst deactivation	42
Chapter 3 Basis for experimental design and methodology	46
3.1 Experimental design	46
3.1.1 Factorial test planning	46
3.1.2 Fluid flow in a packed-bed reactor and recommendations for laboratory reactor design	51
3.2 Elimination of mass transfer resistances	56
3.2.1 Experimental tests	56
3.2.2 Theoretical criteria	62
Chapter 4 Experimental equipment	67
4.1 Preliminary fixed bed catalytic reactor rig	68
4.2 Equipment used for experiments conducted in Poland	73
4.3 Fixed bed catalytic reactor system for vapour phase metathesis reaction studies	80
4.3.1 Liquid feed preparation and delivery	82
4.3.2 Pre-treatment and dilution gas application	88
4.3.3 Fixed bed catalytic reactor module	89
4.3.4 Product collection and sampling	92
4.3.5 G.C. calibration cell	93
4.3.6 Process Safety	95
Chapter 5 Experimental methods	98
5.1 Gas-liquid chromatography	98
5.2 Catalyst preparation	103
5.3 Absorbance measurements	104
5.4 Catalyst characterization	105
5.4.1 Catalyst particle size estimation	105
5.4.2 Surface area measurements	107
5.4.3 Scanning electron microscopy (SEM) and energy dispersive	

x-ray (EDX) spectroscopy	107
5.4.4 Gas-chromatography-mass-spectrometry	107
5.5 Experimental procedures for the preliminary tests	108
5.6 Experimental procedures for the experiments conducted in Poland	108
5.7 Experimental procedures for the optimization study conducted at the University of KwaZulu-Natal	109
 Chapter 6 Results and discussion	 110
6.1 Results of the preliminary tests	110
6.2 Results of the experimental program conducted in Poland	111
6.3 Results of the experimental program conducted at the University of KwaZulu-Natal (UKZN)	124
6.3.1 Results of the investigation of pre-treatment procedures	124
6.3.2 Results of the factorial experimental design	133
6.3.3 Results of the tests for external mass transfer resistance	140
6.3.4 Results of the tests for intraparticle mass transfer resistance	146
6.3.5 Results of the experiments conducted to compare the performance of the two different WO ₃ /SiO ₂ catalysts used for the investigation	149
6.3.6 Results of the final experiments conducted to test the optimized region of operating conditions	151
 References	 156
 Appendix A – Equipment calibration data	 161
 Appendix B – MATLAB® computer simulation and process calculation script files	 171
 Appendix C – Sample process calculations	 196
 Appendix D – Catalyst characterization data	 199
 Appendix E – Solution of the unsteady state material balance for saturation of nitrogen gas with 1-hexene	 205

Appendix F – Mass and energy balances for the 1-hexene feed tank	208
Appendix G – G.C. chromatograms	211
Appendix H – Full experimental results	276

List of figures

Chapter 1

Figure 1.1 Basic representation of the olefin cross-metathesis reaction	2
Figure 1.2 Different modes of olefin metathesis in organic and polymer chemistry	4
Figure 1.3 Shrock's tungsten (1) and molybdenum (2) based metathesis catalysts	5
Figure 1.4 A selection of well-defined ruthenium based metathesis catalysts	7
Figure 1.5 The OCT process (reversed Phillips triolefin process)	10
Figure 1.6 Synthesis of neohexene	11
Figure 1.7 The neohexene process	11
Figure 1.8 Oligomerization of ethene	12
Figure 1.9a Synthesis of cyclooctene – high molecular weight fraction	13
Figure 1.9b Synthesis of cyclooctene – low molecular weight fraction	13
Figure 1.10 Synthesis of polynorbornene	14
Figure 1.11 ROMP of endo-dicyclopentadiene	14
Figure 1.12 Synthesis of Zeonex®	15

Chapter 2

Figure 2.1 Fully hydrated WO_3/SiO_2 catalyst	20
Figure 2.2 Dehydrated WO_3/SiO_2 catalyst	20
Figure 2.3 Various forms of the fully hydrated octahedral tungsten trioxide	21
Figure 2.4 Silicon-bound oligomeric tungsten oxide catalyst	21
Figure 2.5 Dehydration of WO_3/SiO_2 between 825K and 875K	21
Figure 2.6 Removal of water upon heating, from bound silanols on dry silica gel	22
Figure 2.7 Keggin-type structure WO_3/SiO_2	23
Figure 2.8 Quasi-cyclobutane mechanism of the olefin metathesis reaction	23
Figure 2.9 Pair-wise mechanism of the olefin metathesis reaction	24
Figure 2.10 Metal-carbene non-pair-wise mechanism for olefin metathesis	25
Figure 2.11 Break – in of the WO_3/SiO_2 catalyst under hydrogen	28
Figure 2.12 Interaction of 1-hexene with non-reduced WO_3/SiO_2	28
Figure 2.13 Formation of the initial metal-carbene – hydrogen shift mechanism	28
Figure 2.14 Formation of the initial metal-carbene – hydride transfer mechanism	29
Figure 2.15 Formation of the initiator for 1-hexene metathesis	29
Figure 2.16 Structure of the metallacyclobutane intermediate in metathesis reactions	30

Figure 2.17 Structural transformation of the alkylidene intermediate during one metathesis cycle of 1-hexene self metathesis	31
Figure 2.18 Transformation of the $\text{WO}_3/\text{Al}_2\text{O}_3$ surface phase from edge-shared to corner-shared tetrahedra after high temperature oxidative pre-treatment	32
Figure 2.19 Alkoxide and allylic mechanisms of 1-butene isomerization over WO_3/SiO_2	41

Chapter 3

Figure 3.1 Exploration of the limited domain through FFE	47
Figure 3.2 Interaction graph for variables A and B	50
Figure 3.3 Exploration of the limited domain of operating conditions using a factorial experimental design – limits for each test variable (reaction temperature, % feed composition, space time)	51
Figure 3.4 Variation of average void fraction of bed with tube size	55
Figure 3.5 Plug flow model of the fixed bed catalytic reactor	57
Figure 3.6 Mass transfer resistances in heterogeneous catalysis	58
Figure 3.7 Plot of conversion versus space time in the test for external mass transfer resistance	61

Chapter 4

Figure 4.1 Saturation vessel	69
Figure 4.2 Preliminary fixed bed catalytic reactor system – P&I diagram	71
Figure 4.3 Reactor furnace and peripheral heating	73
Figure 4.4 Experimental fixed bed reactor system at the Technical University of Łódź, Poland	74
Figure 4.5 Polish experimental program fixed bed catalytic reactor system – piping and instrumentation diagram	75
Figure 4.6 Fixed bed tubular reactor, fully assembled	76
Figure 4.7 Saturator vessel and condenser unit	77
Figure 4.8 Brooks™ 4-channel volumetric flow controller	78
Figure 4.9 Haake™ cooling water circulator	78
Figure 4.10 Perkin Elmer Autosystem XL™ gas chromatograph	80
Figure 4.11 Fixed bed catalytic reactor system – piping and instrumentation diagram	81
Figure 4.12 Fixed bed catalytic reactor system for vapour phase metathesis studies	82
Figure 4.13 Stainless steel liquid feed tank	83
Figure 4.14 Open-loop response to a step change in the proposed control action	84

Figure 4.15 Feed tank top flange	84
Figure 4.16 Response of tank liquid temperature to a 20% step change in valve position	85
Figure 4.17 Liquid feed preparation and delivery system	87
Figure 4.18 Spectrochrom P100 isocratic pump	87
Figure 4.19 Pre-treatment and dilution gas work-up	88
Figure 4.20 Fixed bed catalytic reactor module	89
Figure 4.21 Fixed bed catalytic reactor module exit assembly	90
Figure 4.22 Laboratory scale fixed bed catalytic reactor	91
Figure 4.23 Modular glass product condenser	93
Figure 4.24 G.C. gas-liquid calibration cell	95

Chapter 5

Figure 5.1 Shimadzu GC-2014 gas chromatograph (liquid and gas analysis)	101
Figure 5.2 Calcination curve for 8% WO ₃ /SiO ₂ catalyst	104

Chapter 6

Figure 6.1 Two variable, three level experimental design	111
Figure 6.2 Plug flow model of the fixed bed reactor	113
Figure 6.3 Calculated reaction rate versus reaction temperature, 2 nd order reaction in a differential bed (different catalyst particle sizes) – Polish experimental program	116
Figure 6.4 Calculated reaction rate versus reaction temperature, 1 st order reaction (different catalyst particle sizes) – Polish experimental program	117
Figure 6.5 Calculated reaction rate versus reaction temperature, 2 nd order reaction (different catalyst particle sizes) – Polish experimental program	117
Figure 6.6 Calculated reaction rate versus reaction temperature, ½ order reaction (different catalyst particle sizes) – Polish experimental program	118
Figure 6.7 Arrhenius plot for parameter k_0 , 2 nd order reaction in a differential bed (different catalyst particle sizes) – Polish experimental program	119
Figure 6.8 Arrhenius plot for parameter k_1 , 1 st order reaction (different catalyst particle sizes) – Polish experimental program	119
Figure 6.9 Arrhenius plot for parameter k_2 , 2 nd order reaction (different catalyst particle sizes) – Polish experimental program	120
Figure 6.10 Arrhenius plot for parameter $k_{0.5}$, ½ order reaction (different catalyst particle sizes) – Polish experimental program	120

Figure 6.11 Carbon balance consistency plot for experiments conducted in Poland	123
Figure 6.12 Conversion versus reaction time – Run 1- Run 3 (investigation of pre-treatment procedures) – experiments conducted at UKZN	124
Figure 6.13 Selectivity ($C_7 - C_{16}$) versus reaction time – Run 1- Run 3 (investigation of pre-treatment procedures) – experiments conducted at UKZN	125
Figure 6.14 Selectivity (C_{10}) versus reaction time – Run 1- Run 3 (investigation of pre-treatment procedures) – experiments conducted at UKZN	125
Figure 6.15 Yield ($C_7 - C_{16}$) versus reaction time – Run 1- Run 3 (investigation of pre-treatment procedures) – experiments conducted at UKZN	126
Figure 6.16 Yield (C_{10}) versus reaction time – Run 1- Run 3 (investigation of pre-treatment procedures) – experiments conducted at UKZN	126
Figure 6.17 EDX elemental analysis – fresh WO_3/SiO_2 (catalyst B) – experiments conducted at UKZN	129
Figure 6.18 EDX elemental analysis – spent WO_3/SiO_2 (catalyst B - 460°C, 96.41% 1-hexene, $W/F = 336 \text{ g.mol.min}^{-1}$, 6 hours on-stream) – experiments conducted at UKZN	129
Figure 6.19 Spent WO_3/SiO_2 catalyst – run 1 (a), run 2 (b) and run 3 (c)	131
Figure 6.20 Fresh 8% WO_3/SiO_2 catalyst (800X magnification)	131
Figure 6.21 Spent 8% WO_3/SiO_2 catalyst (500X magnification) - removed after 6 hours on-stream at 460°C, 96.41% 1-hexene, $W/F = 336 \text{ g.mol.min}^{-1}$	132
Figure 6.22 Fresh 8% WO_3/SiO_2 catalyst (8.00KX magnification)	132
Figure 6.23 Spent 8% WO_3/SiO_2 catalyst (5.03KX magnification)	133
Figure 6.24 Interaction plot of temperature (A) and feed composition (B) – experiments conducted at UKZN	136
Figure 6.25 Interaction plot of temperature (A) and space time (C) – experiments conducted at UKZN	137
Figure 6.26 Interaction plot of feed composition (B) and space time (C) – experiments conducted at UKZN	137
Figure 6.27 Conversion versus space time – Run 4 (420°C, 55% feed composition, $W/F = 221 \text{ g.min.mol}^{-1}$ to $1412 \text{ g.min.mol}^{-1}$) – experiments conducted at UKZN	141
Figure 6.28 Selectivity versus space time – Run 4 (420°C, 55% feed composition, $W/F = 221 \text{ g.min.mol}^{-1}$ to $1412 \text{ g.min.mol}^{-1}$) – experiments conducted at UKZN	141
Figure 6.29 Yield versus space time – Run 4 (420°C, 55% feed composition, $W/F = 221 \text{ g.min.mol}^{-1}$ to $1412 \text{ g.min.mol}^{-1}$) – experiments conducted at UKZN	142

Figure 6.30 Conversion versus space time – Run 7 (420°C, 29% feed composition, $W/F = 142\text{g.min.mol}^{-1}$ to 398g.min.mol^{-1}) – experiments conducted at UKZN	142
Figure 6.31 Selectivity versus space time – Run 7 (420°C, 29% feed composition, $W/F = 142\text{g.min.mol}^{-1}$ to 398g.min.mol^{-1}) – experiments conducted at UKZN	143
Figure 6.32 Yield versus space time – Run 7 (420°C, 29% feed composition, $W/F = 142\text{g.min.mol}^{-1}$ to 398g.min.mol^{-1}) – experiments conducted at UKZN	143
Figure 6.33 Spent WO_3/SiO_2 catalyst – run 7	144
Figure 6.34 Black deposit removed from inside the reactor tube after run 7	144
Figure 6.35 Conversion versus space time – Run 11 (380°C, 95% feed composition, $W/F = 200\text{g.min.mol}^{-1}$ to 400g.min.mol^{-1}) – experiments conducted at UKZN	145
Figure 6.36 Selectivity versus space time – Run 11 (380°C, 95% feed composition, $W/F = 200\text{g.min.mol}^{-1}$ to 400g.min.mol^{-1}) – experiments conducted at UKZN	145
Figure 6.37 Yield versus space time – Run 11 (380°C, 29% feed composition, $W/F = 200\text{g.min.mol}^{-1}$ to 400g.min.mol^{-1}) – experiments conducted at UKZN	146
Figure 6.38 Conversion versus sampling time – run 1 and run 10 (460°C, 95% feed composition and $W/F = 330\text{g.min.mol}^{-1}$) – experiments conducted at UKZN	147
Figure 6.39 Selectivity versus sampling time – run 1 and run 10 (460°C, 95% feed composition and $W/F = 330\text{g.min.mol}^{-1}$) – experiments conducted at UKZN	147
Figure 6.40 Yield versus sampling time – run 1 and run 10 (460°C, 95% feed composition and $W/F = 330\text{g.min.mol}^{-1}$) – experiments conducted at UKZN	148
Figure 6.41 Conversion versus sampling time – run 1 and run 9 (460°C, 95% feed composition and $W/F = 335\text{g.min.mol}^{-1}$) – experiments conducted at UKZN	150
Figure 6.42 Selectivity versus sampling time – run 1 and run 9 (460°C, 95% feed composition and $W/F = 335\text{g.min.mol}^{-1}$) – experiments conducted at UKZN	150
Figure 6.43 Yield versus sampling time – run 1 and run 9 (460°C, 95% feed composition and $W/F = 335\text{g.min.mol}^{-1}$) – experiments conducted at UKZN	151
Figure 6.44 Carbon balance consistency plot for the experiments conducted at UKZN	152

Figure 6.31 Conversion versus space time – Run 11 (380°C, 95% feed composition, 200g.min.mol ⁻¹ to 400g.min.mol ⁻¹)	141
Figure 6.32 Selectivity versus space time – Run 11 (380°C, 95% feed composition, 200g.min.mol ⁻¹ to 400g.min.mol ⁻¹)	142
Figure 6.33 Yield versus space time – Run 11 (380°C, 95% feed composition, 200g.min.mol ⁻¹ to 400g.min.mol ⁻¹)	142
Figure 6.34 Conversion versus reaction time – run 1 and run 10 (460°C, 95% feed composition and 330g.min.mol ⁻¹)	143
Figure 6.35 Selectivity versus reaction time – run 1 and run 10 (460°C, 95% feed composition and 330g.min.mol ⁻¹)	144
Figure 6.36 Yield versus reaction time – run 1 and run 10 (460°C, 95% feed composition and 330g.min.mol ⁻¹)	144
Figure 6.37 Conversion versus reaction time – run 1 and run 9 (460°C, 95% feed composition and 335g.min.mol ⁻¹)	146
Figure 6.38 Selectivity versus reaction time – run 1 and run 9 (460°C, 95% feed composition and 335g.min.mol ⁻¹)	146
Figure 6.39 Yield versus reaction time – run 1 and run 9 (460°C, 95% feed composition and 335g.min.mol ⁻¹)	147
Figure 6.40 Carbon balance consistency plot for the optimization study	148

Appendix A

Figure A.1 G.C detector calibration curve, 1-decene (reference component: 1-hexene)	161
Figure A.2 G.C detector calibration curve, 1-nonene (reference component: 1-hexene)	162
Figure A.3 G.C detector calibration curve, 1-octene (reference component: 1-hexene)	162
Figure A.4 G.C detector calibration curve, 1-heptene (reference component: 1-hexene)	163
Figure A.5 G.C detector calibration curve, 1-pentene (reference component: 1-hexene)	163
Figure A.6 G.C detector calibration curve, 1-butene (reference component: 1-hexene)	164
Figure A.7 G.C detector calibration curve, propylene (reference component: 1-hexene)	164
Figure A.8 G.C detector calibration curve, 1-ethylene (reference component: 1-hexene)	165
Figure A.9 Spectrochrom P100 isocratic pump calibration curve (1-hexene at 30°C)	166
Figure A.10 R102 rotameter calibration curve – Nitrogen (2barg supply)	167
Figure A.11 R102 rotameter calibration curve – Air (2barg supply)	168
Figure A.12 R102 rotameter calibration curve – Hydrogen (2barg supply)	169
Figure A.13 R102 rotameter calibration curve – Nitrogen (3.5barg supply)	170

experiments conducted at UKZN – Air/H ₂ /N ₂ (4 hours, 1 ½ hours and 18 hours, respectively) in blue, H ₂ /N ₂ in red and N ₂ in black	127
Table 6.6 Complete set of results for the optimization and transport effects study – factorial design points in blue, external transport effect runs in red, green and magenta	134
Table 6.7 Three variable, two level full factorial design with a centre-point	135
Table 6.8 Effects and interactions of temperature (A), feed composition (B) and space time (C) – Yates algorithm	135
Table 6.9 Mean response values, temperature (A) – feed composition (B) combination	135
Table 6.10 Mean response values, temperature (A) – space time (C) combination	136
Table 6.11 Mean response values, feed composition (B) – space time (C) combination	136
Table 6.12 Significance test on the results of the factorial design	138
Table 6.13 The effect of different reaction conditions on the quality of the metathesis liquid product colour	139
Table 6.14 Most abundant non-olefin products in the liquid product sample from run 8-01 (420°C, 52% feed composition and $W/F = 660 \text{ g.min.mol}^{-1}$)	139
Table 6.15 Most abundant non-olefin products in the liquid product sample from run 8-02 (460°C, 76% feed composition and $W/F = 403 \text{ g.min.mol}^{-1}$)	139
Table 6.16 Most abundant non-olefin products in the liquid product sample from run 8-03 (500°C, 55% feed composition and $W/F = 697 \text{ g.min.mol}^{-1}$)	140
Table 6.17 Experimental results for run 10 – 123µm particles (460°C, 95% feed composition and $W/F = 330 \text{ g.min.mol}^{-1}$)	148
Table 6.18 Experimental results for run 9 – catalyst A (460°C, 95% feed composition and $W/F = 335 \text{ g.min.mol}^{-1}$)	149
Table 6.19 Carbon balance consistency data for the experiments conducted at UKZN	153

Appendix D

Table D.1 BET Multipoint surface area report (Micrometrics Gemini) – Fresh catalyst A	199
Table D.2 BET Multipoint surface area report (Micrometrics Gemini) – Fresh catalyst B	200
Table D.3 BET Multipoint surface area report (Micrometrics Gemini) – Spent catalyst B (460°C, 96.41% 1-hexene, 336 g.mol.min ⁻¹ , 6 hours on-stream)	201

Appendix G

Table G.1 – G.15 G.C. data calibration (liquid)	211-225
---	---------

Chapter 1

Preliminaries

1.1 Introduction

The growing global demand for speciality chemicals has revived interest in the development of alternative processes with safer, more economical and more environmentally sound routes to valuable products. The olefin metathesis reaction has attracted considerable attention as a catalytic process due to its flexibility to produce desired chemical products with better selectivity and efficiency. As one of the last major discoveries of the past century in the field of organo-metallic chemistry, the reaction has since been used commercially to produce light olefins, feedstock for polymerization processes and oleo-chemical intermediates. A key role for olefin metathesis has been suggested for the valorization of secondary Fischer-Tropsch streams on gas-to-liquid and coal-to-liquid plants. Low-value olefin feed-stock may be used to produce linear internal alkenes in the detergent range ($C_{10} - C_{18}$), required for surfactant synthesis. Linear alkenes are currently produced either by cleavage reactions of high molecular weight alkanes or by oligomerization of ethylene. These processes produce olefins that are less suited to market requirements. Metathesis technology may represent the primary method for production of feedstock for linear alkyl benzene sulfonate processes in the near future.

Linear alkene metathesis is a unique chemical reaction, involving the rupture and reformation of carbon-carbon double bonds in acyclic alkene molecules. It is a double displacement reaction in which there is a cleavage of the double bond in the molecule, followed by a redistribution of alkylidene fragments (Figure 1.1).

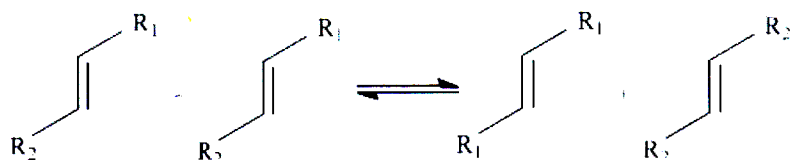


Figure 1.1 Basic representation of the olefin cross-metathesis reaction

The reaction is catalyzed by solid transition metal based catalysts. Under optimum conditions, the technology can be used to produce longer chain internal olefins from low value olefin feedstock. The metathesis system is complex, since the primary reaction products are also able to metathesize, and reactants and products can undergo isomerisation, leading to a broad spectrum of possible products, dependent on reaction conditions. Research in the past, especially for the metathesis of longer chain linear olefins, has largely focused on ruthenium and molybdenum based catalysts. The high operating temperatures of the WO_3/SiO_2 metathesis catalyst are advantageous when considering the possible poisons that may be present in an industrial feed stream. The catalyst is resilient at high temperature to trace quantities of catalyst poisons and impurities, such as oxygenates. Unfortunately, the high temperature application of this catalyst system also promotes various side reactions, including cracking and isomerization. The latter has been found to be responsible for the general lack of high selectivity for tungsten based metathesis systems.

This study employed 1-hexene as the alkene of interest, with 5-decene and ethylene expected as the major products. The reaction was catalyzed by tungsten trioxide on silica dioxide (WO_3/SiO_2), where the solid catalyst particles constituted a fixed bed and the reactant a gas phase. In this work, the basic aspects of the 1-hexene metathesis process have been studied in order to determine the effect of operating conditions on the conversion of 1-hexene as well as the selectivity and yield of the primary metathesis product, decene. Mass transfer resistance effects and the effect of pre-treatment procedures on the performance of the catalyst were also investigated.

1.2 Olefin metathesis and the development of well defined catalysts

Olefin metathesis is a transition metal catalyzed reaction involving the re-organization of bonds on olefins via transalkylidenation. Both heterogeneous and homogeneous catalysts have been found useful in promoting this reaction. The reaction was first observed, although misinterpreted, in the 1950's by industrial chemists. In 1956, Herbert S. Eleutrio, then working at the petrochemicals division of chemicals company DuPont[®], obtained a propylene-ethylene co-polymer from a propylene feed passed over a molybdenum-on-alumina catalyst. The composition of the evolved gas (a mixture of propylene, ethylene and 1-butene) could not be explained with the theory of organo-metallic chemistry available at the time. The first publication on a metathesis type reaction appeared in 1960, where the article was on the ring opening polymerization of norbornene using a catalyst derived from titanium tetra-chloride and lithium-aluminium-tetra-alkyls (Truett et al., 1960).

At the Phillips Petroleum Corporation, this reaction was discovered accidentally by Robert L. Banks and Grant C. Bailey, when they were seeking an effective heterogeneous catalyst to replace a HF acid catalyst for converting olefins into high-octane gasoline via olefin-isoparaffin alkylation. When using a supported molybdenum catalyst, they found that instead of alkylating the paraffin, the olefin molecules were split, and discovered that propene can be catalytically converted into ethene and butene (Mol, 1999). Their results were subsequently published (Banks and Bailey, 1964), but even a partial understanding of the chemistry was only attainable several years later. In 1967, Nissam Calderon and co-workers at the Goodyear Tyre and Rubber Company performed experiments with butene in the presence of a homogeneous catalyst. They concluded that the unexpected products were due to cleavage and re-formation of the olefins' double bonds. The Goodyear researchers named the reaction "olefin metathesis" (Rouhi, 2002).

There are several distinct modes by which olefin metathesis may proceed. These are illustrated in Figure 1.2. Cross metathesis (CM) is the simplest form, where two olefins exchange carbon groups around their double bonds to form new olefins. Here the selectivity of the reaction is important since a competing reaction is self metathesis of an olefin to yield the cross-product (Oakley, 2004). Ring closing metathesis (RCM) is the intra-molecular version of CM, by which dienes can close to form cyclic structures, with the release of ethylene. Ring opening metathesis is the reverse of RCM. Here an acyclic olefin is introduced to the cyclic olefin to yield acyclic dienes. When metathesis reactions are applied to cyclo-alkenes, linear unsaturated polymers are obtained, so-called polyalkenamers. This ring opening metathesis polymerization (ROMP) is driven by the release of ring strain in the starting material. The reaction usually proceeds through homogeneous catalyst-substrate systems. Acyclic diene metathesis polymerization

(ADMET) is a step growth equilibrium poly-condensation reaction that is driven by the release of a small molecule (typically ethylene).

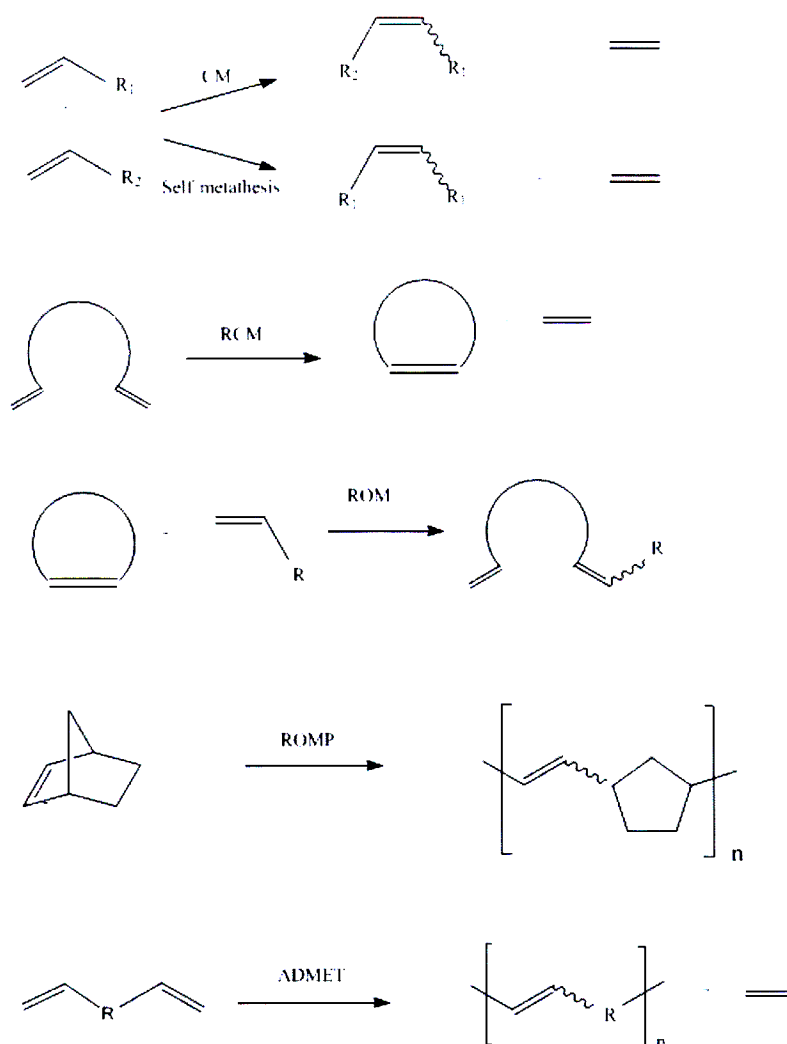


Figure 1.2 Different modes of olefin metathesis in organic and polymer chemistry (Oakley, 2004)

Early on, the two fields were researched independently from one another; the ring opening polymerizations were typically initiated with Ziegler-Natta type catalysts, such as $MoCl_5/Et_3Al$, at or below room temperature, while the exchange reactions were usually conducted with oxide catalysts (MoO_3/Al_2O_3) at elevated temperatures (Oakley, 2004). In 1967, Calderon used $WCl_6/EtAlCl_2/EtOH$ in a 1:4:1 mole ratio to catalyze both types of metathesis reaction, thus recognizing that these two reactions were related.

The heterogeneous transition metal oxide catalysts, usually deposited on a high surface-area support (an inorganic oxide), were not specific to metathesis reactions. These bi-functional catalysts were also used as isomerization and cracking catalysts. Tungsten and molybdenum

based catalysts have since received considerable attention due to their high metathesis activity and because they provide a close relation between heterogeneous and homogeneous catalysis. The development of the heterogeneous transition metal oxide metathesis catalysts has proceeded slowly, with major advances being made in terms of the nature and purity of the support and the reacting substrate. Many of the catalysts that formed the basis of experimentation during the early history of the reaction still prevail. These include the robust WO_3/SiO_2 metathesis catalyst.

The first well-defined catalysts that were active towards olefin metathesis were developed by Richard R. Schrock and co-workers at the Massachusetts Institute of Technology. In 1986/87, tungsten and molybdenum-based complexes were synthesized. The latter were less reactive and therefore more selective in reacting with olefins rather than with other functional groups (Rouhi, 2002). The most common versions of these catalysts (Figure 1.3) are high-oxidation state, 14-electron complexes.

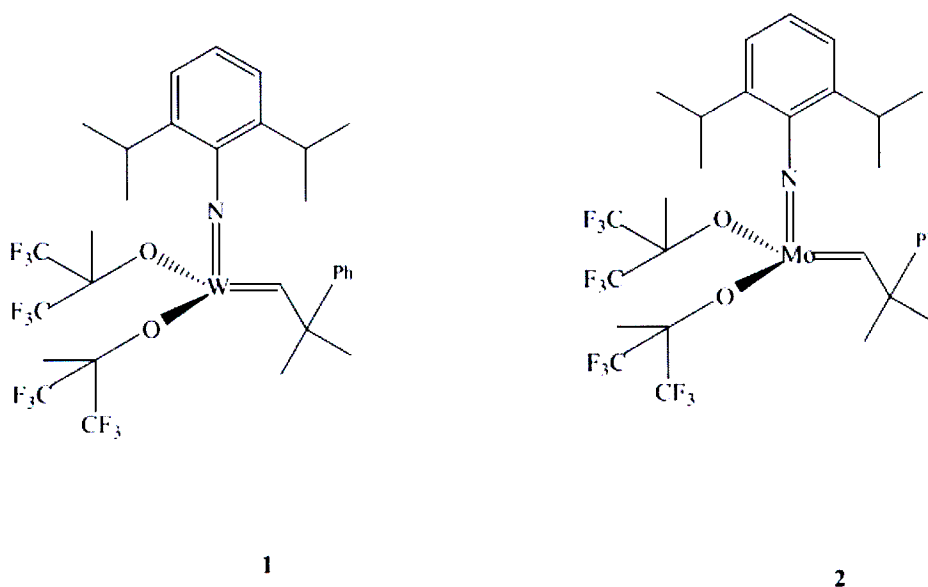


Figure 1.3 Schrock's tungsten (1) and molybdenum (2) based metathesis catalysts (Oakley, 2004)

The catalysts exhibit a pseudo-tetrahedral structure, are electron deficient and only contain bulky, covalently bound ligands. The steric crowding of the ligands accounts for the catalysts stability toward bimolecular decomposition, which was a problem in the development of these catalysts (Oakley, 2004). The catalysts are extremely active, but their use is limited due to their low tolerance of water and oxygen and general functionality on the reacting olefin. Functional groups on the substrate or solvent, as particularly observed in these homogeneous systems, can

interfere with the catalytic process (Grubbs, 2004). Here, competitive binding or direct reaction of the functional group with the active metal centre on the catalyst appears to cause deactivation.

Ruthenium, unlike titanium, tungsten and molybdenum which are generally considered the pioneering elements in metathesis chemistry, reacts preferentially with olefins. Table 1.1 shows the binding trends for these four transition metal olefin metathesis catalysts.

Titanium	Tungsten	Molybdenum	Ruthenium
Acids	Acids	Acids	Olefins
Alcohols, Water	Alcohols, Water	Alcohols, Water	Acids
Aldehydes	Aldehydes	Aldehydes	Alcohols, Water
Ketones	Ketones	Olefins	Aldehydes
Esters, Amides	Olefins	Ketones	Ketones
Olefins	Esters, Amides	Esters, Amides	Esters, Amides

Increasing reactivity ↑

Table 1.1 Functional group tolerance of transition metal olefin metathesis catalysts (Oakley, 2004)

For decades, the stability of ruthenium catalysts towards alcohols, aldehydes, carboxylic acids and water was overlooked due to the low metathesis activity observed for ruthenium salts. Later it was found that aqueous conditions could be used to promote faster ROMP reactions, and the potential of ruthenium catalysts was re-examined. A considerable number of well-defined ruthenium catalysts have been developed since then. Figure 1.4 shows a selection of these.

In 1992, Robert H. Grubbs and co-workers at the California Institute of Technology developed the first metathesis active ruthenium alkylidene catalyst (catalyst **3** in Figure 1.4). With such a catalyst, norbornene could be polymerized in aqueous or anhydrous environments. The catalyst was limited to ROMP of highly strained cyclic monomers. By exchanging the triphenylphosphine (PPh₃) ligands on catalyst **3** with large, electron-donating tricyclohexylphosphine (PCy₃) ligands, metathesis activity was increased tremendously. Unlike its predecessors, catalyst **4** (see Figure 1.4) could perform ROMP of low ring-strain monomers, such as cyclopentene, and it became the first ruthenium catalyst that was active towards acyclic metathesis processes (Oakley, 2004).

A new method of synthesizing substituted ruthenium alkylidenes was developed in 1995. The method made use of diazoalkanes as the carbene source and led to the benzylidene catalyst **5** (see Figure 1.4), the so-called “first-generation Grubbs” catalyst. It is a 16-electron ruthenium

alkylidene and is a combination of the bulky, electron-donating PCy₃ ligand, the more electron-withdrawing halide ligands (Chlorine), and the fast-initiating benzylidene moiety. It exists in a distorted square pyramidal geometry with the alkylidene in the axial position and the alternating phosphines and chlorines in the equatorial positions (Oakley, 2004). The versatility of the catalyst has led to its extensive use in many applications involving olefin metathesis.

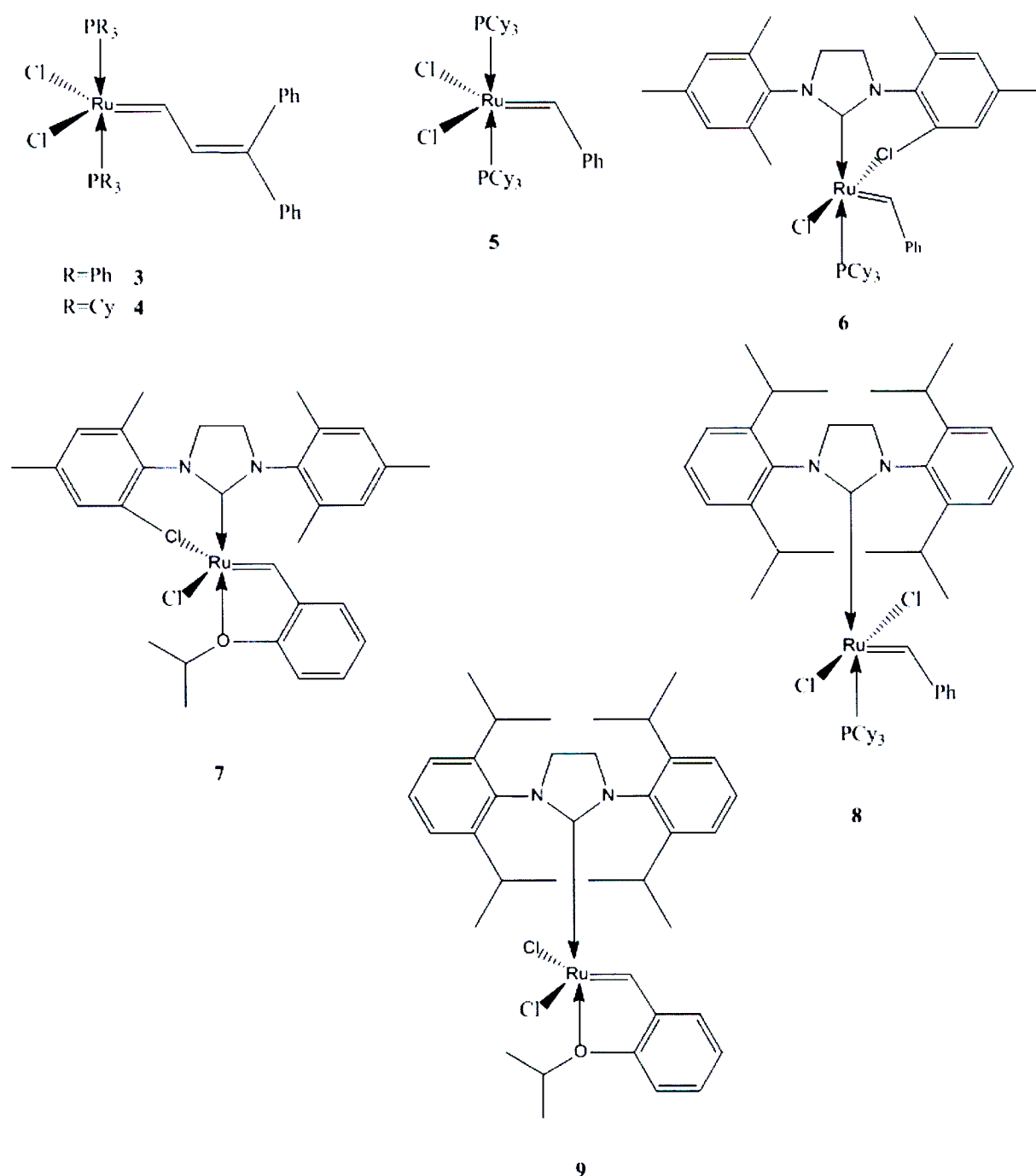


Figure 1.4 A selection of well-defined ruthenium based metathesis catalysts (Oakley, 2004)

In 1999, Grubbs and co-workers developed a new generation of ruthenium-based olefin metathesis catalysts that bore *N*-heterocyclic carbene (NHC) ligands in place of one of the phosphine ligands (catalyst **6** in Figure 1.4). This catalyst has become known as the “second generation Grubbs” catalyst (Oakley, 2004). A mixed ligand system, as in catalyst **6**, was designed in order to utilize the stronger electron-donating ability of the NHC ligand as well as the steric bulk, to more effectively stabilize the electron-deficient, 14-electron intermediates that promote olefin metathesis. Catalyst **6** has superior activity to its predecessor (catalyst **5**), including high reaction rates for ROMP of low-strain cyclic olefins, ROMP of sterically hindered tri-substituted olefins and RCM of sterically demanding dienes to produce tri- and tetra-substituted olefins. Catalyst **6** has comparable activity to the Schrock molybdenum catalyst (catalyst **2** in Figure 1.3) but also maintains the functional group tolerance of catalyst **5**. The catalyst has high thermal stability at high temperatures, and a considerably longer catalyst lifetime (Oakley, 2004).

There exist three further modifications of the “second-generation Grubbs” catalyst which deserve mention (Oakley, 1999). Hoveyda’s catalyst (catalyst **7** in Figure 1.4), Mol’s catalyst (catalyst **8** in Figure 1.4) and the Hoveyda-Mol hybrid (catalyst **9** in Figure 1.4) are specific complexes synthesized from the catalyst **6** base. On Hoveyda’s catalyst, the alkylidene has an isopropyl group in the ortho position of the aromatic ring, on which the oxygen atom coordinates to the ruthenium centre in place of the phosphine ligand. With this arrangement, when undergoing RCM, the original oxygen-coordinated catalyst is reformed from the fragments of the metathesis intermediate, which gives it an extremely long catalyst lifetime in solution. In a specific environment, where intermediate structures can dissociate, the catalyst may decompose. Mol’s catalyst further increases the steric bulk of the NHC ligand with bulky isopropyl groups on its aromatic rings, allowing enhanced rates of reaction even at low temperatures. The Hoveyda-Mol hybrid combines the advantages of the first two variations of Grubbs’s second-generation catalyst. One major disadvantage of the second-generation series of catalysts is that in many of the applied metathesis processes, olefin isomerization has been observed.

1.3 Industrial applications of olefin metathesis

Presently, there are various commercial applications of olefin metathesis. These processes have been successively developed over the four decades since the first industrial use of the reaction. The material presented here is a summary of the comprehensive review by Mol (2004), and also includes processes that are now considered obsolete.

1.3.1. Production of normal olefins

1.3.1.1 Production of propene

About 65% of the world's propene is obtained from naphtha steam crackers, with a similarly large amount coming from fluid catalytic cracking units at oil refineries. Fischer-Tropsch reactions, implicated in coal-to-liquids and gas-to-liquids processes, also produce small amounts of the three-carbon olefin. The uses of propene include polypropylene acrylonitrile, oxo alcohol and acrylic acid manufacture (Mol, 2004; Huang, 2007).

1.3.1.1(a) The Phillips triolefin process

Propene may be produced via the metathesis reaction of a mixture of ethene and 2-butene.



The process, called the Phillips tri-olefin process, which uses a heterogeneous catalyst system, was originally developed by Phillips Petroleum Co., USA and operated from 1966 to 1972 for the conversion of propene into ethene and butene, which were more in demand at the time (Mol, 2004). The true forward process (1) is now offered by ABB Lummus Global, Houston (USA), for license as olefins conversion technology (OCT). The process flow is illustrated in Figure 1.5. Fresh C_4 's and a C_4 recycle are mixed with ethene feed gas plus recycled ethene and sent through a guard bed to remove trace impurities from the mixed feed. The feed is heated before entering the metathesis reactor. The reaction temperature and pressure are 260°C and between 30bar and 35bar, respectively. The reaction is carried out over a mixture of WO_3/SiO_2 and MgO , with the latter driving isomerization reactions and the former acting as a metathesis catalyst. The catalyst must be regenerated regularly to maintain acceptable levels of activity. The conversion attained is greater than 60% and the selectivity for propene exceeds 90%. The Lyondell Petroleum Co. brought a modified process on-stream in 1985. In their process, part of the ethene from the ethane-cracking units is dimerized to 2-butene using a homogeneous nickel

catalyst (developed by Phillips Petroleum Co.), which reacts with the rest of the ethene to produce propene (Mol, 2004).

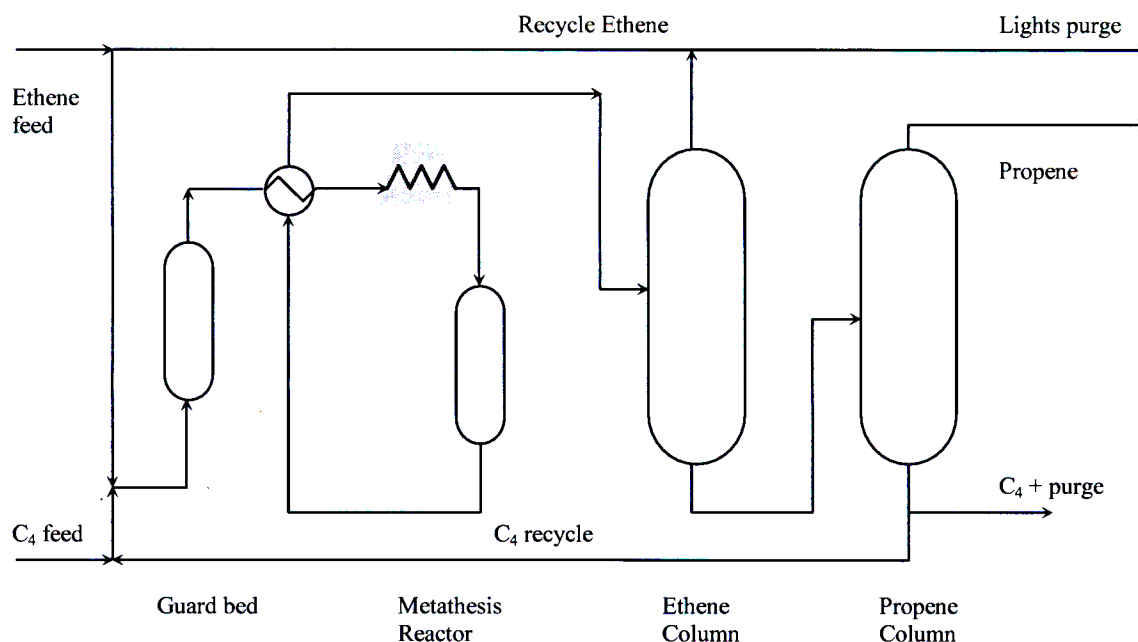


Figure 1.5 The OCT process (reversed Phillips triolefin process) (Mol, 2004)

In 2001, BASF FINA Petrochemicals began operating a naphtha steam cracker with an integrated metathesis unit employing OCT technology to enhance the production of propene in relation to ethene. The OCT process has been used in Japan by Mitsui Chemicals and in China by a joint venture of BP Chemical, Sinopec and Shanghai Petrochemical Corporation for propene production. Further application has been planned by Nippon Petrochemicals and Petrochemical Corporation Singapore, to increase propene capacity at existing installations by more than 100 000 tons-per-year each.

1.3.1.1(b) The Meta-4 process

The Institut Français du Pétrole (IFP) and the Chinese Petroleum Corporation have jointly developed a process for the production of propene, called Meta-4 (Mol, 2004). In their process, ethene and 2-butene react with each other in the liquid phase in the presence of a $\text{Re}_2\text{O}_7/\text{Al}_2\text{O}_3$ catalyst at 35°C and 60bar. The cost of the catalyst remains very high, which is why the process has not yet seen commercial application.

1.3.1.2 Production of 1-hexene

Sinopec's olefin plant in Tianjin (China) uses OCT technology for the metathesis of butene to produce 3-hexene, which is subsequently isomerized into 1-hexene (a high-value comonomer used in the production of polyethylene), together with ethene and propene.

1.3.1.3 Production of neohexene



Figure 1.6 Synthesis of neohexene

Neohexene (3,3-dimethyl-1-butene) is an important intermediate in the synthesis of Tolanide[®], a synthetic musk perfume, and Terbinafine[®], an anti-fungal agent (Mol, 2004). A Chevron Phillips neohexene plant has been operating since 1980, with a capacity of 1400 tons-per-year. The reactant phase consists of a mixture of 2,4,4-trimethyl-2-pentene and 2,4,4-trimethyl-1-pentene. Cross metathesis of the former with ethene yields neohexene, while the latter undergoes isomerization to 2,4,4-trimethyl-2-pentene before being consumed in the metathesis reaction (Figure 1.6).

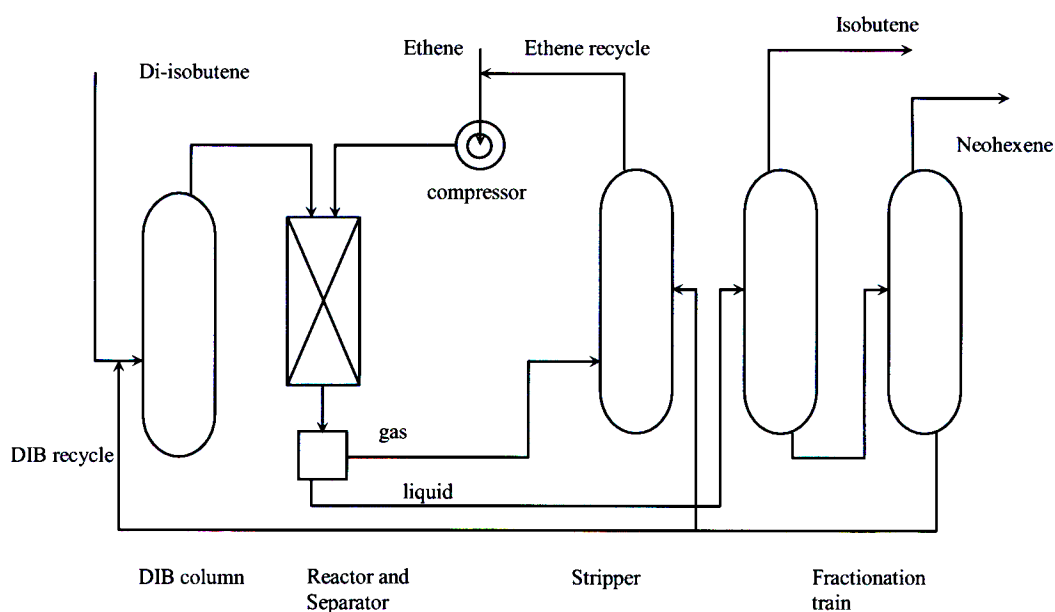


Figure 1.7 The neohexene process (Mol, 2004)

A 1:3 catalyst mixture of WO_3/SiO_2 and MgO is used at 370°C and 30bar. Figure 1.7 shows the process scheme of the neohexene process. Di-isobutane is first distilled to remove an oxidation inhibitor, which poisons the catalyst system (Mol, 2004). The di-isobutene and pressurized ethene (fresh and recycled gas) enters the reactor in down-flow. The separation of reactants and products is achieved by stripping and fractionation. The catalyst is regenerated in a temperature controlled combustion involving air and an inert gas.

1.3.1.4 The Shell higher olefins process (SHOP)

A process exists for producing linear higher olefins from ethene incorporating olefin metathesis. This process is called the Shell higher olefins process and takes place in three stages. First, ethene is oligomerized using a homogeneous nickel-phosphine catalyst, at $90\text{--}100^\circ\text{C}$ and 100–110 bar, in a polar solvent (1,4-butanediol) to yield a mixture of linear even-numbered α -olefins in the C_4 to C_{40} range with a Schulz-Flory type of distribution (Figure 1.8) (Mol, 2004).

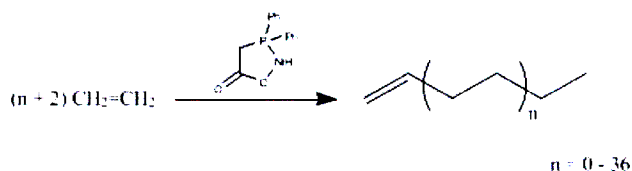


Figure 1.8 Oligomerization of ethene

The catalyst is prepared from a nickel salt (nickel chloride) and a chelating phosphorous-oxygen ligand by reduction with sodium boron hydride. The products that are formed are immiscible with the solvent, which results in simple solvent recovery and product separation. The α -olefins in the C_6 to C_{18} range are separated from the product mixture by distillation. Further separation may yield valuable co-monomers or raw stock for the production of synthetic lubricants, detergent alcohols, etc. The remaining products are purified to remove catalyst and residues. In the second step, these products undergo double-bond isomerization over a solid potassium catalyst to give a mixture of internal alkenes. In the third step, this mixture undergoes cross-metathesis over an alumina-supported molybdate catalyst ($100\text{--}125^\circ\text{C}$ and 10 bar), resulting in a statistical distribution of linear internal alkenes. 10–15 wt% of this yield is the desired $\text{C}_{11}\text{--}\text{C}_{14}$ linear fraction, which is separated out via distillation. The remaining alkenes are recycled. The final product consists of >96% linear internal $\text{C}_{11}\text{--}\text{C}_{14}$ alkenes. These are converted into detergent alcohols, via a hydroformylation process, or into detergent alkylates (Mol, 2004).

1.3.1.5 Production of α -olefins

Sasol Ltd. uses the Fisher-Tropsch process to make olefins from synthesis gas, which comes from coal or natural gas. One of the characteristics of this process is insufficient selectivity, which results in the production of undesirable or low-value olefins (Mol, 2004; van Schalkwyk, 2003 a). Olefin metathesis has been suggested as a method of bringing the products obtained in-line with the market requirements. An example of the conversion of low value olefins to high value olefins that can be employed in downstream processes is the conversion of low-value C_7 α -olefins to internal C_{12} olefins, which can be used as detergent alcohol feedstock (Mol, 2004). The WO_3/SiO_2 metathesis catalyst can be applied for such a purpose.

1.3.2 Production of polymers

Several industrial processes involving catalyzed ring-opening metathesis polymerization (ROMP) reactions of cycloalkenes have been developed and brought into practice.

1.3.2.1 Polyoctenamer

The metathetical polymer of cyclooctene is produced in the presence of a solvent (hexane) and a WCl_6 -based catalyst, with a yield of high molecular weight (Figure 1.9a) and low molecular weight fractions (Figure 1.9b), through propagation and intramolecular backbiting metathesis reactions respectively. The commercial name is Vestenamer[®].

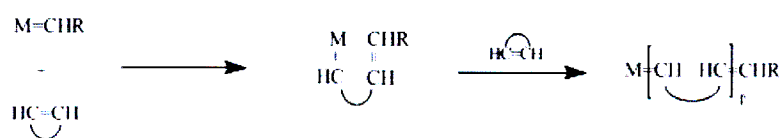


Figure 1.9a Synthesis of cyclooctene – high molecular weight fraction (Mol, 2004)

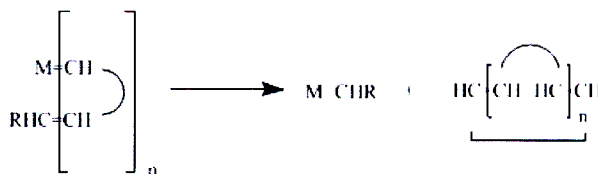


Figure 1.9b Synthesis of cyclooctene – low molecular weight fraction (Mol, 2004)

1.3.2.2 Polynorbornene

Polynorbornene was the first polymer produced commercially via a metathesis process under the trade name Norsorex[®]. The polymer is obtained by ROMP of 2-norbornene (Figure 1.10). The process uses a RuCl_3/HCl catalyst in butanol, under an air atmosphere.

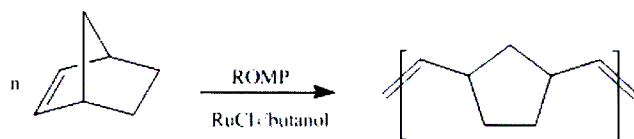


Figure 1.10 Synthesis of polynorbornene

1.3.2.3 Polydicyclopentadiene

ROMP of *endo*-dicyclopentadiene (DCPD), under a certain set of operating conditions, yields a tough, rigid, thermoset cross-linked polymer with excellent impact strength (Figure 1.11, path b), rather than a linear polymer (Figure 1.11, path a). The product has been marketed under the trade names Telene[®] by BFGoodrich Co., and Metton[®] by Hercules Inc. Complex reaction injection moulding processes have been described in the literature (Mol, 2004).

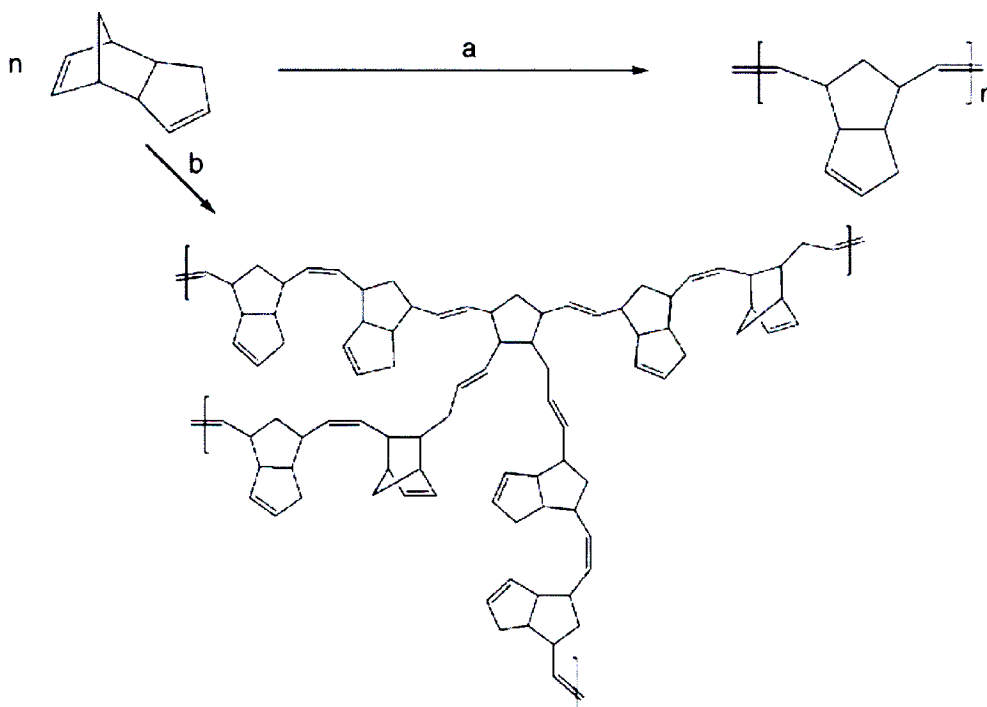


Figure 1.11 ROMP of *endo*-dicyclopentadiene (Mol, 2004)

1.3.2.4 Hydrogenated polymers

Nippon Zeon produces the polymer Zeonex® (i) by ROMP of norbornene followed by partial or total hydrogenation. An example of the process is given in scheme (Figure 1.12). Zeonor® (ii) is an amorphous hydrogenated co-polymer, produced via similar techniques.

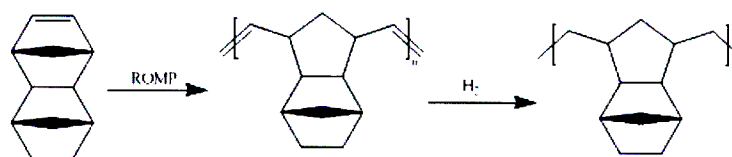
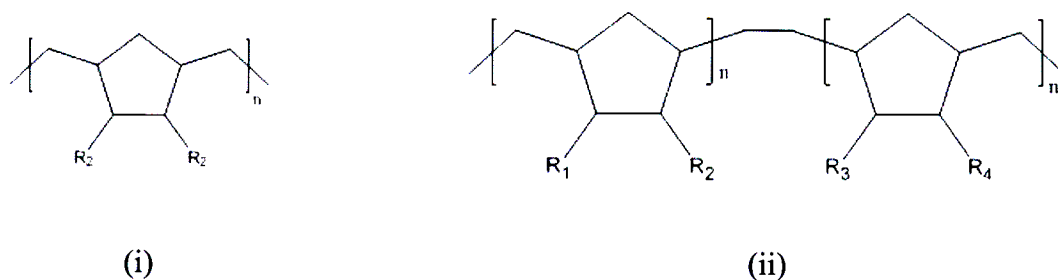


Figure 1.12 Synthesis of Zeonex®

1.3.3 Other applications

The production of fine chemicals based on metathesis processes is currently expanding. In Germany, Symrise is making cyclohexadecadiene by the metathesis of cyclooctene over a heterogeneous rhenium oxide catalyst (Mol, 2004). Pheromones are being produced via metathesis by Materia Inc. (USA), using a ruthenium-based catalyst. Efficient homogeneous and heterogeneous catalysts have also been developed for the oleochemical industry, for the metathesis of unsaturated natural fats and oils.

1.4 Research objectives

The literature is largely devoid of kinetic information regarding the metathesis of longer chain terminal olefins over WO_3/SiO_2 . Intensive research efforts and practical application of this reaction system have been limited to olefins such as propylene and butene. Even basic data, relating to the effect of operating conditions on reaction performance, appears to be lacking. A qualitative examination of the domain of operating conditions for the metathesis of 1-hexene over WO_3/SiO_2 was undertaken in this study, using a full factorial experimental design with two levels and three variables. Two tungsten catalysts of different specific surface area (catalyst A and B), both obtained from Sasol, were used in the experiments. The objective of these experiments was to investigate how the combined effects of reaction temperature, space time and feed gas composition influence selected performance parameters *viz.*, 1-hexene conversion, the selectivity and yield of olefins in the $\text{C}_7 - \text{C}_{16}$ range and the selectivity and yield of decene (the primary metathesis product) in particular. Also, the process conditions were to be optimized to obtain the maximum yield towards decene. In addition, the suitability of the catalyst provided by Sasol for the metathesis of 1-hexene was to be assessed.

The WO_3/SiO_2 metathesis catalyst becomes fully active only after being brought into contact with the reactant alkene for a short period of time. This phenomenon has been ascribed to the fact that the feed material must first reduce the surface phase to a lower oxidation state that is active towards metathesis. Pre-treatment procedures for this catalyst system have been found to affect the length of this induction period, as well as the final conversion and selectivity. For this work, oxidative pre-treatment under air, reduction in H_2 and an inert N_2 purge were considered. The effect of each of these periods on reaction performance (conversion, selectivity) was to be investigated.

The catalyst performance is generally affected by both internal and external mass transfer resistances. In order to assess the effect of intraparticle mass transfer on the overall reaction rate, experiments with different catalyst particle sizes were performed. The results were analyzed in order to determine whether the process was operating under reaction or transport control. In the experimental test for external mass transfer resistance, space time was varied while maintaining all other variables at constant values. Experiments were conducted at low conversions such that axial concentration gradients could be ignored. The assumption of a constant reaction rate and hence negligible external mass transfer resistance was checked by observing the linearity of a plot of conversion versus space time.

1.5 Outline of the dissertation

In this chapter the reader has been afforded the opportunity to familiarize oneself with the fundamental aspects of olefin metathesis, historical development of the reaction system and various commercial applications. The objectives of the study have subsequently been delineated.

In Chapter 2, an overview of the current knowledge about tungsten-based metathesis catalyst systems, in particular olefin metathesis over WO_3/SiO_2 , is presented. The trioxide catalyst is discussed in detail. Surface characteristics and structural properties are treated. The development of the metathesis reaction mechanism, from simple pair-wise swapping to the propagating carbene mechanism currently accepted, is also discussed. Important aspects of olefin metathesis over WO_3/SiO_2 are considered, including isomerization reactions and their effect on overall selectivity. The chapter closes with a brief review of the modes of catalyst deactivation most pertinent to this reaction system.

Chapter 3 deals with the design of the experimental program using factorial methods and the selection of reactor dimensions that ensure that the work is conducted within a range appropriate for laboratory tests. The methods used for the elimination of mass transfer resistances are also discussed.

In Chapter 4 the three sets of experimental equipment used in the study are described in detail. These include an auxiliary rig for preliminary tests, a system commissioned at the Technical University of Łódź, Poland and the final vapour phase reaction system installed at the School of Chemical Engineering, the University of KwaZulu-Natal, and used to carry out the bulk of the experimental work.

Experimental methods are discussed in Chapter 5. Here material is presented on the G.C. quantification techniques used in the study, as well as other instrumental methods such as size estimation, absorbance measurements and catalyst surface characterization via BET and TPD/TPR analyses.

The results of all preliminary tests and the experimental work pertaining to the search for optimal operating conditions, pre-treatment investigation and the study of transport effects are presented and discussed in Chapter 6.

Concluding remarks for this work, as well as recommendations for expanding the research program are given in Chapter 7.

Chapter 2

Literature review

2.1 The WO_3/SiO_2 metathesis catalyst

Although homogeneous metathesis catalyst systems have received a great amount of attention in recent years, with the subsequent development of well defined catalysts that exhibit high activity and selectivity, the industrial application of such systems remains limited. This is due to problems associated with catalyst recovery and product separation. For many current processes, the use of heterogeneous catalysts, including WO_3/SiO_2 , is preferred (Aguado et al., 2005). The performance of heterogeneous metathesis catalyst systems depends on the oxidation state of the metal, the geometry of the surface complex formed, the nature and number of ligands attached to the metal centre and the nature of the support used.

The inferior performance of WO_3 on alumina as a metathesis catalyst has been reported in the literature (Rodriguez-Ramos et al., 1995). WO_3/SiO_2 has exhibited higher selectivity, lower rates of isomerization especially towards branched products and almost constant activity over time. At the high temperatures employed for metathesis reactions, this catalyst appears to resist poisons that would normally have a debilitating effect on the system. The drawback of using this type of catalyst is that in the operating environment, side reactions are also prominent. Supported WO_x clusters are active and stable catalysts for isomerization, dehydration and cracking reactions (Barton et al., 1998). The high isomerization and cracking rates and

selectivity of 1-pentane over WO_x/ZrO_2 have been attributed to the strong surface acidity of the catalyst.

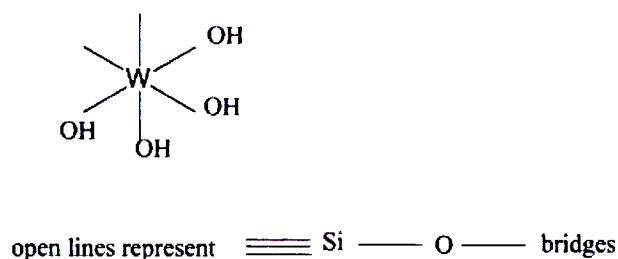


Figure 2.1 Fully hydrated WO_3/SiO_2 catalyst

Several structural forms of WO_3 on SiO_2 have been observed. The fully hydrated state at ambient temperature in air (Figure 2.1) assumes a distorted octahedral form, whereas the dry state (Figure 2.2) shows an isolated and dimeric tetrahedral co-ordination of tungsten.

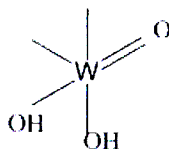


Figure 2.2 Dehydrated WO_3/SiO_2 catalyst

Dependent on the catalyst preparation method, the dehydrated surface complex can be derived from the full octahedral trioxide $\text{W}(\text{OH})_6$. These are attached to the support material either sharing a corner (I), an edge (II) or a plane (III in Figure 2.3). A more than three-fold bonding is not probable owing to the rigid tetrahedral structure of silica gel and silicates. A catalyst prepared via reaction of a solution of tungsten hexachloride and silica in a deoxygenated benzene solvent resembles surface structure II in Figure 2.3. Cogelation of the tungsten hexachloride mixture in tetraethoxysilane and hydrochloric acid results in catalysts exhibiting a hydrated surface structure closer to III in Figure 2.3. Impregnation of silica gel using a solution of ammonium metatungstate may be assigned surface complexes similar to II in Figure 2.3 (van Roosmaalen, 1980).

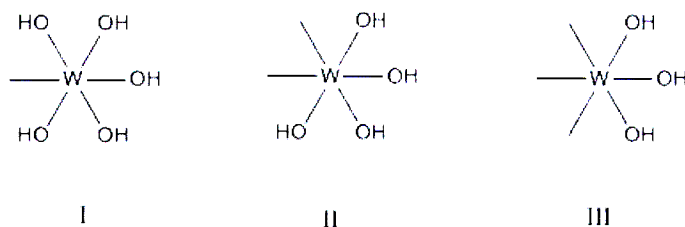


Figure 2.3 Various forms of the fully hydrated octahedral tungsten trioxide

Neighbouring units exhibiting surface structure I may react with each other to form oxo bridges. This would result in a silicon-bound oligomeric tungsten oxide (Figure 2.4). For surface structure II and surface structure III this type of reaction is unlikely because the resultant oxo bridges would be highly strained.

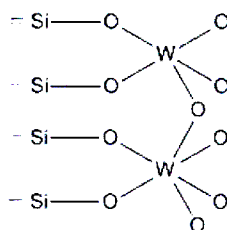


Figure 2.4 Silicon-bound oligomeric tungsten oxide catalyst

Heating tungsten-oxide silica will remove hydroxyl groups with the formation of water (Figure 2.5). For steric reasons the complete dehydration of surface structure II is not achieved (experimentally observed upon heating between 825K and 875K).

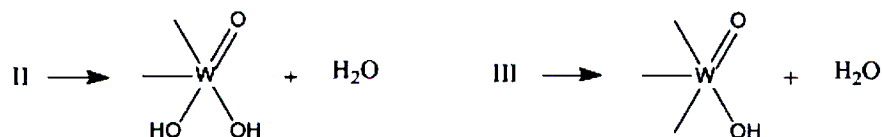


Figure 2.5 Dehydration of WO_3/SiO_2 between 825K and 875K

In a study conducted on dry silica gel, similar results were obtained. When heated under vacuum, the following surface groups were removed in order:

1. physically adsorbed water

2. “bound silanols,” which are mutually hydrogen-bridged $=\text{Si}-\text{OH}$ groups
3. “free silanols,” which are $=\text{Si}-\text{OH}$ groups not involved in H-bonding

Figure 2.6 illustrates point 2 above. Weakly hydrogen-bonded silanol pairs condense upon heating, with the evolution of water (van Roosmaalen and Mol, 1978).

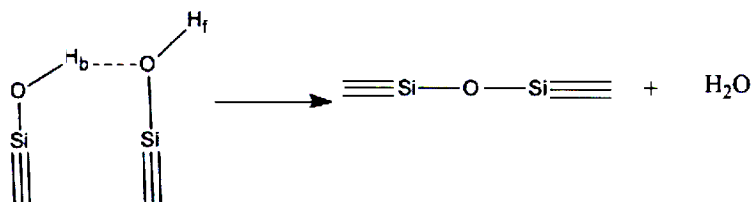


Figure 2.6 Removal of water upon heating, from bound silanols on dry silica gel

The Lewis acid sites of WO_3/SiO_2 are envisaged as tungsten ions in a more or less tetrahedral silica gel matrix. Tungsten is hexavalent, and in order to maintain electrical neutrality, tungsten ions should hold negatively charged species in their co-ordination spheres. On fresh, fully hydrated catalyst these species take the form of hydroxyl groups. These groups may also be retained on the surface of calcined catalyst samples. Surface hydroxyl groups dissociate as $\text{AO}^- + \text{H}^+$ rather than $\text{A}^+ + \text{OH}^-$. This proton release serves an important role in cracking and isomerization reactions over this particular catalyst (Thomas, 1998). Heating of WO_3/SiO_2 in a dry atmosphere removes hydroxyl groups from the surface. As a result of this dehydration the co-ordination number of the tungsten ion decreases from +6 to +5. Van Roosmaalen (1980) measured the surface hydroxylation of 4 wt% and 11 wt% WO_3/SiO_2 , after heating under vacuum at 825K, to be $2.89\mu\text{mol.m}^{-2}$ and $3.47\mu\text{mol.m}^{-2}$ respectively.

Structural analysis of silica supported tungstates indicate formation of strong surface Lewis acid sites related to the presence of co-ordinatively unsaturated W^{6+} species in Keggin-type units formed upon interaction between the metatungstate solution and silica or in supported WO_3 formed by thermal decomposition of these Keggin units (Martin et al., 1998). The structure of the tungsten-containing phase in WO_3/SiO_2 is formed by 12 octahedra (WO_6) around and sharing corners with a central tetrahedron. The 12 octahedra form four clusters (each with three octahedra). The Keggin-type structure is shown in Figure 2.7, where tungsten cations are in a distorted octahedral co-ordination, with short W-O distances due to W-O-W and W-O-Si bridges (Xia et al., 2000).

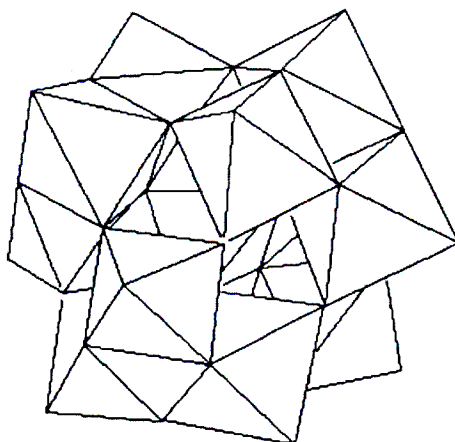


Figure 2.7 Keggin-type structure of WO_3/SiO_2

2.2 The mechanism of the olefin metathesis reaction

The development of an acceptable mechanism for the olefin metathesis reaction has provided one of the most challenging problems in organometallic chemistry (Grubbs et al., 1976). Modelling and theoretical studies have provided evidence for at least three distinct mechanisms. The first mechanism proposed involved a quasi-cyclobutane-metal complex either fulfilling a role as an intermediate or as a transition state (Grubbs et al., 1976). The three reported steps in the process were the formation of a bis-olefin-metal complex, transalkylidenation and a rapid olefin exchange on the metal (Figure 2.8) (Oakley, 2004).

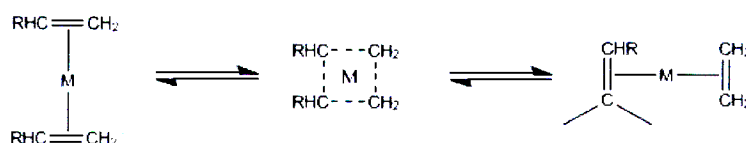


Figure 2.8 Quasi-cyclobutane mechanism of the olefin metathesis reaction (Grubbs et al., 1976)

The mechanism appeared to explain the earliest observations of a $\text{C}=\text{C}$ double bond cleavage rather than the transfer of groups attached to the double bond (transalkylation) and was supported by considerations of the olefin-metal molecular interactions and its ability to provide a low energy pathway for the reaction to proceed. The mechanism also explained why a random distribution of products was observed (Grubbs et al., 1976). Experimental studies, however, showed minimal support for this mechanism. In addition, the formation of the quasi-

cyclobutane-metal complex followed unconventional bonding theory with no precedent to base this type of reaction intermediate on (Oakley, 2004).

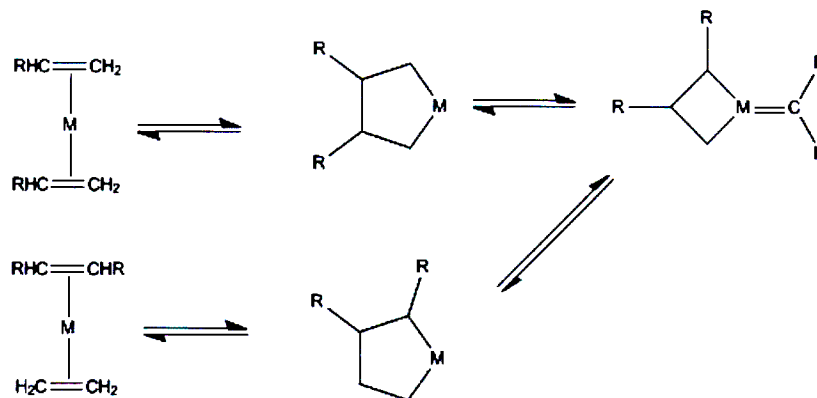


Figure 2.9 Pair-wise mechanism of the olefin metathesis reaction (Grubbs et al., 1976)

The second scheme, involving a “pair-wise” exchange between two olefins in the co-ordination sphere of a metal centre, required a tetramethylene metallacycle as an intermediate (Grubbs et al., 1976). This mechanism required the same bis-olefin-metal complex as a starting point. This reaction received support from the studies of the metal catalyzed cyclo-addition reaction (Figure 2.9). It was claimed that the tetramethylene metallacycle was formed by reacting 1,4-dilithiobutane with WCl_6 , which would then decompose to form metathesis products. However, no proof that the five-membered ring intermediate was actually formed was found, and it was later proven that this mechanism was indeed incorrect (Oakley, 2004).

A third scheme which is distinctly different from the other two, involves a chain reaction in which a metal-carbene complex serves as the active centre (Grubbs et al., 1976). Herrisson and Chauvin (1970) proposed this scheme in 1970 and suggested that it would account for the appearance of cross-products in the initial stages of the reaction between cyclic and acyclic olefins. The propagation reaction involves a transition-metal carbene as the active species with a vacant co-ordination site at the transition metal. The alkene co-ordinates at this vacant site, and subsequently a metallacyclobutane intermediate is formed. The metallacycle is unstable and cleaves to form a new metal carbene complex and a new alkene (Fig 2.10). This new carbene can then continue in the catalyst cycle and reacts with other olefins. The complete sequence of elementary steps is illustrated in Figure 2.10. The initial alkylidene reacts with an olefin to form a methyl alkylidene. This carbene can then continue along in the catalyst cycle as the catalytically active species. Eventually new products are formed from the pieces of the

original olefin. There is a small, practically negligible, amount of a by-product ($R'HC=CHR$) that is formed from the initial alkylidene. The metal-carbene mechanism was the only one of the three proposed mechanisms that did not require unusual bonding theory for an intermediate of the mechanism. The metal-carbene mechanism has become well established as the proper mechanism for olefin metathesis (Oakley, 2004).

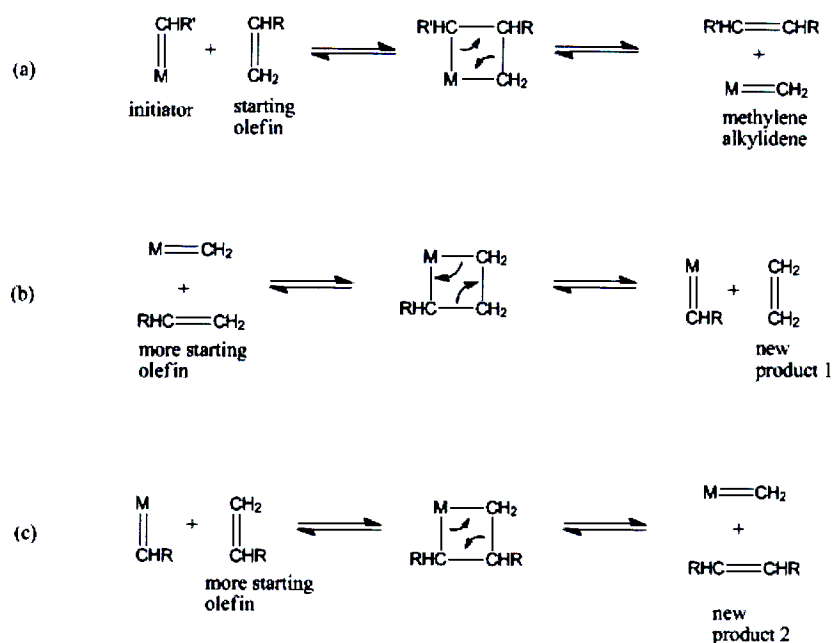


Figure 2.10 Metal-carbene non-pair-wise mechanism for olefin metathesis (Oakley, 2004)

2.3 Alkene metathesis over WO_3/SiO_2

2.3.1 Mechanism

Linear alkene metathesis occurs via a mechanism that involves co-ordination of alkenes to W^{6+} Lewis acid centres on WO_3/SiO_2 (Rodriguez-Ramos et al., 1995). The transalkylidenation reaction is catalytic as it requires a metal centre capable of both generating a metal carbene species ($\text{M}=\text{CHR}$) and leaving a vacant co-ordination site in order to form the necessary metallacyclobutane intermediate.

For metathesis reactions carried out over supported WO_3 catalysts, the literature mentions several instances of a break-in or induction period, where a steady increase in the activity of the catalyst was observed during the initial stages of the reaction before a stable maximum was reached (Gangwal et al., 1977). Reduction of the promoter from WO_3 to $\text{WO}_{2.9}$ was also observed. A reactant flow interruption of just 30 seconds resulted in a 50% reduction in the activity, which was subsequently re-established after 5-10 minutes on-stream. These observations showed that the reduced state of the catalyst that corresponded to a stoichiometric phase that gave maximum activity could only be established and maintained by the reactant hydrocarbon. An early explanation for the observed catalyst induction was that the alkene initially reacts with the surface to form an organic fragment which acts as an active but unstable site. There is a continuous formation and destruction of these sites as the reaction proceeds, until steady-state is achieved (Gangwal et al., 1977).

The induction period was presumed to proceed through two steps: reduction of the WO_3 precursor followed by the formation of the metallacarbene intermediate through which the metatheses occur (Basrur et al., 1991). Basrur et al. (1991) found that during the initial stages of the metathesis of propene over WO_3/SiO_2 , an oxygenated species of propene was formed. This species, later identified as acetone, was a by-product of the reduction of the metal centre by the reactant alkene. When pre-reduced catalysts were used (after pre-treatment under CO or H_2) a decrease in the amount of acetone produced was observed. It was also shown that the temperature for the onset of propene metathesis coincided with that which was required for the reduction of tungsten oxide. Reduction of WO_3 resulted in a non-stoichiometric surface phase. The exact form of this species was not confirmed by these researchers, but the observed colour change from pale yellow to blue-violet after catalysis indicated that the final oxidation state was probably $\text{WO}_{2.9}$.

The early work of Westhoff and Moulijn (1977) shows some agreement with these results. It was observed that the most active stoichiometric composition of tungsten oxide for metathesis lies between WO_3 and $\text{WO}_{2.95}$. Hence, reduction of the metal centre was an important step in the sequence of elementary surface processes. Pre-reduction under H_2 was also undertaken, with improved induction periods. It was stated that active sites on the surface may have been blocked by adsorbed oxygen after oxygen calcination of fresh catalyst. Hydrogen treatment was suggested as an efficient method of removing this oxygen.

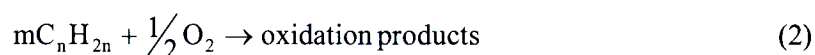
Propene metathesis reaction studies conducted by Luckner and Wills (1973) also showed a change in the stoichiometric state of the transition metal centre from WO_3 to $\text{WO}_{2.9}$. They found that under a reducing atmosphere and between 400°C and 500°C , 120 minutes were

required to achieve such a state. Further reduction to WO_2 (a brown oxide) is thermodynamically unfavourable in this temperature range, and will only proceed with some difficulty at temperatures greater than 600°C for periods longer than 240 minutes. The lower oxidation state did result in a 30% increase in metathesis activity.

Brønsted acid sites form on WO_3 clusters when a lower valent element replaces the W^{6+} metal centre, or when the surface is reduced, e.g. via H_2 or hydrocarbon treatments. A net negative charge is caused by slight reduction of the W^{6+} centres in reactant hydrocarbon environments. The temporary charge imbalance leads to the formation of Brønsted acid centres on the support. H_2 is also involved in the generation and maintenance of Brønsted acid sites during catalytic reactions (Barton et al., 1998). On contact with H_2 , Lewis acid sites are converted to Brønsted acid sites, which cannot remain extant in the absence of this reducing environment. Migration of species from the support onto the exposed surface of the otherwise active metal centre, during high temperature H_2 pre-treatments, has also been reported (Thomas, 1998). Such events could be used as a possible explanation for changes in catalyst activity and especially selectivity in a variety of hydrocarbon conversions, including metathesis.

Yellow WO_3 crystallites are readily reduced during alcohol reactions above 523K to a stoichiometry corresponding to $\text{WO}_{2.5}$. This slightly reduced blue oxide was found to be more active than WO_3 and to re-oxidize in air at room temperature (Barton et al., 1998; Thomas, 1998). The structure of metal oxide catalysts is rarely wholly stoichiometric, like for example MO_3 , where M represents the transition metal centre. The actual stoichiometry, prior to reductive pre-treatments, may be closer to $\text{MO}_{2.95}$ (Thomas, 1998). The highly dispersed, amorphous surface complex WO_3 , co-ordinated on an inert support, is much more difficult to reduce than the crystal form of WO_3 (Horsley et al., 1987).

Thermodynamically, a reduction reaction can be divided into two steps, i.e. oxygen dissociation from a metal oxide (1) and oxygen uptake by an olefin (2) (Aso et al., 1979):



The break-in or induction period which is observed for many of the heterogeneous metathesis catalyst systems, particularly WO_3/SiO_2 , is a reduction step (van Roosmalen and Mol, 1982). A co-ordinated oxygen atom is removed from the dehydrated complex, with the formation of

water or an oxygenated hydrocarbon (Figure 2.11). Silica protects tungsten from being reduced beyond the +4 state by shielding a large part of the co-ordination sphere.

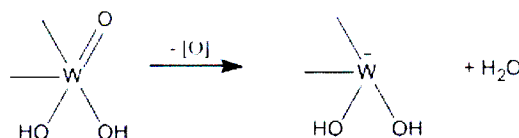


Figure 2.11 Break – in of the WO_3/SiO_2 catalyst under hydrogen

The interaction of an alkene with the non-reduced surface species produces a carbenium ion intermediate, with subsequent proton release and metal-alkene compound formation (Figure 2.12). The proton has been linked to the formation of the initiator for metatheses, as well as isomerization.

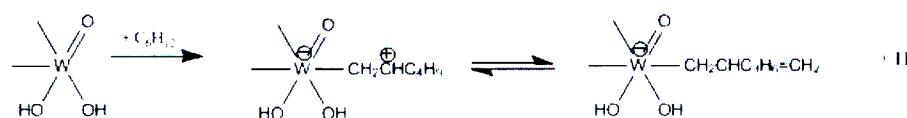


Figure 2.12 Interaction of 1-hexene with non-reduced WO_3/SiO_2

The way in which the initial metal-carbene is formed was for many years not clearly understood. The most accepted routes to the first metal carbene include the formation of a π -complex between the reactant alkene and the transition metal, followed by either a 1,2-hydrogen shift mechanism (Figure 2.13), or a hydride transfer to form successively a π -allyl complex, a metallacyclobutane and the metal carbene (Figure 2.14) (Mol, 1999). On solid oxidic catalysts, these hydrides are believed to originate from the interaction of reduced transition-metal ions with Brønsted surface hydroxyls of the support (van Roosmalen and Mol, 1982).

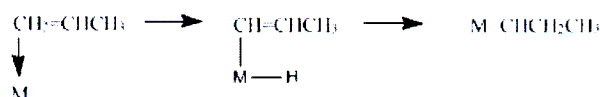


Figure 2.13 Formation of the initial metal-carbene – hydrogen shift mechanism

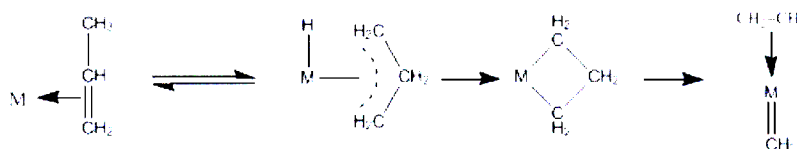


Figure 2.14 Formation of the initial metal-carbene – hydride transfer mechanism

Activated WO_3/SiO_2 , through ammonia and pyridine adsorption, was not found to hold strong Brønsted acid sites. A limited number of metatheses proceed through the initiator before the chain of reactions terminate. Such a scheme has been linked to catalyst selectivity and effectiveness (van Roosmalen and Mol, 1982). The detailed mechanism of carbene formation is illustrated in Figure 2.15. First, protonation of the reduced surface species leads to a tungsten hydride complex. The initial H^+ comes from the interaction of the reactant alkene with the non-reduced surface species. Adsorption of 1-hexene and a $\beta\text{-H}_2$ addition yields an intermediate, which through back donation of the proton gives a carbenoid chain initiator (van Roosmalen and Mol, 1982). The lifetime of this metal-carbene is very short.

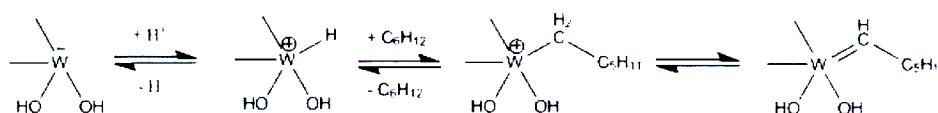


Figure 2.15 Formation of the initiator for 1-hexene metathesis

The key intermediate in the carbene mechanism is supposed to be a metallacyclobutane complex. The stereo-selectivity of metathesis might be related to the structure of this intermediate (Kapteijn and Mol, 1982). A flat ring and puckered ring formation has been indicated for this type of complex (Figure 2.16) but the synthesis of stable tungsta-, titania- and platina-cyclobutanes appears to suggest that the intermediate structure is not flat, but the ring is bent across the C1-C3 axis. The larger the ring substituents, the larger the dihedral angle (between 10° and 30°).

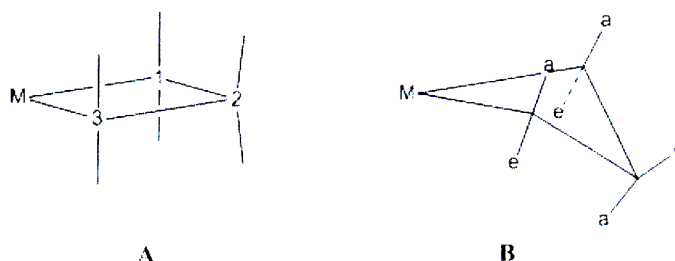


Figure 2.16 Structure of the metallacyclobutane intermediate in metathesis reactions (Kapteijn and Mol, 1982)

It has also been suggested that the repulsive interactions between the ring substituents as well as the interactions of the substituents with the ligands on the transition metal (or catalyst surface) govern the stereoselectivity of the reaction. Steric repulsions in the metallocyclobutane transition state would cause an increase in activation energy, and lower the rate of its formation (Kapteijn and Mol, 1982).

The structural transformation of this alkylidene intermediate during one metathesis cycle is illustrated in Figure 2.17 for the self-metathesis reaction of two molecules of 1-hexene (Kapteijn and Mol, 1982). The initiator ($M=CH-C_5H_{11}$) reacts with a 1-hexene molecule to yield a by-product ($C_4H_9HC=CHC_5H_{11}$) and a methyl alkylidene (Fig. 2.17a). The actual metathesis cycle thus begins, with the coupling of the methyl alkylidene and a 1-hexene molecule through bond shearing of the alkene double bond, and weak bond formation to yield the puckered ring metallacycle (Fig. 2.17b). The ephemeral intermediate decomposes into the first product (ethylene) and a new alkylidene. The leaving group (ethylene) is sketched in red and the newly formed alkylidene in blue. Interaction with another molecule of 1-hexene results in the formation of a second cyclic intermediate (Fig. 2.17c), that subsequently decomposes to yield the second product (5-decene) and the original methyl alkylidene. The methyl alkylidene is recycled, i.e. used in another metathesis cycle which must include a terminal olefin as its reactant (metathesis of isomerized hexene will begin with a different alkylidene). Overall, two molecules of 1-hexene are used per cycle to produce a molecule of ethylene and 5-decene each, which is commonly regarded as the surface reaction. Formation of the initiator and methyl alkylidene, which occurs only once for a large number of such reactions, is not considered part of this cycle. The location of the substituents attached to the three carbon atoms that, together with the tungsten centre, form the puckered ring as indicated in Figure 2.17, are merely for explanatory purposes. A rigorous quantum chemical analysis, minimizing bond energies, would have to be used to obtain the correct equatorial and axial positions for each of the substituents in the intermediate.

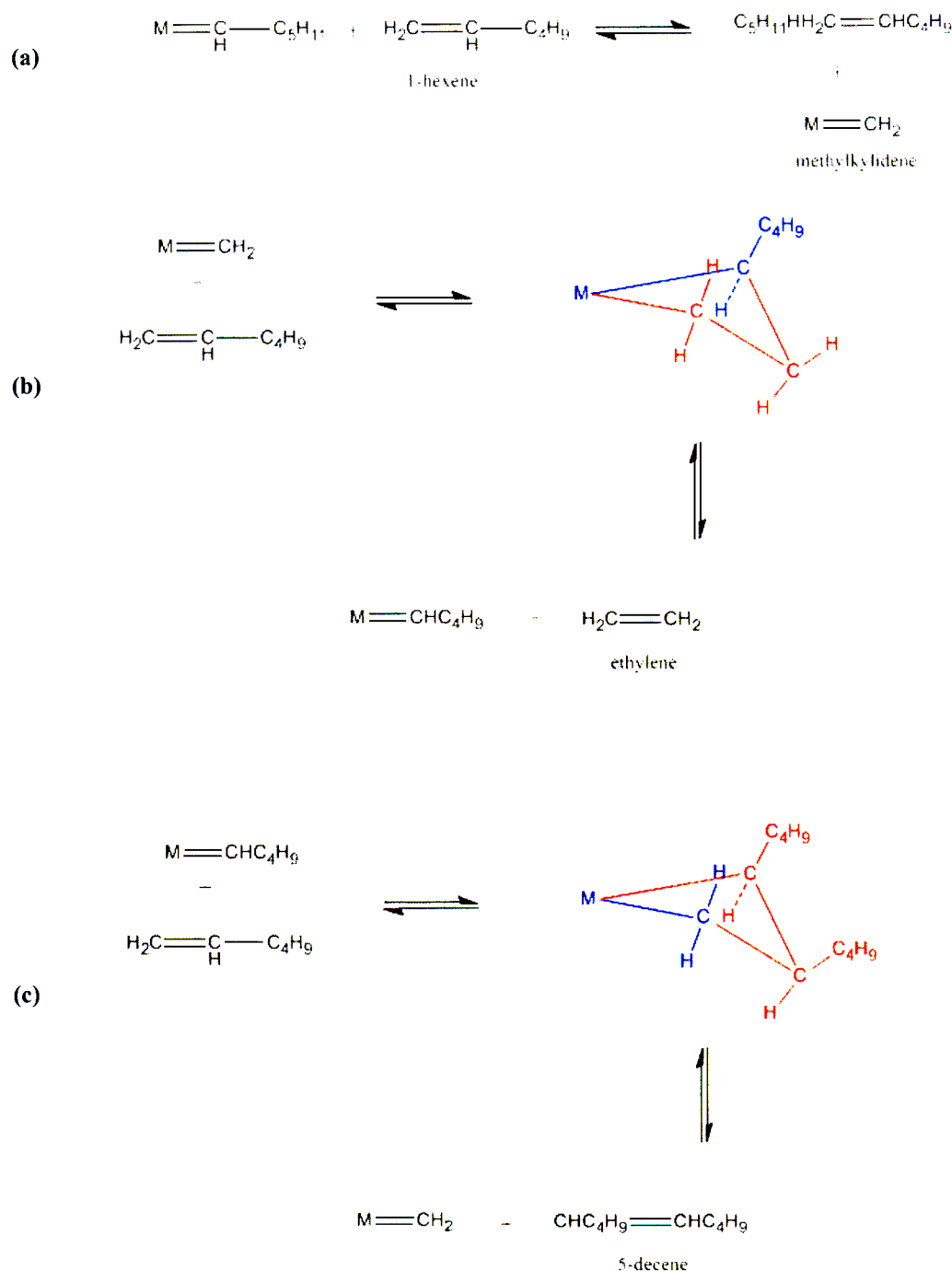


Figure 2.17 Structural transformation of the alkylidene intermediate during one metathesis cycle of 1-hexene self metathesis (Kapteijn and Mol, 1982)

The rate of metathesis reactions was observed to increase with increased dispersion of WO_3 over inert catalyst supports. WO_x surface coverage on Al_2O_3 supports increases with increasing temperature of oxidative pre-treatments which sinter the Al_2O_3 crystallites and force a structural transformation of the inert oxide (Barton et al., 1998). Brønsted acid site density also increases with increased oxidation temperature. This increase appears to be related to the conversion of isolated tungstate groups into polytungstate clusters which delocalize protons among

neighbouring WO_x species. For $\text{WO}_3/\text{Al}_2\text{O}_3$ the increase in Brønsted acidity with surface coverage results from the conversion of edge-shared to corner-shared dehydrated tetrahedra on the catalyst surface (Figure 2.18). The WO_4 clusters are more crowded, with the H^+ required for the conversion being supplied by surface water (Bernholc et al., 1987). Some researchers have found that overall, rather than Brønsted, acidity was attenuated by high temperature oxidative treatments (Gayubo et al., 1993).

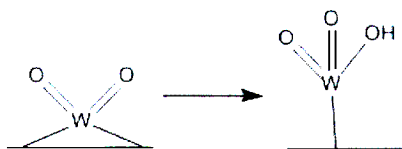


Figure 2.18 Transformation of the $\text{WO}_3/\text{Al}_2\text{O}_3$ surface phase from edge-shared to corner-shared tetrahedra after high temperature oxidative pre-treatment

Pre-treatment of $\text{WO}_3/\text{Al}_2\text{O}_3$ under either air or helium between 873K and 1073K prior to propene metathesis yielded very similar activities. An oxidative treatment for this catalyst combination does not appear to have an effect on metathesis rates. Proper activation here is only attainable under the reactant propene atmosphere (Rodriguez-Ramos et al., 1995). Isomerization and cracking rates (both side-reactions of metathesis reaction systems) depend strongly on the temperature at which fresh catalyst batches are treated in air. High isomerization rates occur in range of high oxidation temperature (900K-1250K for WO_x supported clusters). High temperatures may also result in loss of catalyst surface and a subsequent decrease in WO_x surface coverage (Barton et al., 1998).

In a series of kinetic studies, van Schalkwyk and co-workers investigated the possible application of a WO_3/SiO_2 metathesis catalyst in an industrial environment (van Schalkwyk et al., 2003 a,b and c). A recycle reactor unit was used for the experimental work, with the option of operating in once-through mode. Either a pure 1-Octene feed or an industrial cut 1-heptene stream consisting of 75% 1-heptene, 10% *n*-alkane and 15% branched hydrocarbons were delivered to the unit. The first program focused on the optimization of process conditions for the production of higher alkenes via metathesis. It was found that a reaction temperature of 420°C, a liquid-hour-space-velocity (LHSV, defined as the volumetric liquid flow-rate per hour divided by the volume of the reactor) of 22h^{-1} and a feed to recycle ratio of 1:4 gave a conversion of 74%, $\text{C}_{10}\text{-C}_{13}$ selectivity of 67.6%, C_{12} selectivity of 55% and an online lifetime of about 700h when using the 1-heptene feed stream. An induction period was observed during the first few hours online, as well as improved selectivity to primary metathesis products with time on-stream. It was assumed that the acidity of the catalyst and hence the isomerization

activity decreases with time online, possibly occurring because of blocking of some of the acid sites due to oligomer formation or coking at high temperatures. An investigation of inter-particle mass transfer limitations revealed that the metathesis catalyst did not suffer from such debilitating effects, showing almost constant conversion with varying particle size (0.1mm to 1.0 mm range).

Their second effort was concerned with the regeneration of spent WO_3/SiO_2 after noticeable coking. Activation of the catalyst using reducing gases was also investigated. Earlier works found that the reduction process occurred in two steps, with various stoichiometric forms of the metal oxide implicated (Venables and Brown, 1997). WO_3 was first reduced to $\text{W}_{20}\text{O}_{58}$ followed by a second step to form $\text{W}_{18}\text{O}_{49}$. The second stage of the reduction corresponds to a large mass loss on the surface of the catalyst, which may be attributed to the formation of metal carbenes. The catalyst in this study was reduced in a stream of H_2 or butene after regeneration. WO_3 and $\text{W}_{24}\text{O}_{68}$ were extant on the surface after regeneration under air (the crystalline trioxide is non-active for metathesis). It appears that the WO_3 phase is mobile during treatments, spreading onto the uncovered silica support and with better dispersion, improved selectivity was observed. A pronounced increase in primary metathesis products was observed with reduction in H_2 , even though overall conversion of the feed alkene decreased.

The last set of experiments was used to investigate the metathesis reaction of 1-octene over WO_3/SiO_2 in the presence of different additives (van Schalkwyk et al., 2003 c). Oxygenates used for the poison testing were 2-pentanone, hexanal, acetic acid, butanol and water. These represent the possible components in an industrial 1-heptene feed stream that might have an influence on the performance of the catalyst. The 8% WO_3/SiO_2 catalyst used in this investigation is able to tolerate branched olefins (especially vinylidenes) in the feed without losing significant activity. This might be due to the high operating temperatures employed when dealing with tungsten based metathesis systems, allowing the metal-carbene to overcome steric hindrance. A critical composition of 500ppm was found for each oxygenate used. Above this amount, the additive caused the reaction to become unstable, significantly reducing the rate. A permanent change in the morphology of the catalyst surface was indicated by improved selectivity and activity towards the primary metathesis products when a fresh pure feed was delivered thereafter. The Lewis bases (and Brønsted acids) of about 100-300 ppm present in the feed could actually be beneficial in blocking strong acid sites responsible for side-reactions and the selectivity towards primary metathesis products is increased.

Literature exists on the activity and selectivity of WO_3/SiO_2 metathesis catalysts in the presence of short-chain alkenes like propylene and butene (Basrur et al., 1991; Gangwal et al., 1977;

Huang et al., 2007 a and b; Kapteijn and Mol, 1982; Luckner and Wills, 1973; Wang et al., 2003; Westhoff and Moulijn, 1977). Almost no attention has been given to the behaviour of this metathesis catalyst in the presence of long-chain alkenes like 1-hexene. In the cases where research was done on long-chain alkenes, mostly rhenium and molybdenum based metathesis systems have been studied (Spronk and Mol, 1991; Spronk et al., 1992). The reactivity of different alkenes in the liquid phase over a $\text{Re}_2\text{O}_7/\gamma\text{-Al}_2\text{O}_3$ catalyst as well as the kinetics of deactivation were investigated. The general conclusions of earlier studies on reactivity were that the reactivity of normal alkenes decreases with increasing chain length, that 1-alkenes are less reactive than internal alkenes and that branching close to the double-bond decreases the reactivity. The causes for these differences in reactivity were attributed to differences in metal-carbene stability, steric hindrance during the reaction and thermodynamic limitations. Some researchers attribute the decrease in activity with increasing chain length of the 1-alkene to the fact that the increasing chain length results in an increase in repulsive interaction in the metallacyclobutane intermediate. Spronk and Mol (1991) found this to be less likely. The amount of steric hindrance in this intermediate would largely depend on the interactions between carbon atoms and hydrogen atoms of the substituents which are in close proximity to the ring. These interactions are the same with all linear 1-alkenes. The rate determining step in the metathesis reaction could be the adsorption of the reactant, the inter-conversion of the reactant-carbene complex into the product-carbene complex or desorption of the products. In lieu of the foregoing considerations and the fact that the differences between the alkenes are most obvious in the product alkenes, it seems more likely that desorption of the product is the rate-determining step. Further research and kinetic model development (Spronk et al., 1992) showed that either inter-conversion of the alkene-carbene complex or product desorption could be the rate determining step. The results of their experimental work could not differentiate between the two. The kinetic model developed (including deactivation kinetics) was satisfactory in describing and predicting the product stream for the metathesis of 1-octene over $\text{Re}_2\text{O}_7/\gamma\text{-Al}_2\text{O}_3$.

2.3.2 Reaction kinetics

The development of a realistic kinetic model for the metathesis of olefins over a WO_3/SiO_2 catalyst has been hampered by the propensity for this system to promote isomerization and cracking reactions, reducing the selectivity and increasing the level of complexity. Although a number of researchers have conducted kinetic studies and uncovered various facts concerning the metathesis of linear alkenes over WO_3/SiO_2 (Luckner and Wills, 1973; Westhoff and Moulijn, 1977; Basrur et al., 1991; Gangwal et al., 1977), a model of the reaction has not been presented. Reaction rate expressions for the metathesis of propene over $\text{Re}_2\text{O}_7/\gamma\text{-Al}_2\text{O}_3$ were

derived by Kapteijn et al. (1981) from several kinetic models, using the steady-state approximation, assuming surface uniformity, one or two elementary processes not in quasi-equilibrium and also assuming that the total number of active sites was independent of the partial pressure of the reactants. From the five different models considered:

- a Langmuir-Hinshelwood model
- a Langmuir-Hinshelwood-Hougen-Watson extended model representing consecutive adsorption of two propene molecules on one active centre followed by a surface reaction and desorption of products
- a model based on the formation of an alkene surface complex, reaction with propene and desorption of products
- a second model based on the formation of an alkene surface complex, reaction with propene and exchange of products with a new propene molecule
- a model based on the non-pairwise carbene mechanism

the model based on the non-pairwise exchange of alkylidene groups was found to describe the experimental data better than the other rate expressions (Kapteijn et al., 1981; Gomes and Fuller, 1996). Moreover, the desorption steps have been shown to be the most likely rate-determining steps in the following sequence (M denotes an active site):

Step 1: $C_3H_6 + M=CH_2 \leftrightarrow C_3H_6M=CH_2$

Step 1a: $C_3H_6M=CH_2 \leftrightarrow C_2H_4M=CHCH_3$

Step 2: $C_2H_4M=CHCH_3 \leftrightarrow C_2H_4 + M=CHCH_3$

Step 3: $C_3H_6 + M=CHCH_3 \leftrightarrow C_3H_6M=CHCH_3$

Step 3a: $C_3H_6M=CHCH_3 \leftrightarrow C_4H_8M=CH_2$

Step 4: $C_4H_8M=CH_2 \leftrightarrow C_4H_8 + M=CH_2$

With steps 2 and 4 as the rate determining processes, the kinetic expression is given by

$$r = \frac{k_r K_P (p_P^2 - p_B p_E / K_{eq})}{p_P + K_P p_P^2 + K_E p_E + K_B p_B + K_{PE} p_P p_E + K_{PB} p_P p_B} \quad (2.1)$$

where

$$k_r = L_r k_2 k_4 / (k_2 + k_4)$$

$$K_P = K_1 K_3 (k_2 + k_4) / (k_2 K_1 + k_4 K_3)$$

$$K_E = k_2 / (k_2 K_1 + k_4 K_3) K_2$$

$$K_B = k_4 / (k_2 K_1 + k_4 K_3) K_4$$

$$K_{PE} = k_2 K_1 / (k_2 K_1 + k_4 K_3) K_2$$

$$K_{PB} = k_4 K_3 / (k_2 K_1 + k_4 K_3) K_4$$

$$K_{eq} = K_1 K_2 K_3 K_4$$

L_r is the concentration of active sites for the reaction and p_i is the partial pressure of component i in the system (either ethylene, propene or 2-butene).

Importantly, the Langmuir-Hinshelwood model was rejected on the basis of their results (Kapteijn et al., 1981). Other studies retained the Langmuir-Hinshelwood approach, assuming that the surface reaction between two chemisorbed propene molecules was the rate-controlling step. The following expression was found to be most adequate for describing the reaction kinetics (El-Sawi et al., 1981):

$$r = \frac{k K_P^2 (p_P^2 - p_E p_B / K_{eq})}{(1 + K_E p_E + K_P p_P + K_B p_B)^2} \quad (2.2)$$

Alternatively, the assumption that the reaction takes place between two molecules of propene chemisorbed on two sites of the same active centre in two successive adsorption steps, yields the following expression (surface reaction is rate-determining):

$$r = \frac{k K_P K_P' (p_P^2 - p_E p_B / K_{eq})}{1 + K_E p_E + K_P p_P + K_P K_P' p_P + K_B p_B + K_{EB} p_E p_B} \quad (2.3)$$

Kinetic rate expressions were derived by Spronk, Dekker and Mol (1992) for the metathesis of 1-octene in the liquid phase over a $\text{Re}_2\text{O}_7/\gamma\text{-Al}_2\text{O}_3$ catalyst. The generally accepted carbene mechanism was used as the basis for the kinetic model. The rate expression obtained took the following form:

$$r = k_{\text{exp}} (1 - 2X + (1 - 0.25 / K_{eq}) X^2) \quad (2.4)$$

where

$$k_{\text{exp}} = \frac{NkK_o[O]_0}{1 + K_o[O]_0}$$

X is the fractional conversion of 1-octene, N is the total number of active sites and $[O]_0$ is the initial concentration of 1-octene. The equilibrium constant K_{eq} was pre-determined. The model showed a good statistical fit to experimental data.

The only kinetic rate expressions available in the literature for the heterogeneous gas-phase metathesis of 1-hexene to ethylene and 5-decene were developed by Krasnov, Musaev and Atlas (1986). The expressions were derived using a complex, general-purpose computer code, STEN, and were based on three fundamental reaction mechanisms (ignoring side reactions):

I. Adsorption of two 1-hexene molecules on two neighbouring catalytic sites according to the Langmuir-Hinshelwood mechanism:

1. $C_6H_{12} (H) + S \leftrightarrow C_6H_{12} \cdot S (HS)$
2. $2 C_6H_{12} \cdot S \leftrightarrow C_2H_4 \cdot S (ES) + C_{10}H_{20} \cdot S (DS)$
3. $C_2H_4 \cdot S \leftrightarrow C_2H_4 (E) + S$
4. $C_{10}H_{20} \cdot S \leftrightarrow C_{10}H_{20} (D) + S$

II. Subsequent adsorption of two 1-hexene molecules on one catalytic site according to the Langmuir-Hinshelwood mechanism:

1. $C_6H_{12} (H) + S \leftrightarrow C_6H_{12} \cdot S (HS)$
2. $C_6H_{12} \cdot S + C_6H_{12} \leftrightarrow (C_6H_{12})_2 \cdot S (H_2S)$
3. $(C_6H_{12})_2 \cdot S \leftrightarrow (C_2H_4, C_{10}H_{20}) \cdot S (EDS)$
4. $(C_2H_4, C_{10}H_{20}) \cdot S \leftrightarrow C_{10}H_{20} \cdot S (DS) + C_2H_4 (E)$
5. $(C_2H_4, C_{10}H_{20}) \cdot S \leftrightarrow C_2H_4 \cdot S (ES) + C_{10}H_{20} (D)$
6. $C_{10}H_{20} \cdot S \leftrightarrow C_{10}H_{20} (D) + S$
7. $C_2H_4 \cdot S \leftrightarrow C_2H_4 + S$

III. A mechanism involving the formation of carbene intermediates:

1. $C_6H_{12} (H) + C_5H_{10} \cdot S (AS) \leftrightarrow (C_6H_{12}, C_5H_{10}) \cdot S (HAS)$
2. $(C_6H_{12}, C_5H_{10}) \cdot S \leftrightarrow (C_{10}H_{20}, CH_2) \cdot S (DMS)$
3. $(C_{10}H_{20}, CH_2) \cdot S \leftrightarrow C_{10}H_{20} (D) + CH_2 \cdot S (MS)$
4. $C_6H_{12} + CH_2 \cdot S \leftrightarrow (C_6H_{12}, CH_2) \cdot S (HMS)$
5. $(C_6H_{12}, CH_2) \cdot S \leftrightarrow (C_2H_4, C_5H_{10}) \cdot S (EAS)$
6. $(C_2H_4, C_5H_{10}) \cdot S \leftrightarrow C_2H_4 (E) + C_5H_{10} \cdot S (AS)$

The rates of reaction, as derived by STEN for each mechanism, are presented below.

$$r_I = K_2 K_H^2 (C_H^2 - C_E C_D / K_P) / (\sum_1)^2 \quad (2.5)$$

$$r_{II} = (K_3 + K_4) \times K_H K_H^* (C_H^2 - C_E C_D / K_P) / \sum_2 \quad (2.6)$$

$$r_{III} = K_2 K_H / (K_{2+4} + 1) \times (C_H^2 - C_E C_D / K_P) / \sum_3 \quad (2.7)$$

where

$$\sum_1 = K_H C_H + K_E C_E + K_D C_D$$

$$\sum_2 = 1 + K_H C_H + K_E C_E + K_D C_D + K_H K_H^* C_H^2$$

$$\sum_3 = C_H + K_H C_H^2 + K_E C_E + K_D C_D + K_H K_H^* C_H^2 + \frac{C_E}{K_{4P}(1 + K_{2+4})}$$

$$+ \frac{K_{2+4} C_D}{K_{2P}(1 + K_{2+4})} + \frac{K_H K_{2+4} C_H C_D}{K_{2P}(1 + K_{2+4})} + \frac{K_H C_H C_E}{K_{2P}(1 + K_{2+4})}$$

$$K_{2P} = K_2 / K_{-2}, \quad K_{4P} = K_4 / K_{-4}, \quad K_{2+4} = K_2 / K_4$$

K_p is the equilibrium constant of the overall reaction and K_H^* is the adsorption constant for the second 1-hexene molecule adsorbed on the single catalytic site in mechanism II.

The validity of each of these proposed rate expressions was not verified through experimentation.

2.4 Isomerization of alkenes over WO_3/SiO_2

Isomerization reactions proceed on acid sites via protonation-deprotonation with intervening intramolecular methyl shifts that form isomers before desorption. The strength of these acid sites and hence the isomerization activity of supported transition metal-based catalysts depends largely on the properties of the material used as the support. Research has shown that the dual oxide support $\text{Al}_2\text{O}_3 \cdot \text{SiO}_2$ shows high isomerization activity and hence reduced selectivity when coupled with Re_2O_7 for the metathesis of 1-hexene in the liquid phase (Tarasov et al., 1997). The $\text{Re}_2\text{O}_7/\text{Al}_2\text{O}_3$ catalyst does not suffer from this drawback. The isomerization reactions that occur over WO_3 based heterogeneous catalysts have been observed to be reversible first-order reactions.

Spamer et al. (2003) investigated the isomerization activity of WO_3/SiO_2 as a metathesis catalyst for 1-octene conversions. It is evident that the observed isomerization activity for this reaction system can be almost wholly attributed to isomerization of the feed olefin alone and not metathesis products, as was discovered when a detailed analysis of the product stream was undertaken (van Schalkwyk et al., 2003 a). It was also stated that the metathesis reaction proceeds via a metallacyclobutane intermediate and that a non-symmetrical olefin (extant through isomerization of alpha-olefins) can co-ordinate in two different ways to the active site responsible for the reaction. Various important conclusions were drawn as to the relationship between the catalyst morphology and surface characteristics, and the selectivity of the reaction (which is a measure of the degree of isomerization). First, a higher selectivity to primary metathesis products was obtained at lower WO_3 loadings (surface loadings of between 3% and 20% WO_3 were used). Apart from double-bond isomerization, skeletal isomerization was also observed resulting in branched metathesis products. The selectivity to branched metathesis products increased with increasing loading up to 8% WO_3 . Both conversion and selectivity reached a maximum at 8% and higher loadings, and catalysts with loadings lower than 6% experienced attenuated rates of deactivation. These experiments contributed to the view that 8% WO_3 was the best surface loading to use for further kinetic model development.

According to van Schalkwyk et al. (2003 b), strong Brønsted type acid sites on the surface of the catalyst were responsible for skeletal isomerization, whereas milder Lewis acid sites lead to

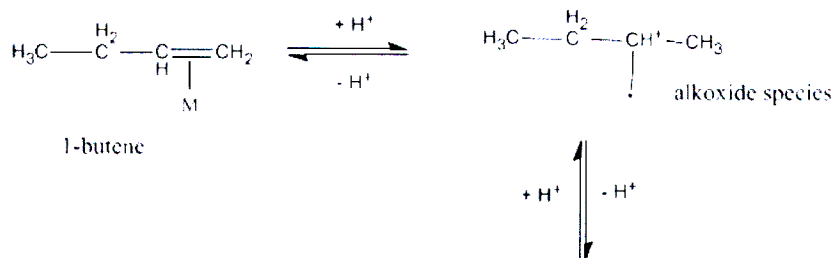
double-bond isomerization. Two forms of WO_3 were found on the surface of the catalyst used in the investigation. The first form was a surface complex which exhibited a strong interaction with the support, which made it difficult to reduce. This form contained the catalytic sites. The second was a non-active crystalline trioxide (Verpoort et al., 1995). Brønsted acid sites were not implicated in the metathesis mechanism.

A detailed study by van Roosmalen et al. (1980) showed that activated WO_3/SiO_2 contains silanol groups with Lewis acidity (Figure 2.3). The $=\text{Si}-\text{O}$ bridges to the silica lattice are electron-attracting groups resulting in Lewis acidity (due to p_p-d_p back bonding between oxygen and silicon). An olefin can chemisorb onto the tungsten surface compound to form a Lewis acid-alkene complex. If an alkene molecule adsorbs molecularly, it forms a π -complex on the surface, with the $\text{C}=\text{C}$ bond co-ordinated to the supported metal-Lewis acid site. If Brønsted acid sites are present, protonation of the alkene can occur, which leads to an alkoxide intermediate (carbenium ion) where the $\text{C}=\text{C}$ character is lost. Subsequent loss of a proton from a different carbon atom results in isomerization (Figure 2.19) (Spamer et al., 2003).

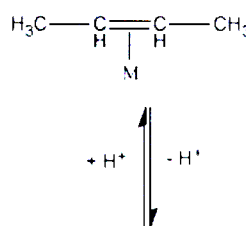
Hydroxyl groups on the catalyst surface are not the source of the protons necessary for the formation of the carbenium ion intermediate. Rather, an interaction of the reactant alkene with Lewis acid sites on activated tungsten-oxide/silica leads to the evolution of H^+ species (Figure 2.12). It was also found that surface silanols make gas-phase butene molecules accessible for proton exchange by reverse physisorption during butene isomerization reactions over WO_3/SiO_2 (van Roosmalen and Mol, 1982).

If the first step in the isomerization mechanism involves a $\text{C}-\text{H}$ bond cleavage, an allylic intermediate is formed with a resonant $\text{C}=\text{C}=\text{C}$ bond co-ordinated to the supported metal atom. Subsequent hydrogenation at a different carbon atom results in isomerization. Both mechanisms have been observed to occur on WO_3/SiO_2 , with an alkoxide mechanism responsible for skeletal isomerization and double-bond isomerization proceeding through an allylic mechanism (Ramani et al., 1998). Skeletal isomerization of 1-octene during metathesis at $\sim 460^\circ\text{C}$ appeared to be minimal. If competition between mechanisms was extant, then it may be concluded that the allylic mechanism was favoured for the reaction conditions that were used.

Brønsted catalyzed mechanism



2-butene



Allylic mechanism

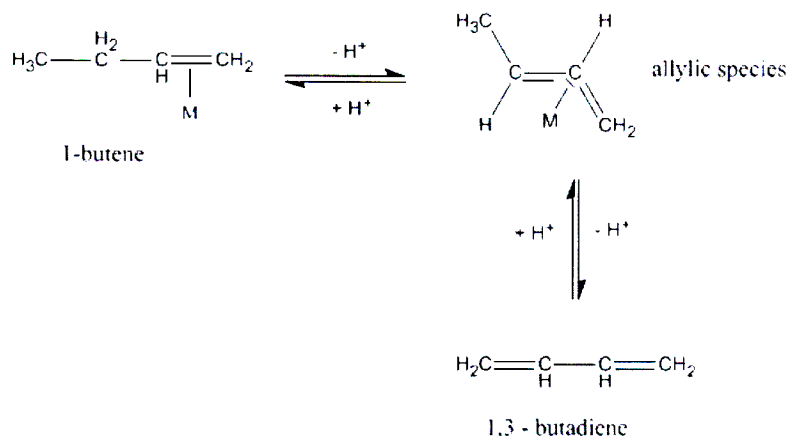


Figure 2.19 Alkoxide and allylic mechanisms of 1-butene isomerization over WO_3/SiO_2 (Ramani et al., 1998)

Doping the catalyst with small amounts of alkali-earth metals resulted in a significant decrease in branched metathesis products, brought about by a possible destruction of the strong acid sites responsible for skeletal isomerization. Impregnation of the inert silica gel with ammonium metatungstate in a high pH solution improved the dispersion of the metal oxide on the support. The improved dispersion translated into an improved selectivity towards primary metathesis products (Spamer et al., 2003).

The skeletal isomerization of 1-hexene over $\text{WO}_3/\text{Al}_2\text{O}_3$ was investigated by Logie et al. (1999). Similar conclusions were drawn from their experiments. They concluded that Brønsted acid sites account for skeletal isomerization itself, whereas Lewis acidic W^{6+} sites were responsible for the adsorption of the reactant and formation of the appropriate intermediate structures. Selectivity towards 2-methyl pentene and 3-methyl pentene, the major isomerization products,

were 43.1% and 38.9% respectively. Some cracking was also observed, but total selectivity towards these products was less than 5%.

2.5 Catalyst deactivation

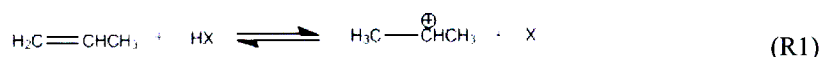
During the transformation of organic compounds over solid catalysts, there is always the formation and retention of heavy side-products, either in the pores or on the outer surface or in both positions (Guisnet and Magnoux, 2001). The formation of these non-desorbed products, often called coke, is the most frequent cause of catalyst deactivation. The deactivation is due to the poisoning of the active sites or pore blockage. Intrinsic mechanisms of catalyst deactivation cannot be limited only to coke formation; indeed they can be classified into six distinct types: (i) poisoning, (ii) fouling, (iii) thermal degradation, (iv) vapour compound formation accompanied by transport, (v) vapour-solid and/or solid-solid reactions, and (vi) attrition/crushing. Deactivation types (i), (iv) and (v) are chemical in nature and (ii) and (vi) are mechanical. The three causes of deactivation are thus chemical, thermal and mechanical in nature (Guisnet and Magnoux, 2001). Poisoning is the strong chemisorption of species on catalytic sites, thereby blocking sites for catalytic reaction. Thermally induced loss of catalytic surface area and support area can also result in deactivation. Vapour formation involves the reaction of a gas with the catalyst phase to produce volatile compounds. The gas or solid support may also react with the catalytic phase to produce an inactive phase (vapour-solid and solid-solid reactions). Attrition/crushing refer to the loss of catalytic material due to abrasion or loss of internal surface area due to mechanical-induced crushing of the catalyst particle. These are usually significant only in large or moving beds. Fouling is the physical deposition of species from the fluid phase onto the catalytic surface and in catalytic pores. Due to the elevated temperatures that are used for hydrocarbon conversions over WO_3/SiO_2 , this catalyst is prone to coke formation but is tolerant to many known poisons that may form part of the feed stream (van Schalkwyk et al., 2003 c). The discussion henceforth deals solely with this form of catalyst deactivation.

Important examples of fouling include mechanical deposits of carbon and coke in porous catalysts. Carbon and coke-forming processes may also involve chemisorption of different types of carbon or condensed hydrocarbons which may act as catalyst poisons. Carbon is typically a product of CO disproportionation while coke is produced by decomposition or condensation of hydrocarbons on catalyst surfaces and typically consists of polymerized heavy hydrocarbons (Bartholomew, 2001). Actual chemical structures of cokes or carbons vary with reaction type, catalyst type and more importantly, reaction conditions. The mechanism of formation usually depends strongly on the catalyst type (metal or metal oxide based). The formation of coke on oxides is principally the result of cracking reactions involving coke

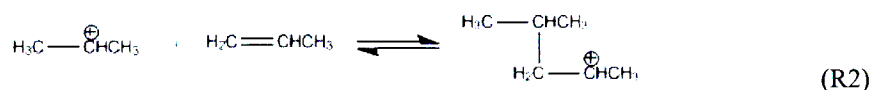
precursors (typically olefins and aromatics) catalyzed by acid sites (Guisnet and Magnoux, 2001). Dehydrogenation and cyclization reactions of carbocation intermediates formed on acid sites lead to aromatics which react further to higher molecular weight polynuclear aromatics and condense as coke (Scheme 2.1) (Bartholomew, 2001).

a. Polymerization of olefins

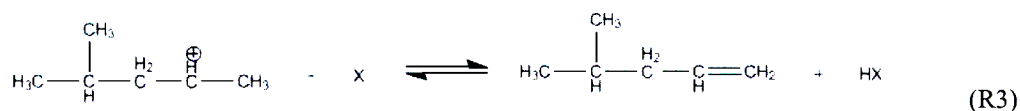
Step 1: Reaction of olefin with Brønsted acid to form secondary carbenium ion:



Step 2: Condensation reaction of a C₃ carbocation with a C₃ olefin to form a condensed, branched C₆ product with a carbenium ion:

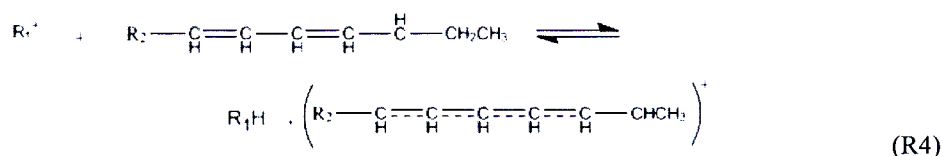


Step 3: Reaction of carbenium ion with Brønsted base to form olefin:

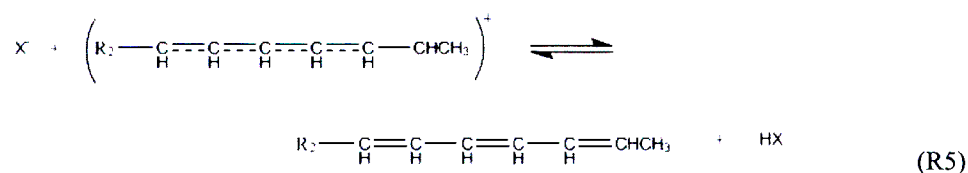


b. Cyclization from olefins

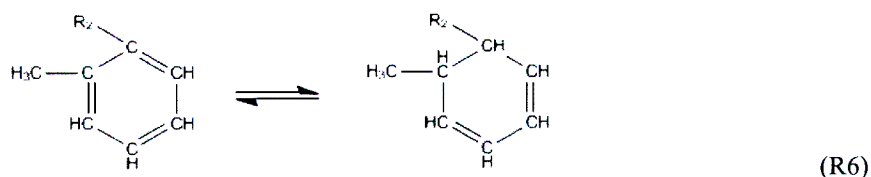
Step 1: Formation of an allylic carbocation ion by reaction of a diene with a primary carbocation ion:



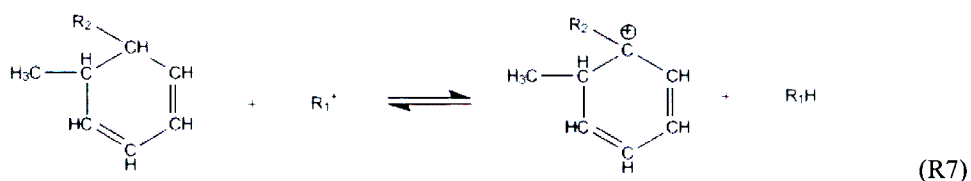
Step 2: Reaction of an allylic carbocation ion with a Brønsted base to form a triene:



Step 3: Cyclization of a triene to form a substituted cyclohexadiene:

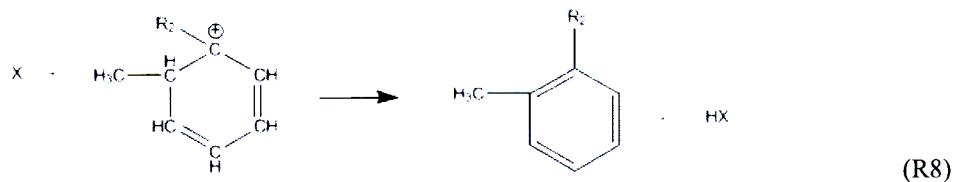


Step 4: Formation of a tertiary carbocation ion:



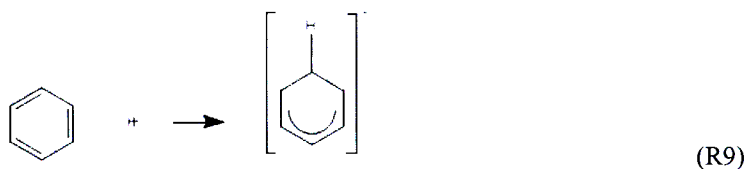
Scheme 2.1 Coke forming reactions of alkenes and aromatics on oxide catalysts (Bartholomew, 2001)

Step 5: Reaction of tertiary carbocation ion with Brønsted base to form substituted benzene:

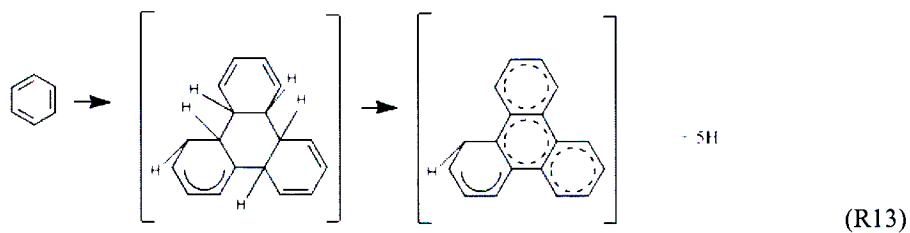
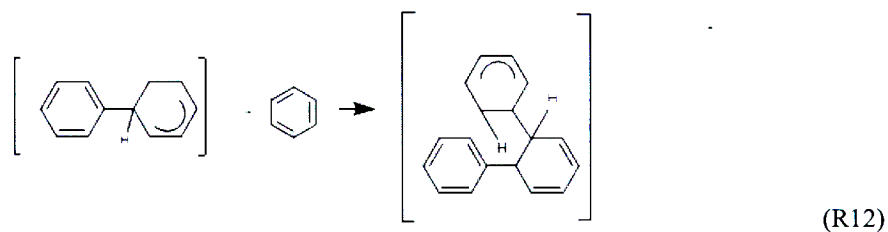
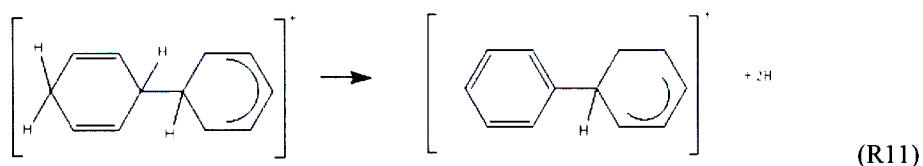
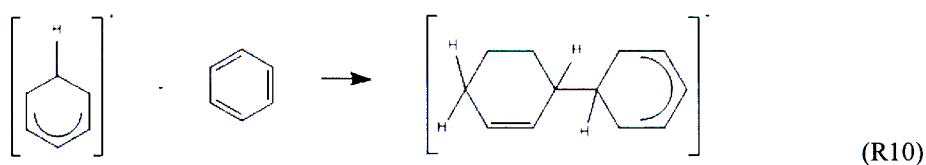


c. Formation of polynuclear aromatics from benzene

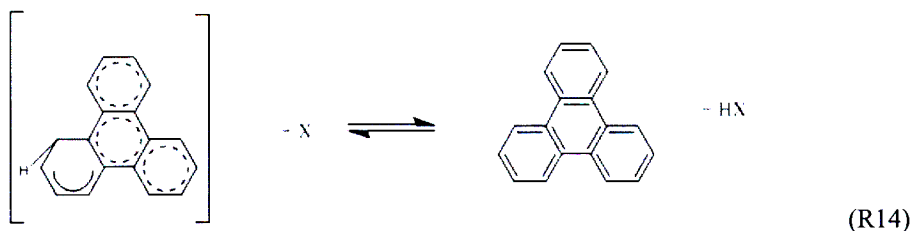
Step 1: Initiation (protonation of benzene):



Step 2: Propagation (condensation reaction of carbocation with benzene followed by H abstraction):



Step 3: Termination (reaction of carbocation with Brønsted base):



Scheme 2.1 (Continued)

In bi-functional catalysts, such as supported metal oxide systems, the acid sites catalyze the condensation and rearrangement steps of unsaturated species and the metal sites catalyze the dehydrogenation steps (Guisnet and Magnoux, 2001). Because of the high stability of the polynuclear carbocations (formed in reactions R10-R13), they can continue to grow on the surface for a relatively long time.

The extent and rate of coke formation are also a function of the acidity and pore structure of the catalyst. Generally, the rate and extent of coke formation increase with increasing acid strength and concentration.

Some methods of preventing or reducing the effects of coke formation include operating under conditions that minimize this type of deactivation (usually lower temperatures and reactant flow-rates), optimization of catalyst acidity and purification of the feed to remove precursors that accelerate carbon or coke formation. Regeneration of coked catalyst (combustion of deposits) may be carried out at lower temperatures under a stream of air (Bartholomew, 2001).

Moodley et al. (2007) undertook an extensive study of coke formation on the WO_3/SiO_2 metathesis catalyst, using 1-octene and an industrial cut 1-heptene feed along with various additives, including 2-pentanone and water. During previous studies it was found that the catalyst remained active for metathesis reactions even at high coke levels (van Schalkwyk et al., 2003 a). The coking profile along the length of the fixed-bed reactor that was used indicated that the heavier internal alkene products coked more rapidly than the 1-octene feed. High, consistent conversions were reported up till a total coke content of 49 wt%. It was suggested that the coke build-up occurred in the pores of the catalyst with the active tungsten complex extant either near the mouths of pores or outside the pores. As coke was gradually laid down inside the pores of the catalyst, the activity was retained. Eventually the pores were filled, and coke deposition moved over the active centres, leading to a decrease in activity. It appeared that during the synthesis of the WO_3/SiO_2 metathesis catalysts via wet impregnation of the silica support, the active phase was irregularly dispersed over a small portion of the total surface area. Coke deposition was prevalent over much of the exposed catalyst surface (in particular the inactive surface) during the first few hundred hours on-line, but due to this inhomogeneous dispersion of active material, the effect on activity was only observed after the coke content had reached a level of 49 wt%. The addition of small amounts (100 ppm) of oxygenates to the feed did not have a significant effect on the activity of the catalyst. Trace amounts of these additives reduced the amount of coke formed, possibly by being adsorbed onto the most acidic sites of the catalyst which are known to promote coke formation. Water may also aid in desorption of coke precursors.

Chapter 3

Basis for experimental design and methodology

In this work, the optimization of operating conditions for the metathesis of 1-hexene over WO_3/SiO_2 was carried out. The objective quantity for this optimization was the yield of the primary metathesis product, decene. The techniques of statistical test planning that were used for the optimization study and the subsequent design of the experiments are discussed in this chapter. These techniques include the use of a factorial test plan and the selection of flow conditions and reactor dimensions that ensure that the work is conducted within a range appropriate for laboratory tests. As an extension of this optimization study, experimental tests were also carried out to determine the extent of mass transfer resistance effects for the range of flows and catalyst particle sizes that were employed. Therefore, the theoretical basis and mathematical development of these tests are also discussed in this chapter.

3.1 Experimental design

3.1.1 Factorial test planning

For catalysts that show some promise for a particular process it is necessary to explore the constrained domain of process conditions in order to determine the optimum operational

parameters of the industrial reactor. The one-variable-at-a-time (OVAT) approach to experimental design consists of changing a single process variable and then observing the effect on conversion. Often, two excursions are made for each variable from a set of base conditions. This method has been shown to be inefficient and the results can often be misleading (Antony, 2003). The method requires a large amount of resources and time to obtain a limited amount of information. It also does not account for possible interactions between process variables. Interactions occur when the effect of one process parameter depends on the level of another. A proper study requires that all factors be varied simultaneously. The exploration of the limited domain can be conducted as is shown in Figure 3.1. The plan is the simplest two-level, three variable statistical design with $2^3 = 8$ experiments needed for the full replica (or full factorial experiment (FFE)). With an added centre point, 9 experimental conditions are used in all. The three variables are temperature, feed gas composition and space time. If the experiments are very costly or time consuming or both, then a half replica of the factorial experimental plan, representing the corners of a tetrahedron, can be executed (solid dots on Figure 3.1). The reaction temperature was selected as a parameter because it was the least constrained variable.

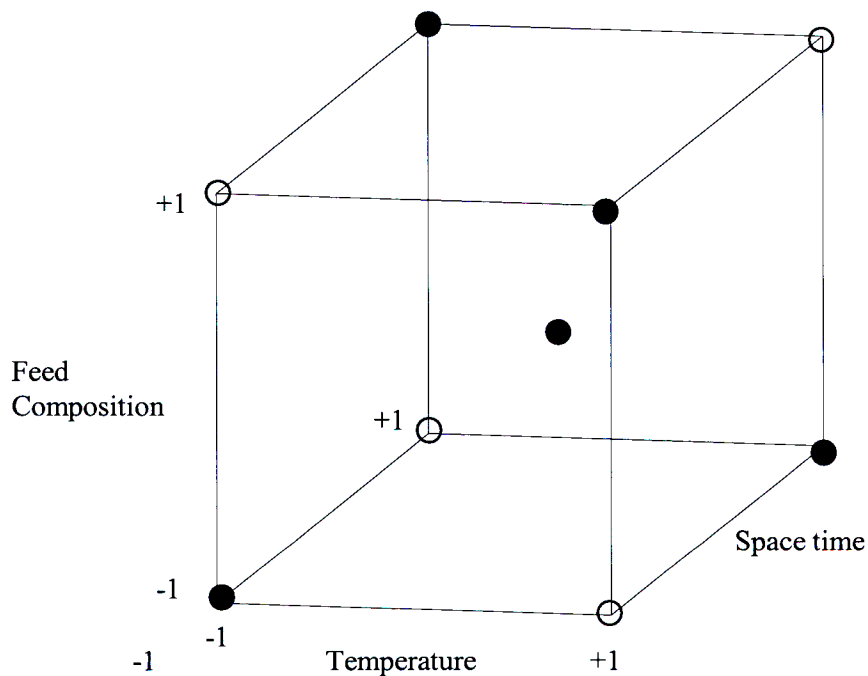


Figure 3.1 Exploration of the limited domain through FFE

The FFE responses (excluding the centre point) are presented in Table 3.1 for a process with three independent variables A, B and C. The high level and low level value of each parameter is denoted by +1 and -1, respectively.

Run no.	Designation	Variable			Response
		A	B	C	
1	(1)	-1	-1	-1	R 1
2	a	+1	-1	-1	R 2
3	b	-1	+1	-1	R 3
4	ab	+1	+1	-1	R 4
5	c	-1	-1	+1	R 5
6	ac	+1	-1	+1	R 6
7	bc	-1	+1	+1	R 7
8	abc	+1	+1	+1	R 8

Table 3.1 (2^3) - full factorial experimental design

The interaction between parameters may be estimated from their average response for different combinations.

Run no.	A	B	Average Response
1,5	-1	-1	$R_{1,5}=(R1+R5)/2$
3,7	-1	+1	$R_{3,7}=(R3+R7)/2$
2,6	+1	-1	$R_{2,6}=(R2+R6)/2$
4,8	+1	+1	$R_{4,8}=(R4+R8)/2$

Table 3.2 Average responses for variables A and B at different levels

The interaction between variable A and variable B is then given by the following equation (the mean of the effect of factor A at the high level of B and the effect of factor A at the low level of B):

$$I_{A,B} = \frac{1}{4} [(R_{4,8} - R_{3,7}) - (R_{2,6} - R_{1,5})] \quad (3.1)$$

The effects of the variables are expressed relative to the mean value of all the measurements and half of the difference between levels, for example:

$$E_A = \frac{1}{8} [(R2 - R1) + (R4 - R3) + (R6 - R5) + (R8 - R7)] \quad (3.2)$$

All effects and interactions, including multi-fold interactions (ABC), can be calculated rapidly using the Yates scheme (Hagen, 1999). The tests are arranged in the standard order (Table 3.1). Then the first and second, third and fourth, etc., responses are added together to give the top half of a new column (column 1 in Table 3.3). The first response is subtracted from the second, the third from the fourth and so on, to give the bottom half of the column. The calculation is

continued until n columns are obtained (i.e. equal to the number of variables). The last column is divided by 2^n to give the corresponding effect or interaction.

Experiment	Response	1	2	3	Effect or interaction
(1)	R 1	$i1=R1+R2$	$j1=i1+i2$	$k1=j1+j2$	$k1/2^n$
a	R 2	$i2=R3+R4$	$j2=i3+i4$	$k2=j3+j4$	$k2/2^n$
b	R 3	$i3=R5+R6$	$j3=i5+i6$	$k3=j5+j6$	$k3/2^n$
ab	R 4	$i4=R7+R8$	$j4=i7+i8$	$k4=j7+j8$	$k4/2^n$
c	R 5	$i5=R2-R1$	$j5=i2-i1$	$k5=j2-j1$	$k5/2^n$
ac	R 6	$i6=R4-R3$	$j6=i4-i3$	$k6=j4-j3$	$k6/2^n$
bc	R 7	$i7=R6-R5$	$j7=i6-i5$	$k7=j6-j5$	$k7/2^n$
abc	R 8	$i8=R8-R7$	$j8=i8-i7$	$k8=j8-j7$	$k8/2^n$

Table 3.3 Yates scheme for the 2^3 factorial design

The significance of each effect or interaction is determined using a hypothesis test. The variance of the effects is calculated from the variance of the measurements by means of the error-propagation law,

$$s_{eff} = \frac{1}{2^n} \sigma^2 \quad (3.3)$$

where σ = standard deviation of measurements

$$\sigma_{eff} = \sqrt{s_{eff}} \quad (3.4)$$

The null hypothesis asserts that the effects belong to a normal distribution with zero mean and variance σ_{eff} . With a chosen level of confidence of 95%, the test quantity is calculated:

$$z = \frac{\text{Effect} - \mu}{\sigma_{eff}} = \frac{\text{Effect} - \mu}{\sigma_{eff}} \quad (3.5)$$

and compared with the significance number $c = 2$ (from Gaussian distribution tables; two-sided statistical decision). The effects are deemed significant if $z > c$.

Interaction graphs are another method of investigating the interaction effect between sets of parameters.

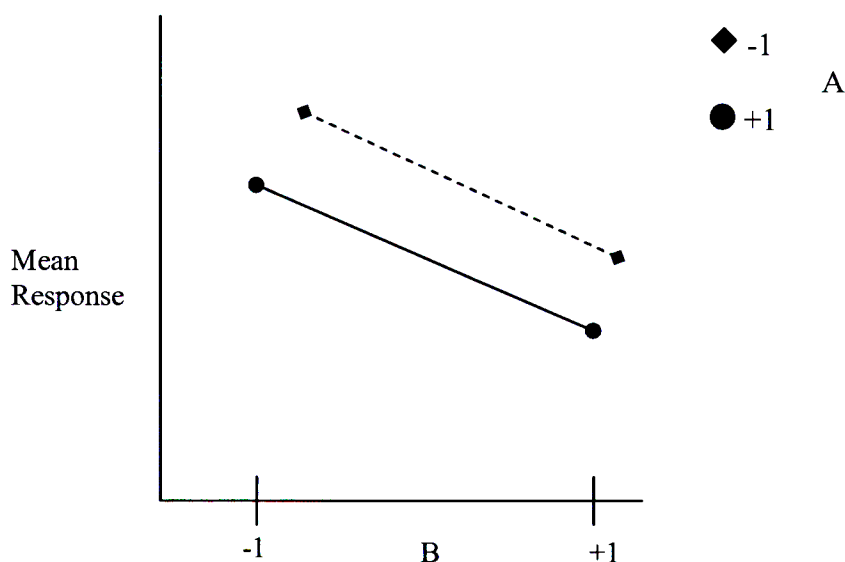


Figure 3.2 Interaction graph for variables A and B

If the response lines are parallel on the interaction graph, as is the case in Figure 3.2, then there is little interaction between variables. A strong effect is indicated by lines that are not parallel. If the response lines cross one another, antagonistic interaction is said to be extant, otherwise the system is said to exhibit synergistic interaction. For the case of antagonistic interaction, the trend in response values for variable A would be different at different levels of variable B, i.e., increasing for one level of B with a positive gradient on the interaction plot and decreasing for the other level of B with a negative gradient on the interaction plot.

In this work, reaction temperature, feed gas composition and space time were chosen as the variables to be tested in the optimization of operating conditions for the metathesis of 1-hexene over WO_3/SiO_2 . The two levels for each variable that constituted the full factorial experimental design were chosen based on the values that were used by van Schalkwyk et al. (2003 a) for the optimization of operating conditions for the metathesis of 1-heptene over WO_3/SiO_2 . The high level and low level of reaction temperature were 500°C and 420°C , respectively. The high level and low level of feed composition were 90% and 55% 1-hexene (mole based), respectively, and the high level and low level of space time W/F were 670g.min.mol^{-1} and 220g.min.mol^{-1} respectively. The exploration of this limited domain of operating conditions was conducted as is shown in Figure 3.3. Each solid dot in Figure 3.3 represents a specific set of operating conditions that were investigated. The results of this factorial experimental design were used to predict the region of operating conditions that gave the maximum yield of decene.

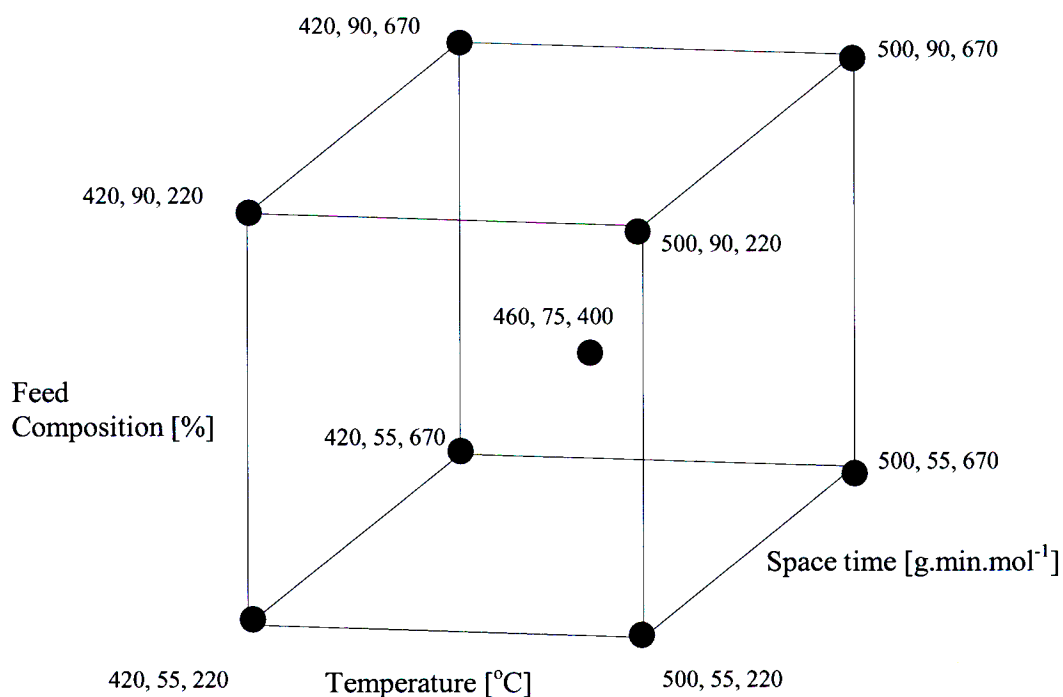


Figure 3.3 Exploration of the limited domain of operating conditions using a factorial experimental design – limits for each test variable (reaction temperature, % feed composition, space time)

3.1.2 Fluid flow in a packed-bed reactor and recommendations for laboratory reactor design

Great care must be taken when selecting limits for each test variable in the factorial experimental design. For all experiments, the chosen conditions should be such that inter-bed gradients are minimized and plug flow is maintained (Hagen, 1999). In this respect, the dimensions of the catalyst bed must also be appropriately selected, in order to avoid flow phenomena such as axial dispersion, bypassing, channelling, mal-distribution and wall effects, all of which can affect the conversion and distort the data that are generated. Each of these effects will be discussed in detail in this subsection, together with recommendations for laboratory reactor design.

Axial mixing, axial dispersion and longitudinal dispersion are all terms used to describe a phenomenon that causes a distribution of residence times for a reaction gas mixture in a packed bed. It is largely the result of stream splitting, acceleration, deceleration and trapping (Rase, 1977). These phenomena are described using effective axial diffusivities D_z , and conductivities

K_z , in the Fick and Fourier type terms, respectively. They find their place in the fluid-phase material and energy balances for a fixed bed reactor. At steady state, and in dimensionless form, these balances are written out as follows:

$$0 = -\frac{\partial \bar{C}}{\partial \bar{z}} + \frac{1}{Pe_z n} \frac{\partial^2 \bar{C}}{\partial \bar{z}^2} + \frac{A}{Pe_r m} \left(\frac{\partial^2 \bar{C}}{\partial \bar{r}^2} + \frac{1}{\bar{r}} \frac{\partial \bar{C}}{\partial \bar{r}} \right) + \bar{N} \quad (3.6)$$

$$0 = -\frac{\partial \bar{T}}{\partial \bar{z}} + \frac{1}{Pe_z^T n} \frac{\partial^2 \bar{T}}{\partial \bar{z}^2} + \frac{A}{Pe_r^T m} \left(\frac{\partial^2 \bar{T}}{\partial \bar{r}^2} + \frac{1}{\bar{r}} \frac{\partial \bar{T}}{\partial \bar{r}} \right) + \bar{q} \quad (3.7)$$

where the axial and radial Peclet numbers are:

$$Pe_z = \frac{ud_p}{D_z} \quad (3.8)$$

$$Pe_r = \frac{ud_p}{D_r} \quad (3.9)$$

$$Pe_z^T = \frac{ud_p}{K_z} \rho C_p \quad (3.10)$$

$$Pe_r^T = \frac{ud_p}{K_r} \rho C_p \quad (3.11)$$

Aspect ratios are given by:

$$n = \frac{L}{d_p} \quad (3.12)$$

$$m = \frac{D}{d_p} \quad (3.13)$$

$$A = \frac{L}{D} \quad (3.14)$$

where L = bed length [m]

D = bed diameter [m]

d_p = catalyst particle diameter [m]

The reduced dependent variables \bar{C} and \bar{T} are usually based on inlet conditions. \bar{N} and \bar{q} are the dimensionless fluid-solid mass transport and heat transport terms, respectively.

Axial concentration gradients would exist within the reactor, if higher conversions are to be achieved, and hence there exists the possibility of axial dispersion. While radial dispersion is desirable for achievement of plug flow (a condition which must be met in order to apply the plug flow model to the experimental fixed bed), axial dispersion lowers the conversion and results in a deviation from the ideal of plug flow (Anderson and Pratt, 1985). For negligible axial dispersion or mixing, Pe_z approaches infinity (Carberry, 1964).

Equation 3.6 contains a coefficient $\frac{1}{Pe_z n}$ that quantifies the extent of axial dispersion. If $Pe_z n$ is large, then dispersion is negligible. If $Pe_z n$ is less than 300, then in principle the plug flow model does not fully apply. However, for $Pe_z n > 100$, the system is nearly plug flow, or may be modeled as such.

Various correlations exist for the axial Peclet number in terms of the fluid phase Reynolds number and the Schmidt number. One such equation is of the form,

$$\frac{1}{Pe_z} = \frac{0.3}{Re Sc} + \frac{0.5}{1 + \frac{3.8}{Re Sc}} \quad (3.15)$$

where

$$Pe_z = \frac{d_p u}{D_z}$$

$$Re = \frac{d_p u \rho}{\mu}$$

$$Sc = \frac{\mu}{\rho D_m}$$

and D_m is the ordinary molecular diffusion coefficient (Crynes, 1982).

In order to use Equation 3.15, D_m must be estimated for Sc . The following Stefan-Maxwell relation is applicable for a multi-component gas mixture (Gomes and Fuller, 1996):

$$D_{im} = (1 - y_i) \left[\sum_{j=1}^n \frac{y_j}{D_{ij}} \right]^{-1} \quad (3.16)$$

where D_{ij} are the mutual or binary diffusion coefficients for all combinations except those which would yield self diffusing coefficients ($i = j$). D_{ij} may be estimated using the following empirical equation of Fuller, Schettler and Giddings (1966):

$$D_{AB} = \frac{0.00143T^{1.75}}{PM_{AB}^{0.5} \left[\left(\sum v \right)_A^{1/3} + \left(\sum v \right)_B^{1/3} \right]^2} \quad (3.17)$$

where D_{AB} is in $\text{cm}^2 \cdot \text{s}^{-1}$, P is in atmospheres, T is in Kelvin,

$$M_{AB} = \frac{2}{\left(\frac{1}{M_A} \right) + \left(\frac{1}{M_B} \right)} \quad (3.18)$$

M_i is the molar mass and $\sum v$ = summation of atomic and structural diffusion volumes.

Carberry (1964) analyzed correlations for axial Peclet numbers as functions of the Reynolds number and stated that plug flow fixed bed reactor operation is best conducted at particle Reynolds numbers greater than 30. Further it was stated that at these conditions, for an axial aspect ratio $n > 150$, no axial dispersion should be evident (Carberry, 1976). Studies of isothermal and adiabatic fixed bed reactors indicate that the effect on conversion and rate is negligible for $n > 50$ (Rase, 1977). Other studies, in particular the gas-phase propylene metathesis study of Hattikudur and Thodos (1975), mention $n > 100$ as the benchmark for plug-flow operation. For Reynolds numbers below 30 it is necessary to check n as well as $Pe_z n$ against the given criteria.



Poor distribution in large diameter beds, causing bypassing and discontinuities in the velocity profile produces deviations from the plug flow assumption orders of magnitude greater than

effects such as axial mixing (Rase, 1977). Laboratory experimental reactors are restricted to smaller diameters. However, eliminating back mixing or axial dispersion does not necessarily solve the problems of channeling and mal-distribution, which are particularly difficult in smaller systems because the wall effect is so dominant. Also, the difficulty of packing short beds uniformly may lead to serious mal-distribution of flow. In a randomly packed bed, a variation in the void fraction is extant. The average void fraction (for similar sized particles) has been shown to be a function of the ratio of bed diameter to particle diameter, $\frac{D}{d_p}$ (Rase, 1977; Chorkendorff and Niemantsverdriet, 2003). Packing different sized tubes with the exactly the same particles has revealed that above a $\frac{D}{d_p}$ ratio of 10, the average void fraction is constant (Figure 3.4), whereas below 10, the variation of average void fraction with $\frac{D}{d_p}$ is dramatic, indicating a strong wall effect (Rase, 1977).

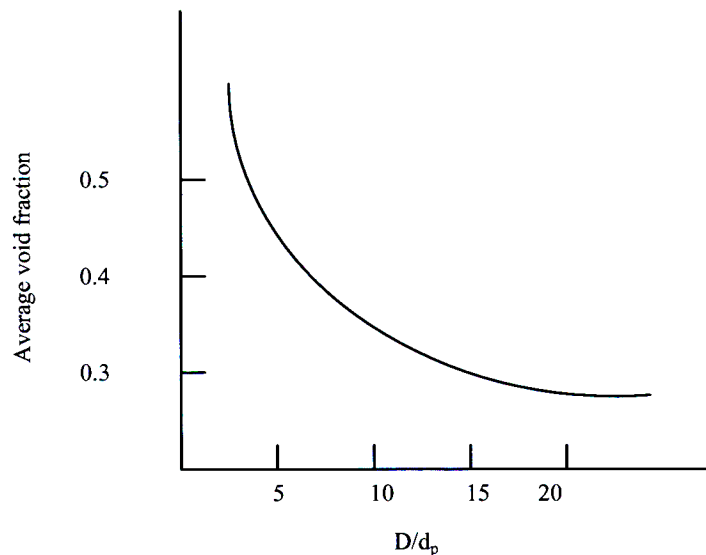


Figure 3.4 Variation of average void fraction of bed with tube size (Rase, 1977)

In the fixed bed reactor, the lower packing density of the catalyst at the wall, especially for particles of a large size relative to the reactor tube, may result in some bypassing of the reactant.

A $\frac{D}{d_p}$ ratio above 10 has been recommended to eliminate the influence of the reactor wall (Chorkendorff and Niemantsverdriet, 2003). Some investigations suggest that the value should be above 30 (Anderson and Pratt, 1985). Another rule is that the ratio of the bed length to

reactor diameter, $\frac{L}{D}$, should lie between 5 and 10, to ensure that the amount of catalyst is sufficient to avoid axial gradients. Higher values are preferable, but these may cause problems such as temperature gradients and pressure drops (Chorkendorff and Niemantsverdriet, 2003).

For the experiments that constituted part of the optimization program, particle Reynolds numbers were low, typically in the range 0.70 to 4.97. Flow-rates were limited by the necessity to operate at higher values of space time in order to maximize the selectivity and yield of decene. The axial aspect ratio $\left(\frac{L}{d_p}\right)$ was always greater than 132 and $\frac{D}{d_p}$ was 20, ensuring uniformity of flow through the bed and the elimination of wall effects. $\frac{L}{D}$ was between 6.5 and 10, well within the optimum region for experimental work. The three aspect ratios were maintained within acceptable limits by carefully selecting an appropriate mass of catalyst (2g) for the experimental tests. Pe_z was calculated using Equation 3.15 to be between 1.49 and 3.07 for the different conditions that were employed. $Pe_z n$ was between 198 and 405.

3.2 Elimination of mass transfer resistances

3.2.1 Experimental tests

Whether laboratory studies are devoted to the development of kinetic models of the reaction system or to catalyst screening and optimization, it is important that the data derived is free from mass transfer resistance effects. Results may be obscured by these purely physical processes occurring simultaneously with the catalytic reaction. Catalyst evaluation based on such data may actually lead to the rejection of the best set of operating conditions for commercial use. If the study is to be extended to a full kinetic investigation, then these transport resistances must first be eliminated. Experience has shown that the use of high gas flow-rates and small particle sizes usually helps to alleviate this problem (Carberry, 1964). The experimental test for external mass transfer resistance effects in a laboratory reactor may be developed from a simple plug flow model of the fixed catalyst bed (refer to Figure 3.5).

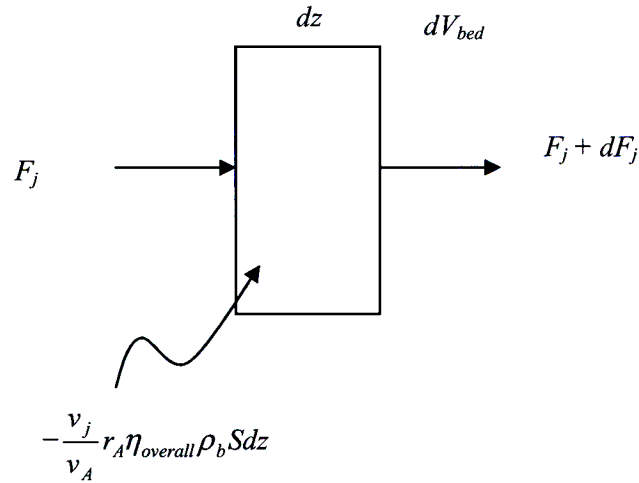


Figure 3.5 Plug flow model of the fixed bed catalytic reactor

At steady state:

$$F_j - \frac{v_j}{v_A} r_A \eta_{\text{overall}} dW_{\text{cat}} = F_j + dF_j \quad (3.19)$$

hence:

$$dF_j = -\frac{v_j}{v_A} r_A \eta_{\text{overall}} dW_{\text{cat}} \quad (3.20)$$

In particular, for component A:

$$dF_A = -r_A \eta_{\text{overall}} dW_{\text{cat}} \quad (3.21)$$

At low conversions the reactant concentration inside the layer can be assumed to be practically constant and the reactor to be gradientless. Integration of Equation 3.21, under the assumption of a constant reaction rate, results in the following expression:

$$F_{A_0} - F_A = -r_A \eta_{\text{overall}} W_{\text{cat}} \quad (3.22)$$

In terms of conversion, Equation 3.22 may be re-written as:

$$X_A = -r_A \eta_{\text{overall}} \left(\frac{W_{\text{cat}}}{F_{A_0}} \right) \quad (3.23)$$

The transport processes involved in a porous catalyst particle are illustrated schematically in Figure 3.6. The reactants must first be transported from the bulk fluid to the exterior of the catalyst particle by diffusion across the stagnant fluid film surrounding the particle. Then follows a process of simultaneous diffusion, adsorption and reaction at the active centres, as the reactants diffuse through the internal pore structure of the catalyst. The reaction products are desorbed from the surface and return to the bulk fluid stream by the reverse path. Similar considerations apply to the transfer of heat to or from the catalyst, except that a path for heat transfer by conduction through the catalyst pellet itself now exists. To account for resistance to mass transfer through different regions of the porous catalyst particle, the overall catalyst effectiveness factor $\eta_{overall}$ is included in Equation 3.22 and Equation 3.23. The overall effectiveness factor is a combination of the internal effectiveness, η_{int} (to account for intraparticle resistance) and external effectiveness, η_{ext} (to account for external resistance).

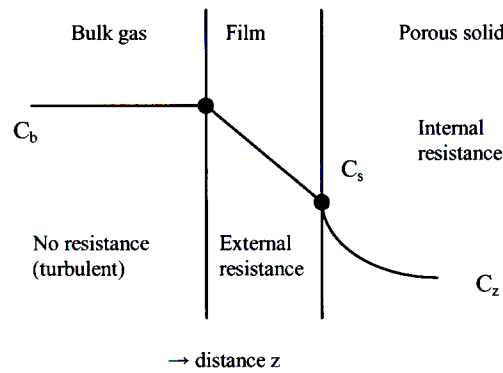


Figure 3.6 Mass transfer resistances in heterogeneous catalysis

Under steady state conditions the amount of gas transported to the particle from outside across the gas film, i.e.:

$$N_A = k_c a_p (c_b - c_s) \quad (3.24)$$

is consumed by the reaction,

$$N_A = \eta_{int} r_A(c_s) S_p = \eta_{int} r_A(c_s) S_g \rho_p V_p \quad (3.25)$$

where c = molar concentration [kmol.m^{-3}]

k_c = gas phase mass transfer coefficient [m.s^{-1}]

a_p = external surface area of single particle [m^2]

r_A = reaction rate [$\text{kmol.m}^{-2}.\text{s}^{-1}$]

S_p = internal surface area of single particle [m^2]

ρ_p = particle density [kg.m^{-3}]

V_p = volume of single particle [m^3]

S_g = specific surface area of catalyst [$\text{m}^2.\text{kg}^{-1}$]

Thus, for a single particle (at steady-state):

$$k_c a_p (c_b - c_s) = \eta_{\text{int}} r_A(c_s) S_g \rho_p V_p \quad (3.26)$$

or for the entire bed:

$$k_c a_c (c_b - c_s) = \eta_{\text{int}} r_A(c_s) S_g \rho_p V_c \quad (3.27)$$

where a_c = total external surface area in the bed [m^2]

V_c = total particle volume in the bed [m^3]

Eventually, Equation 3.27 can be rearranged to:

$$k_c a_c (c_b - c_s) = \eta_{\text{int}} r_A(c_s) S_g \rho_b \quad (3.28)$$

with $\rho_b = \rho_p (1 - \varepsilon_b)$

$$a_c = \frac{\text{m}^2 \text{ external area}}{\text{m}^3 \text{ bed}}$$

$$\varepsilon_b \text{ is the bed porosity } \left[\frac{\text{m}^3 \text{ void space}}{\text{m}^3 \text{ bed}} \right]$$

In Equation 3.28 the surface concentration c_s is unknown. However, a simple analytical solution can be obtained for the first order reaction case:

$$r_A(c_s) = k_s c_s \quad (3.29)$$

Assuming a constant value of the intraparticle effectiveness factor η_{int} :

$$k_c a_c c_b = (k_c a_c + \eta_{\text{int}} k_s S_g \rho_b) c_s \quad (3.30)$$

$$c_s = \frac{c_b}{1 + \eta_{\text{int}} k_s S_g \rho_b / k_c a_c} \quad (3.31)$$

Thus the observed reaction rate is:

$$(-r_A) = \eta_{\text{int}} k_s c_s = \eta_{\text{overall}} k_s c_b \quad (3.32)$$

where

$$\eta_{\text{overall}} = \frac{\eta_{\text{int}}}{1 + \frac{\eta_{\text{int}} k_s S_g \rho_b}{k_c a_c}} \quad (3.33)$$

For an n^{th} order reaction and with the assumption of negligible intraparticle mass transfer resistance, the reaction rate is given by:

$$r_A = k_s c_s^n \quad (3.34)$$

At steady state this rate is equal to the rate of mass transfer of component A from the bulk gas to the surface of the catalyst:

$$r_A = k_c a_c (c_b - c_s) \quad (3.35)$$

Solving for c_s from Equation 3.35 and substituting into Equation 3.34 gives:

$$r_A = k_s \left(c_b - \frac{r_A}{k_c a_c} \right)^n \quad (3.36)$$

Substituting this rate expression into the integrated form of the material balance for a differential plug flow reactor ($r_A \approx \text{constant}$) gives:

$$X_A = k_s \left(c_b - \frac{r_A}{k_c a_c} \right)^n \left(\frac{W_{\text{cat}}}{F_{A_0}} \right) \quad (3.37)$$

Consider isothermal, differential operation of a fixed bed reactor of constant catalyst mass (W_{cat}). Sufficiently small catalyst pellets are used such that internal resistances may be ignored. The external mass transfer coefficient is generally a function of the fluid Reynolds number, so by varying the molar inlet flow-rate, hence superficial velocity, changes may be made to this parameter. Reaction rate is assumed constant for low conversions, due to an almost uniform reactant concentration across the length of the bed. Consequently, for a first-order reaction, a plot of conversion (X_A) versus space time $\left(\frac{W_{cat}}{F_{A_0}}\right)$, see Equation 3.23, should yield a straight line through the origin where external mass transfer limitations are negligible (k_c is large enough to ensure that $\eta_{overall} \rightarrow \eta_{int} \rightarrow 1$). Similarly for a n^{th} order reaction, a very large mass transfer coefficient (negligible external mass transfer resistance) would result in a linear plot of conversion (X_A) versus space time $\left(\frac{W_{cat}}{F_{A_0}}\right)$, see Equation 3.37. A deviation from linearity would indicate the influence of external mass transfer resistance. In Figure 3.7, the observed reaction rate is dependent solely on the reaction kinetics, for values of space time less than τ . At lower flow-rates and hence higher values of space time, the plot becomes strongly non-linear, indicating that the observed reaction rate is now influenced by external mass transfer resistance.

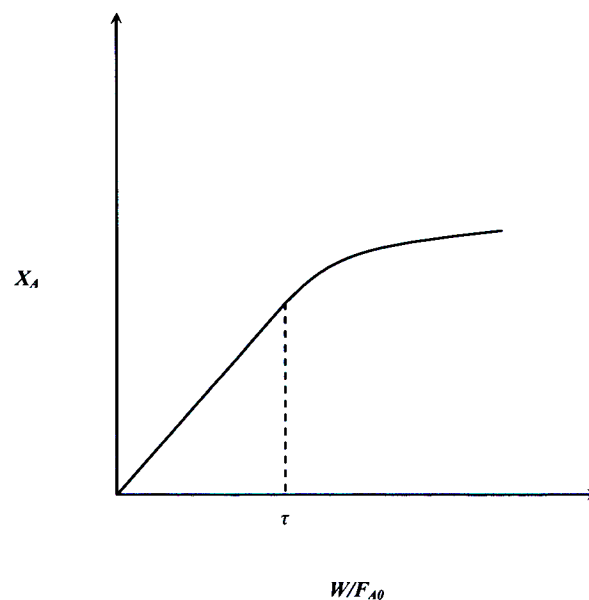


Figure 3.7 Plot of conversion versus space time in the test for external mass transfer resistance

In this work, tests for external mass transfer resistances were conducted using a single bed of catalyst, maintaining reaction temperature and feed composition at constant values and varying space time in the range 200 g.min.mol⁻¹ to 600 g.min.mol⁻¹. The range of space time that was considered in these tests was the same as the values that constituted the full factorial experimental design, such that the results obtained for these mass transfer resistance tests could be applied to the optimization study as well.

In the experimental tests for intraparticle mass transfer resistance, two different catalyst particle sizes were used and exactly the same operating conditions were employed. The conversions of 1-hexene obtained from the two experiments were compared. A lower conversion for larger catalyst particles would have indicated that the reaction was limited by intraparticle mass transfer resistance effects.

The results of both the external and intraparticle mass transfer resistance tests are discussed in Chapter 6.

3.2.2 Theoretical criteria

A number of criteria have been published that make possible the estimation of whether or not a packed bed reactor or a single catalyst particle is being studied under essentially ideal conditions. The accuracy of these calculation methods is limited by the accuracy with which physical properties are predicted and by the complexity of the reaction.

The Weisz-Prater criterion can be used to determine the significance of intraparticle mass transfer resistance effects (Missen et al, 1999). For negligible intraparticle mass transfer resistance,

$$\frac{(n+1)(-r_A)_{obs} r_p^2}{D_{eff} c_{A,s}} < 4.5 \quad (3.38)$$

where $(-r_A)_{obs}$ = observed reaction rate [kmol.m⁻³.s⁻¹]

r_p = catalyst particle radius [m]

D_{eff} = effective diffusivity [m².s⁻¹]

$c_{A,s}$ = surface concentration of component A [kmol.m⁻³]

n = reaction order

The result of a single experiment conducted at low conversion was used to evaluate this parameter. The differential operation of the reactor meant that the observed reaction rate could be calculated directly. Assuming negligible external mass transfer resistance, the known bulk concentration of component A ($c_{A,b}$) was used instead of the surface concentration ($c_{A,s}$) in Equation 3.38. The effective diffusivity was estimated using the following equation:

$$\frac{1}{D_{eff}} = \frac{1}{D_{K,eff}} + \frac{1}{D_{12,eff}} \quad (3.39)$$

where $D_{K,eff}$ = Knudsen diffusion coefficient

$D_{12,eff}$ = bulk diffusion coefficient per unit cross section of porous catalyst

$D_{K,eff}$ was obtained from:

$$D_{K,eff} = 19400 \frac{\theta^2}{\tau_m S_g \rho_p} \sqrt{\frac{T}{M}} \quad (3.40)$$

where θ = void fraction of the catalyst

τ_m = tortuosity factor

S_g = specific surface area [$\text{cm}^2 \cdot \text{g}^{-1}$]

ρ_p = particle density [$\text{g} \cdot \text{cm}^{-3}$]

T = temperature [K]

M = molecular weight [$\text{g} \cdot \text{mol}^{-1}$]

In the absence of other information, recommended values of $\tau_m = 4$ and $\theta = 0.5$ were used (Satterfield, 1991).

The bulk diffusion coefficient per unit cross section of porous catalyst was given by:

$$D_{12,eff} = \frac{D_{12}\theta}{\tau_m} \quad (3.41)$$

where D_{12} = binary diffusion coefficient [$\text{cm}^2 \cdot \text{s}^{-1}$]

The binary diffusion coefficient was estimated using Equation 3.17. All other quantities were known. For the experiment conducted at 380°C, 95% feed composition and $W/F = 403 \text{ g.min.mol}^{-1}$ and assuming first-order reaction kinetics,

$$\frac{(n+1)(-r_A)_{obs} r_p^2}{D_{eff} c_{A,s}} = 0.056 < 4.5 \quad (3.42)$$

which indicates that there is negligible intraparticle mass transfer resistance. The criterion holds for a second order reaction as well.

The Mears criteria (Fogler, 1999) can be used to check the significance of external concentration and thermal gradients. Under isothermal conditions, a concentration difference between the bulk fluid and outside particle surface will be insignificant if,

$$\frac{(-r_A)_{obs} r_p n}{k_c c_{A,b}} < 0.15 \quad (3.43)$$

where k_c = mass transfer coefficient [m.s^{-1}]

$c_{A,b}$ = bulk fluid concentration [kmol.m^{-3}]

The mass transfer coefficient was estimated using j-factor correlations of Petrovic and Thodos given by Satterfield (1991) for Reynolds numbers between 3 and 2000:

$$j_D = \frac{k_c \rho}{G} Sc^{2/3} \quad (3.44)$$

$$j_D = \frac{0.357}{\varepsilon_b Re^{0.359}} \quad (3.45)$$

where ρ = bulk fluid density [kg.m^{-3}]

ε_b = bed voidage

G = mass velocity [$\text{kg.m}^{-2}.\text{s}^{-1}$]

For the experiment conducted at 380°C, 95% feed composition and $W/F = 403 \text{ g.min.mol}^{-1}$ and assuming first-order reaction kinetics,

$$\frac{(-r_A)_{obs} r_p^n}{k_c C_{A,b}} = 0.0017 < 0.15 \quad (3.46)$$

Therefore there is negligible external mass transfer resistance. The criterion holds for a second order reaction as well.

In order for the observed reaction rate not to deviate by more than 5 percent because of a temperature difference between the catalyst particle and the bulk fluid, the following inequality must hold (Satterfield, 1999)

$$\left| \frac{(-\Delta H_r)(-r_A)_{obs} r_p E_a}{h T_b^2 R_g} \right| < 0.15 \quad (3.47)$$

where $(-\Delta H_r)$ = heat of reaction [J.mol⁻¹]

E_a = activation energy [J.mol⁻¹]

h = heat transfer coefficient [W.m⁻².K⁻¹]

T_b = bulk fluid temperature [K]

R_g = universal gas constant [J.mol⁻¹.K⁻¹]

The Mears thermal criterion contains several quantities that are unknown, such as the heat of reaction and activation energy. The heat transfer coefficient may be estimated using j-factor correlations and the heat and mass transfer analogy. The literature states that the metathesis reaction is essentially thermo-neutral (Kapteijn et al., 1981). Therefore if $(-\Delta H_r)$ can be assumed to be very small ($\Delta H_r \rightarrow 0$), the criterion is met and the temperature at the catalyst surface is equal to the bulk fluid temperature.

In this work, the packed bed laboratory reactor was usually operated as an integral reactor i.e. with substantial conversion from entrance to exit. Inter-bed gradients of concentration and temperature were likely to be extant. However, for meaningful results to be obtained for any set of experiments, isothermality should be achieved in both the radial and axial directions. This is usually difficult to attain. Mears developed the following criterion for the observed reaction rate not to deviate more than 5 percent from the radially isothermal case, assuming plug flow and that there are no external or intraparticle concentration or temperature gradients:

$$\left| \frac{(-\Delta H_r)(-r_A)_{obs} r_R^2 E_a}{k_{eff} T_w^2 R_g} \right| < 0.4 \quad (3.48)$$

where r_R = reactor radius [m]

k_{eff} = effective thermal conductivity of the bed [$\text{W.m}^{-1}.\text{K}^{-1}$]

T_w = wall temperature [K]

The criterion of Equation 3.48 is very sensitive to reactor radius. This emphasizes the importance of using small-diameter laboratory reactors to obtain isothermality. The criterion was not evaluated because of the unknown quantities $(-\Delta H_r)$ and E_a . However, for a thermo-neutral reaction ($\Delta H_r \rightarrow 0$) such as the metathesis reaction and for a sufficiently small reactor radius, the criterion should be met.

Chapter

4

Experimental equipment

The investigation of the 1-hexene metathesis reaction was conducted in three stages and the experimental work was performed using three different sets of laboratory reactor equipment. In the first stage, preliminary testing of the WO_3/SiO_2 catalyst was carried out in order to determine appropriate feed gas flow-rates and reaction temperatures for the optimization study. These experiments were performed using an auxiliary reactor rig. The feed gas was prepared by saturating a stream of nitrogen with 1-hexene by bubbling through an agitated vessel containing the liquid reactant maintained at 40°C using a constant temperature bath. Consequently, the composition of the feed gas was limited to less than 30% 1-hexene (mole based). The experiments were unsuccessful, since very low conversions of 1-hexene were obtained and heavy reaction products were not detected in the exit product stream. Further details of this set of experimental equipment are given in section 4.1.

The second set of experiments was conducted at the Department of Process and Environmental Engineering of the Technical University of Łódź, Poland, using an experimental set-up that was very similar to the preliminary design. The results of the preliminary investigation were unreliable, due to inaccurate flow measurement and composition analysis. The experimental program conducted in Poland used essentially the same setup as the preliminary investigation but included several improvements such as a digital volumetric flow-meter for gas flow measurement and complete G.C. composition analysis of both liquid and gas product streams. These experiments were once again carried out in order to determine appropriate feed gas flow-rates and reaction temperatures for the optimization study, using a more sophisticated apparatus.

The feed gas was once again prepared by saturation of a stream of nitrogen with 1-hexene and the composition was limited to less than 30%. A different batch of WO_3/SiO_2 metathesis catalyst with a lower specific surface area was used for these tests. This was the only WO_3/SiO_2 catalyst that was available for experimentation in Poland at the time. At feed flow-rates that were similar to those used for the preliminary investigation, an improved 1-hexene conversion and selectivity to higher olefins were obtained. The yield of the primary metathesis product, decene, was still very low because the conversion was typically below 40%. In order to obtain higher conversions, the feed gas concentration and space time had to be increased. Further details of this set of experimental equipment are given in section 4.2.

After returning to South Africa and reviewing the results of the preliminary tests and the experiments conducted in Poland, it was decided that major revisions had to be made to the experimental set-up. In particular, higher feed concentrations of 1-hexene had to be employed in order to obtain higher conversions and the saturation method of feed preparation could not be used for this purpose. A new bench-scale reactor unit was commissioned to carry out the experimental work of stage three. This stage of the investigation was the most important, since the experiments that were performed during this stage constituted the entire optimization study. The saturator assembly was replaced by a fine metering pump, such that higher feed concentrations of 1-hexene could be achieved and lower feed flow-rates could be employed. During the commissioning phase it was found that even at moderate reaction temperatures, a conversion of at least 80% could be achieved. The optimization study commenced after the successful operation of the third set of equipment was proven. Further details of this set of experimental equipment are given in section 4.3.

4.1 Preliminary fixed bed catalytic reactor rig

Preliminary testing of a newly prepared batch of WO_3/SiO_2 metathesis catalyst (Catalyst B) was performed using an auxiliary rig assembled from components that had previously formed part of an undergraduate catalysis research study conducted at the school. A simple form of feed preparation and delivery was used. Nitrogen was saturated with liquid 1-hexene in a glass vessel by bubbling through a sintered glass sparger, and delivered to the top of a vertically positioned fixed-bed tubular reactor. The contents of the saturation vessel was agitated by means of a Teflon™ coated magnetic stirrer bar and mechanism, to maintain smaller bubble sizes and increase residence time through an even distribution of gas within the vessel. It was maintained at 40°C using a constant temperature bath. The greater surface area to bubble volume ratio envisioned for smaller bubbles enhances the rate of mass transfer at the gas-liquid interface. A conical glass flask contained the 1-hexene, sealed at the mouth with a Teflon™ cap

(Fig. 4.1). Glass tubing, integrated into the seal, allowed streams of gas to enter and leave the vessel. The inlet tube terminated at the bottom of the flask with a sintered glass sparger, designed to produce bubbles of diameter less than 2mm at low gas flow-rates. The glass flask was immersed in a constant temperature bath.

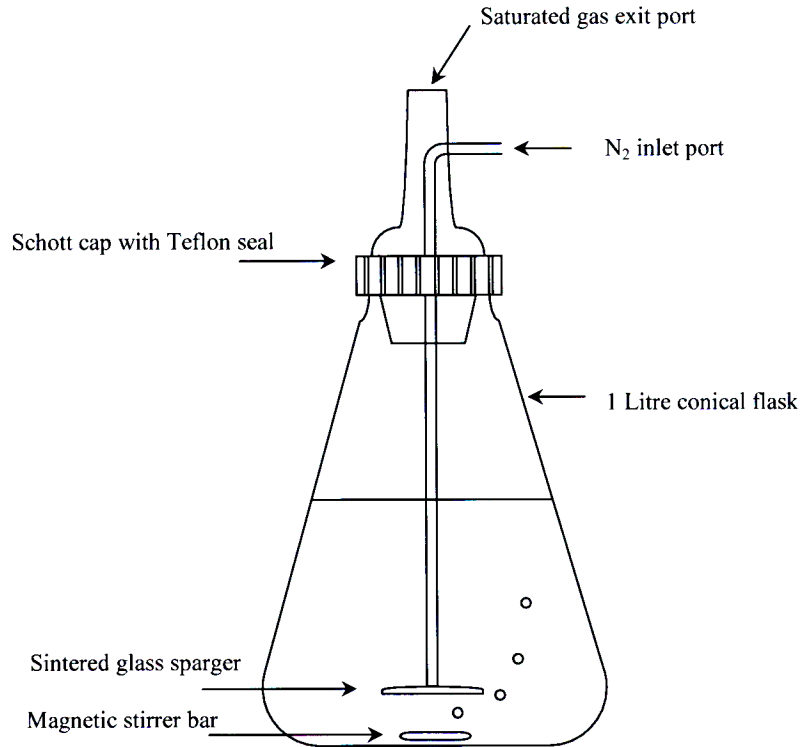


Figure 4.1 Saturation vessel

Assuming that 100% saturation of the nitrogen gas with 1-hexene is achieved within the saturation vessel, the exit mole fraction of 1-hexene is given by the following equation:

$$y_{hex} = \frac{P_{hex}^0}{P} \quad (4.1)$$

where P_{hex}^0 is the saturated vapour pressure of 1-hexene at the saturation temperature:

$$\ln P_{hex}^0 = 15.8089 - \frac{2654.8}{T - 47.3} \quad (4.2)$$

From the volumetric flow-rate of nitrogen, the molar flow-rate of the inert is calculated using the ideal gas equation:

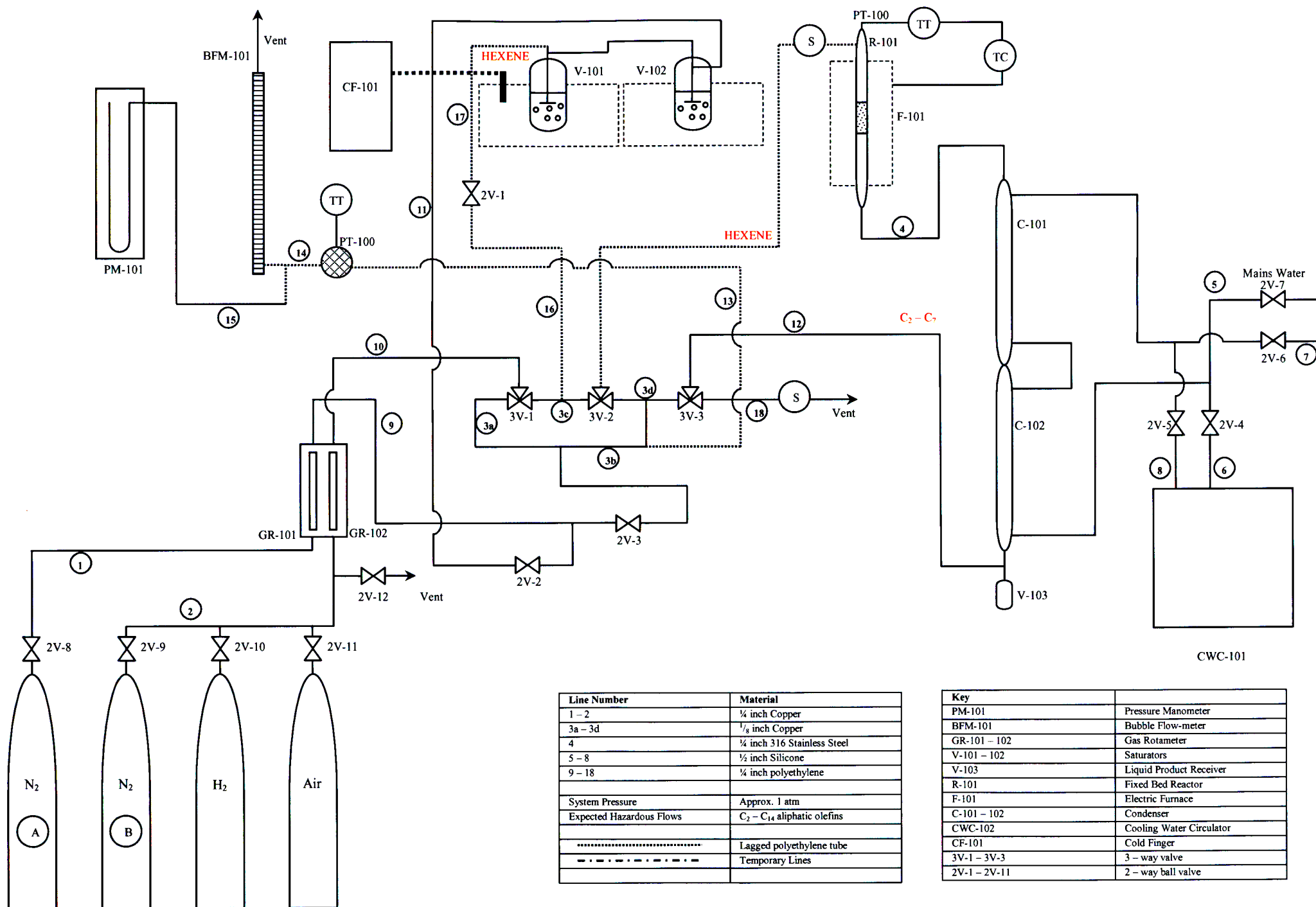


Figure 4.2 Preliminary fixed bed catalytic reactor system – piping and instrumentation diagram

During the commissioning of this system, the measured mole fraction of 1-hexene in the feed gas was found to be within 5% of the theoretical value estimated using Equation 4.1. In the application of this type of feed preparation and delivery, the saturation vessel is occasionally filled with a form of random packing e.g. Intalox saddles (Hattikudur and Thodos, 1975), which may increase the contact time and aid in achieving an acceptable level of saturation. Such systems are not agitated. For the system investigated, agitation adds energy to break larger bubbles into smaller ones. The inclusion of packing would negate this effect, causing bubbles to coalesce as they move to the top of the vessel.

Two types of reactor material were chosen for the preliminary investigation, viz. quartz glass and 316 stainless steel. Either 316 or 310 grade stainless steel may be used for this catalyst system since these materials contain less chromium and nickel and will not promote dehydrogenation/hydrogenation side reactions. The deactivating nature of stainless steel was neither proven nor refuted through the preliminary investigation. The advantage of using quartz glass is that it is effectively inert. Metal reactors are more robust, however, not susceptible to cracking under high temperatures and during catalyst changeover. The reactor dimensions are given in Table 4.1. A wire mesh was placed at the bottom of the bed for support and was separated from the catalyst by a thin layer of glass wool. Connections, for the quartz tube, to metal piping were made via commercial glass to metal adapters (Cajon™), sealed using high temperature Neoprene o-rings. Standard Swagelok™ unions were used for the metal reactor tube.

	Quartz glass	316 Stainless steel
Length [mm]	400	400
ID [mm]	10	9.4
OD [mm]	12	10.2

Table 4.1 Reactor dimensions (auxiliary rig)

The feed gas leaving the saturation vessel was heated and mixed in a parallel system of ¼ inch 304 stainless steel pipes. Nichrome resistance wire wrapped along the length of each pipe provided heating. A Type-K thermocouple mounted inside the reactor tube was used as the temperature measuring element. An on-off controller and solid state relay were used to control the temperature inside the reactor tube. Oscillations of temperature around the set-point were reduced to a minimum of $\pm 2^{\circ}\text{C}$ with the addition of Fibrefax™ insulation. The furnace itself was a combination of a simple tube furnace and a block furnace, hinged to allow easy removal

of the reactor tube. Electrical heating elements were secured to a cylindrical recess cut into each half of a block of ceramic insulation. The two blocks were mounted inside a steel case that could be latched on one side once the reactor tube had been placed inside. The input voltage was adjusted, using a step-down transformer, to 100V. Heavy reaction products were condensed in a modular water-cooled condenser and subsequently analysed. The non-condensable products were sampled for analysis and flow-rates were measured using a bubble flow-meter.

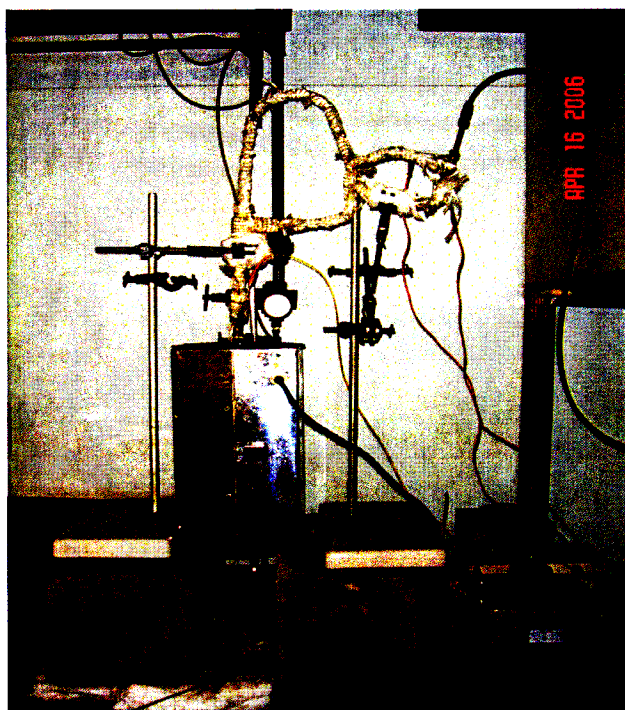


Figure 4.3 Reactor furnace and peripheral heating

4.2 Equipment used for experiments conducted in Poland

Further tests were conducted at the Department of Process and Environmental Engineering of the Technical University of Łódź, Poland, on equipment assembled by Dr. Marek Stelmachowski. Another batch of WO_3/SiO_2 catalyst (Catalyst A) with an average pellet size of 2mm x 3mm was ground and sieved into various size fractions for experimentation. This system was similar to the preliminary design at the University of KwaZulu-Natal. However, a digital volumetric flow-controller was used to measure and control the flow-rate of the nitrogen gas and the composition of the gas and liquid product samples were determined via gas chromatography using G.C. apparatus that had been optimized specifically for these analyses. The experimental setup was thus much more sophisticated. A saturator was employed as the means of feed preparation and delivery, heavy reaction products were condensed, separated and

analysed, and product gas flow-rates were measured using a bubble flow-meter prior to sampling.

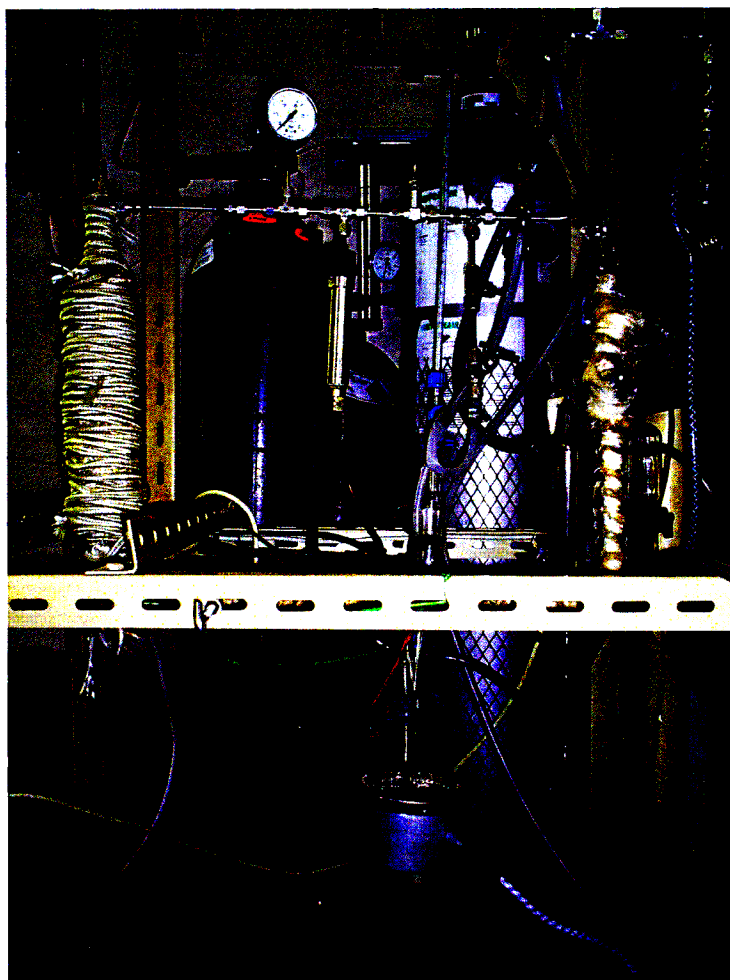


Figure 4.4 Experimental fixed bed reactor system at the Technical University of Łódź, Poland

The fixed bed catalytic reactor was constructed of 316 stainless steel, partitioned in two and assembled by means of grub-screws. The reactor tube was 250mm long, with an inner diameter of 10mm. The reactor was secured in a vertical position to facilitate a downward flow of reactant gas, ensuring good packing of the catalyst bed. The catalyst was packed into the tube, leaving a void above for mixing and pre-heating of the reactant gas phase. The bed was secured in position inside the tube by means of quartz wool plugs at the top and the bottom.

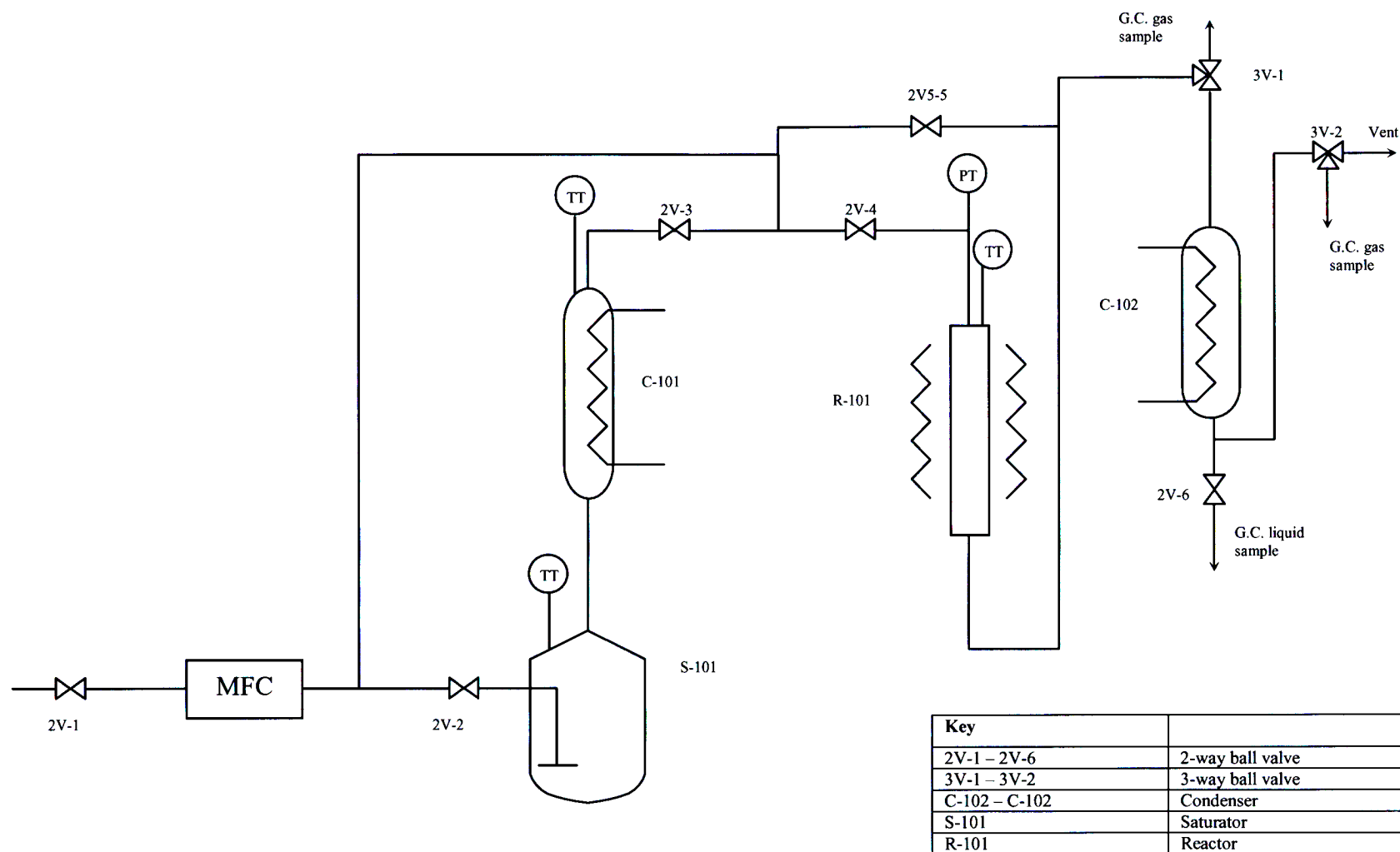


Figure 4.5 Polish experimental program fixed bed catalytic reactor system – piping and instrumentation diagram

Heating of the reactor tube was accomplished by means of a coil of nichrome wire, powered by a 240V, 5A voltage regulator. The nichrome coil was covered by a set of ceramic sleeves. The entire reactor tube, once en-coiled by the heating wire, was wrapped in glass-cloth and glass-fibre rope to provide additional insulation. Temperature measurement inside the reactor was made possible by incorporating a sheathed type-K thermocouple into the upper Swagelok™ union. Data acquisition was accomplished by the use of the computer package GeniDaq™ Runtime. The exit line from the reactor assembly was also heated, using a method similar to that of the reactor itself, but was insulated with glass-tape.



Figure 4.6 Fixed bed tubular reactor, fully assembled

Preparation of the feed gas was carried out in two stages. First, nitrogen was bubbled through a vessel containing liquid 1-hexene at approximately 45°C. The exit vapour was passed through a water cooled condenser at 30°C before entering the reactor tube. The approach to saturated conditions at 30°C in the condenser, from a higher level of concentration at the exit of the saturator, was essentially the same as the method using a series arrangement of bubblers maintained at different temperatures (refer to section 4.1).

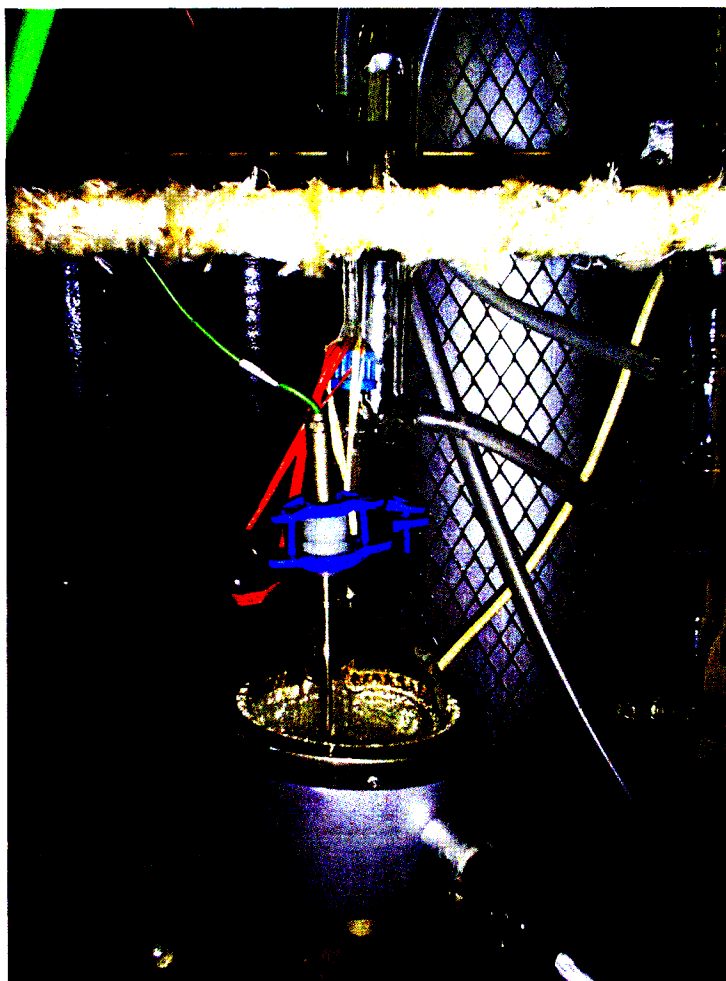


Figure 4.7 Saturator vessel and condenser unit

Two distinct parts constituted the primary saturator assembly. The saturation vessel was a 1000ml round-bottom flask with three exit ports. The central port was used as the entry point for the nitrogen gas. A glass tube, sealed to a screw-type fitting, was inserted into the flask via this port. The bottom end of this glass tube terminated with a sintered glass sparger. A sheathed thermocouple was sealed inside the flask through the second port. The last port was fitted to the bottom end of the saturator condenser. This condenser was a glass, water-cooled condenser with the utility stream flowing through the central channel. A mercury-bulb thermometer was inserted into the top of the condenser via a screw-type fitting. Rising vapour was allowed to exit the condenser through a separate branch. The cooling water flowing to this condenser was maintained at 30°C by means of a Haake™ refrigerated cooling water circulator. The round-bottom flask was heated using a laboratory heating mantle. The flow-rate of nitrogen was controlled using a 4-channel Brooks™ volumetric flow controller.



Figure 4.8 Brooks™ 4-channel volumetric flow controller

Heavy reaction products were condensed using a water-cooled glass condenser. Volumetric flow-rates of the non-condensed phase were measured using a simple laboratory bubble flow-meter. Gas samples were drawn for G.C. analysis from a sample port using a gas syringe.



Figure 4.9 Haake™ cooling water circulator

The analyses of liquid and gas products were performed using two Perkin Elmer Autosystem XL™ gas chromatographs each equipped with a flame-ionization detector (FID). The column characteristics and temperature methods for each type (liquid and gas) are presented in Tables 4.2 and 4.3.

Column		PE-Volatile N931-6393		
Length	[m]	75		
ID	[mm]	0.45		
film thickness	[μm]	2.55		
Detector		FID		
Program				hold time
		T ₁	120°C	8 min
		rate1	20°C/min	
		T ₂	150°C	5 min
		rate2	40°C/min	
		T ₃	240°C	30 min
Detector Temperature	[°C]	260		
Injector Temperature	[°C]	240		
Split		100:1		
Carrier gas	[ml.min ⁻¹]	2	(helium)	

Table 4.2 Column characteristics: liquid analysis

Column		Supelco SPB-1 NR CAT. 25349		
Length	[m]	60		
ID	[mm]	0.53		
film thickness	[μm]	5		
Detector		FID		
Program				hold time
		T ₁	35°C	5 min
		rate1	23°C/min	
		T ₂	150°C	12 min
		rate2	30°C/min	
		T ₃	210°C	15 min
Detector Temperature	[°C]	240		
Injector Temperature	[°C]	210		
Split		100:1		
Carrier gas	[ml.min ⁻¹]	2	(helium)	

Table 4.3 Column characteristics: gas analysis



Figure 4.10 Perkin Elmer Autosystem XL™ gas chromatograph

4.3 Fixed bed catalytic reactor system for vapour phase metathesis reaction studies

A new, modified bench-scale reactor unit was designed and commissioned at the School of Chemical Engineering of the University of KwaZulu-Natal to carry out most of the experimental work. Features of this system included a fine metering pump for the delivery of liquid 1-hexene from a temperature controlled feed tank and precision mass flow control valves used for the application of pre-treatment and dilution gases. The reaction was carried out in a 316 stainless steel reactor mounted inside an electrically heated tube furnace, capable of operating at temperatures up to 1200°C. Reaction conditions were monitored by a control and data acquisition package. Reaction products were once again condensed and sampled and the flow-rates of non-condensed products were tested using a bubble flow-meter. Several components of the auxillary rig were incorporated into this new system. These included valves, fittings, controllers and display units. Each module of the new reactor system will be discussed in detail in the sub-sections that follow.

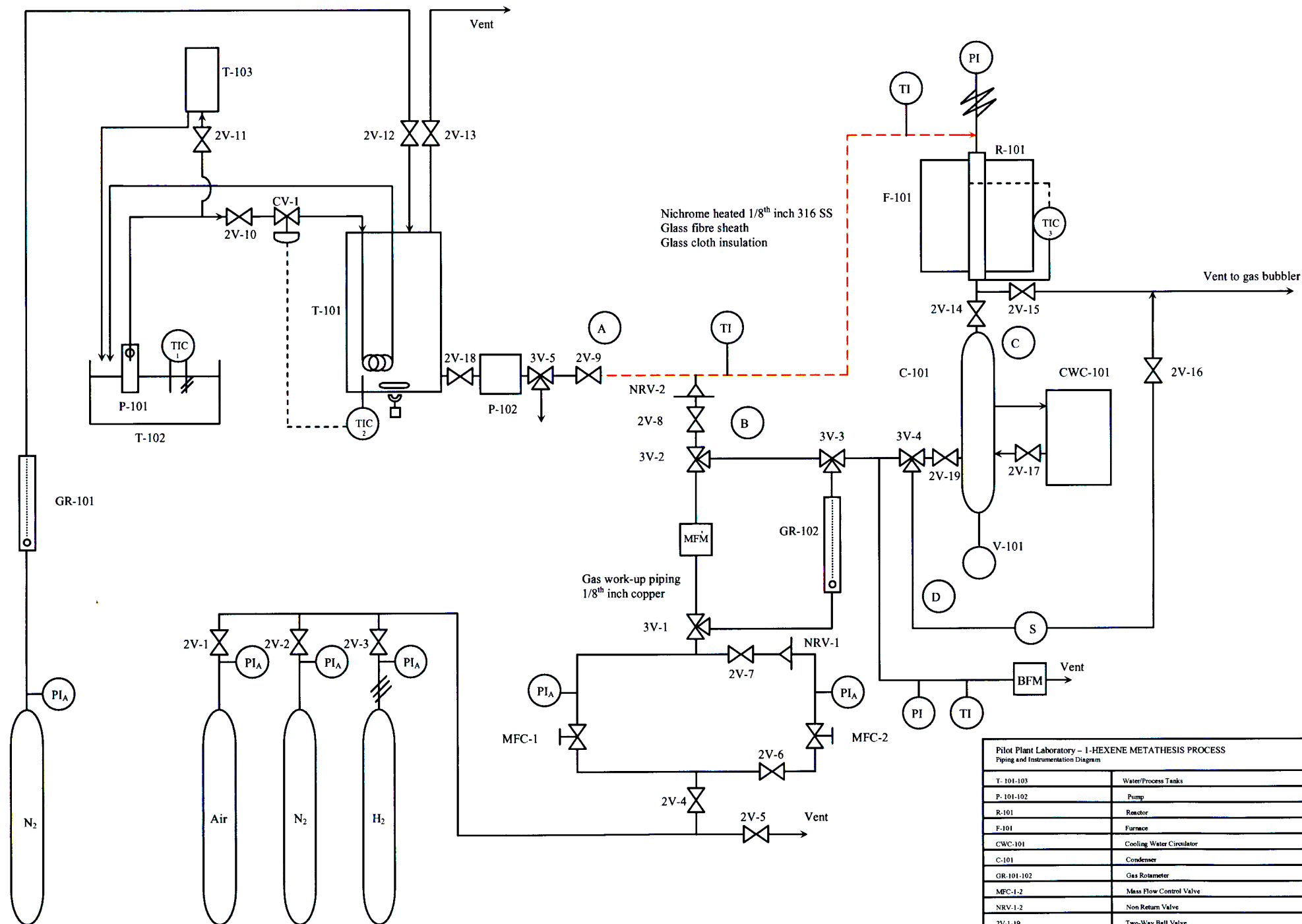


Figure 4.11 Fixed bed catalytic reactor system – piping and instrumentation diagram

Pilot Plant Laboratory – 1-HEXENE METATHESIS PROCESS Piping and Instrumentation Diagram	
T-101-103	Water/Process Tanks
P-101-102	Pump
R-101	Reactor
F-101	Furnace
CWC-101	Cooling Water Circulator
C-101	Condenser
GR-101-102	Gas Rotameter
MFC-1-2	Mass Flow Control Valve
NRV-1-2	Non Return Valve
2V-1-19	Two-Way Ball Valve
3V-1-5	Three-Way Ball Valve
V-101	Cold Trap

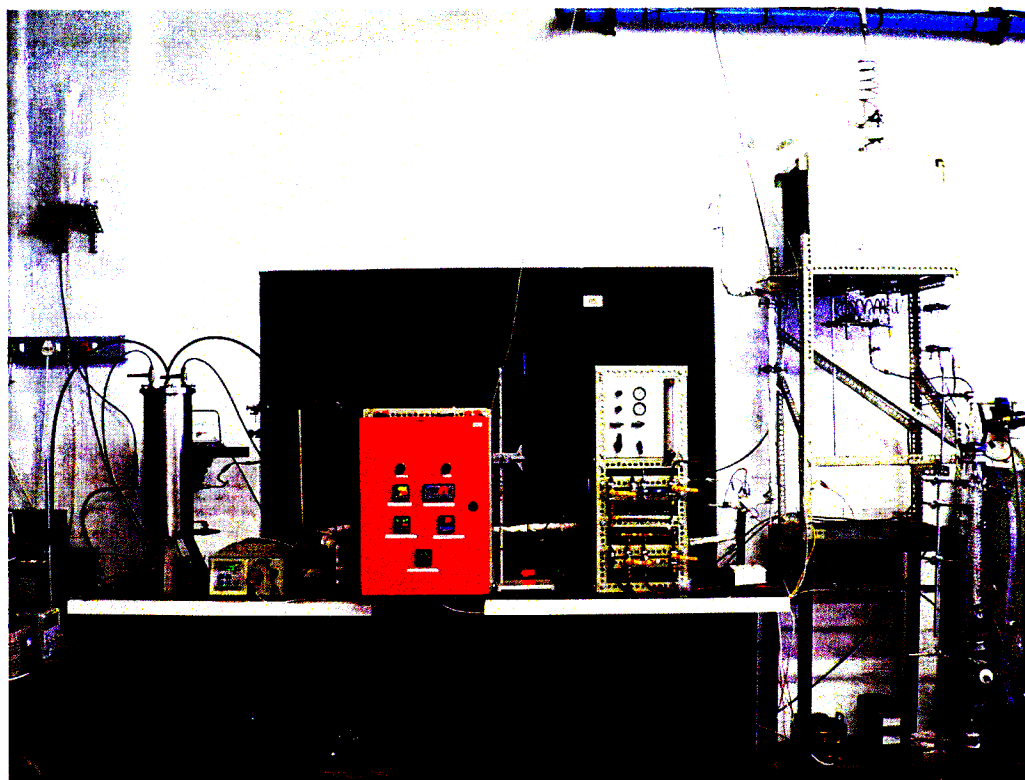


Figure 4.12 Fixed bed catalytic reactor system for vapour phase metathesis reaction studies

4.3.1 Liquid feed preparation and delivery

An existing stainless steel tank was retrofitted to enable temperature control of the contents. The tank, fabricated from 316 stainless steel, was equipped with a glass level sight for monitoring liquid level. Cylinder dimensions are presented in Table 4.4.

Height	[mm]	570
OD	[mm]	155
ID	[mm]	150
Wall thickness	[mm]	2.5
Flange thickness	[mm]	10

Table 4.4 Feed-tank cylinder dimensions

Fixed to the top flange were two valves that were used as inlet and outlet points for an inert gas purge. This vapour blanket ensured minimal contact of the reactant liquid with air, safeguarding against the formation of oxygenates which would otherwise poison the catalyst. It also provided a positive pressure on the pump suction side, to keep the pump properly primed throughout operation. Nitrogen was fed to the tank via a low-flow Porter A-125-3 variable area flow-meter, where the flow-rate was set at $25\text{ml}\cdot\text{min}^{-1}$. Also mounted on the top flange was a $\frac{3}{8}$

inch OD copper coil which facilitated heating of the tank contents by hot water. Electrical heating elements were not considered for this purpose due to the risk of fire and explosion. The top flange was fixed to the tank by means of six wing-nuts. A gas-tight seal was provided by a 3mm Viton o-ring mounted within grooves machined into the top flange and tank mouth.

Hot water from a temperature controlled bath was pumped through the copper coil. A class A Pt-100 temperature probe, fixed through the base of the tank, was used to measure the liquid temperature. Temperature was controlled by throttling the flow of hot water to the tank. Control elements included an RKC CB-100 digital temperature controller and a ¼ inch Bauman series 51000 control valve, complete with a Fischer Type-3661 electro-pneumatic positioner and a 67 CFR regulator. Tuning of the controller was accomplished by means of the reaction curve tuning method (Richards, 1979), based on the open-loop response of the system to a step change in the proposed control action (Δm , change in control valve position). The response of the proposed feedback variable T (Figure 4.14) was used to obtain controller settings.

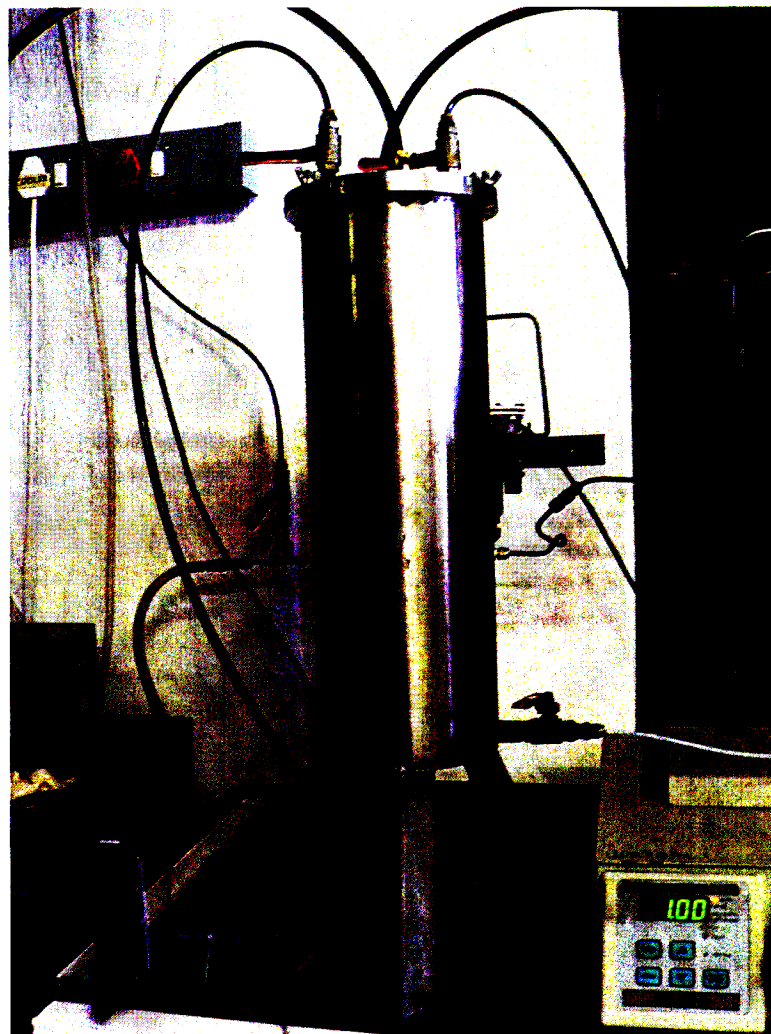


Figure 4.13 Stainless steel liquid feed tank

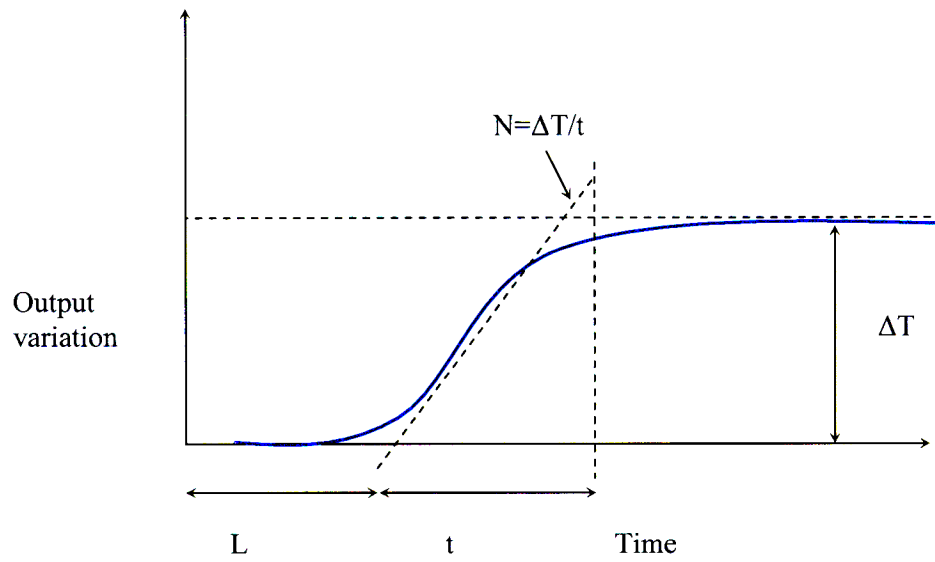


Figure 4.14 Open-loop response to a step change in the proposed control action

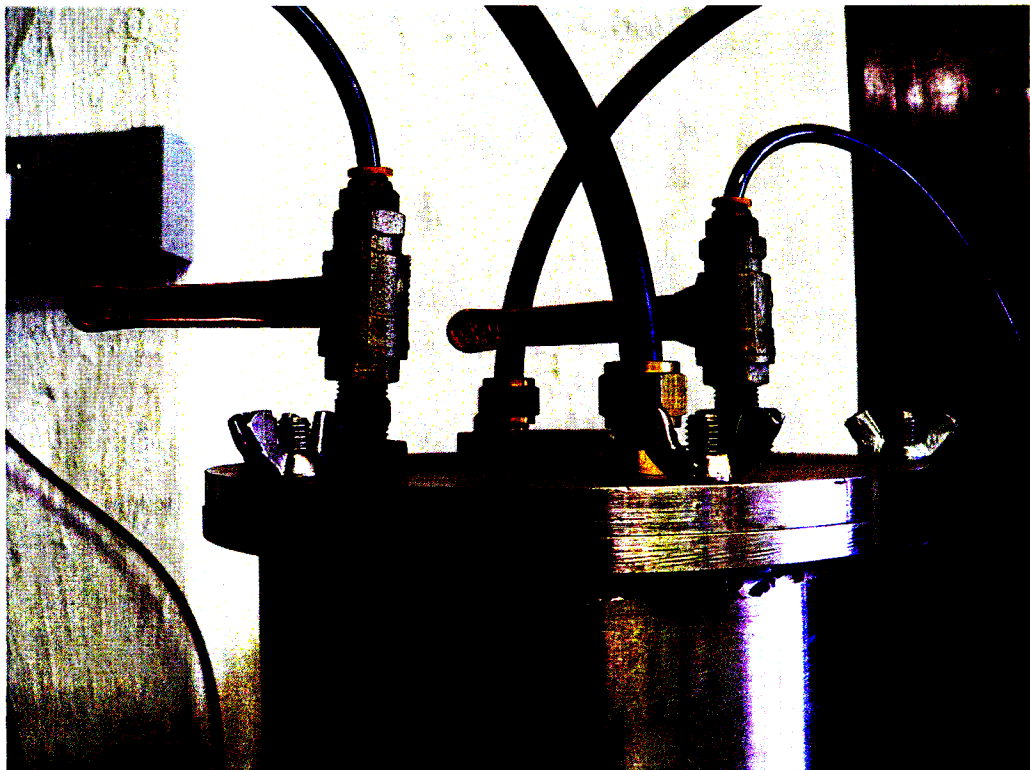


Figure 4.15 Feed tank top flange

The Ziegler-Nichols settings for the controller were given by:

$$K_c = 1.2 \frac{\Delta m}{NL} \quad (4.6)$$

$$\tau_I = \frac{L}{0.5} \quad (4.7)$$

$$\tau_D = 0.5 \times L \quad (4.8)$$

The step response for the system was obtained from a process simulation, implemented in MATLAB®, which was based on the mass and energy balances around the feed tank (see Appendix F). The response could not be measured directly since a 4-20mA signal generator, used for manipulating the position of the control valve, was unavailable at the time.

The response of tank temperature to a 20% step change in the valve position (100% → 80% of travel) is presented in Figure 4.16.

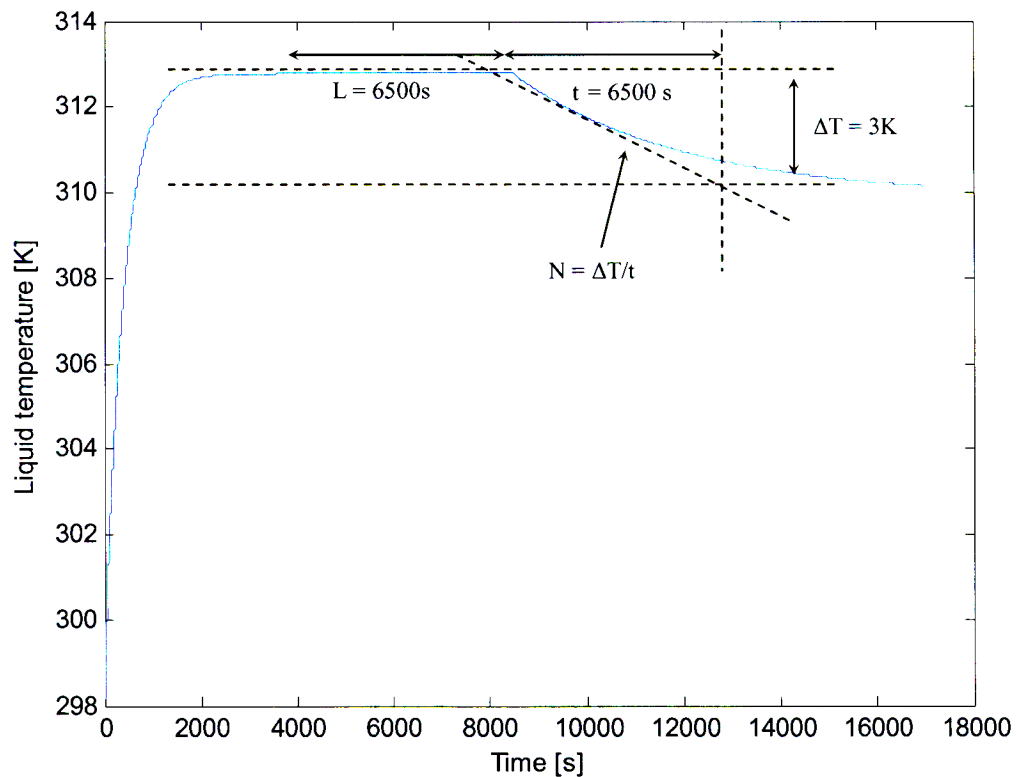


Figure 4.16 Response of tank liquid temperature to a 20% step change in valve position

From this curve the following parameters were calculated:

$$K_c = 0.08$$

$$t_I = 13000\text{s}$$

$$t_D = 3250\text{s}$$

The actual measured response from start-up was found to be very similar to the simulated results. Temperature in the tank could be maintained to within 0.2°C of the set-point (30°C) using this control scheme even with the very slow process dynamics. In the event of the valve failing closed, flow was diverted to a surge tank mounted above the rig.

A Spectrochrom P100 isocratic pump was used to deliver the liquid to the reactor module. The pump was calibrated gravimetrically for the range of flows that were used during the experiment (Appendix A). A split in the feed line allowed calibration and feed samples to be drawn for G.C. analysis. The feed line from the sample point to the reactor head (1/8 inch stainless steel) was maintained at approximately 100°C with a coil of nichrome resistance wire, tightly wound around the piping and powered by two 250V variacs (AC/DC Dynamics; Yokoyama Electric Works). A voltage setting of 75V between the sample point and the inert gas mixing point and 60V between the mixing point and reactor head proved adequate. The purpose of such an arrangement was to ensure complete vapourization of the liquid feed prior to mixing with nitrogen. The flows of the respective species (1-hexene and nitrogen) could be set to create the required composition of feed gas for the reaction. The heated piping was lagged with a glass fibre sheath, Fibrefax™ insulation and finally a layer of glass cloth. Pt-100 resistance thermometers were mounted in-line at the mixing point and reactor inlet, connected to I-on electro-m® and CB-100 temperature displays, respectively.

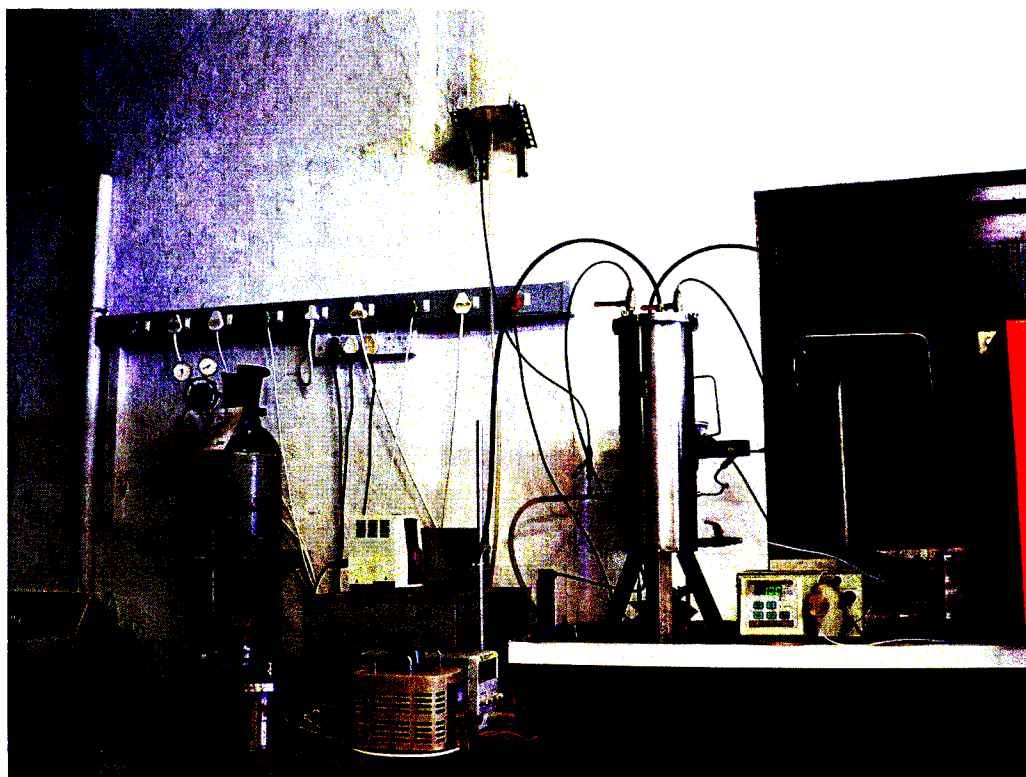


Figure 4.17 Liquid feed preparation and delivery system

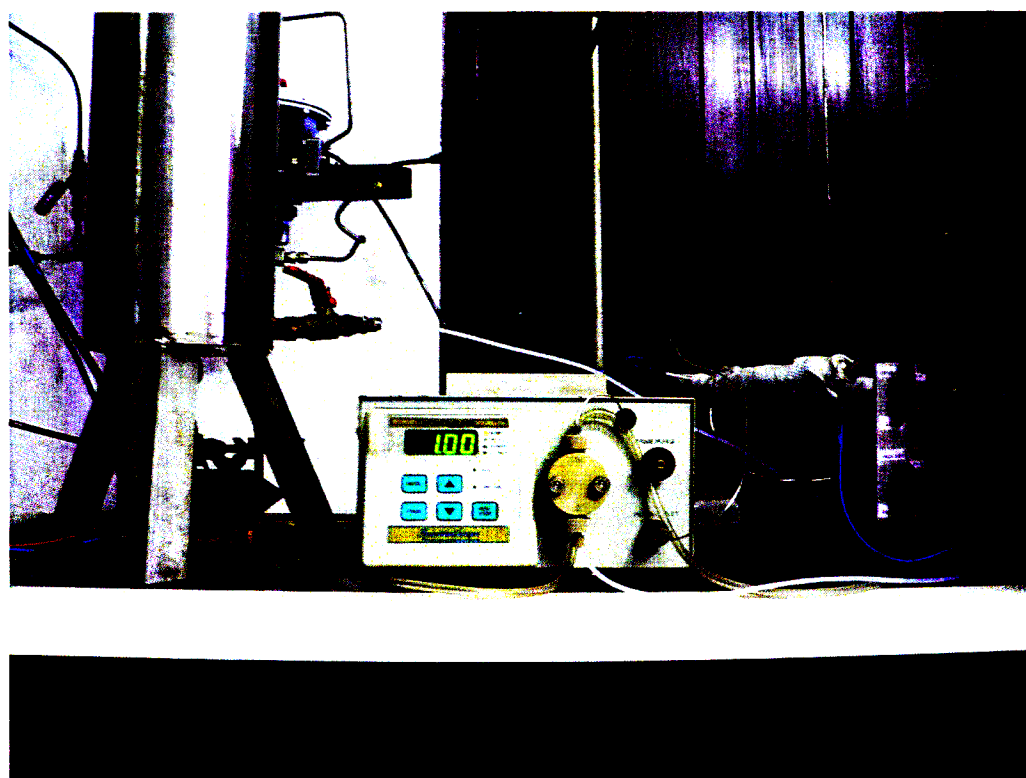


Figure 4.18 Spectrochrom P100 isocratic pump

4.3.2 Pre-treatment and dilution gas application

Pre-treatment and dilution gases, *viz.* air, hydrogen and nitrogen (all UHP > 99.999% purity, Afrox) were supplied in standard cylinders. Afrox Saffire™ multi-stage regulators were used to provide a supply pressure of 200kPa (gauge) for the gas work-up. A series of isolation, shut-off and 3-way ball valves (Swagelok, 317®, Nupro) were used to control the flow path of each of these gases (Figure 4.11). Pre-treatment and dilution gas flow-rates were controlled by two Porter VCD 1000 mass flow control valves (MFCV) mounted in parallel. For low flow-rates the second MFCV was isolated via two shut-off valves. A non-return valve eliminated the possibility of reverse flow on this second line. Flow-rates were measured using a Bailey/Porter/Fischer precision bore rotameter, calibrated for all gases at supply conditions (Appendix A). 3-way valves enabled the operator to select either this instrument or a mass flow-meter, for process flow measurement. The Sierra™ thermal mass flow-meter originally intended for this system was in need of major repairs and was subsequently discarded.

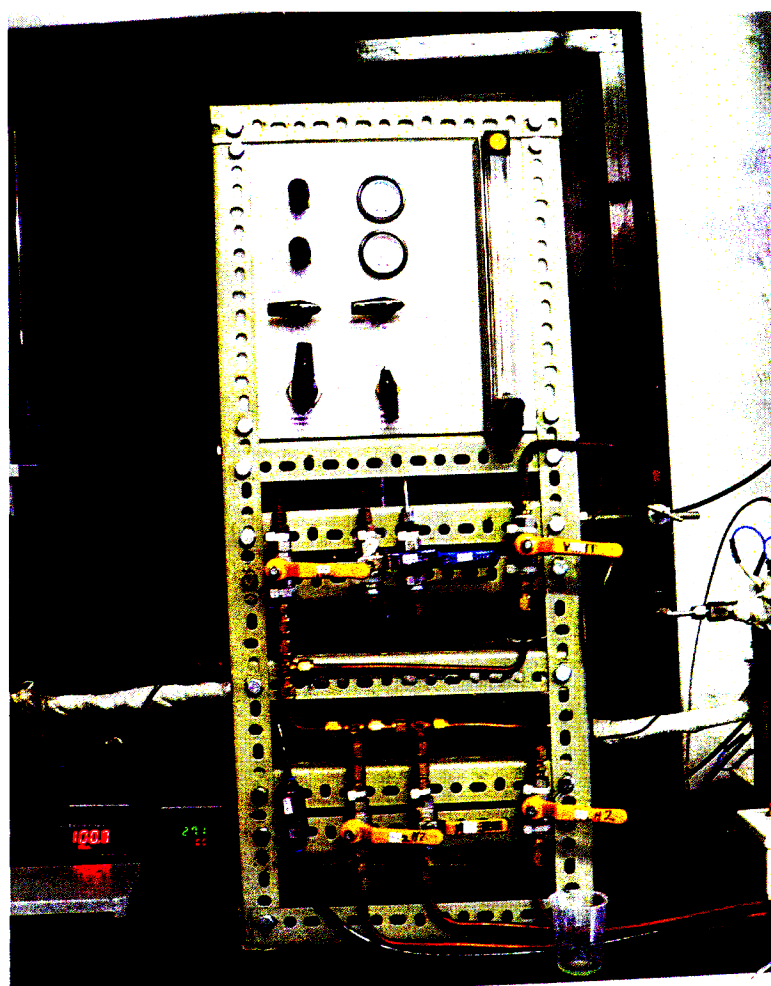


Figure 4.19 Pre-treatment and dilution gas work-up

The flow-rates of pre-treatment and dilution gases were also checked before and after an experiment using a bubble flow-meter. Analogue pressure gauges (ENFM instruments) were mounted in-line directly after the MFCV to monitor the secondary supply pressure and line pressure during preliminary pressure and leak testing. Residual gas was discharged, via a vent valve, to the atmosphere. All piping was $\frac{1}{8}$ inch copper. The primary concern with this arrangement was the possibility of 1-hexene entering this system through high pressure/reverse-flow conditions, since most of the instruments could be damaged by this chemical. A non-return valve was installed to eliminate this possibility. A master isolation valve was installed as a redundant safety feature, directly after this system. The final gas piping leading off this network met the heated liquid feed line at the mixing point. The entire valve bank was mounted on a Dexion™ frame.

4.3.3 Fixed bed catalytic reactor module

Tubular laboratory reactors are most often used vertically, to eliminate the effects of settling and reactant bypassing (Anderson and Pratt, 1985). The reactant gas is also in down-flow, which maintains the packing of the bed. The vertical arrangement of the reactor tube was used in this investigation.



Figure 4.20 Fixed bed catalytic reactor module

The smallest system practicable was chosen in order to make the reactor as near as possible to isothermal. Owing to its robust nature, the metal reactor was retained for use in the new system. A longer $\frac{1}{2}$ inch OD, heavy gauge 316 stainless steel tube 437mm long with an inner working diameter of 9.4mm, was used. The reactor was connected to the feed and exit points using standard Swagelok™ reducing unions. A Wika S-10 pressure transmitter was fixed to the reactor head via a helical copper coil, 1200mm long, which separated the sensor from the high temperature conditions extant in the reactor below. Reactor pressure was displayed on a TOHO TTM-004 digital controller. The exit assembly consisted of two parallel valves, one for the gravity flow of reaction products and the other a vent valve to be used during the catalyst pre-treatment stages. The vent valve terminated in a 3m length of $\frac{1}{8}$ inch copper tubing, coiled, and connected to the final vent line.

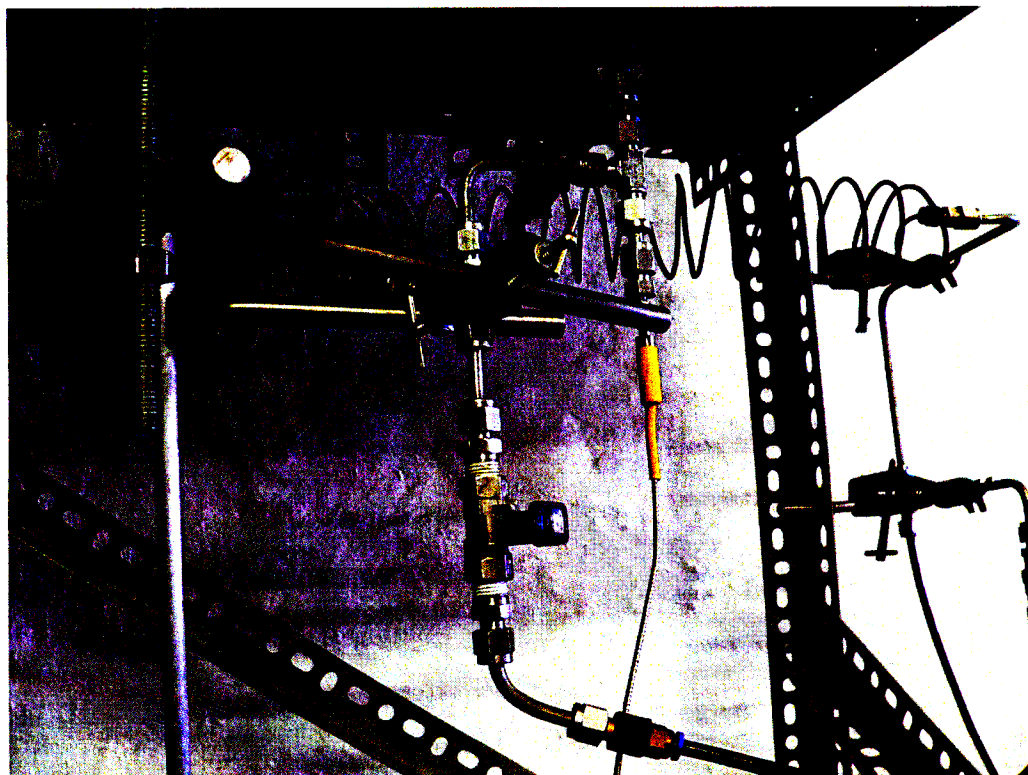


Figure 4.21 Fixed bed catalytic reactor module exit assembly

Temperature at the centre of the catalyst bed and the tube was measured using a $\frac{1}{16}$ inch sheathed Type-K thermocouple (chromel-alumel). The bed was supported by a 1000 micron stainless steel mesh plate, secured to the thermocouple sheathe using a grub-screw (Figure 4.22). A layer of quartz wool separated the catalyst from the mesh. Another layer of wool was placed above the bed once the reactor had been filled.

The reactor tube was heated in a Carbolite MTF single zone electrical furnace with a ceramic tube diameter of 30mm. Temperature control was established by a Shinko JCS digital PID controller and solid-state relay. The relay activated the furnace heating elements in relation to the output signal of the controller. An on-line trial and error tuning technique (Luyben, 1999) was used to obtain controller parameters. For pure pre-treatment gases (N_2 , H_2 and air) the first set of parameters given in Table 4.5 (PID control) gave the tightest control without amplifying noise in the process measurement signal. Temperature could be maintained to within 1°C of the set-point value. The controller was also tuned online for the reaction, using these parameters as initial estimates. A faster control response was required during the reaction period, which resulted in the second set of parameters.

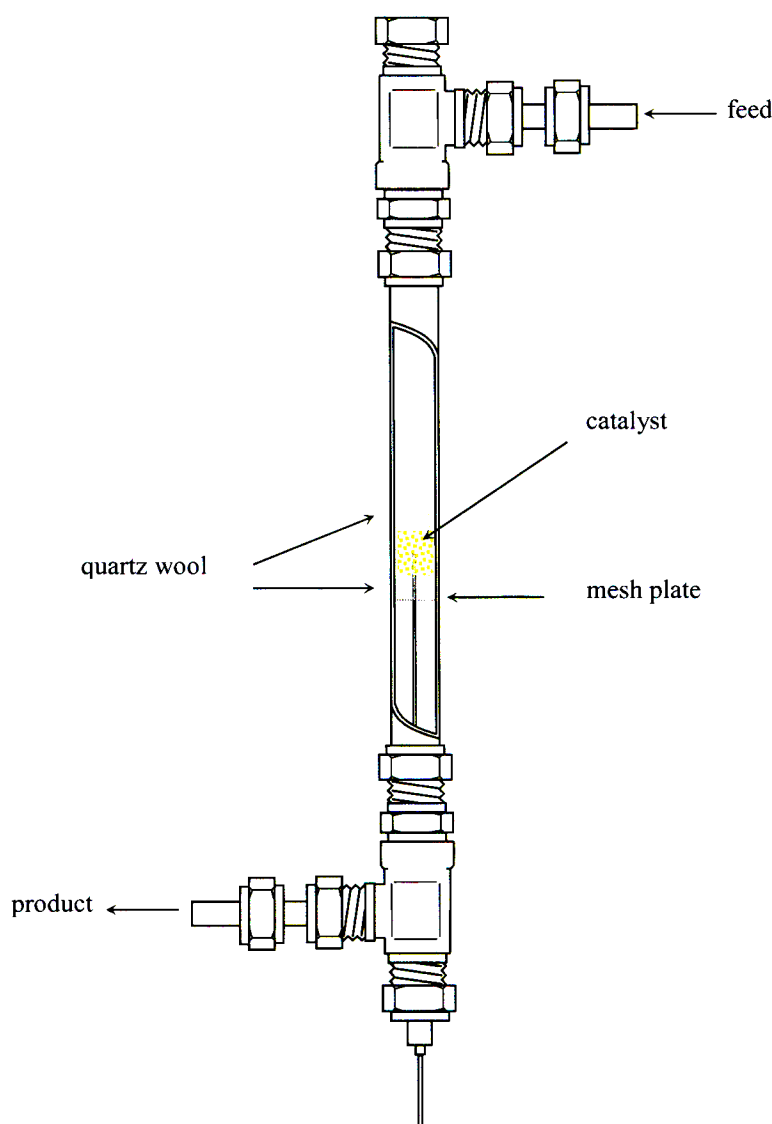


Figure 4.22 Laboratory scale fixed bed catalytic reactor

A $\pm 2^{\circ}\text{C}$ deviation from the set-point was observed for a varied range of reaction conditions. For lower feed gas concentrations ($< 30\%$), control was improved by reducing the amount of integral and derivative action (Set 3 in Table 4.5). The bulk of the experimental work was done in the higher range of feed gas concentration. The reaction pressure and temperature were monitored and logged using a proprietary SCADA package (Shinko JC-300 monitoring software). The entire reactor module was raised by construction of a tiered Dexion support structure, to facilitate gravity flow of the heavy reaction products.

	Controller settings		
	PB	t_i [seconds]	t_d [seconds]
Set 1 - Pre-treatment	10	400	90
Set 2 - Reaction A	5	200	90
Set 3 - Reaction B	5	220	85

Table 4.5 Furnace controller parameter settings

4.3.4 Product collection and sampling

Heavy reaction products were condensed in a 550mm long, 60mm OD, Corning QVF – HE 1½ glass condenser rated to 8bar. The modular condenser, top cap, gas tee and collection pot were assembled using standard cork and steel flange plates and 8mm bolts. Teflon caps, sealed with viton o-rings, and poly-flow push-in fittings were used to make connections to inlet and outlet piping. A single ball valve fixed to the bottom of the conical collection pot was used to drain the condensed liquid. The condenser was linked to a Labcon TBR-100 refrigerated cooling water circulator, maintained at 2°C . During preliminary runs it was found that this vessel was able to condense more than 96% of the reaction products that were heavier than 1-hexene.

The volumetric flow-rate of the non-condensed reaction products was measured using a bubble flow-meter. Temperature and pressure were also measured at this point using a Pt-100 temperature probe and Honeywell Sensotec TJE absolute pressure transducer (0-6bar) with an accuracy of 0.1% of full scale. The pressure transducer was calibrated using a Wika 0-1bar pressure standard. The molar flow-rate was calculated using the ideal gas equation. A sample of this product gas was drawn from a septum sealed sample-point and analyzed via gas chromatography. The non-condensed gas was passed through a water filled bubbler (used for

monitoring process flow and to act as a liquid trap for hydrocarbons) before being vented. Process, pre-treatment and feed-tank primer gases were vented to a pilot plant extractor.

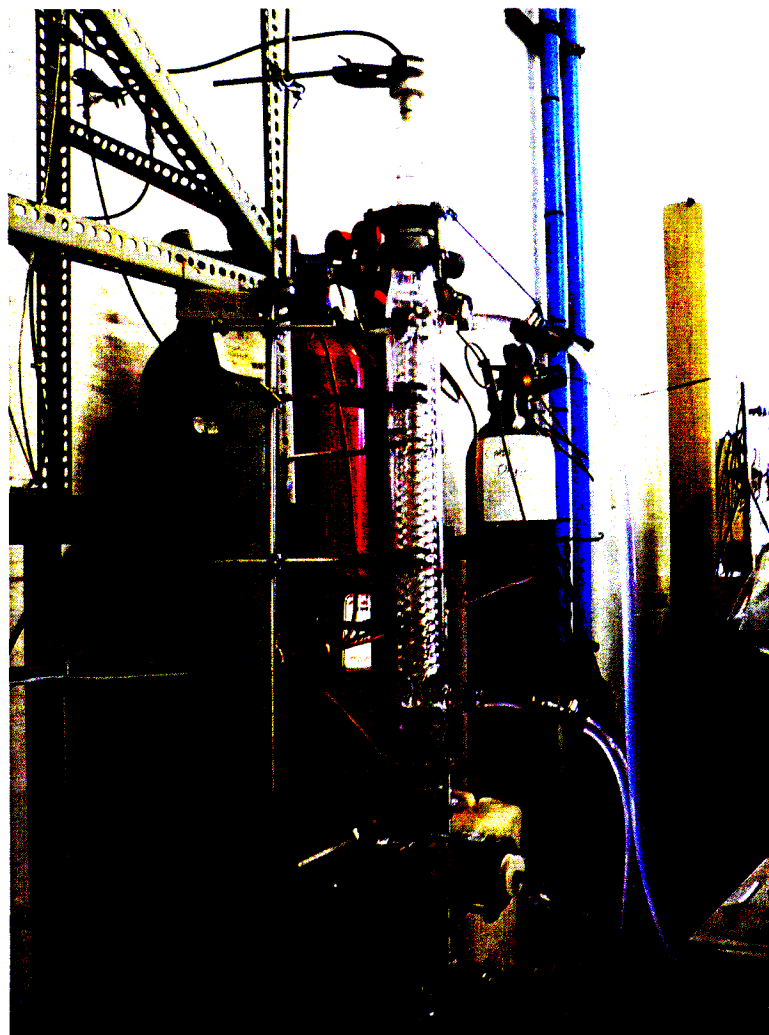


Figure 4.23 Modular glass product condenser

4.3.5 G.C. calibration cell

One of the most difficult G.C. calibration problems is that for a mixture of a gas and a vapourized liquid. Light olefins ethylene, propylene and butene as well as $C_5 - C_{10}$ olefins were found to be present in the non-condensed gas exiting the condenser. For quantitative analysis of this mixture via gas-liquid chromatography, calibration plots had to be prepared*. Synthetic gas mixtures of known composition were required to fulfil this task. Known concentrations of liquids vapourized into a gas were prepared using a specially constructed calibration cell, with

* Gas-liquid chromatograph detector calibration and the method of quantitative analysis are discussed under Experimental methods, Chapter 5.

elements of the design based on the more sophisticated apparatus of Raal and Mühlbauer (Raal and Mühlbauer, 1998).

Cylinder dimensions are presented in Table 4.6. The contents of the cylinder were agitated by means of a central stainless steel impeller mounted over a circular, magnetized metal block. The block itself was secured to the base of the cell using a loose bolt and rested on sixteen 2mm ball bearings. Impeller speed was adjusted by varying the voltage applied to the magnetic drive outside the cell.

OD	[mm]	90
ID	[mm]	84
Wall thickness	[mm]	3
Height	[mm]	110
Capacity	[ml]	700

Table 4.6 Calibration cell dimensions

All ports for gas entry and exit, temperature probes and sample and injection ports were fitted onto the top flange of the cell. The flange was secured to the cell by six 8mm bolts and a gas-tight seal was provided by a graphite gasket. The two ball-valves mounted to the reactor head were used for an inert gas purge and to isolate the system during operation. Temperature inside the cell was measured using a Pt-100 temperature sensor. An 800W electrical band heater (Giletric) was fitted around the outside of the calibration cylinder. Temperature control was achieved using a TOHO TTM-004 digital controller and solid-state relay. Also attached to the top flange was a high temperature sample septum port, for injecting liquids and drawing gas samples for analysis, and a 6mm L-shaped cartridge heater secured through a compression fitting. A second Pt-100 probe was used to measure the temperature of a circular metal block attached to the end of the cartridge heater. The temperature of this block was controlled using a RKC CB-100 digital temperature controller and solid-state relay. The temperature inside the cell was maintained at 150°C and the block temperature at 200°C.

During operation the cell was initially purged using nitrogen gas and then sealed. The temperature inside the cell and that of the metal block were brought to their respective set-points. A 60ml gas sample containing ethylene, propylene and butene was drawn from a sample line connected to the supply cylinder using a SGE ground glass gas syringe. Temperature and pressure were also measured at this point and the molar amount of gas drawn was calculated using the ideal gas equation. The sample was then injected into the cell. A liquid sample (1-hexene reference component), between 1µl and 10µl was injected from a syringe through the

sample septum in the top flange onto the heated metal block, where the stirring action of the impeller rapidly evaporated the liquid and homogenized the mixture. A final gas sample was withdrawn from the septum port and analyzed via gas-liquid chromatography.

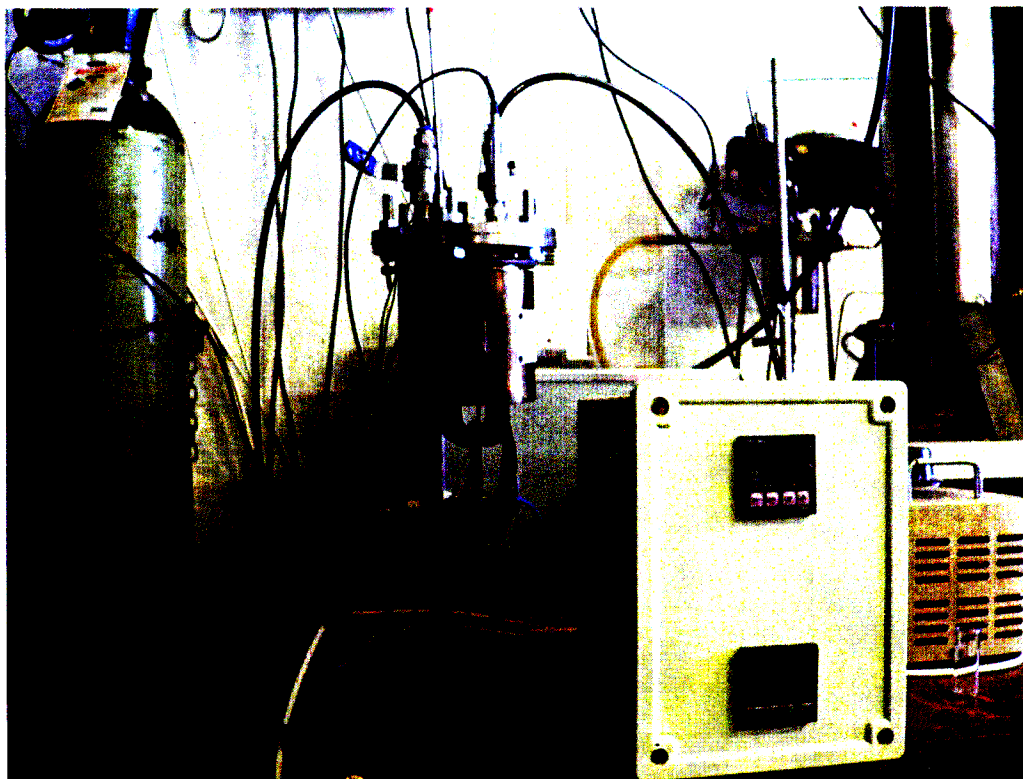


Figure 4.24 G.C. gas-liquid calibration cell

4.3.6 Process Safety

The design of high temperature reaction equipment handling volatile materials demands special attention to process safety. Hazardous materials identified in this system included 1-hexene as the bulk contaminant in the event of a release, light olefins $C_2 - C_5$ and heavy olefins $C_7 - C_{16}$ in small amounts during operation. The composition of feed gas was maintained above the upper flammability limit of 9.2% for 1-hexene. The reaction temperatures were generally higher than the auto-ignition temperature of 1-hexene (253°C). Vapour release at the reactor exit could have resulted in a fire or possibly an explosion through flash-back. Apart from the sampling points, the entire system was sealed, leak tested and pressure tested to 8 bar using dry air during the commissioning phase. Prior to each experiment, the rig was pressure tested again at 4bar. The maximum operating pressure was observed to be 2.3bar. The bulk reactant liquid was stored in a sealed vessel, grounded to eliminate a source of ignition. Since the system operates as a gas-phase heterogeneous reaction system, the major potential health hazard is inhalation of

1-hexene vapours following a release. The threshold limit for 1-hexene is 130mg.m^{-3} (American Conference of Governmental Industrial Hygienists). Engineering controls for the system included ventilation in the form of a pilot-plant extractor, eyewash stations and safety showers. The use of a vapour respirator during operation has been recommended. A general HAZOP study was conducted in conjunction with workshop technicians and safety officers. The final recommendations are presented below.

HAZOP Study - 1-Hexene Metathesis over WO_3/SiO_2

Guideword Deviation Cause Consequences Action

Vessel: Feed-tank

Intention: Supply 1-hexene feed to reactor

Line Number: A

Intention: transfer 1-hexene from feed-tank to reactor

No	Flow	pump failure line blocked	no hexene to reactor line temperature increases possibility of burnout overpressure on post-pump line no flow to reactor	High temperature alerts operator fault light on pump activates, signals operator as above
Less	Flow	pump malfunction leak on pipeline	low flow to reactor possibility of high line temperature hazardous release of toxic substances fire hazard	High temperature alerts operator fault light on pump activates, signals operator as above
More	Pressure	blockage on line	over-pressure on post-pump line no flow to reactor	as above
Reverse	Flow	pump failure high post pump pressure and failure of N_2 pump primer	hot hexene through pump, possibility of damage to pump internals	always maintain a full primer N_2 cylinder
Less	Temperature	Variac fault broken live line	liquid flow to reactor possible distribution problem live piping	Monitor temperature operator shutdown avoid contact and insulate/isolate
More	Temperature	no flow through line	possibility of burnout	High temperature alerts operator

Line Number: B**Intention: Supply dilution gas to reactor/supply pre-treatment gas to reactor**

No	Flow	line blockage	pressure build-up in line	line pressure tested to above maximum operating pressure Rotameter indicates no flow
More	Pressure	line blockage	pressure build-up in line	as above
Less	Flow	leak on line	release of ethylene (toxic) or hydrogen (explosive)	Rotameter indicates lower flow if leak occurs before flow meter Monitor reactor pressure
Reverse	Flow	back-pressure from reactor	damage to mass control valves	NRV-1 prevents reverse flow

Vessel: Reactor**Intention: 1-hexene metathesis ~ 1atm and 500°C****Line Number: C****Intention: product gas to condenser and vent**

No	Flow	line blocked	overpressure in reactor	line pressure tested to above maximum operating pressure Monitor reactor pressure
Less	Flow	leak on line	release of flammable gas 1-hexene above auto-ignition temperature risk of fire and explosion	blast shield installed around furnace exit point Immediate shut-down of gas/pump/furnace Temperature probe mounted near exit activates alarm

Vessel: Condenser**Intention: Condense heavy products for sample collection****Line Number: D****Intention: product gas to vent**

No	Flow	blockage on line	over-pressure ground-glass joints rupture releasing toxic vapours	secure ground-glass joint with spring clamps to act as safety relief valves
Less	Flow	leak on line	release of toxic vapours	monitor exit gas flow-rate using bubble flow-meter

Chapter

5

Experimental methods

5.1 Gas-liquid chromatography

Gas-liquid chromatography is the most widely used method for analyzing multi-component organic mixtures. There exists a large body of literature on the equipment and chromatographic methods used for such analyses (Raal and Mühlbauer, 1998). The G.C. does not provide an absolute method for composition evaluation as it only produces peak areas proportional to the amounts of the various substances. For proper quantitative analysis of products and reactants, calibration procedures must be carried out. For liquid mixtures, high accuracy in calibration can be achieved by gravimetrically preparing and analyzing standard mixtures (Raal and Mühlbauer, 1998).

The response factor F is defined as the proportionality constant between the number of moles passing the detector and the peak area A obtained on the chromatogram:

$$n_i = F_i A_i \quad (5.1)$$

The flame ionization detector (FID) is sensitive only to molecules containing carbon atoms. The sensitivity of the FID is not the same for all hydrocarbons, even those that are of the same type but of different carbon number. If detector sensitivity is superior for some species and

inferior for others, then the observed G.C. peak areas for these species must be corrected before quantitative calculations are carried out. At least a 4% variation between actual mole fractions and those obtained from peak area percentage has been reported for various types of hydrocarbons in the C₅-C₁₀ range (Matisova, 1998). Published response factors (mass basis) range from 0.8 to 1.2 for most hydrocarbons (Matisova, 1998; Beens et al., 1998). The area A is dependent on the amount of sample injected, which is not generally reproducible. Hence it is advisable to work with area ratios:

$$\frac{n_i}{n_k} = \frac{x_i}{x_k} = \left(\frac{A_i}{A_k} \right) \left(\frac{F_i}{F_k} \right) \quad (5.2)$$

where x = mole fraction

i, k = any pair of components in the mixture.

The response factor ratio is not, in general, constant over large composition ranges, even when small amounts of liquid sample are injected (usually of the order of 1 μ l). In mixture calibration, area ratios for pairs of components are plotted versus their mole fraction ratios. For quantitative tests an internal standard is often added to the mixture prior to injection. In this case component k in Equation 5.2 would represent the internal standard and the calibration plots would be prepared with reference to this component. The response factor ratios obtained from the calibration plots may, for example, be used to correct the observed G.C. peak areas for a sample of unknown composition when carrying out a quantitative analysis. In the very dilute region of component i , the plot should be linear and should extrapolate through the origin. The response factor ratios cannot be assumed to be 1, and in fact are often far from 1. Response factor ratios can be influenced by several factors such as oven temperatures, carrier gas flow rate, and sample size, and must be determined for the same conditions for which analyses are to be done. If the area ratio versus mole fraction ratio plot is not linear through the origin for a particular pair of components, it implies that the F ratio is composition dependent and G.C. operating conditions may have to be changed to make the plot linear. Substituting mole ratios for mass ratios should also be tested in this case.

The method of internal normalization for quantitative analysis is used for mixtures in which each compound has been identified by its elution peak. Each of the peaks must be well separated from the others in order to fully characterize the sample. For this method, the peak area of an exiting component of the sample mixture serves as the internal standard. Again areas must be corrected for detector sensitivity. In Equation 5.3 the response factor ratio F_i / F_k is denoted by $F_{i,k}$. Component k is now the reference component. Calibration plots are prepared

for each component i with reference to the chosen component k , as was described earlier*. For an analysis of a mixture of unknown composition, the following equation is then used to determine mole fractions:

$$x_i = \frac{F_{i,k} \times A_i}{\sum_{j=1}^n F_{j,k} \times A_j} \quad (5.3)$$

where x_i and A_i are the mole fraction and peak area for component i in the sample of unknown composition. A mass-based instead of mole-based method may be used, depending on the nature of the response ratio coefficients. Mass response factors for hydrocarbons can also be calculated theoretically (Beens et al., 1998). In the flame ionization detector the detection principle is based on the electrical conductivity of the flame. The mechanism of the response origin has been explained as chemi-ionization. The net response is proportional to the molar rate of entry of the analyte in the flame, as well as the number of carbon atoms in the molecule of the analyte. Isomers of hydrocarbons produce only slightly different responses. A fair approximation of the absolute response factor is given as:

$$f_i = \frac{M_i}{N_i^c} \quad (5.4)$$

where N_i^c is the number of carbon atoms of component i and M_i is the molecular mass. Relative response factors are then calculated from the relevant pairs of f_i . The approximation is not always adequate, since the sensitivity will depend largely on the detector employed, so it may be necessary to carry out proper calibration techniques (Cuadros-Rodríguez et al., 2007). According to Matisova (1998), all calculations and calibrations must be performed on a mass basis, since the FID is a mass detector. Cuadros-Rodríguez et al. (2007), in the mathematical development of the proposed method of quantification, recommend the use of mass response factors and mass fractions. Consequently, in this work, all calibrations and subsequent calculations were performed on a mass-basis according to the following equations:

* The reference component is chosen as the most abundant of the species that constitute the test mixture (Matisova, 1998)

$$\frac{w_i}{w_k} = \frac{F_i}{F_k} \left(\frac{A_i}{A_k} \right) = F_{i,k} \left(\frac{A_i}{A_k} \right) \quad (5.5)$$

$$w_i = \frac{F_{i,k} \times A_i}{\sum_{j=1}^n F_{j,k} \times A_j} \quad (5.6)$$

The analysis of liquid and gaseous metathesis products were performed using a Shimadzu GC-2014 gas chromatograph equipped with a flame-ionization detector and packed column (Figure 5.1).

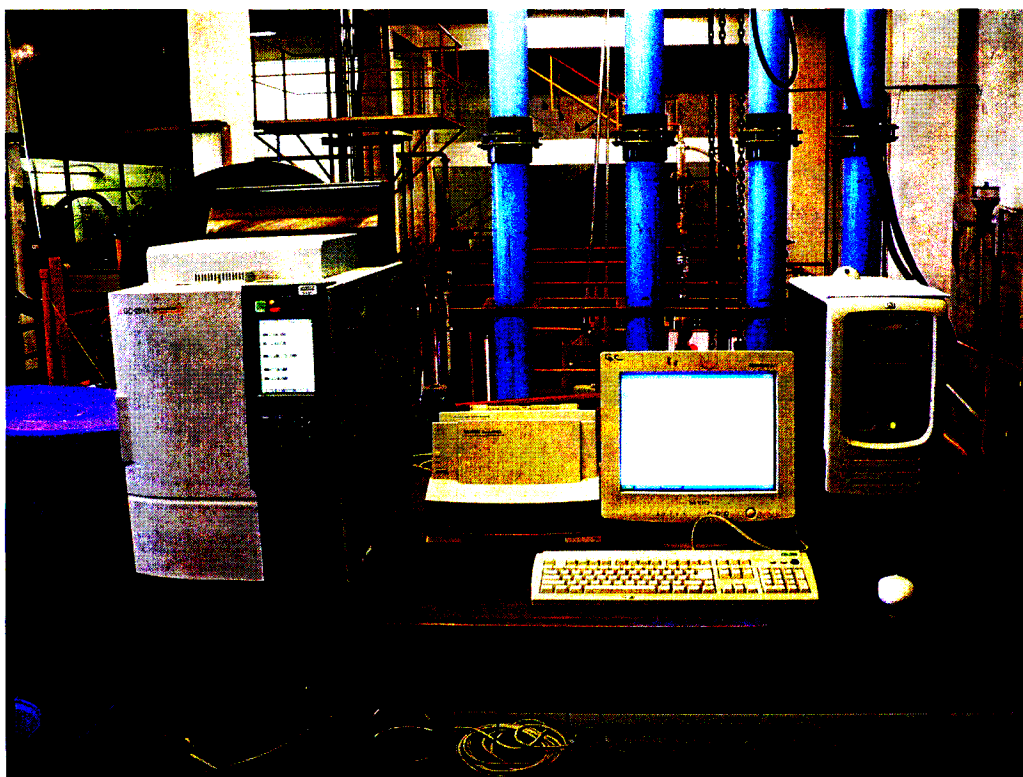


Figure 5.1 Shimadzu GC-2014 gas chromatograph (liquid and gas analysis)

The column specifications were as follows:

Column		CRS Chromosorb (10% Silicone SE-30)		
Length	[m]	3.02		
ID	[mm]	0.53		
film thickness	[μm]	5		
Detector		FID		
Program				hold time
		T ₁	40°C	5 min
		rate1	35°C/min	
		T ₂	145°C	4 min
		rate2	50°C/min	
		T ₃	245°C	17 min
Detector Temperature	[°C]	300		
Injector Temperature	[°C]	270		
Carrier gas (nitrogen)	[ml.min ⁻¹]	25		

Table 5.1 Column characteristics – liquid product analysis

Column		CRS Chromosorb (10% Silicone SE-30)		
Length	[m]	3.02		
ID	[mm]	0.53		
film thickness	[μm]	5		
Detector		FID		
Program				hold time
		T ₁	35°C	6 ½ min
		rate1	40°C/min	
		T ₂	195°C	10 min
		rate2	-	
		T ₃	-	-
Detector Temperature	[°C]	300		
Injector Temperature	[°C]	260		
Carrier gas (nitrogen)	[ml.min ⁻¹]	25		

Table 5.2 Column characteristics – gas product analysis

Conditioning of the G.C. column was accomplished using the method recommended by the manufacturer. The column was treated with a standard flow (25ml.min⁻¹) of nitrogen at ambient temperature for 30 minutes[†]. Thereafter the temperature was ramped at a rate of 2°C.min⁻¹ to 280°C (20°C below the maximum allowable temperature for the column phase and

[†] Connections to the detector were not made during any part of the conditioning sequence.

approximately 35°C above the program temperature used during analyses), and held at these conditions overnight.

Calibration plots were obtained as discussed, preparing and analysing standard mixtures gravimetrically for liquids and by the method described in section 4.3.5 for gases. Area ratios for each component, with reference to 1-hexene, were plotted against their mass fraction ratios. The resultant linear plots are presented in Appendix A. The gradient of each of these graphs represents the response factor ratio for each component with reference to 1-hexene (Table 5.3). For olefins higher than C₁₀ no standards were available and the response factors were estimated using Equation 5.4. The resultant response ratios were unity for all these components.

Component	Symbol	$F_{i,k}$
ethylene	C ₂	1.2689
propylene	C ₃	1.1797
butene	C ₄	1.1631
pentene	C ₅	1.0131
heptene	C ₇	1
octene	C ₈	0.9212
nonene	C ₉	0.9648
decene	C ₁₀	0.9206
undecene	C ₁₁	0.9822
dodecene	C ₁₂	1
tridecene	C ₁₃	1
tetradecene	C ₁₄	1
pentadecene	C ₁₅	1
hexadecene	C ₁₆	1

Table 5.3 G.C. response factor ratios for olefins (reference component, 1-hexene)

5.2 Catalyst preparation

The two batches of WO₃/SiO₂ metathesis catalyst were prepared at Sasol as follows. For a desired catalyst mass of 100g (8% WO₃/SiO₂), exactly 8.4496g of ammonium metatungstate hydrate (Aldrich) and 92g of silica gel (Davisil grade 646, Aldrich) were used. The silica was dried at 150°C under air for 2 hours. The ammonium metatungstate hydrate crystals were dissolved in distilled water. The outer surface of the dry silica was wetted before mixing with

the dissolved metal solution. The mixture was allowed to stir on a rotary evaporator for 2 hours. The catalyst was then calcined according to the following temperature schedule (Figure 5.2):

- Drying at 110°C for 2 hours
- Temperature ramp (10°C/min to 250°C)
- Hold temperature at 250°C for 2 hours
- Temperature ramp (3°C/min to 600°C)
- Hold temperature at 600°C for 8 hours

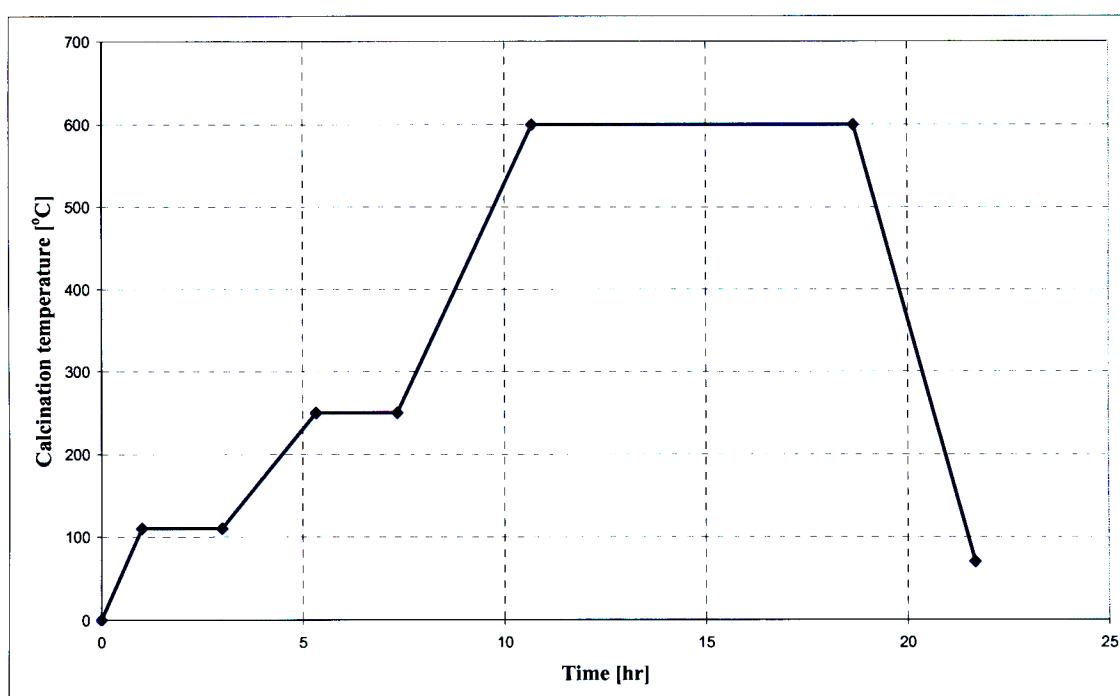


Figure 5.2 Calcination curve for 8% WO_3/SiO_2 catalyst

5.3 Absorbance measurements

The colour of the liquid product from selected runs was determined by using UV-vis absorption measurements in the 400nm range. A Corning 253 colorimeter was used to carry out these tests. A sample of the liquid feed, 1-hexene, was used as the blank solvent, with all subsequent measurements relative to this base absorbance. The liquid product samples from each of the experiments contained two broad groups of organic compounds, viz. colourless linear and

branched alkenes (including di-enes and tri-enes) and polynuclear aromatics, with the latter imparting a dark colour to the sample. Since qualitative G.C.-M.S. analysis could not be carried out for all of the experiments, the absorbance measurements were used as an indication of the amount of unwanted polynuclear aromatics present in the product liquid.

5.4 Catalyst characterization

5.4.1 Catalyst particle size estimation

A scanned image of a representative sample of WO_3/SiO_2 was used, in conjunction with a program written and implemented in MATLAB[®], to obtain an estimate for the catalyst particle size. The program screens each particle in an image, clustering and logging the number of pixels that constitute that particle. With the actual scanned resolution extracted from the image file (pixels per inch), it computes the area of the particle in physical units of length squared (mm^2). This area is equated to the area of a flat circular disc with a diameter d_c , which is subsequently solved for using the area formula of a circle. The reader should bear in mind that the image is a two dimensional one, and therefore restricts the user from fully appreciating the three dimensional nature of the particle. Irregular particles tend to settle on a side that provides greater stability, usually a side that is flat. For lack of a more rigorous method, this phenomenon has been largely ignored. The volume of each particle is then calculated by assuming a spherical geometry and applying the relevant formulae. These individual volumes are summed to obtain a total volume for a particular particle size (D_i) and total volume for all particle sizes. The ratio of $V_{\text{tot}, D_i} / V_{\text{tot}, \Sigma D_i}$ is also the mass fraction for that particular D_i (with densities assumed constant across the range of particle sizes). A cumulative mass fraction or distribution curve was generated for the sample via this method (Appendix D).

The mean particle size or diameter is given by the following equation:

$$\bar{D} = \frac{\int_0^{\infty} D E(D) dD}{\int_0^{\infty} E(D) dD} \quad (5.7)$$

where the function $E(D)$ is the relative mass distribution curve for particle sizes D_i (Perry, 1999). According to particle size distribution theory, the area under the frequency or relative distribution curve must equal 1. Thus the denominator in Equation 5.7 becomes unity and the expression reduces to:

$$\overline{D} = \int_0^{\infty} DE(D)dD \quad (5.8)$$

The relative (E) and cumulative (F) mass fraction curves are related by the following equation:

$$E(D) = \frac{dF(D)}{dD} \quad (5.9)$$

Substitution of Equation 5.9 in Equation 5.8 yields:

$$\overline{D} = \int_0^{\infty} DdF(D) \quad (5.10)$$

The mean diameter for the catalyst sample is obtained by Euler integration of the cumulative data.

$$\overline{D} = \sum_{i=1}^{N-1} D_i (F_{i+1} - F_i) \quad (5.11)$$

Tests revealed that for particles smaller than 1000 μm , the method suffered from optical effects and the results were extremely sensitive to the properties of the scanned image, in particular the selected threshold of black and white. To obtain sufficiently accurate results, calibration of the scanner settings would have had to be carried out using particles of similar material and size. The catalyst particle size and mean diameter were also determined via laser diffraction on a Malvern Mastersizer 2000E. These procedures were carried out at the School of Geological Sciences of the University of KwaZulu-Natal. This technique is mass based (equivalent to volume). The mean particle diameter obtained from the image analysis for one of the catalyst size fractions was 390 μm . For the same catalyst the laser diffraction technique reported a mean particle diameter of 460 μm .

5.4.2 Surface area measurements

The specific surface area of the catalyst was determined by the BET-method on a Gemini™ (Micrometrics) gas adsorption analyzer. Measurements were performed with nitrogen as the adsorbate at -77K, after degassing at 200°C under nitrogen flow for 18 hours.

5.4.3 Scanning electron microscopy (SEM) and energy dispersive x-ray (EDX) spectroscopy

Images of the catalyst surface topology and changes in the surface morphology were captured via scanning electron microscopy on a LEO 1450 SEM at the Electron Microscope Unit of the University of KwaZulu-Natal. Energy dispersive x-ray elemental analysis of the fresh and spent catalyst was performed using the same equipment, in the 10-20keV range.

5.4.4 Gas-chromatography-mass-spectrometry

Qualitative analyses of selected samples of liquid product were carried out using an Agilent 6890 gas chromatograph equipped with an Agilent 5973 mass spectrometer in the 35-500 m/z mass scan range. The column specifications are presented in Table 5.4.

GC model		Agilent 6890 GC/5973 MS	
Column		J and W HP5-MS	
Length	[m]	30	
OD	[μm]	250	
film	[μm]	0.25	
MS properties			
Scan	[amu]	35-500	
Source	[°C]	230	
Quad	[°C]	150	
Solvent delay for 4 minutes			
Temperature program			
			hold time
	T ₁	50°C	2min
	rate1	20°C/min	
	T ₂	300°C	10min
Injector temperature	[°C]	250	
Split		none	

Table 5.4 G.C-M.S. Specifications

5.5 Experimental procedures for the preliminary tests

After cleaning the reactor using benzene and acetone, approximately 1.5g – 2g of the WO_3/SiO_2 catalyst was loaded into the tube and sealed. The reactor temperature set-point was ramped in 40°C intervals up to the final pre-treatment temperature (500°C). Nitrogen gas at a flow-rate of $25\text{ml}\cdot\text{min}^{-1}$ was purged through the system. The catalyst was pre-treated at 500°C under a flow of air ($25\text{ml}\cdot\text{min}^{-1}$), hydrogen ($50\text{ml}\cdot\text{min}^{-1}$) and finally nitrogen ($25\text{ml}\cdot\text{min}^{-1}$) for 6 hours, 2 hours and 18 hours respectively. Saturator assemblies were then allowed to reach temperature set-points (40°C and 20°C). The refrigeration unit was powered up and cooling water was applied to the glass product condenser. The reactor was allowed to cool down to the reaction temperature under an inert atmosphere. Nitrogen flow was diverted from the reactor head to the first saturator vessel. Inlet flow-rates were tested at the beginning of the run using a bubble flow-meter. The reactor remained online for 6 hours at the same operating conditions. Liquid and non-condensed gas samples were drawn for analysis after every 1.5 hours. The flow-rate of non-condensed gas was also tested at those points. No samples were withdrawn during the first hour of operation, as it was assumed that steady-state conditions were being established during that period.

5.6 Experimental procedures for the experiments conducted in Poland

After cleaning the reactor using benzene and acetone, approximately 1.5g of the WO_3/SiO_2 catalyst was loaded into the tube and sealed. The heating apparatus was installed and a controlled flow of $150\text{ml}\cdot\text{min}^{-1}$ of nitrogen was applied to the system. The input voltage was manually adjusted to achieve a reactor temperature of 450°C . The system was maintained at these pre-treatment conditions for 18 hours.

The saturator vessel was half filled with liquid 1-hexene (Fluka, >96% by assay) and sealed. Cooling water flows were then applied. The flow of nitrogen was diverted from the reactor head to the saturator vessel. During start-up, the reactor temperature was manually controlled by the adjustment of the input voltage to the nichrome coil. At least 30 minutes had elapsed before a stable temperature was achieved. The reactor temperature and flow-rates were changed on-line after two hours of stable operation. A further one hour was allowed between set-points for the system to re-establish steady-state conditions. Gas samples were drawn every 30 minutes within a particular sub-set and analyzed via gas chromatography. The reactor inlet flow-rate was tested using a bubble flow-meter at the beginning of each sub-set. The flow-rate of non-condensed gas was measured every 15 minutes. Liquid product samples were withdrawn at the end of each run.

5.7 Experimental procedures for the optimization study conducted at the University of KwaZulu-Natal

The reactor tube was thoroughly cleaned using benzene, acetone and emery paper. Approximately 2g of the WO_3/SiO_2 catalyst (Catalyst B) was loaded over the catalyst mesh support and a thin layer of quartz wool. The bed was consolidated by tapping the tube gently. Another thin layer of quartz wool was placed over the catalyst bed. A small amount of a nickel based thread lubricant was applied to the $\frac{1}{2}$ inch Swagelok™ reducers before tightening. PTFE thread tape was placed over the ferrules to prevent galling of the fittings. The reactor tube was then mounted in place. The catalyst was pre-treated at 500°C under a flow of air ($28\text{ml}\cdot\text{min}^{-1}$), hydrogen ($35\text{ml}\cdot\text{min}^{-1}$) and finally nitrogen ($28\text{ml}\cdot\text{min}^{-1}$) for 4 hours, 1.5 hours and 18 hours respectively. The feed-pot utility water tank was brought to 40°C . The feed-pot temperature controller was taken off manual, the instrument air was turned on and the temperature was brought up to the set-point (30°C) by pumping hot water through the inner heating coils. The reactor exit gas was diverted from the pre-treatment vent to and through the product condenser. Nitrogen was allowed to purge the condenser for 15 minutes. The refrigeration unit was powered up, set at 2°C and cooling water was applied to the glass product condenser. Feed line variable voltage dc power supplies were switched on at pre-set output voltages. The required flow of nitrogen was set using the precision mass flow control valves and tested using the bubble flow-meter assembly. The reactor was allowed to cool to below the required operating reaction temperature. Pump primer nitrogen flow ($25\text{ml}\cdot\text{min}^{-1}$) was applied to the flange head of the 1-hexene feed-tank. The isocratic pump was set at the required pumping speed, opened to the process line and switched on. After the initial rise in process temperature, the reaction temperature set-point was changed to the required value and the controller tuning parameters were changed to cope with the new process dynamics. The system was allowed to reach steady-state. Liquid product collected during this period was discarded. After a prescribed collection time, non-condensed product gas flow-rates were tested using the bubble flow-meter assembly and sampled for G.C. analysis. The liquid product was collected and stored at low temperatures for analysis the following day. The reactor conditions were changed on-line and a period of stabilization of at least two hours was observed. Three to four settings were investigated during one full day of operation. During the investigation of the pre-treatment procedures no changes were made to the operating conditions. The reaction was on-line for at least 7 hours, with product samples being withdrawn and tested every hour. The product was also tested for the first hour of operation to investigate the catalyst induction period.

Chapter 6

Results and discussion

6.1 Results of the preliminary tests

The five experiments performed using the auxiliary rig were inherently qualitative. An appropriate G.C. column for gas phase analysis was not available during this period. It was impossible to close the carbon balance with the limited data that was generated. Nevertheless, the condensed liquid product was analyzed and the quantities of higher olefin products were monitored in a preliminary search for appropriate feed gas flow-rates and reaction temperatures. The results revealed that at the conditions that were employed (a low feed gas composition of 20% (mole based) and reaction temperatures of 470°C and 490°C) very small amounts of higher olefins were produced. In fact, the selectivity to higher olefins was almost negligible. The deactivating nature of the stainless steel reactor walls was initially believed to be the cause for the poor performance. Subsequent tests performed on a quartz glass reactor tube partially dismissed these presumptions, as a similar trend was observed. It was concluded that the low feed gas composition accounted for the poor conversion and/or selectivity.

Inspection of the reaction equipment revealed that a small amount of liquid product had accumulated within the exit piping from the reactor module to the heavy products condenser. G.C. analysis of this liquid confirmed that it consisted of several isomers of nonene and decene. The reactor module was elevated to facilitate gravity-flow of the condensate, and a final run was

performed. However, no appreciable change in the composition of the condensed liquid product was observed.

6.2 Results of the experimental program conducted in Poland

The Polish experimental program commenced soon after the preliminary tests were performed on the auxiliary rig. The efforts represented a limited search of the parameter space, typically at a low feed gas composition. Three reaction temperatures were investigated, viz. 470°C, 480°C and 490°C. Their effects were coupled with a variation in space time W/F . Large cylindrical pellets of catalyst A were crushed and sieved into three size fractions. A geometric mean diameter was calculated for each size fraction using the upper and lower limit of the sieve series that was used. In all, 12 experiments were conducted, representing a reduced two variable, three level design (Figure 6.1). Two excursions were made from a base level (0), varying parameters simultaneously. For all runs, the average percent mole fraction of 1-hexene in the feed gas was 20%, approximately 10 percentage points lower than the saturation value at 30°C (30%). Poor gas distribution in the saturation vessel, the lack of agitation and a shallow tank were suggested as possible reasons for this discrepancy. During quantification of chromatographic data, closely eluted peaks were lumped together to represent an olefin with a particular carbon number. Without mass spectrometry, a complete resolution of the product spectrum could not be obtained.

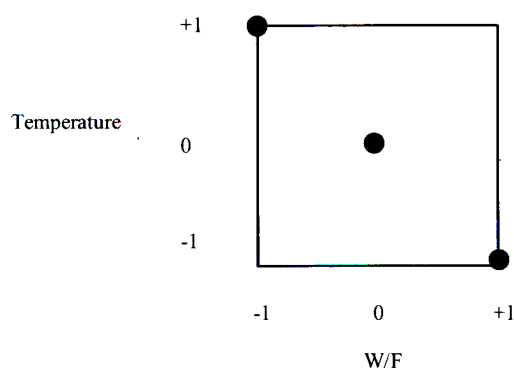


Figure 6.1 Two variable, three level experimental design

The results of the experimental program that was conducted in Poland are presented in Table 6.1 and Table 6.2. The conversion is defined as the molar flow-rate of reactant that is consumed divided by the inlet molar flow-rate of the reactant, expresses as a percentage:

$$X = \frac{F_{\text{hexene},in} - F_{\text{hexene},out}}{F_{\text{hexene},in}} \times 100\% \quad (6.1)$$

The selectivity is defined as the molar flow-rate of the product (or products) produced divided by the molar flow-rate of reactant that is consumed, expressed as a percentage:

$$S_{\text{product}} = \frac{F_{\text{product},out}}{F_{\text{hexene},in} - F_{\text{hexene},out}} \times 100\% \quad (6.2)$$

The yield is defined as the molar flow-rate of the product (or products) produced divided by the inlet molar flow-rate of the reactant, expressed as a percentage:

$$Y_{\text{product}} = \frac{F_{\text{product},out}}{F_{\text{hexene},in}} \times 100\% \quad (6.3)$$

Run No.	Temp [°C]	dp [μm]	Feed composition [mol % 1-hexene]	W/F [g.min.mol ⁻¹]	X [%]	Sel C ₇ -C ₁₆ [%]	Sel C ₁₀ [%]	Y C ₇ -C ₁₆ [%]	Y C ₁₀ [%]
1	470	300	19.63	176	12.84	6.37	3.23	0.82	0.41
2	480.1	300	21.54	126	22.05	27.84	5.21	6.14	1.15
3	490.3	300	20.88	100	34.27	19.45	6.28	6.67	2.15
4	469.6	346	19.24	214	4.42	31.44	2.23	1.39	0.10
5	480	346	21.46	152	12.06	13.02	1.22	1.57	0.15
6	490	346	22.27	119	23.79	12.86	3.45	3.06	0.82
7	470	346	19.13	214	6.34	17.53	1.04	1.11	0.07
8	479.8	346	21.49	152	14.51	8.65	0.48	1.25	0.07
9	470	447	19.02	271	17.55	7.22	0.38	1.27	0.07
10	480.4	447	21.7	191	27.66	11.14	2.04	3.08	0.57
11	489.9	447	18.2	158	32.92	30.81	7.72	10.14	2.54
12	480	447	18.92	199	36.62	15.71	3.25	5.75	1.19

Table 6.1 Polish experimental program, complete set of results

Run No.	Temp [°C]	dp [μm]	Feed composition [mol % 1-hexene]	W/F [g.min.mol ⁻¹]	X [%]	Sel C ₇ -C ₁₆ [%]	Sel C ₁₀ [%]	Y C ₇ -C ₁₆ [%]	Y C ₁₀ [%]
1	470	300	19.63	176	12.84	6.37	3.23	0.82	0.41
2	480.1	300	21.54	126	22.05	27.84	5.21	6.14	1.15
3	490.3	300	20.88	100	34.27	19.45	6.28	6.67	2.15
4,7	469.8	346	19.19	214	5.38	24.49	1.63	1.32	0.09
5,8	479.9	346	21.48	152	13.29	10.83	0.85	1.44	0.11
6	490	346	22.27	119	23.79	12.86	3.45	3.06	0.82
9	470	447	19.02	271	17.55	7.22	0.38	1.27	0.07
10,12	480.2	447	20.31	195	32.14	13.42	2.65	4.31	0.85
11	489.9	447	18.20	158	32.92	30.81	7.72	10.14	2.54

Table 6.2 Polish experimental program, results after averaging

The relationships between each of the operating variables (reaction temperature and space time W/F) and the performance parameters (conversion of 1-hexene, selectivity and yield of higher olefin products and in particular the primary metathesis product, decene) could not be separately established. The results were all highly intercorrelated since the experiments were not designed to uncouple the effects of temperature and space time W/F . As an alternate approach, simple reaction rate expressions for the metathesis of 1-hexene were derived using at first a differential plug flow model for a second order reaction and subsequently various concentration dependent models of different orders based on mass action kinetics. This approach was far from being rigorous. The actual kinetics would be more complex, possibly requiring numerical solution.

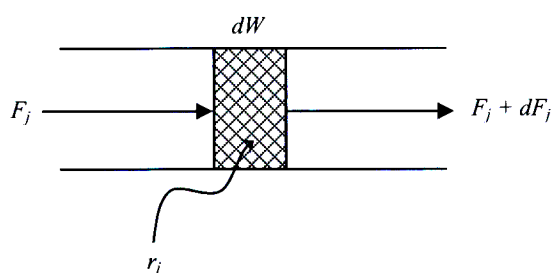


Figure 6.2 Plug flow model of the fixed bed reactor

At steady-state the material balance of the plug flow reactor shown in Figure 6.2 may be written as:

$$F_j + r_j dW = F_j + dF_j \quad (6.4)$$

The conversion of component j is defined as:

$$X = \frac{F_{j,0} - F_j}{F_{j,0}} \quad (6.5)$$

Therefore,

$$dF_j = -F_{j,0} dX \quad (6.6)$$

Rearrangement and substitution of Equation 6.6 in Equation 6.4 results in:

$$r_j dW = -F_{j,0} dX \quad (6.7)$$

In a reactor where differential (sufficiently low) conversion is achieved, the concentration of the reactant is assumed to be constant and hence the rate, r_j , may also be assumed constant. Integration of Equation 6.7 gives:

$$(-r_j) = \left(\frac{X}{W / F_{j,0}} \right) \quad (6.8)$$

Equation 6.8 is valid for all reaction orders in a differential reactor. Since two molecules of 1-hexene are involved in the metathesis reaction, a second order irreversible reaction was considered, where the rate is given by:

$$(-r_{hex}) = k_0 C_{hex}^2 \quad (6.9)$$

The assumption of a differential reactor with constant axial reactant concentration was relaxed and variable reaction rate expressions were developed from Equation 6.7, assuming first, second and $\frac{1}{2}$ order reactions. For a first order reaction,

$$(-r_{hex}) = k_1 C_{hex} \quad (6.10)$$

$$\Rightarrow \frac{dX}{(1-X)} = \frac{k_1 C_{hex,0} dW}{F_{hex,0}} \quad (6.11)$$

Rearranging and integrating Equation 6.11 gives:

$$\frac{-\ln(1-X)}{W / F_{hex,0}} = k_1 C_{hex,0} = (-r_{hex,0}) \quad (6.12)$$

where $(-r_{hex,0})$ is the initial rate of 1-hexene consumption.

For a second order reaction,

$$(-r_{hex}) = k_2 C_{hex}^2 \quad (6.13)$$

$$\Rightarrow F_{hex,0} dX = k_2 (C_{hex,0})^2 (1-X)^2 dW \quad (6.14)$$

Rearranging and integrating Equation 6.14 gives:

$$\frac{\left(\frac{X}{1-X}\right)}{W / F_{hex,0}} = k_2 (C_{hex,0})^2 = (-r_{hex,0}) \quad (6.15)$$

For a ½ order reaction,

$$(-r_{hex}) = k_{0.5} C_{hex}^{0.5} \quad (6.16)$$

$$\Rightarrow F_{hex,0} dX = k_{0.5} (C_{hex,0})^{0.5} (1-X)^{0.5} dW \quad (6.17)$$

Rearranging and integrating Equation 6.17 gives:

$$\frac{2[1 - (1-X)^{0.5}]}{W / F_{hex,0}} = k_{0.5} (C_{hex,0})^{0.5} = (-r_{hex,0}) \quad (6.18)$$

From Equation 6.9 the reaction rate constant (for a second order reaction in a differential bed) is given by:

$$k_0 = \frac{(-r_{hex})}{C_{hex}^2} \quad (6.19)$$

where $(-r_{hex})$ is obtained from Equation 6.8. For a first order reaction the reaction rate constant is given by:

$$k_1 = \frac{(-r_{hex})}{C_{hex,0}} \quad (6.20)$$

where $(-r_{hex})$ is obtained from Equation 6.12. For a second order reaction the reaction rate constant is given by:

$$k_2 = \frac{(-r_{hex})}{(C_{hex,0})^2} \quad (6.21)$$

where $(-r_{hex})$ is obtained from Equation 6.15. For a $\frac{1}{2}$ order reaction the reaction rate constant is given by:

$$k_{0.5} = \frac{(-r_{hex})}{(C_{hex,0})^{0.5}} \quad (6.22)$$

where $(-r_{hex})$ is obtained from Equation 6.18.

For each of the catalyst particle sizes, the reaction rates were calculated using Equations 6.8, 6.12, 6.15 and 6.18 for the different models. These calculated reaction rates are plotted against reaction temperature in Figures 6.3 to 6.6. For the 346 μ m particles the result of run 6 was not included since it was regarded as an outlier (see Table 6.1). A much higher conversion was expected for the operating conditions that were employed in this run. For the models that were considered, the calculated reaction rate for the 346 μ m catalyst particles was the lowest at all reaction temperatures. The calculated reaction rate for first order and $\frac{1}{2}$ order expressions (all particle sizes) were very similar.

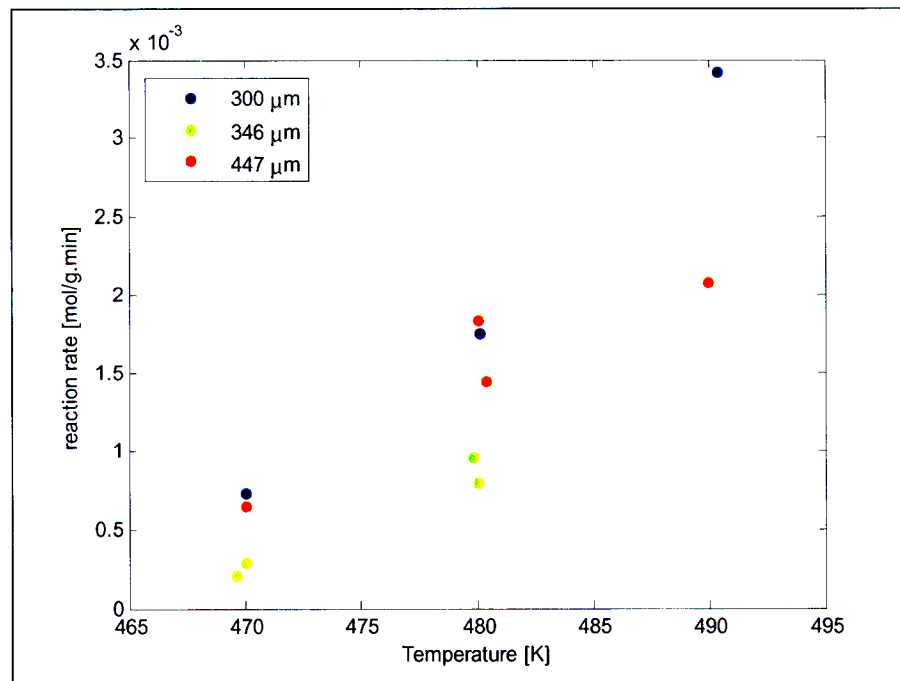


Figure 6.3 Calculated reaction rate versus reaction temperature, 2nd order reaction in a differential bed (different catalyst particle sizes) – Polish experimental program

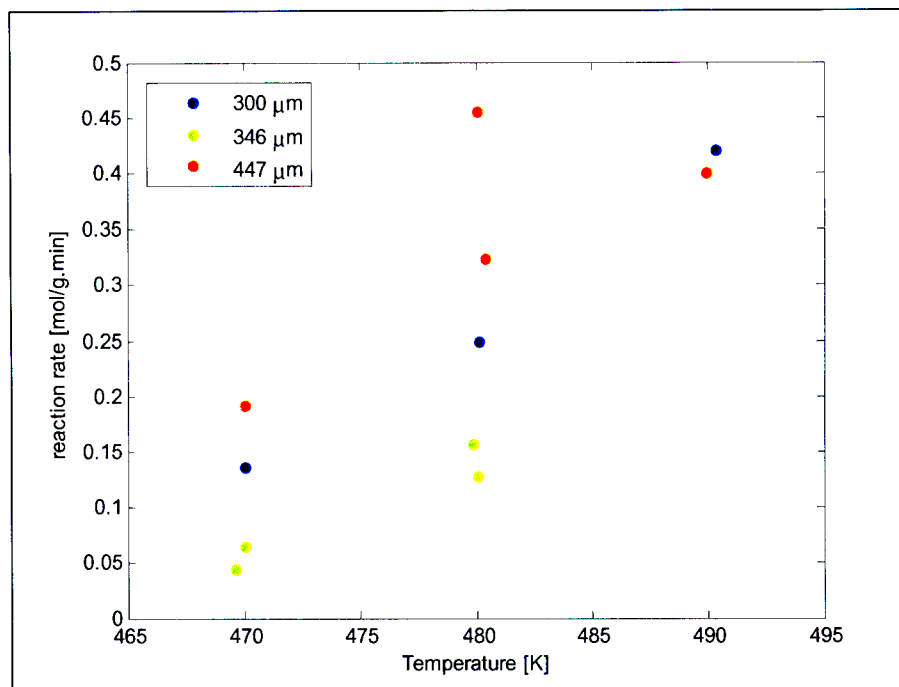


Figure 6.4 Calculated reaction rate versus reaction temperature, 1st order reaction (different catalyst particle sizes) – Polish experimental program

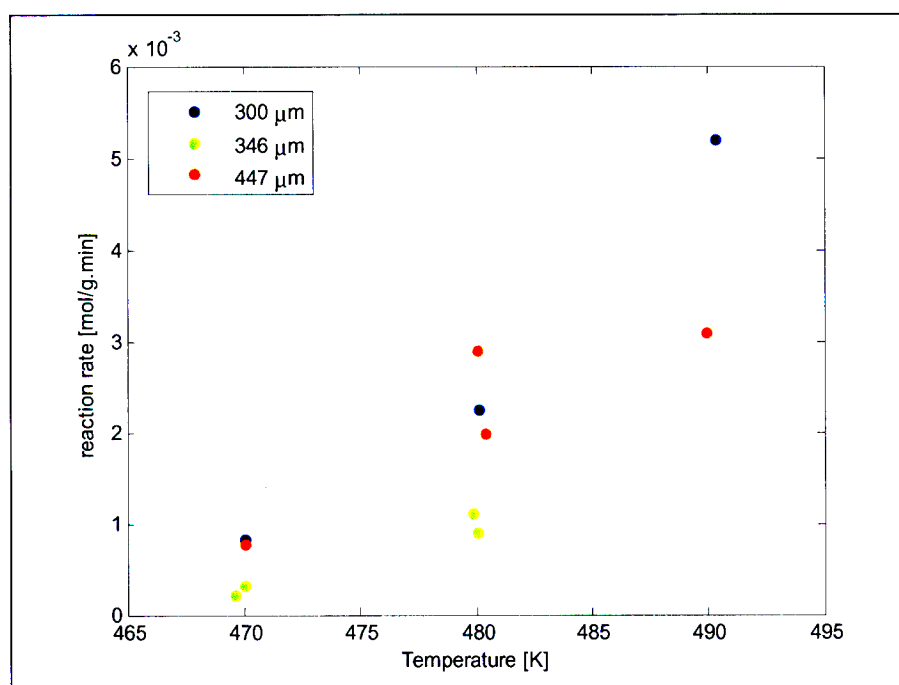


Figure 6.5 Calculated reaction rate versus reaction temperature, 2nd order reaction (different catalyst particle sizes) – Polish experimental program

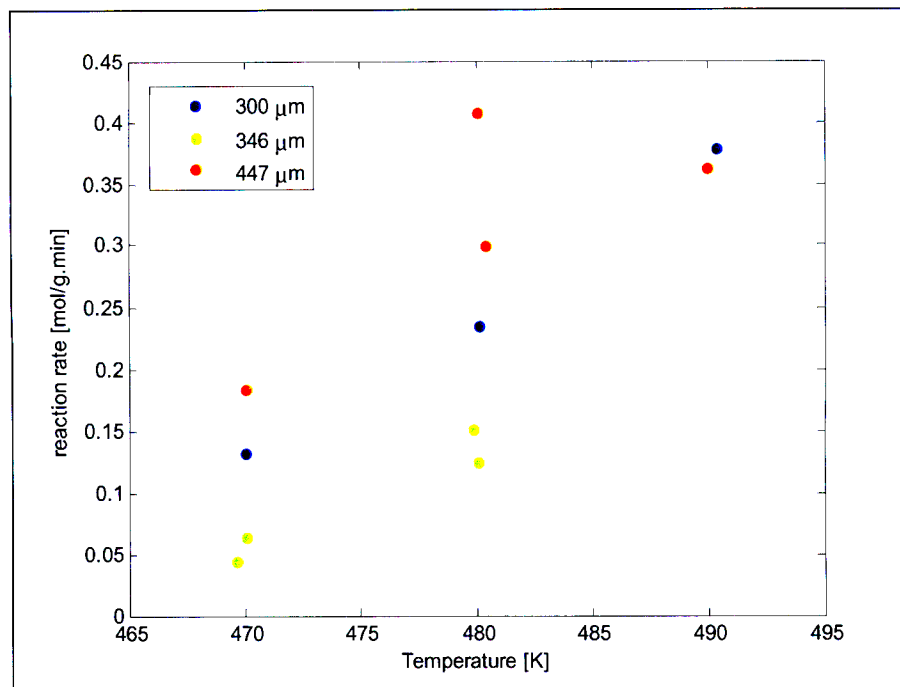


Figure 6.6 Calculated reaction rate versus reaction temperature, $\frac{1}{2}$ order reaction (different catalyst particle sizes) – Polish experimental program

Arrhenius plots of $\ln k$ versus $1/T$ were prepared for each catalyst particle size and for each model that was considered (Figure 6.7 to 6.10). Assuming that all the rate constants for the different models follow the Arrhenius relationship:

$$k_i = A_i \exp\left(\frac{-E_a}{RT}\right) \quad (6.23)$$

or

$$\ln k_i = \ln A_i - \frac{E_a}{RT} \quad (6.24)$$

the activation energy, E_a , is obtained from the gradient of the Arrhenius plot. The results of the linear regression are presented in Table 6.3.

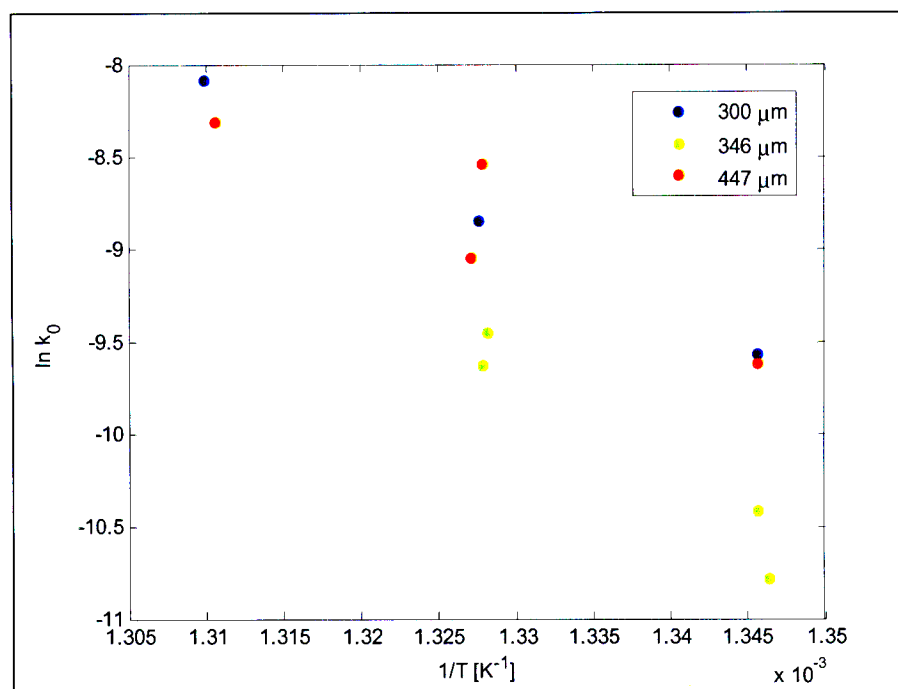


Figure 6.7 Arrhenius plot for parameter k_0 , 2nd order reaction in a differential bed (different catalyst particle sizes) – Polish experimental program

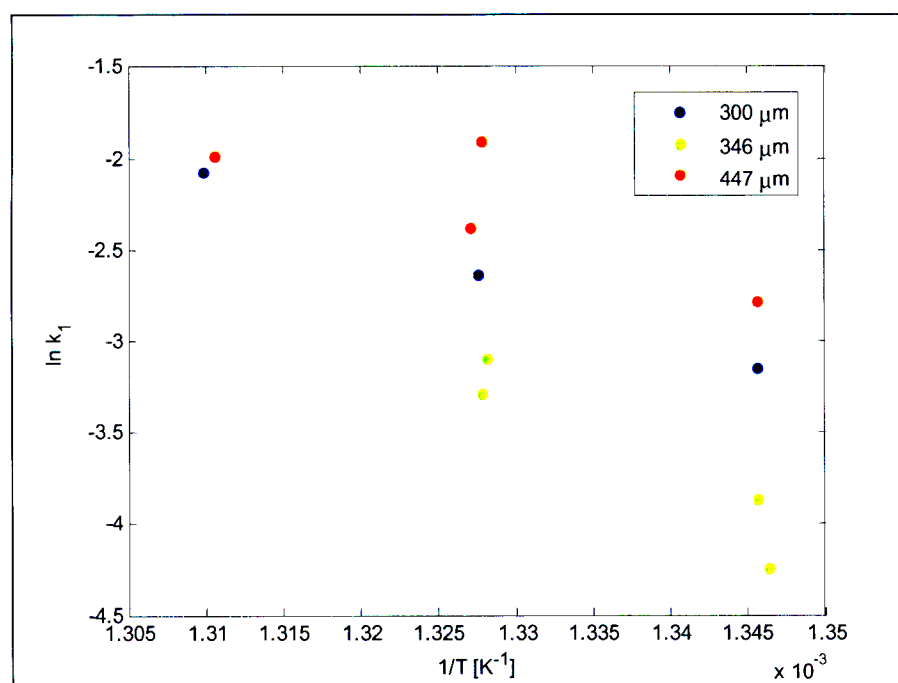


Figure 6.8 Arrhenius plot for parameter k_1 , 1st order reaction (different catalyst particle sizes) – Polish experimental program

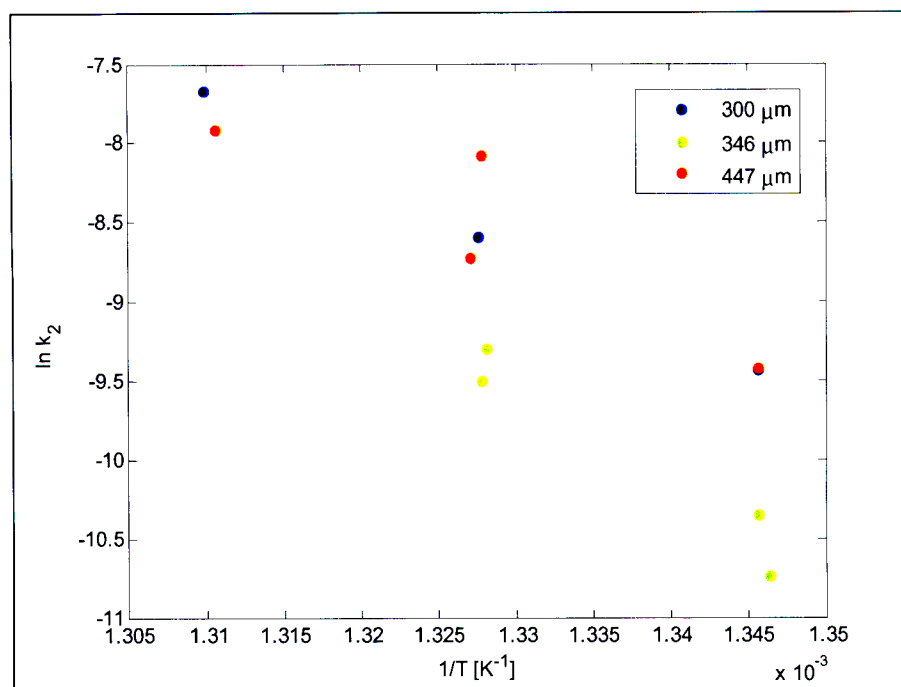


Figure 6.9 Arrhenius plot for parameter k_2 , 2nd order reaction (different catalyst particle sizes) – Polish experimental program

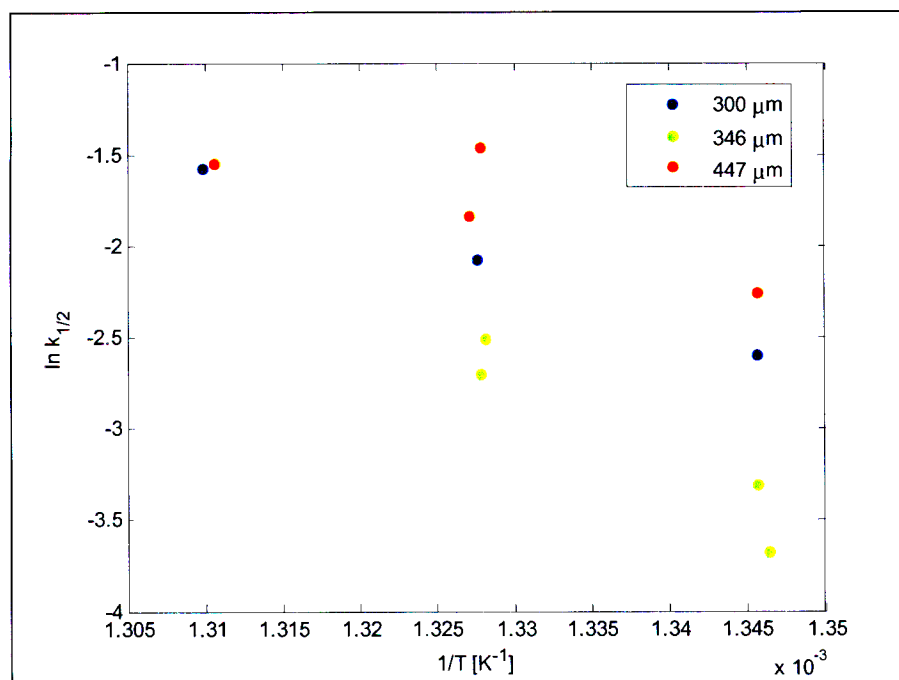


Figure 6.10 Arrhenius plot for parameter $k_{0.5}$, $\frac{1}{2}$ order reaction (different catalyst particle sizes) – Polish experimental program

Model	units	Catalyst particle size		
		300μm	346μm	447μm
E_a , differential, 2 nd order	[kJ.mol ⁻¹]	343	490	308
E_a , 1 st order	[kJ.mol ⁻¹]	253	398	189
E_a , 2 nd order	[kJ.mol ⁻¹]	409	530	357
E_a , 1/2 order	[kJ.mol ⁻¹]	240	411	169

Table 6.3 Estimates for the activation energy, E_a , based on different reaction models (different catalyst particle sizes) – Polish experimental program

The parameter estimates for the activation energy are very high. For gas-phase reactions, E_a is typically between 80-240 kJ.mol⁻¹ (Levenspiel, 1998). The estimated activation energy for the 346μm particles is well above the upper limit of this range. The results of the first order and ½ order cases can be used to determine the extent of intraparticle mass transfer resistance. The observed activation energy for reactions influenced by strong pore resistance is approximately one-half the true activation energy (Levenspiel, 1998):

$$E_{obs} = \frac{E_{true}}{2} \quad (6.25)$$

The activation energy for 447μm particles is three quarters the activation energy for 300μm particles. There is an increase in the resistance to mass transfer within the pores of the catalyst when the particle size is increased from 300μm to 447μm. The pore diffusion effect was not fully developed, however, such that the activation energy for 447μm particles did not fall to half the activation energy of the 300μm particles. It was concluded that the reaction suffered from the effects of internal mass transfer resistance for particles sizes between 300μm and 447μm.

In all the experiments, the selectivity towards higher olefins was poor. The predominant products were the lighter olefins, ethylene, propylene and the butenes which, together, accounted for over 70% of the product distribution. Among the higher olefins produced, heptene selectivity was found to be the greatest, at an average of 10% for all runs, significantly more than any other product in the C₇ – C₁₀ range. Cracking of 1-hexene has been suggested as a possible basis for the formation of shorter chain olefins. It would appear that at low concentrations of 1-hexene in the feed gas, cracking reactions over this WO₃/SiO₂ metathesis catalyst were prominent. Progressive dilution of the gas in the reactor with cracked products (ethylene and propylene) may have strongly inhibited the formation of decene, yet did not have a significant effect on the overall rate of heptene production.

Checking the carbon mass balance consistency across the reaction system is a useful technique for assessing the accuracy of the catalyst performance measurements (conversion, selectivity and yield). Obtaining good carbon mass balance closure indicates internal data consistency and provides a higher level of confidence in the accuracy of the underlying data (Schell et al., 2003). If a large discrepancy is found between the total carbon flow into and out of the system, then the calculated conversion, selectivities and yields cannot be deemed reliable and the accuracy of measuring one or more of the carbon-containing process streams is suspect. The molar flow-rate of individual species exiting the reactor were calculated separately from the total molar flow-rate of condensed liquid and non-condensed vapour product streams and the measured mole fractions. The total carbon flow-rate into and out of the system was calculated using the following expression:

$$\text{Total carbon flow in/out} = \sum N_i^c F_i \quad (6.26)$$

where F_i = molar flow-rate of component i in inlet/outlet stream

N_i^c = number of carbon atoms in component i

The carbon balance consistency was then evaluated using the following equation:

$$\text{Carbon balance consistency (\%)} = \frac{\text{Total carbon flow in} - \text{Total carbon flow out}}{\text{Total carbon flow in}} \times 100 \quad (6.27)$$

The results of these calculations are presented in Table 6.4 and Figure 6.11.

Run No.	Temp [°C]	dp [μm]	Feed composition [mol % 1-hexene]	W/F [g.min.mol ⁻¹]	Carbon balance consistency [%]
1	470	300	19.63	176	-6.41
2	480.1	300	21.54	125	-3.60
3	490.3	300	20.88	100	-12.76
4	469.6	346	19.24	214	1.30
5	480	346	21.46	152	-1.36
6	490	346	22.27	119	-9.60
7	470	346	19.13	214	1.38
8	479.8	346	21.49	152	-5.04
9	470	447	19.02	271	-2.86
10	480.4	447	21.7	191	-9.91
11	489.9	447	18.2	158	-1.86
12	480	447	18.92	199	-11.69

Table 6.4 Carbon balance consistency data for experiments conducted in Poland

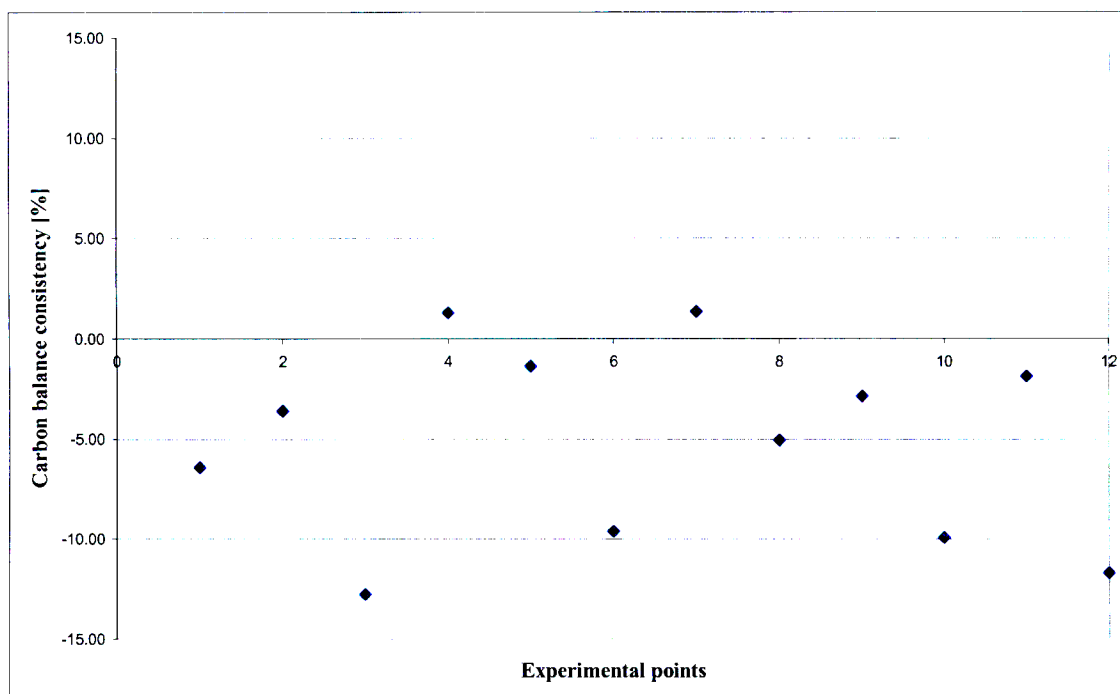


Figure 6.11 Carbon balance consistency plot for experiments conducted in Poland

The carbon balance consistency was satisfactory, generally within 10% error (absolute). This value compares favourably with the 10% mass balance error reported in a Sasol patent publication, for a similar study of heptene/octene metathesis (van Schalkwyk et al., 2004).

In order to operate in a region conducive to the production of larger amounts of higher olefin products, the feed gas composition had to be increased, preferably above 80% (mole based). The saturation method of feed preparation and delivery is not recommended for high reactant concentrations (Anderson and Pratt, 1985), since total saturation of the carrier gas and stable flow is not guaranteed when operating the saturator at temperatures close to the boiling point of the liquid (a condition that was required for $y_{1\text{-hexene}} > 0.8$). Measurement of the total feed flow-rate via the bubble flow-meter and delivery to the reactor module required the application of heated piping to avoid condensation. These lines had to be maintained at a temperature above that of the saturation vessel. The bubble flow-meter assembly could not be heated. After carefully considering the inherent degree of uncertainty associated with the measurement of flow in the proposed, modified system, a decision was made to replace the entire unit with a new vapour-phase experimental rig incorporating a fine metering pump for reactant delivery.

6.3 Results of the experimental program conducted at the University of KwaZulu-Natal (UKZN)

6.3.1 Results of the investigation of pre-treatment procedures

The experimental work performed on the new gas-phase rig commenced with an investigation of pre-treatment procedures for the WO_3/SiO_2 catalyst. Oxidative and reductive pre-treatments of the fresh catalyst were compared to a conventional pre-treatment under nitrogen in terms of their effect on conversion and product distribution. Details of the change in the structural characteristics of the active metathesis centres and acid sites on the tungsten catalyst have been reported in the literature (Basrur et al., 1991; Barton et al., 1998; Bernholc et al., 1987; Rodriguez-Ramos et al., 1995; Thomas, 1998), but the effect on the performance of the catalyst has not received appropriate attention. Three extended experimental runs of 6 hours each were conducted. Samples were withdrawn and analyzed at hour intervals in order to monitor the progress of the reaction. The results are presented in Table 6.5 and Figures 6.12 to 6.16. The first run was conducted after a pre-treatment sequence of 4 hours under air, 1 ½ hours under hydrogen and 18 hours under nitrogen. The period under air was omitted for run 2, where a pre-treatment sequence of 1 ½ hours under hydrogen and 18 hours under nitrogen was used. For run 3, the catalyst was pre-treated under a stream of nitrogen for 18 hours only.

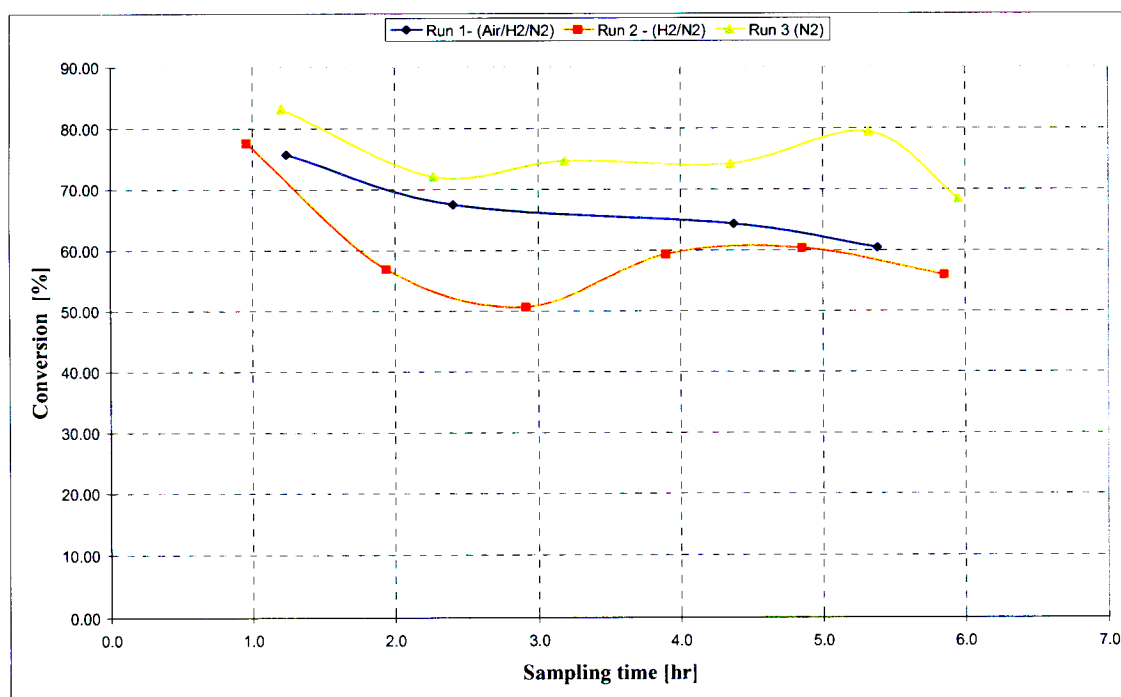


Figure 6.12 Conversion versus sampling time – Run 1- Run 3 (investigation of pre-treatment procedures) – experiments conducted at UKZN

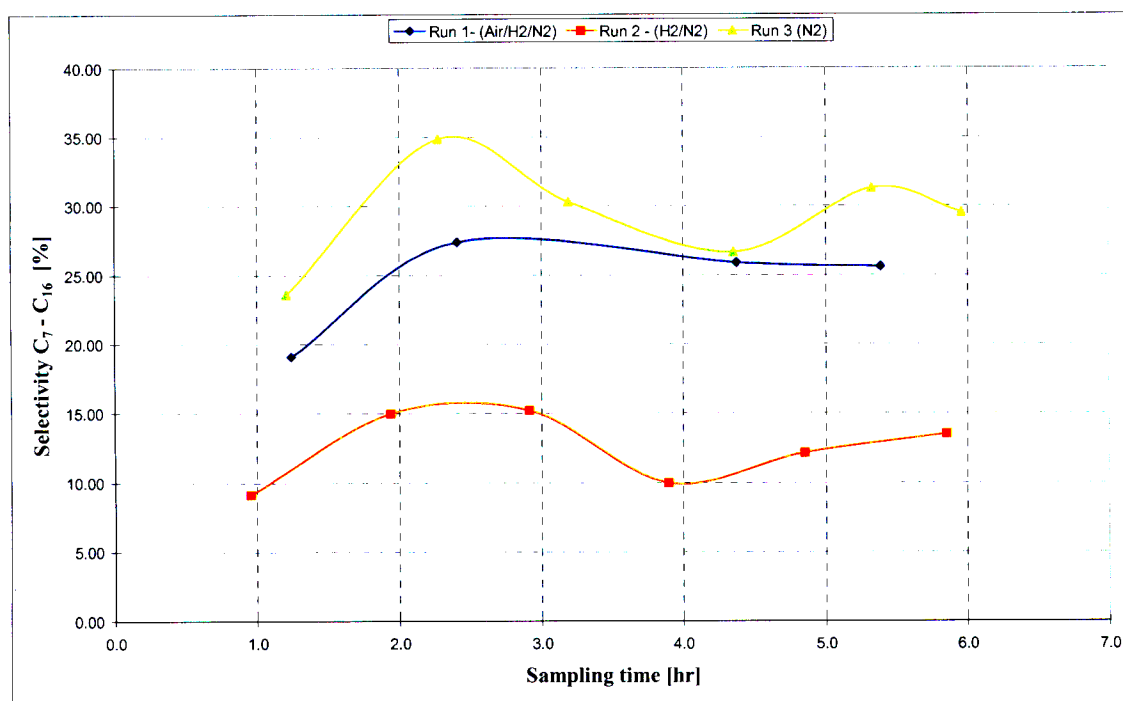


Figure 6.13 Selectivity ($C_7 - C_{16}$) versus sampling time – Run 1- Run 3 (investigation of pre-treatment procedures) – experiments conducted at UKZN

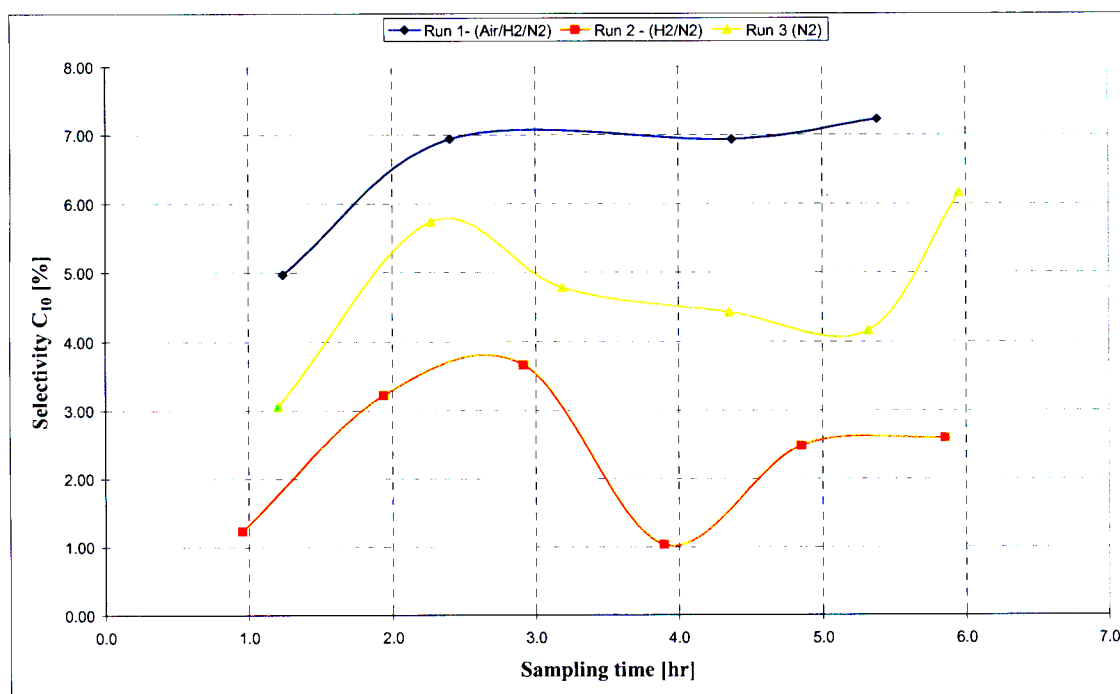


Figure 6.14 Selectivity (C_{10}) versus sampling time – Run 1- Run 3 (investigation of pre-treatment procedures) - experiments conducted at UKZN

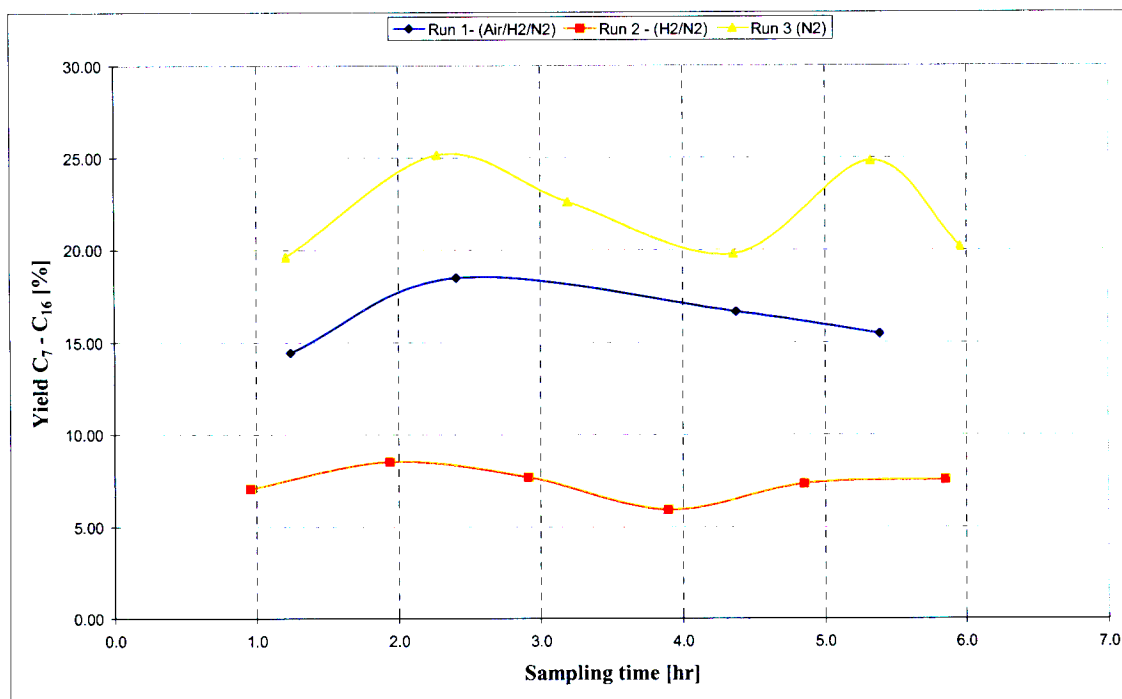


Figure 6.15 Yield ($C_7 - C_{16}$) versus sampling time – Run 1- Run 3 (investigation of pre-treatment procedures) - experiments conducted at UKZN

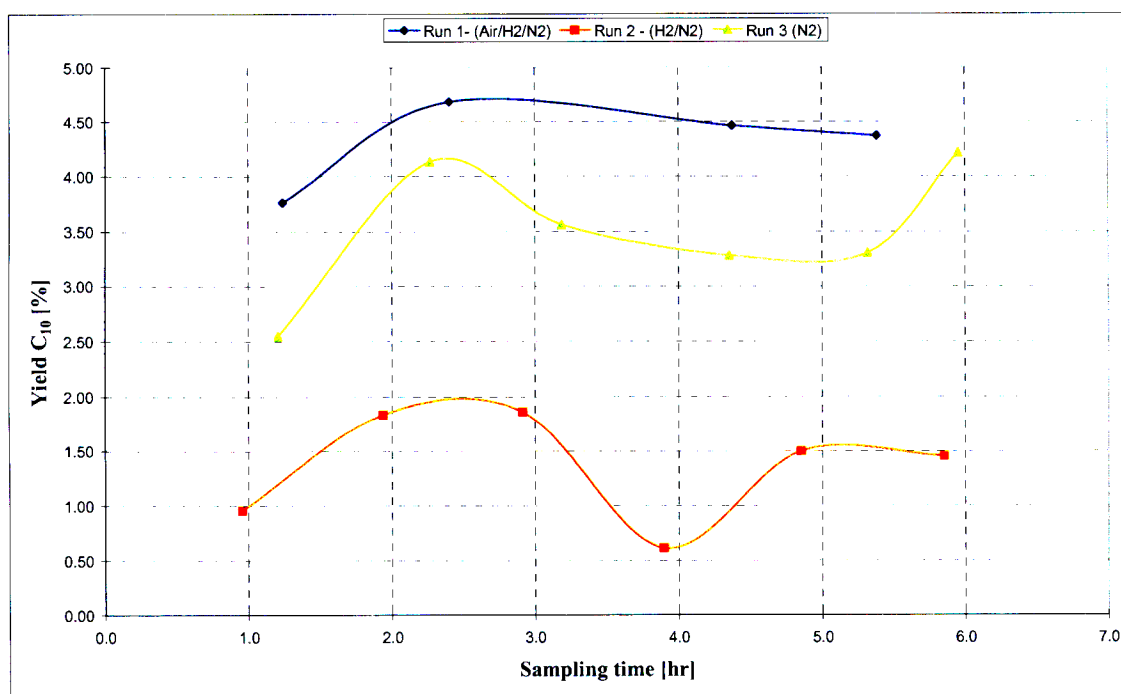


Figure 6.16 Yield (C_{10}) versus sampling time – Run 1- Run 3 (investigation of pre-treatment procedures) - experiments conducted at UKZN

Run No.	Temp [°C]	Feed composition [mol % 1-hexene]	W/F [g.min.mol ⁻¹]	X [%]	Sel C ₇ -C ₁₆ [%]	Sel C ₁₀ [%]	Y C ₇ -C ₁₆ [%]	Y C ₁₀ [%]	Sampling time [hr]
R1-01	460	96.41	336	75.77	19.09	4.97	14.46	3.76	1.24
R1-02	460	96.41	336	67.52	27.39	6.94	18.49	4.68	2.40
R1-04	460	96.41	336	64.35	25.91	6.94	16.67	4.46	4.37
R1-05	460	96.41	336	60.47	25.62	7.23	15.49	4.37	5.38
R2-01	460	95.84	334	77.62	9.13	1.23	7.08	0.96	0.95
R2-02	460	95.84	334	57.01	14.96	3.22	8.53	1.84	1.93
R2-03	460	95.84	334	50.74	15.18	3.66	7.70	1.86	2.91
R2-04	460	95.84	334	59.40	9.98	1.03	5.93	0.61	3.89
R2-05	460	95.84	334	60.39	12.15	2.48	7.34	1.50	4.85
R2-06	460	95.84	334	55.98	13.51	2.60	7.56	1.45	5.85
R3-01	460	95.90	334	83.19	23.59	3.06	19.63	2.55	1.20
R3-02	460	95.90	334	72.11	34.87	5.73	25.14	4.13	2.27
R3-03	460	95.90	334	74.65	30.30	4.77	22.62	3.56	3.18
R3-04	460	95.90	334	74.14	26.65	4.42	19.76	3.28	4.35
R3-05	460	95.90	334	79.35	31.28	4.16	24.82	3.30	5.32
R3-06	460	95.90	334	68.39	29.51	6.16	20.18	4.21	5.95

Table 6.5 Experimental results, investigation of pre-treatment procedures – experiments conducted at UKZN – Air/H₂/N₂ (4 hours, 1 ½ hours and 18 hours, respectively) in blue, H₂/N₂ in red and N₂ in black

The selectivity and yield of the primary metathesis product, decene, was found to be marginally higher after the air/hydrogen/nitrogen sequence compared to the conventional pre-treatment under nitrogen, even though the conversion of 1-hexene was lower. A structural transformation of the catalyst and an increase in the rate of metathesis reactions with increased dispersion of the active tungsten phase (through migration of active material over the surface of the catalyst) after oxidative pre-treatment may be responsible for the improved yield (Barton et al., 1998; Spamer et al., 2003). The conversion of 1-hexene was lower after reductive pre-treatments compared to the conventional pre-treatment under nitrogen. This may be ascribed to the fact that Lewis acid sites were converted to weak Brønsted acid sites, with the former responsible for metathesis type reactions (Thomas, 1998). The low 1-hexene conversion, selectivity and yield of higher olefins and decene reported after reductive pre-treatment under hydrogen may also be due to over-reduction of the tungsten metal centres on the catalyst and the formation of an inactive non-stoichiometric surface phase. These results are contradictory to what was published in the literature, where an improved yield of primary metathesis products was observed for the metathesis of 1-octene after hydrogen pre-treatments (van Schalkwyk et al., 2003 b). The true final oxidation state of the metal centres in that study may have been affected by regenerative exposure to air immediately afterward. The reducing effect observed for this work may have also been negated by the oxidative period under air during run 1. The results for

run 1 are thus much more positive. For all subsequent experiments, the combination of 4 hours under air, 1 ½ hours under hydrogen and 18 hours under nitrogen was retained, because the yield of the primary metathesis product, decene, was found to be highest after this particular sequence.

Following a relatively stable period under pure nitrogen, a sharp temperature rise was observed immediately after activating the 1-hexene feed system and delivering the reactant to the reactor module. After 30 minutes on-stream, the temperature once again stabilized around the set-point value. This initial temperature rise cannot be attributed to the heat effect of the metathesis reaction. The literature reports that similar olefin metathesis reactions are either mildly endothermic or exothermic, or even thermo-neutral (Kapteijn et al., 1981). The temperature rise was not sustained through the remainder of the experiment. It was further suggested that the heat effect may be due to the catalyst break-in or induction period, during which the active phase undergoes a transformation that results in the formation of a metathesis initiator or metallacarbene intermediate. The break-in period for tungsten-based metathesis catalysts has been found to proceed through two steps (reduction of the tungsten precursor and subsequent formation of the surface intermediate). The reduction step is not exothermic and cannot account for the observed temperature rise (Basrur et al., 1991). Several competing side reactions also proceeded during this initial period, viz. cracking and isomerization, but a final conclusion as to the cause of this exothermic effect was not reached. The effect of catalyst pre-reduction (under hydrogen) on the induction period could not be ascertained due to the instability of reaction temperature during start-up.

BET surface characterization of the fresh and spent tungsten catalysts from Run 1 revealed that the specific surface area decreased from $275.7\text{m}^2\cdot\text{g}^{-1}$ to $147.8\text{m}^2\cdot\text{g}^{-1}$ over the 6 hour period, due to the deposition of coke. The catalyst activity was observed to reach a maximum value (in terms of conversion) during the first hour on-stream. Analysis of reaction data was found to be unreliable during this initial period due to the instability of reaction temperature. The conversion level stabilized after 3 hours on-stream.

An elemental analysis of the fresh and spent catalyst surface was obtained using energy dispersive x-ray spectroscopy (EDX analysis). The results are presented in Figures 6.17 to 6.18. The method can be used to detect elements in the upper 5-10nm of the catalyst surface. Carbon detected by the system was omitted from the results because it was already present in the sample chamber and it was impossible to tell how much was coming directly from the sample. Clusters of the tungsten surface phase that were covered by a layer of coke thicker than 10nm were not detected.

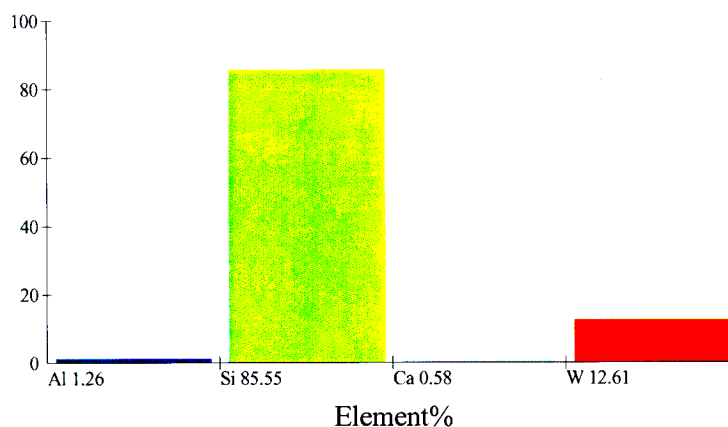


Figure 6.17 EDX elemental analysis – fresh WO_3/SiO_2 (catalyst B) – experiments conducted at UKZN

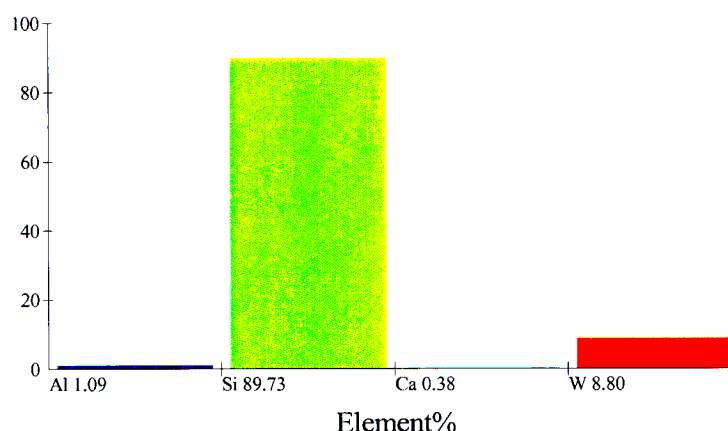


Figure 6.18 EDX elemental analysis – spent WO_3/SiO_2 (catalyst B - 460°C , 96.41% 1-hexene, $W/F = 336 \text{ g}\cdot\text{min}\cdot\text{mol}^{-1}$, 6 hours on-stream) – experiments conducted at UKZN

The EDX spectra showed a significant decrease in the amount of exposed tungsten on the catalyst surface. This result indicates a high level of coke formation, even over the active metathesis tungsten centres. Impurities including aluminium and calcium were also found on the surface. Aluminium can form acidic sites that can act as sites for olefin isomerization. Alkali metal impurities such as calcium can form basic sites that can act as active sites for double-bond isomerization (Gartside et al., 2002). To eliminate the effect of these impurities, high purity silica should be used when synthesizing the WO_3/SiO_2 catalyst. Specifically, the high purity silica support should contain less than about 900ppm calcium and less than about 200ppm aluminium (Gartside et al., 2002). The EDX analysis unfortunately does not provide an absolute indication of the amount of each element present.

The drop in the conversion level during the first 3 hours on-stream (10%) was much greater than the values reported in the literature for the metathesis of 1-heptene and 1-octene over WO_3/SiO_2 , which was less than 10% over 600 hours in a recycle and single-pass reactor (van Schalkwyk et al., 2003, a and c). The selectivity towards ethylene and propylene (>65%) was also much higher than the 15% obtained in the study performed by van Schalkwyk and co-workers. The rate of coke formation was probably much higher in this work than in the van Schalkwyk study, which may be due to excessive cracking of 1-hexene. Intermediates formed during the cracking of olefins undergo fast coupling and polymerization reactions that eventually lead to coke deposits (Bartholomew, 2001). The presence of large amounts of light olefins (ethylene and propylene) provides further evidence of cracking. The only discernable difference between the system used in this work and the study conducted by van Schalkwyk was the feed alkene used (a shorter-chain terminal alkene, 1-hexene, as opposed to an industrial cut 1-heptene and 1-octene feed, respectively) and the specific surface area of the catalyst ($275.7 \text{ m}^2 \cdot \text{g}^{-1}$ for this work and $257.7 \text{ m}^2 \cdot \text{g}^{-1}$ for the Sasol study). It is possible that shorter-chain alkenes are more susceptible to cracking over 8% WO_3/SiO_2 than longer-chain terminal alkenes. The selectivity and yield of higher olefins and decene improved with the time on-stream, probably due to blocking of some of the acid sites on the catalyst surface by coke, limiting the rate of side reactions.

Inspection of the spent catalyst from runs 1, 2 and 3 revealed that the particles had assumed a dark black/blue metallic appearance compared to the yellow-white powdery texture of the fresh catalyst, with little signs of visible coke (Figure 6.19(a), (b) and (c)).

SEM analysis of the fresh and spent catalyst was also carried out. A close inspection of Figure 6.20 revealed grooves in the catalyst particle that originated from the SiO_2 support. The grooves were still visible in the spent catalyst sample (Figure 6.21), evidence of the fact that coke formation occurs predominantly in the pores of the catalyst and not to a great extent on the outer surface of the particle. From a simple geometrical analysis it was found that the contribution of the external area of the catalyst particles to the total specific surface area was negligible. As a result, the observed drop in the specific surface area after reaction can be completely attributed to a change in the intraparticle surface area through coke deposition. Further magnification of the surface of both the fresh and spent catalyst (Figure 6.22 and Figure 6.23) revealed that there were some small deposits of coke over the surface resulting in a rougher texture. Small catalyst fragments were visible on the surface of both the fresh and spent catalyst.

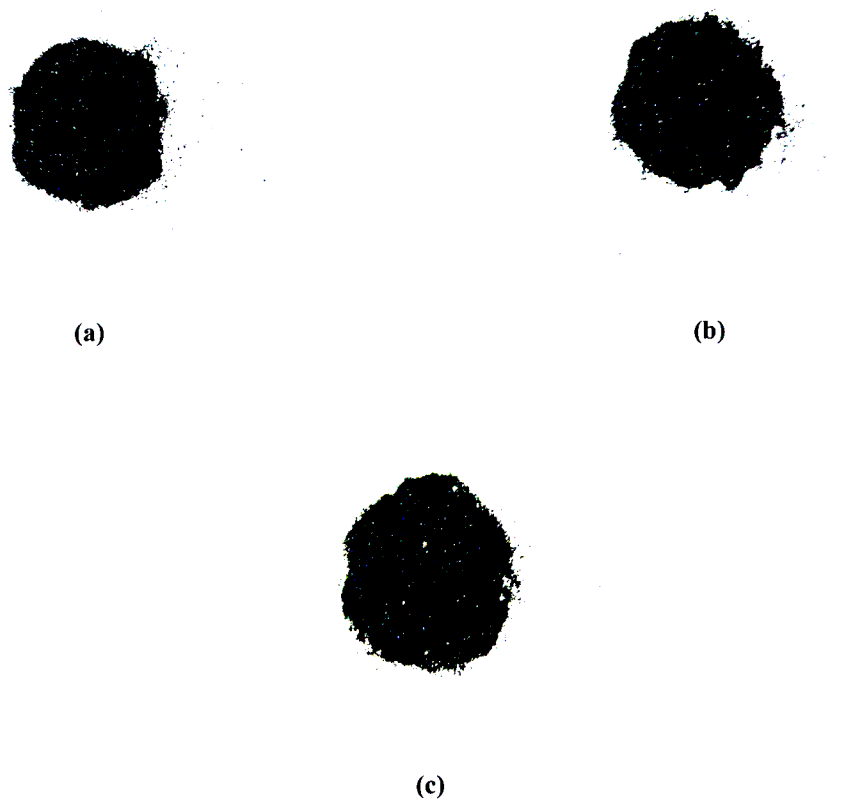


Figure 6.19 Spent WO_3/SiO_2 catalyst – run 1 (a), run 2 (b) and run 3 (c)

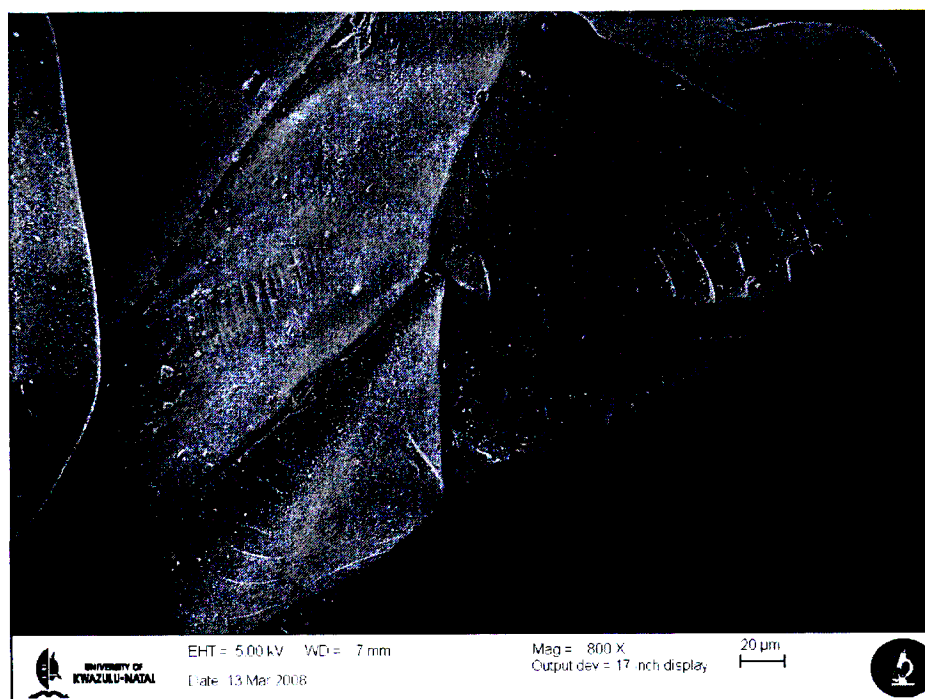


Figure 6.20 Fresh 8% WO_3/SiO_2 catalyst (800X magnification)

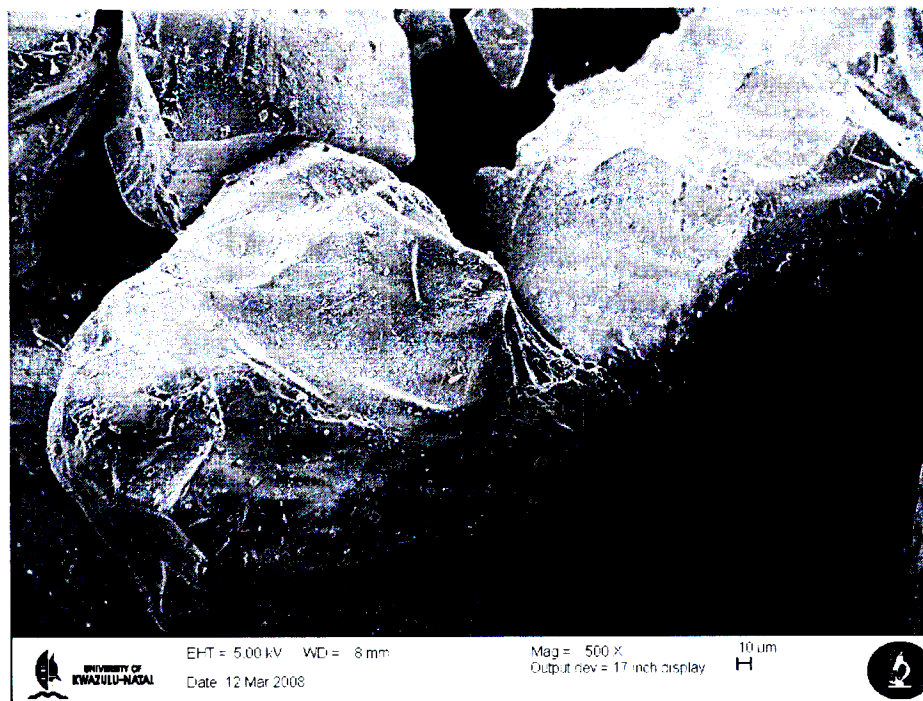


Figure 6.21 Spent 8% WO_3/SiO_2 catalyst (500X magnification) - removed after 6 hours on-stream at 460°C, 96.41% 1-hexene, $W/F = 336 \text{ g.min.mol}^{-1}$

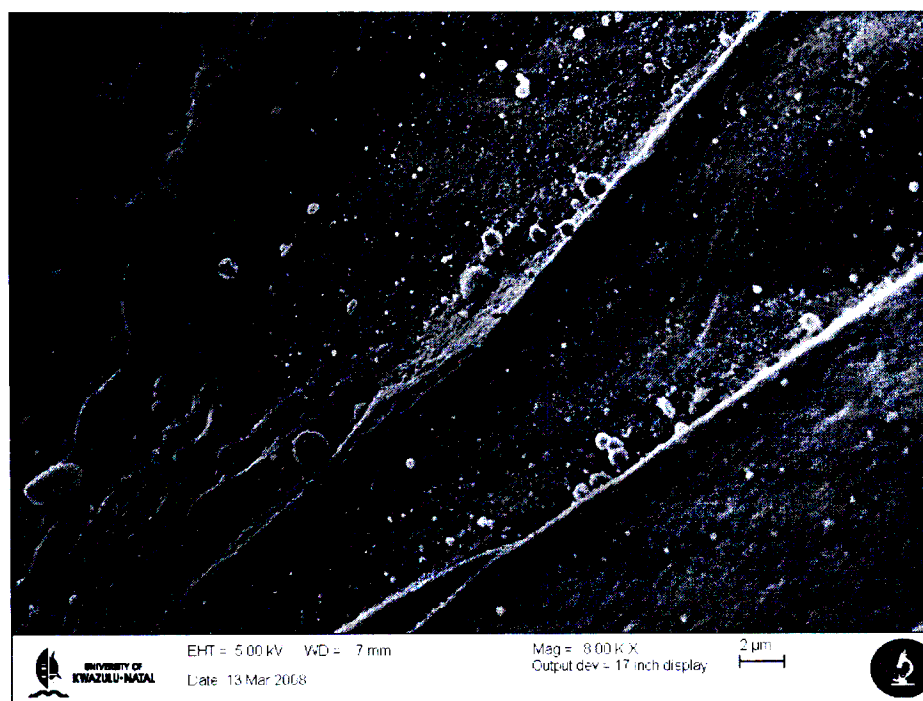


Figure 6.22 Fresh 8% WO_3/SiO_2 catalyst (8.00KX magnification)

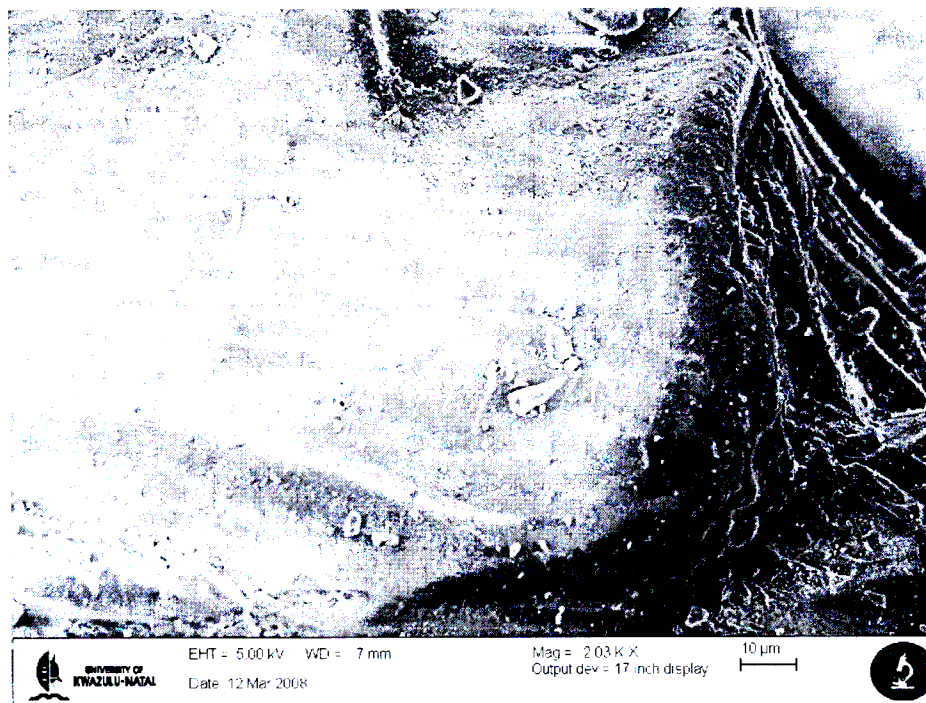


Figure 6.23 Spent 8% WO₃/SiO₂ catalyst (5.03KX magnification)

6.3.2 Results of the factorial experimental design

The complete set of results for the optimization and transport effects study is presented in Table 6.6. Of these, nine experimental points make up the factorial experimental design. These are given in Table 6.7 together with the objective response values for the yield of decene. From the data generated for each of the points that constituted the factorial design, general effects and interactions for each one of the variables were calculated using the Yates algorithm (Table 6.8).

Calculations revealed that the yield of decene decreased by 0.11% when the reaction temperature was raised by 40°C, and by 0.17% when the feed gas composition was raised by 17.5%. The yield also increased by 0.21% when the space time was increased by 223g.min.mol⁻¹. The average theoretical yield of decene was 1.29% at the average conditions 460°C, 72.5% feed composition and 443g.min.mol⁻¹. The measured yield of decene at 460°C, 76.2% feed composition and 403g.min.mol⁻¹ was 1.34%. The results demonstrated that the performance of catalyst B (in terms of yield of decene) was adversely affected by high reaction temperatures, high feed gas compositions and low space time. These absolute predictions were valid only for the measurement range. Interaction plots (Figures 6.24 – 6.26) for combinations of the three variables were obtained from mean response values (Tables 6.9 – 6.11).

A strong antagonistic interaction was observed between reaction temperature and feed composition. At low temperature, the yield decreased substantially when the feed composition was raised, yet at high temperature the yield increased marginally at higher feed compositions. A weaker interaction was observed between reaction temperature and space time. At both high and low temperatures, the yield of decene improved when the space time was increased. The rate of improvement was very much greater, however, at higher temperatures. No interaction was observed between feed composition and space time. At both high and low feed gas compositions, the yield of decene improved when the space time was increased, and at almost the same rate. The best yield of decene obtained from the experimental design was 2.19% at 420°C, 51% feed composition and 661g.min.mol⁻¹. For all experiments (excluding run 12 and run 13) the highest yield obtained was 4.37% (for catalyst B) at 460°C, 96% feed composition and 336g.min.mol⁻¹.

Run No.	Temp [°C]	Feed composition [mol % 1-hexene]	W/F [g.min.mol ⁻¹]	X [%]	Sel C ₇ -C ₁₆ [%]	Sel C ₁₀ [%]	Y C ₇ -C ₁₆ [%]	Y C ₁₀ [%]
R1-05	460	96.41	336	60.47	25.62	7.23	15.49	4.37
R4-01	420	63.62	1413	71.59	11.22	1.56	8.03	1.12
R4-02	420	54.71	646	46.05	24.01	4.17	11.06	1.92
R4-03	420	54.81	221	9.04	35.92	20.87	3.25	1.89
R5-01	480	54.84	221	91.14	7.13	0.70	6.50	0.64
R5-02	500	62.44	1405	90.68	9.34	0.87	8.47	0.79
R5-03	460	100.00	869	99.07	8.63	0.75	8.55	0.74
R5-04	460	74.54	648	98.62	13.67	1.16	13.48	1.14
R5-05	500	54.37	220	91.30	13.37	0.87	12.21	0.79
R6-01	420	88.95	221	18.90	14.46	4.79	2.73	0.90
R6-02	420	90.86	670	96.03	7.66	0.67	7.36	0.64
R6-03	500	90.76	669	98.57	24.39	2.20	24.05	2.17
R6-04	500	89.37	222	60.58	30.47	1.30	18.46	0.79
R7-01	420	27.98	393	96.51	21.76	2.95	21.00	2.84
R7-04	420	28.42	399	95.52	8.62	1.11	8.24	1.06
R7-02	420	28.93	196	93.18	10.16	1.13	9.46	1.05
R7-03	420	28.80	142	71.87	22.93	4.48	16.48	3.22
R8-01	420	51.59	661	95.08	23.70	2.31	22.54	2.20
R8-02	460	76.28	403	99.52	12.98	1.34	12.92	1.34
R8-03	500	54.50	698	99.31	33.19	1.02	32.97	1.01
R11-01	380	94.53	200	4.27	39.90	16.41	1.70	0.70
R11-02	380	94.10	300	6.75	34.35	14.65	2.32	0.99
R11-03	380	95.00	403	10.61	64.77	28.07	6.87	2.98
R12-01	380	100.00	3200	83.15	25.75	6.12	21.41	5.09
R13-01	380	55.15	2874	94.36	27.01	13.56	25.49	12.79

Table 6.6 Complete set of results for the optimization and transport effects study - factorial design
points in blue, external transport effect runs in red, green and magenta

Run	A Temp [°C]	B Feed composition [mol % 1-hexene]	C W/F [g.min.mol ⁻¹]	Response Y C ₁₀ [%]
R4-03	-1	-1	-1	1.88
R5-05	+1	-1	-1	0.79
R6-01	-1	+1	-1	0.90
R6-04	+1	+1	-1	0.79
R8-01	-1	-1	+1	2.19
R8-03	+1	-1	+1	1.01
R6-02	-1	+1	+1	0.64
R6-03	+1	+1	+1	2.16
R8-02	0	0	0	1.33

Table 6.7 Three variable, two level full factorial design with a centre-point.

Run	Response Y C ₁₀ [%]	1	2	3	Effect or Interaction	Meaning
R4-03	1.888	2.678	4.372	10.392	1.299	Total
R5-05	0.790	1.695	6.019	-0.870	-0.109	A
R6-01	0.904	3.210	-1.212	-1.384	-0.173	B
R6-04	0.790	2.809	0.342	3.688	0.461	AB
R8-01	2.196	-1.098	-0.983	1.647	0.206	C
R8-03	1.015	-0.114	-0.401	1.554	0.194	AC
R6-02	0.643	-1.181	0.983	0.582	0.073	BC
R6-03	2.166	1.523	2.704	1.721	0.215	ABC

Table 6.8 Effects and interactions of temperature (A), feed composition (B) and space time (C) – Yates algorithm

Run	A Temp [°C]	B Feed composition [mol % 1-hexene]	Avg Response Y C ₁₀ [%]
R4-03, R8-01	-1	-1	2.042
R6-01, R6-02	-1	+1	0.774
R5-05, R8-03	+1	-1	0.902
R6-04, R6-03	+1	+1	1.478

Table 6.9 Mean response values, temperature (A) – feed composition (B) combination

Run	A Temp [°C]	C W/F [g.min.mol ⁻¹]	Avg Response Y C ₁₀ [%]
R4-03, R6-01	-1	-1	1.396
R8-01, R6-02	-1	+1	1.419
R5-05, R6-04	+1	-1	0.790
R8-03, R6-03	+1	+1	1.590

Table 6.10 Mean response values, temperature (A) – space time (C) combination

Run	B Temp [°C]	C W/F [g.min.mol ⁻¹]	Avg Response Y C ₁₀ [%]
R4-03, R5-05	-1	-1	1.339
R8-01, R8-03	-1	+1	1.605
R6-05, R6-04	+1	-1	0.847
R6-02, R6-03	+1	+1	1.405

Table 6.11 Mean response values, feed composition (B) – space time (C) combination

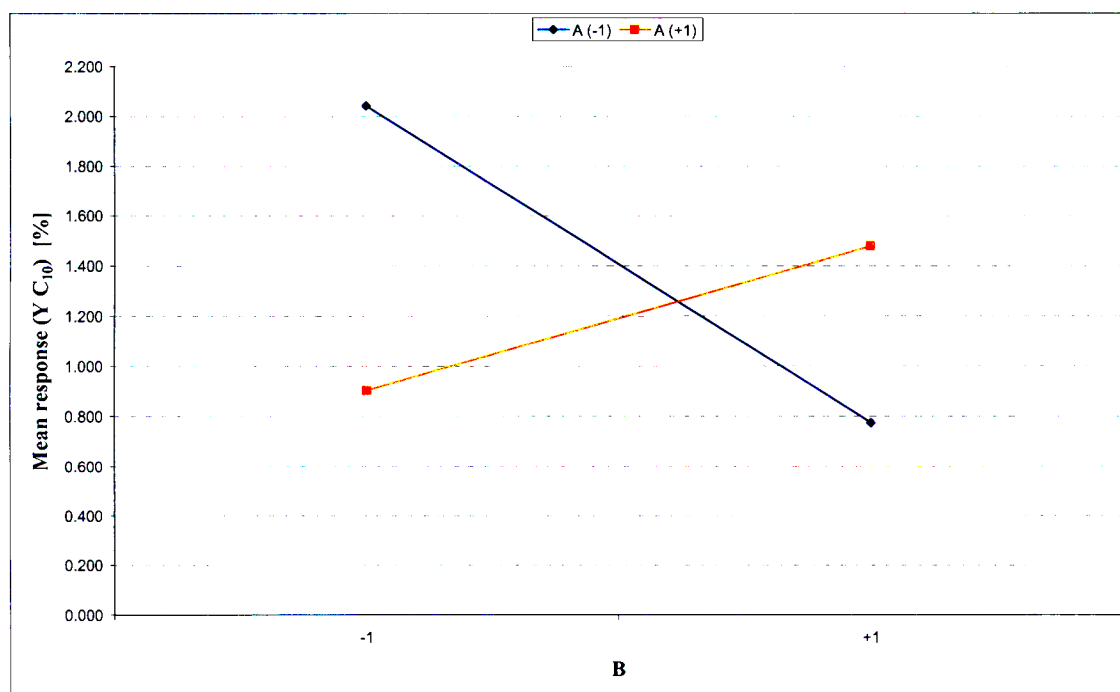


Figure 6.24 Interaction plot of temperature (A) and feed composition (B) – experiments conducted at UKZN

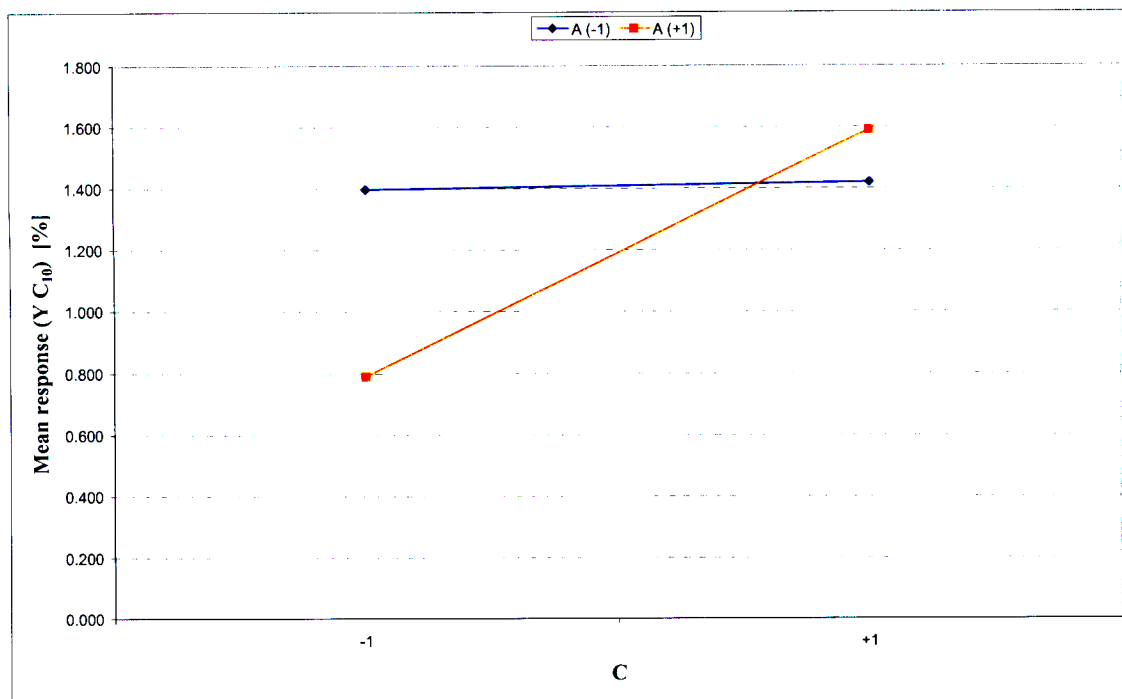


Figure 6.25 Interaction plot of temperature (A) and space time (C) – experiments conducted at UKZN

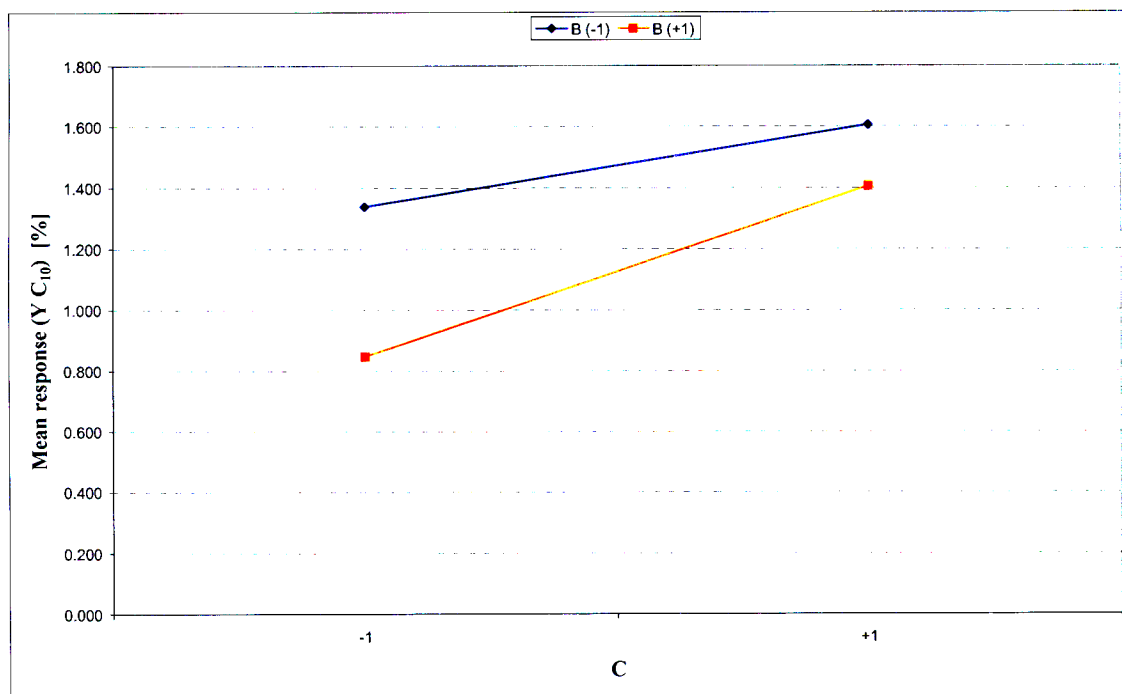


Figure 6.26 Interaction plot of feed composition (B) and space time (C) – experiments conducted at UKZN

The significance of the effects and interactions of the factorial experimental design were checked by the statistical methods discussed in chapter 3. The standard deviation of the yield of decene for the experiments was estimated from replicate data to be 0.058%. At the 95% level of confidence, all effects and interactions were found to be significant (Table 6.12).

	Effects	z (test quantity)	z > c (significance number)
A	-0.109	5.310	yes, significant
B	-0.173	8.451	yes, significant
AB	0.461	22.519	yes, significant
C	0.206	10.057	yes, significant
AC	0.194	9.487	yes, significant
BC	0.073	3.552	yes, significant
ABC	0.215	10.508	yes, significant

Table 6.12 Significance test on the results of the factorial design

The colour of the liquid product from selected runs was determined using UV-vis absorption measurements in the 400nm range. These results are presented in Table 6.13. The colour of the liquid product was darker at higher reaction temperatures, regardless of feed composition or space time, indicating the presence of high molecular weight polynuclear aromatics (pure 1-alkenes are colourless). These aromatics are the product of dehydrogenation and cyclization reactions of intermediates formed on acid sites during cracking of olefins. G.C. – M.S. analysis of the liquid product from run 8 (at 420°C, 460°C and 500°C) confirmed that high molecular weight polynuclear aromatics were present in the liquid samples. The G.C. – M.S. analysis was purely qualitative, since the detector had not been calibrated for different compounds. These analyses were performed only to identify the non-olefin products that were present in the liquid sample and not to determine their actual concentrations. The G.C. – M.S. analyses were performed at the School of Chemistry of the University of KwaZulu-Natal. The most abundant non-olefin products that were found in the liquid product samples from run 8 (at 420°C, 460°C and 500°C) are listed in Tables 6.14 to 6.16. Lighter products in the liquid samples (C₅ – C₉) were lost during the storage period between sample collection and analysis, which was typically three days. Nevertheless it was observed that at higher reaction temperatures more complex aromatics containing a larger number of carbon atoms were found in the liquid samples. Side reactions such as cracking and isomerization advanced with greater ease at higher reaction temperatures.

Run No.	Temp [°C]	Feed composition [mol % 1-hexene]	W/F [g.min.mol ⁻¹]	Absorbance at 400nm
R4-03	420	54.81	221	0.075
R5-05	500	54.37	220	0.560
R6-01	420	88.95	221	0.365
R6-04	500	89.37	222	0.790
R8-01	420	51.59	661	0.412
R8-03	500	54.50	698	0.883
R6-02	420	90.86	670	0.205
R6-03	500	90.76	669	0.845
R8-02	460	76.28	403	0.868

Table 6.13 The effect of different reaction conditions on the quality of the metathesis liquid product colour

No.	Component	Area %
1	Styrene	13.5
2	Naphthalene	7.1
3	Benzene, 1-propynyl-	6.5
4	Ethylbenzene	5.6
5	2,4-Octadiene	4.3
6	Benzene, 1,3-dimethyl-	4
7	Bicyclo[4.2.0]octa-1,3,5-triene, 7-methyl-	3.4
8	Benzene, 1-butynyl-	2.5
9	Bicyclo[2.2.1]hept-2-ene, 2-methyl-	2
10	1H-Indene, 1,3-dimethyl-	2

Table 6.14 Most abundant non-olefin products in the liquid product sample from run 8-01 (420°C, 52% feed composition and $W/F = 660 \text{ g.min.mol}^{-1}$)

No.	Component	Area %
1	Styrene	7.8
2	Naphthalene	7.2
3	Indene	5.3
4	2-Methylindene	3.4
5	1H-Indene, 1-methyl-	3.4
6	4,7-Methano-1H-indene, 3a,4,7,7a-tetrahydro-	3.2
7	Ethylbenzene	3.1
8	Naphthalene, 1-methyl-	2.9
9	Benzene, ethenylmethyl-	2.8
10	1,4-Methanonaphthalene, 1,4-dihydro-	2.6

Table 6.15 Most abundant non-olefin products in the liquid product sample from run 8-02 (460°C, 76% feed composition and $W/F = 403 \text{ g.min.mol}^{-1}$)

No.	Component	Area %
1	Styrene	8.0
2	Indene	5.7
3	Benzene, 1-ethenyl-3-methyl-	3.6
4	Phenanthrene	3.5
5	Naphthalene, 2-methyl-	3.2
6	2-Methylindene	3.1
7	Ethylbenzene	3.0
8	2-Methylindene	3.0
9	Biphenylene	3.0
10	Naphthalene, 1-methyl-	2.8

Table 6.16 Most abundant non-olefin products in the liquid product sample from run 8-03 (500°C, 55% feed composition and $W/F = 697\text{g.min.mol}^{-1}$)

After reviewing the results of the factorial experimental design it was concluded that a combination of lower temperature, lower feed gas composition and higher space time should be used to maximize the yield of decene. The decision was based on the absolute response values, the interaction and effects of each of the variables and the colour of the liquid product.

6.3.3 Results of the tests for external mass transfer resistance

Three attempts were made at achieving differential fixed-bed reactor conditions in the reactor tube (conversion < 10%). The differential operation of the reactor is a requisite for extending the program for development of a kinetic model*, however the motive for carrying out such experiments was to investigate the extent of external mass transfer effects. The conversion, selectivity and yield of higher olefins and decene at 420°C, 55% feed composition and between 221g.min.mol^{-1} and $1412\text{g.min.mol}^{-1}$ are presented in Figures 6.27 to 6.29 and at 420°C, 29% feed composition and between 142g.min.mol^{-1} and 398g.min.mol^{-1} are presented in Figures 6.30 to 6.32. At these conditions the reactor was still found to operate as an integral bed, with very high conversions obtained at a feed composition of 29%. At this low feed gas composition the product contained excessive amounts of ethylene and propylene (selectivity > 75%), indicating increased rates of cracking.

* Several advantages accrue from the use of the differential mode. Most importantly, the rate can be calculated directly at feed concentrations.

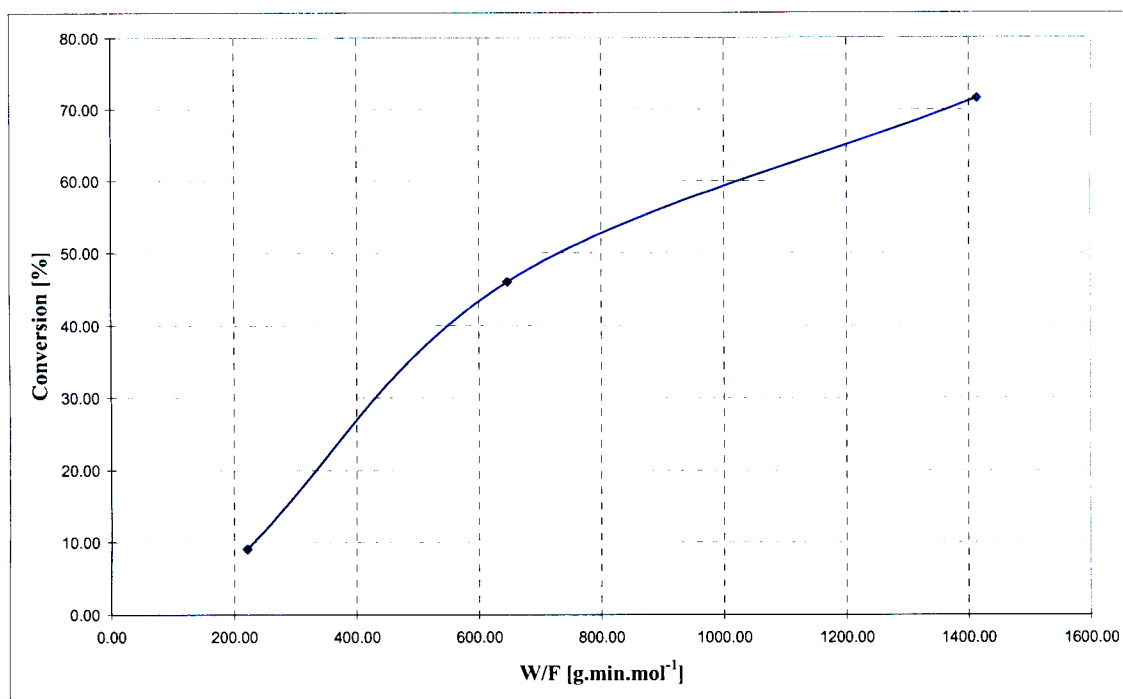


Figure 6.27 Conversion versus space time – Run 4 (420°C, 55% feed composition, $W/F = 221\text{g.min.mol}^{-1}$ to $1412\text{g.min.mol}^{-1}$) – experiments conducted at UKZN

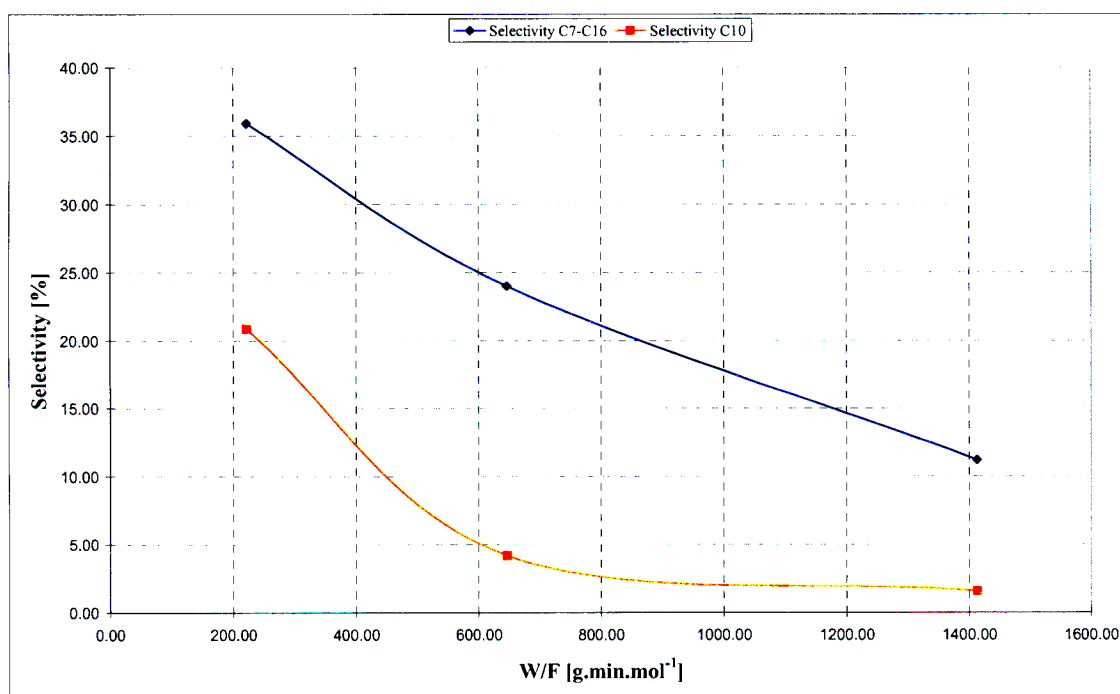


Figure 6.28 Selectivity versus space time – Run 4 (420°C, 55% feed composition, $W/F = 221\text{g.min.mol}^{-1}$ to $1412\text{g.min.mol}^{-1}$) – experiments conducted at UKZN

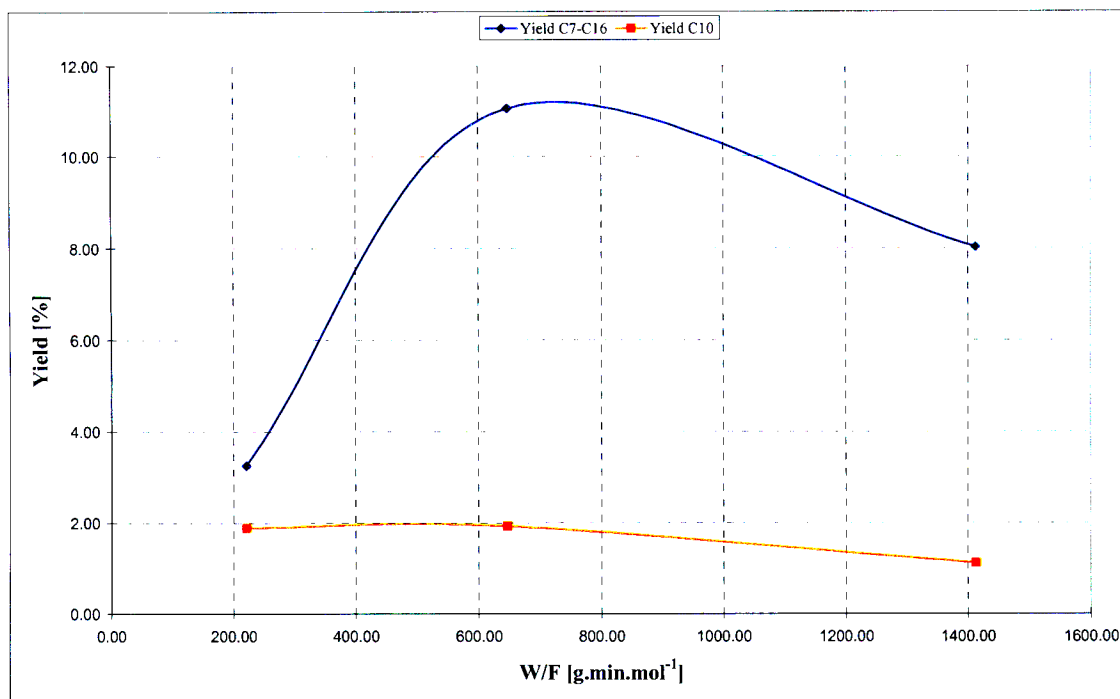


Figure 6.29 Yield versus space time – Run 4 (420°C, 55% feed composition, $W/F = 221\text{g.min.mol}^{-1}$ to $1412\text{g.min.mol}^{-1}$) – experiments conducted at UKZN

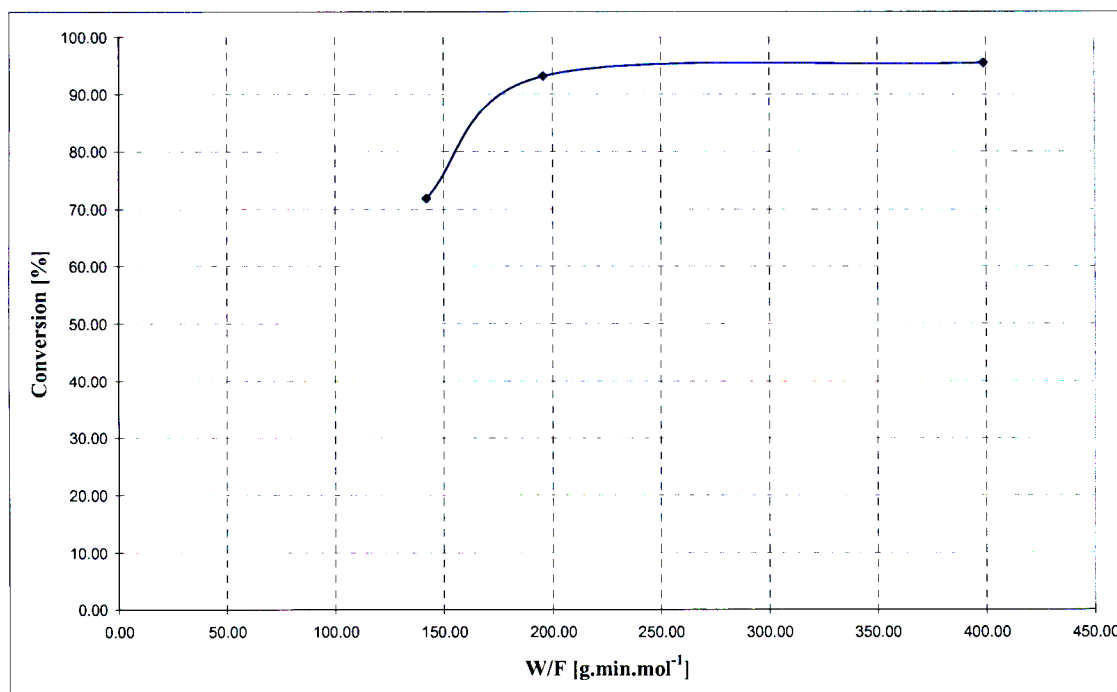


Figure 6.30 Conversion versus space time – Run 7 (420°C, 29% feed composition, $W/F = 142\text{g.min.mol}^{-1}$ to 398g.min.mol^{-1}) – experiments conducted at UKZN

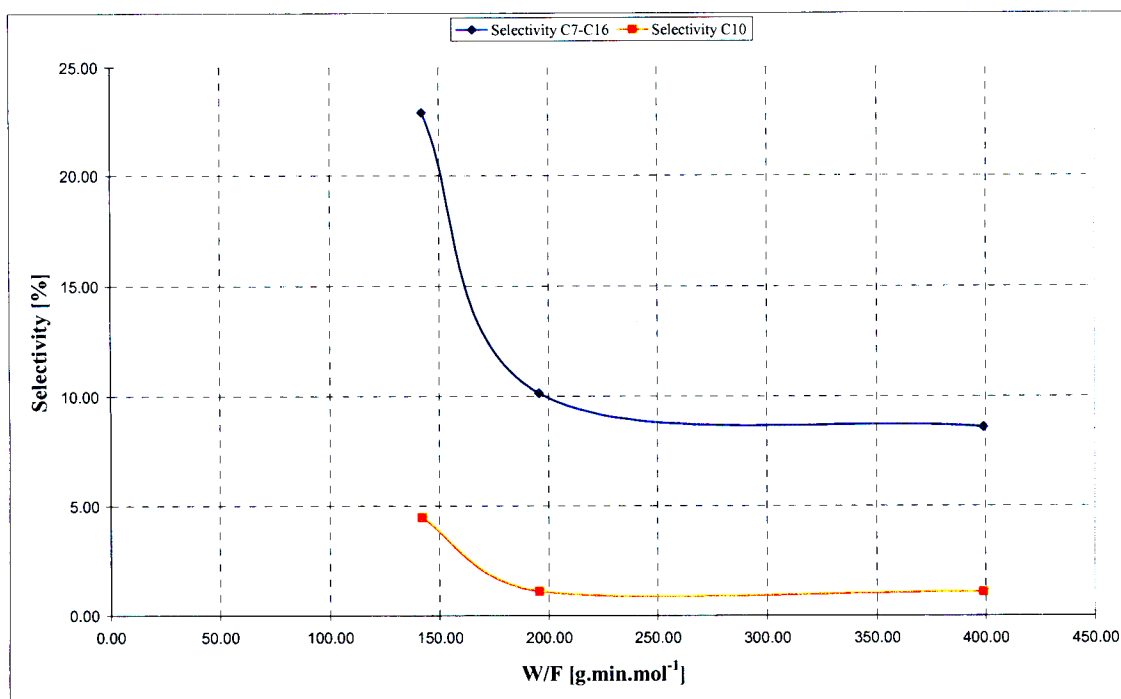


Figure 6.31 Selectivity versus space time – Run 7 (420°C, 29% feed composition, $W/F = 142\text{g.min.mol}^{-1}$ to 398g.min.mol^{-1}) – experiments conducted at UKZN

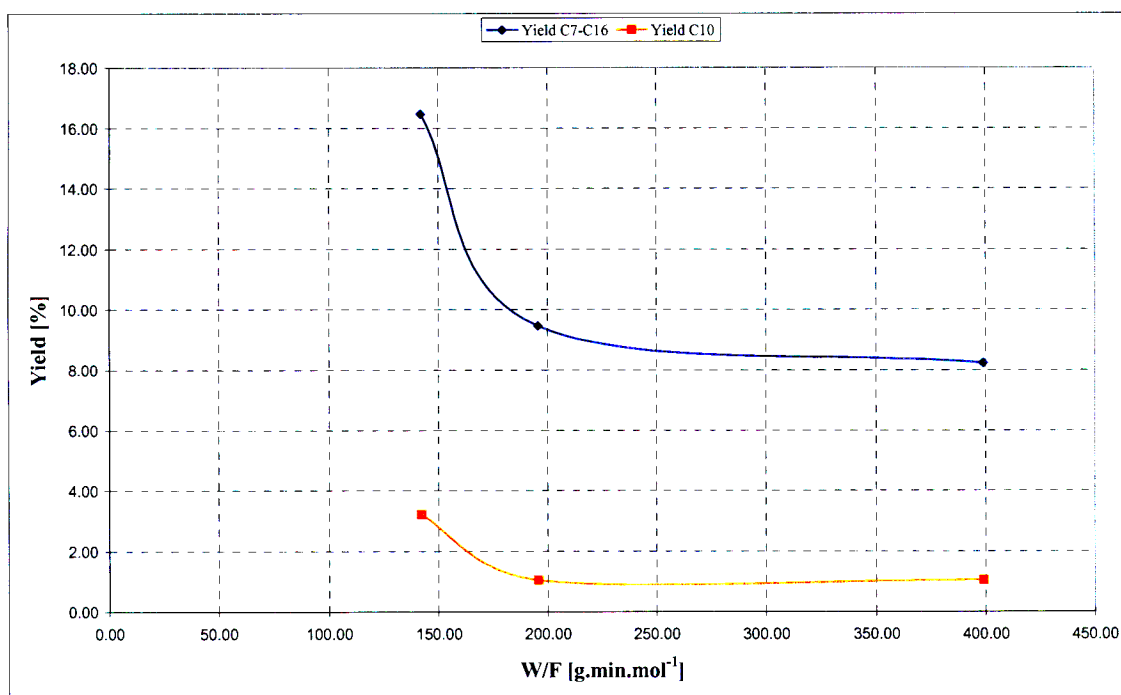


Figure 6.32 Yield versus space time – Run 7 (420°C, 29% feed composition, $W/F = 142\text{g.min.mol}^{-1}$ to 398g.min.mol^{-1}) – experiments conducted at UKZN

A thin layer of visible coke was found on the surface of the catalyst and on the inner walls of the reactor tube after run 7 (at 29% feed composition). The surface did not have a metallic black/blue appearance (Figure 6.33). The black deposit was removed and inspected (Figure 6.34) and it was concluded that it was probably a form of coke produced from cracking reaction intermediates.

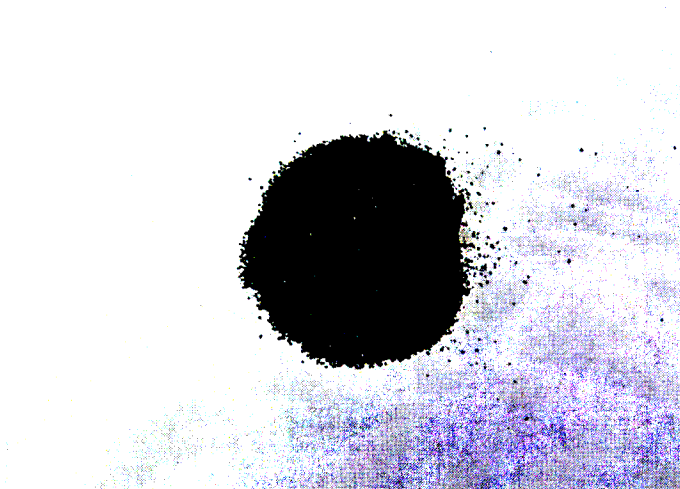


Figure 6.33 Spent WO_3/SiO_2 catalyst – run 7

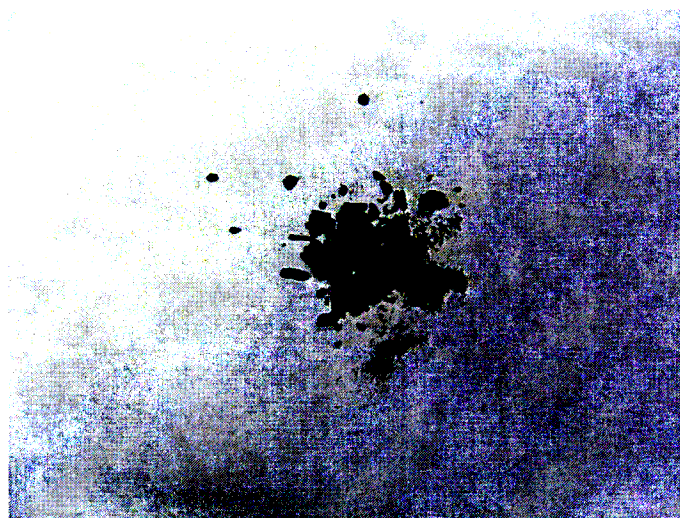


Figure 6.34 Black deposit removed from inside the reactor tube after run 7

At 380°C , 95% feed composition and between $200\text{g}\cdot\text{min}\cdot\text{mol}^{-1}$ and $400\text{g}\cdot\text{min}\cdot\text{mol}^{-1}$, a conversion between 4.3% and 10.6% was obtained. The plot of conversion versus space time (Figure 6.35) produced a straight line, indicating a constant rate for the reaction conditions that were employed and therefore it was concluded that there was no appreciable external mass transfer

resistance at the flow-rates that were used for the optimization study. The selectivity towards decene was 28% at 380°C, 95% feed composition and 403g.min.mol⁻¹, which was significantly greater than the values achieved in all other experiments.

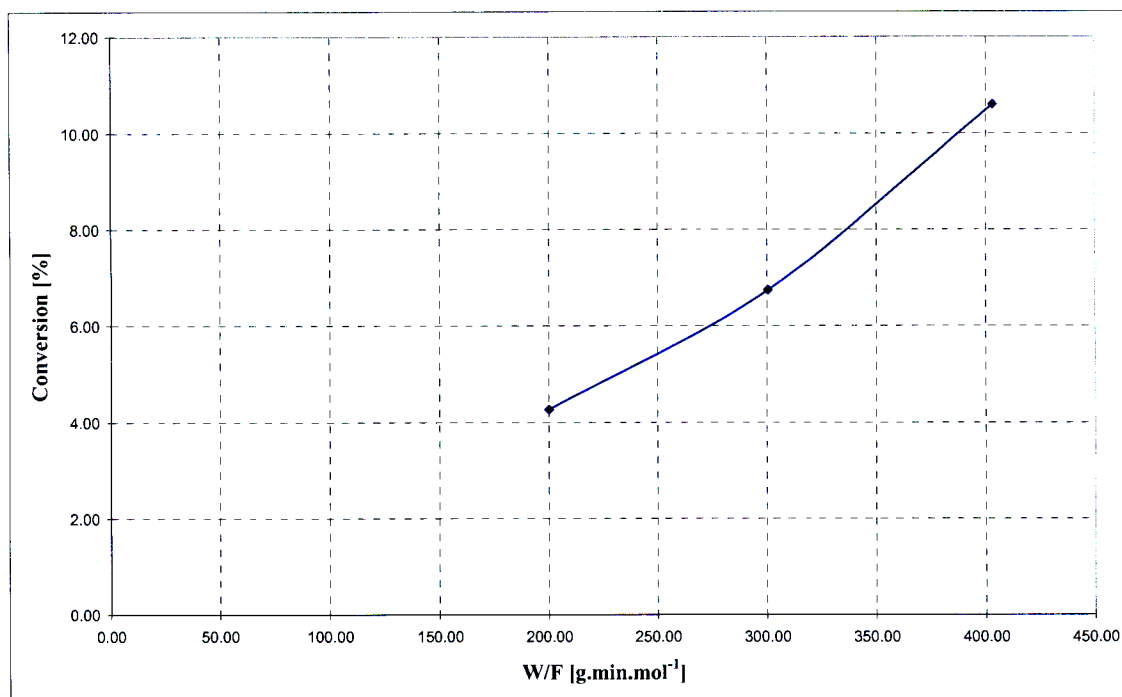


Figure 6.35 Conversion versus space time – Run 11 (380°C, 95% feed composition, $W/F = 200\text{g.min.mol}^{-1}$ to 400g.min.mol^{-1}) – experiments conducted at UKZN

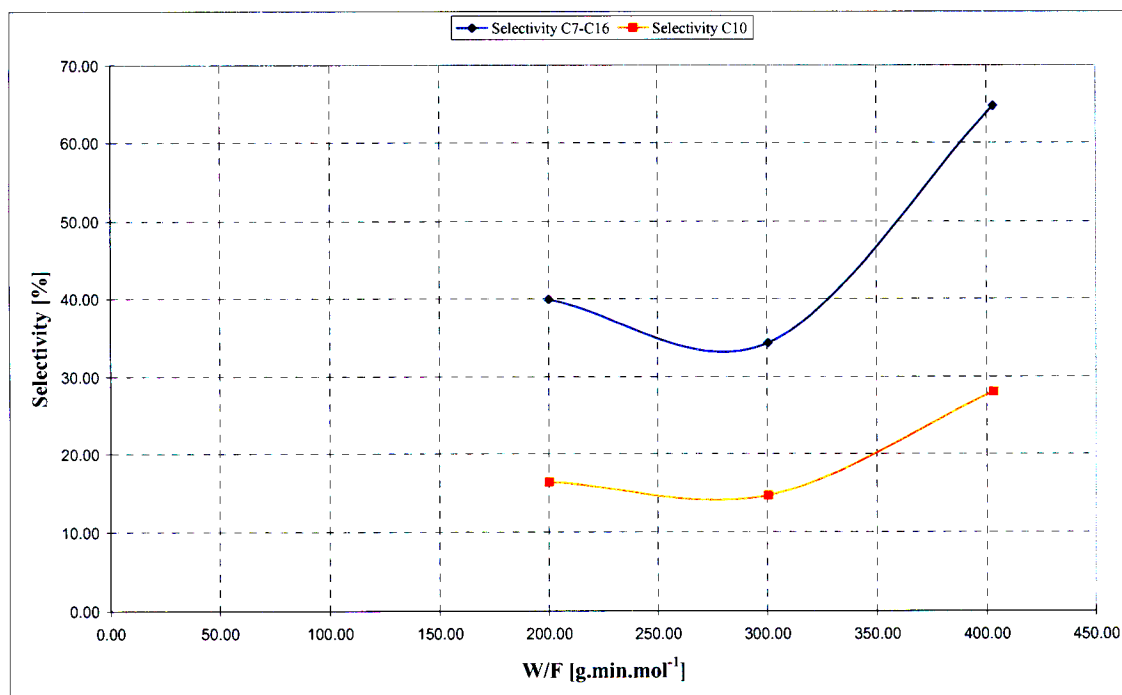


Figure 6.36 Selectivity versus space time – Run 11 (380°C, 95% feed composition, $W/F = 200\text{g.min.mol}^{-1}$ to 400g.min.mol^{-1}) – experiments conducted at UKZN

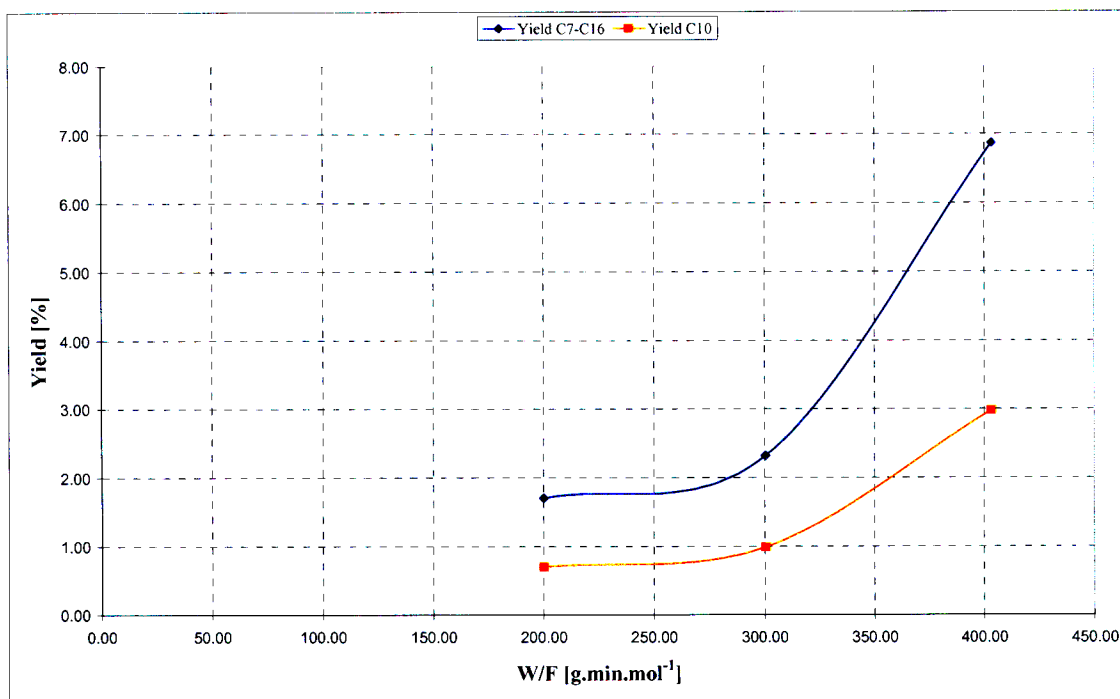


Figure 6.37 Yield versus space time – Run 11 (380°C, 95% feed composition, $W/F = 200\text{g.min.mol}^{-1}$ to 400g.min.mol^{-1}) – experiments conducted at UKZN

6.3.4 Results of the tests for intraparticle mass transfer resistance

In the test for intraparticle mass transfer resistance effects, different catalyst particle sizes were employed at identical operating conditions and the conversion levels were monitored for changes. The first particle size under consideration was taken from the bulk batch of WO_3/SiO_2 catalyst that was obtained from Sasol (catalyst B). The catalyst was prepared using Davisil grade 646 silica gel (35 – 60 mesh) which was in the size range of $250\mu\text{m} - 500\mu\text{m}$. The second particle size was prepared from this batch by crushing and grinding using a pestle and mortar. The average particle size for the larger particles was estimated using the image analysis software discussed in section 5.4.1 and via laser diffraction. The average particle size obtained from the image analysis was $390\mu\text{m}$, which was lower than the $460\mu\text{m}$ obtained using the laser diffraction procedure (Appendix D). For the crushed sample, only laser diffraction analysis was carried out since it was almost impossible to obtain a satisfactory image of the sample for image analysis, mainly due to overlapping of the particles. The size distribution was much broader for the crushed sample than for the freshly prepared Sasol catalyst (Appendix D). The average particle size for this sample was $123\mu\text{m}$. The results for run 1 and run 10 (large and small particle sizes, respectively) are presented in Figures 6.38 to 6.40 and Table 6.17. At 460°C , 95% feed composition and 330g.min.mol^{-1} , the average conversion over the 6 hour period was

65% for both particle sizes. The average selectivity and yield of decene was also the same for both sizes, at 6% and 4%, respectively.

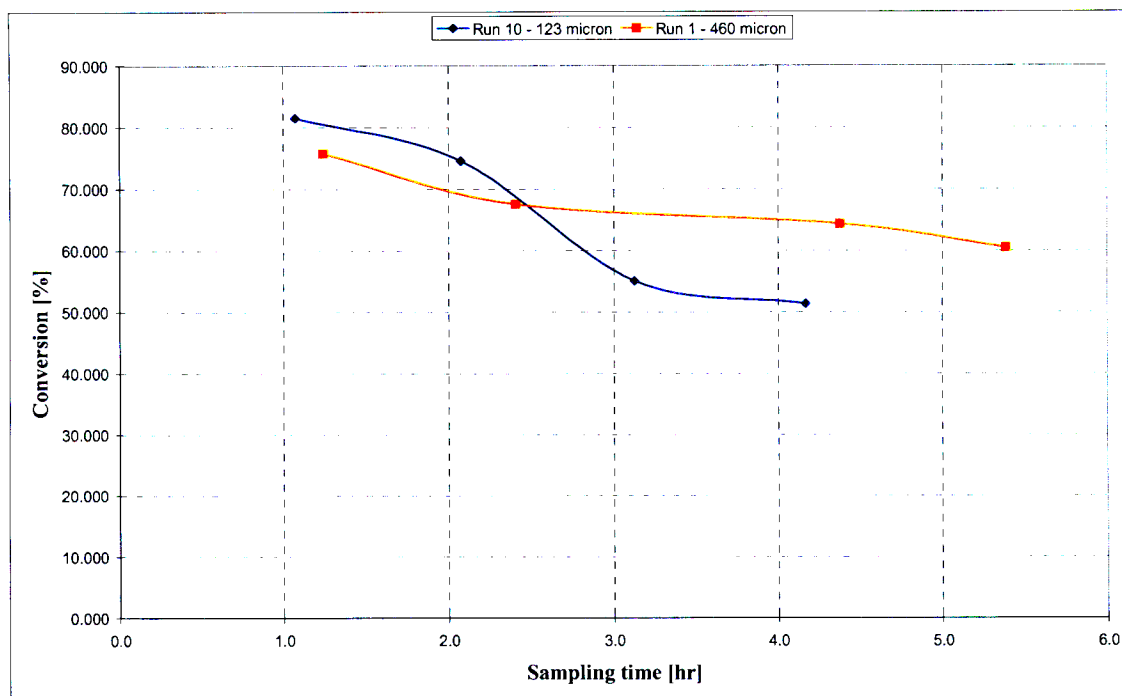


Figure 6.38 Conversion versus sampling time – run 1 and run 10 (460°C, 95% feed composition and $W/F = 330\text{g.min.mol}^{-1}$) – experiments conducted at UKZN

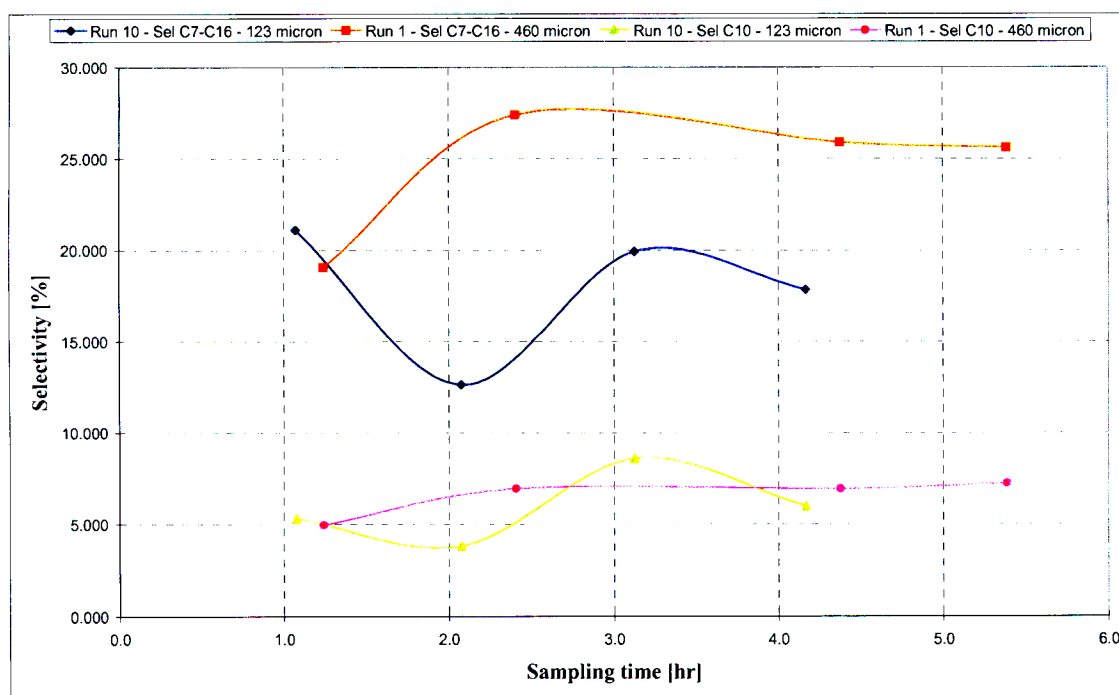


Figure 6.39 Selectivity versus sampling time – run 1 and run 10 (460°C, 95% feed composition and $W/F = 330\text{g.min.mol}^{-1}$) – experiments conducted at UKZN

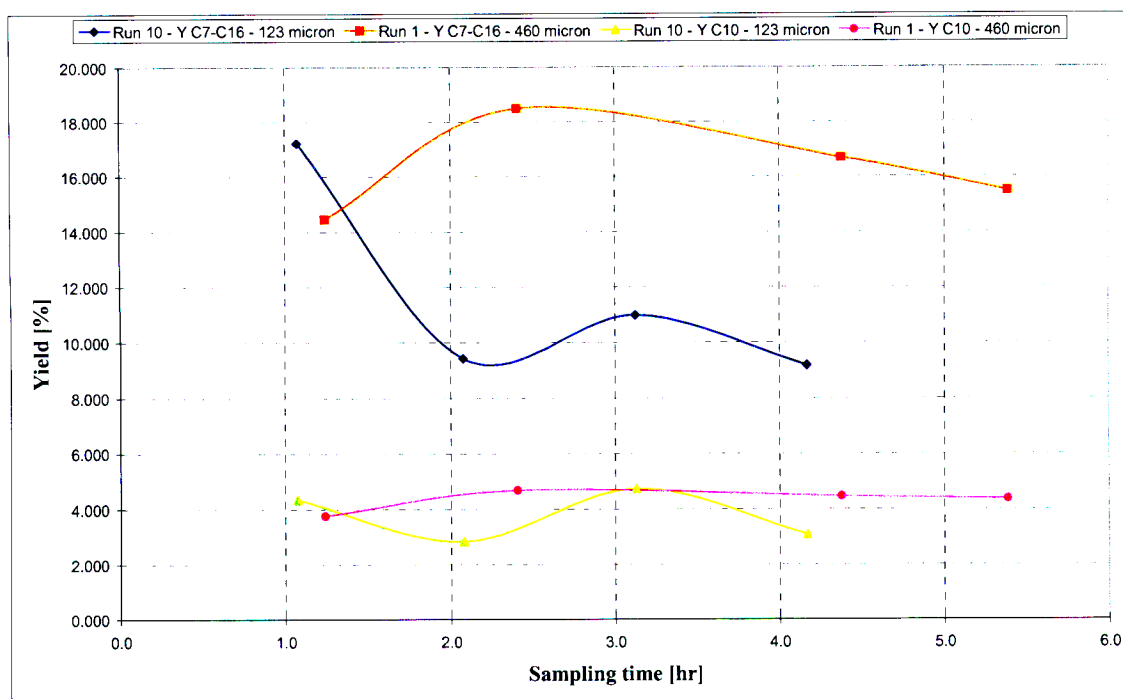


Figure 6.40 Yield versus sampling time –run 1 and run 10 (460°C, 95% feed composition and $W/F = 330 \text{ g.min.mol}^{-1}$) – experiments conducted at UKZN

Run No.	Temp [°C]	Feed composition [mol % 1-hexene]	W/F [g.min.mol ⁻¹]	X [%]	Sel C ₇ -C ₁₆ [%]	Sel C ₁₀ [%]	Y C ₇ -C ₁₆ [%]	Y C ₁₀ [%]	Sampling time [hr]
R10-01	460	94.61	330	81.52	21.12	5.30	17.22	4.32	1.07
R10-02	460	94.61	330	74.58	12.64	3.79	9.42	2.83	2.07
R10-03	460	94.61	330	55.10	19.93	8.56	10.98	4.72	3.12
R10-04	460	94.61	330	51.39	17.85	5.97	9.17	3.07	4.16

Table 6.17 Experimental results for run 10 – 123µm particles (460°C, 95% feed composition and $W/F = 330 \text{ g.min.mol}^{-1}$)

The reaction was not limited by intraparticle mass transfer resistance effects for the catalyst size range that was employed, possibly due to the high operating temperature and the fact that the active sites for metathesis are located near the mouths of the pores of the catalyst, thereby reducing the need for extensive mass transfer within the particle (van Schalkwyk et al., 2003 a). During the operation of the rig using the smaller catalyst pellets, the observed pressure drop

over the bed was 35 times greater (1bar) than when operating using the normal sized catalyst pellets (0.03bar).

6.3.5 Results of the experiments conducted to compare the performance of the two different WO_3/SiO_2 catalysts used for the investigation

In order to link the results that were obtained for catalyst A (Polish program) with the results for catalyst B (optimization study), experiments were performed at identical conditions for each catalyst and conversion levels, selectivity's and yields were compared (Figures 6.41 to 6.43 and Table 6.18). At 460°C, 95% feed composition and 336g.min.mol^{-1} the 1-hexene conversion, selectivity and yield of decene was 60.5%, 7.2% and 4.4% respectively for catalyst B. At 460°C, 95% feed composition and 334g.min.mol^{-1} the 1-hexene conversion, selectivity and yield of decene was 43.3%, 21.8% and 9.4% respectively for catalyst A. BET surface analysis of the two catalysts revealed that the specific surface area of catalyst A was $181\text{m}^2.\text{g}^{-1}$ and for catalyst B was $275.7\text{m}^2.\text{g}^{-1}$. For the same mass of each catalyst, and with both assumed to contain 8wt% WO_3 , catalyst A had a better dispersed active phase and a smaller number of strong acid sites than catalyst B, thus limiting the extent of side reactions such as cracking and isomerization. This could be the reason why catalyst A appeared to behave so much differently from catalyst B, producing a significantly greater yield of decene.

Run No.	Temp [°C]	Feed composition [mol % 1-hexene]	W/F [g.min.mol ⁻¹]	X [%]	Sel C ₇ -C ₁₆ [%]	Sel C ₁₀ [%]	Y C ₇ -C ₁₆ [%]	Y C ₁₀ [%]	Sampling time [hr]
R9-01	460	95.99	335	65.65	19.60	6.74	12.87	4.42	1.02
R9-02	460	95.99	335	41.86	39.57	22.62	16.56	9.47	2.12
R9-03	460	95.99	335	45.30	40.27	21.71	18.24	9.83	3.12
R9-04	460	95.99	335	43.34	38.61	21.78	16.73	9.44	4.12

Table 6.18 Experimental results for run 9 – catalyst A (460°C, 95% feed composition and $W/F = 335\text{g.min.mol}^{-1}$)

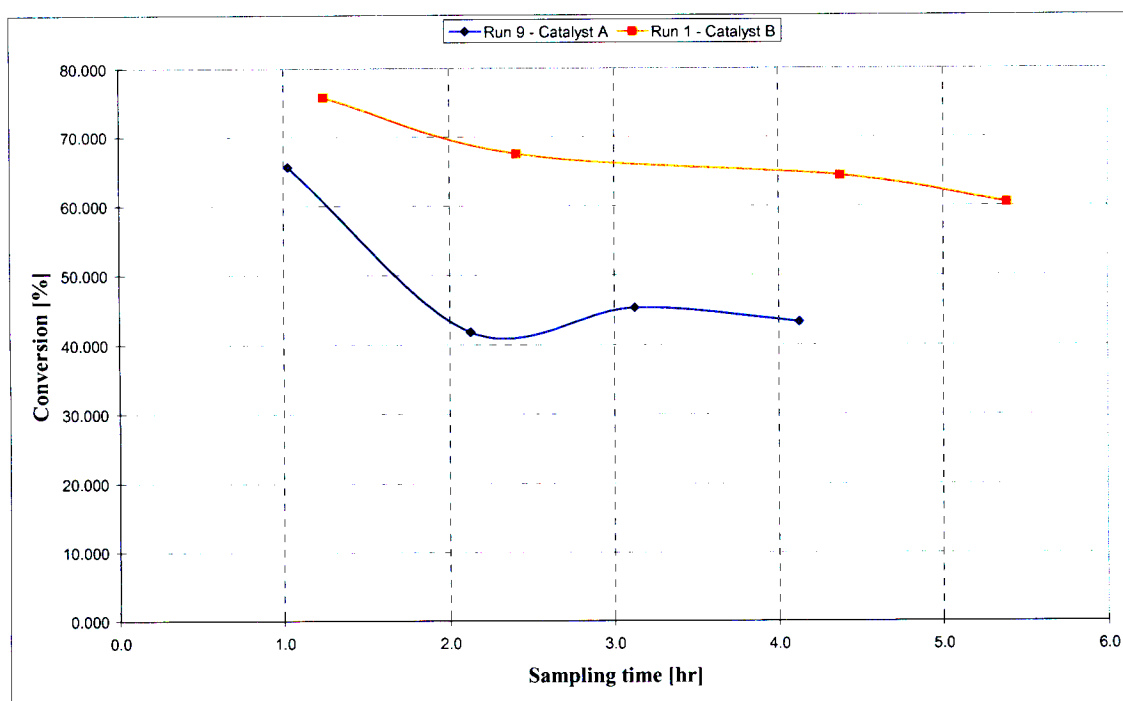


Figure 6.41 Conversion versus sampling time – run 1 and run 9 (460°C, 95% feed composition and $W/F = 335\text{g}\cdot\text{min}\cdot\text{mol}^{-1}$) – experiments conducted at UKZN

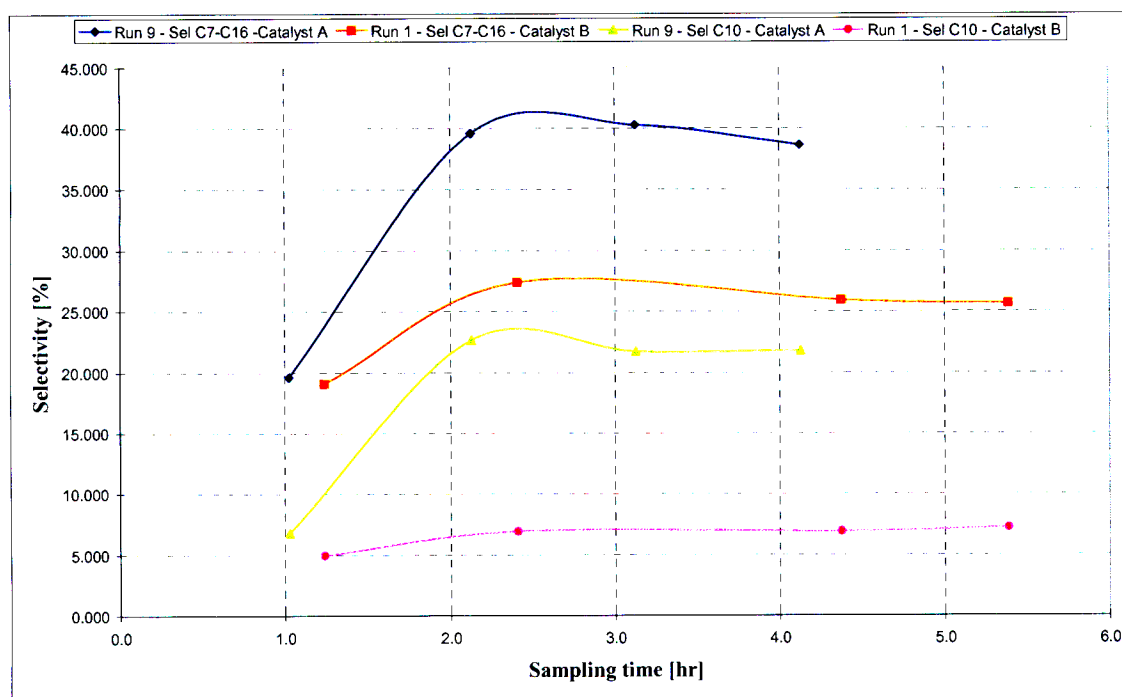


Figure 6.42 Selectivity versus sampling time – run 1 and run 9 (460°C, 95% feed composition and $W/F = 335\text{g}\cdot\text{min}\cdot\text{mol}^{-1}$) – experiments conducted at UKZN

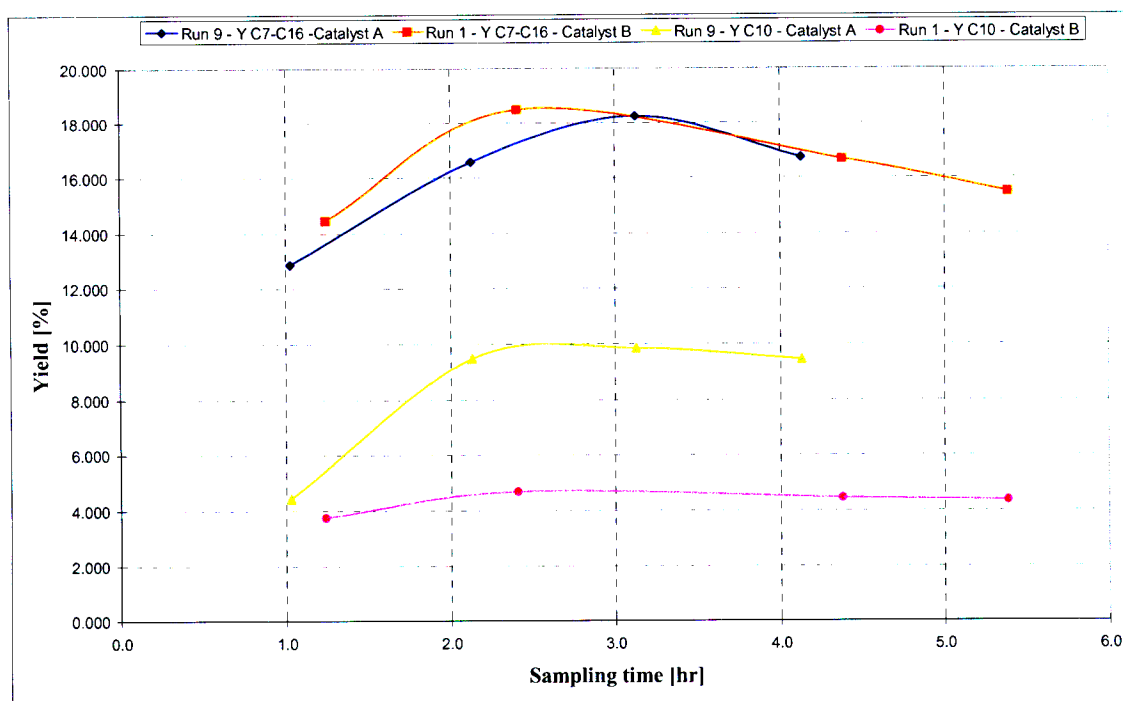


Figure 6.43 Yield versus sampling time – run 1 and run 9 (460°C, 95% feed composition and $W/F = 335 \text{ g} \cdot \text{min} \cdot \text{mol}^{-1}$) – experiments conducted at UKZN

6.3.6 Results of the final experiments conducted to test the optimized region of operating conditions

After taking the results of the experimental tests for transport effects into consideration, it was clear that the lowest practicable temperature should be employed in order to maximize the yield of decene. The same is not true of the feed gas composition. At moderate feed compositions (50% - 70%) relatively high yields of decene were obtained. At very low compositions (< 30%), increased rates of cracking were observed, resulting in excessive amounts of lighter olefins (ethylene and propylene) and coke. In the experimental range that was considered, higher values of space time resulted in improved yields of decene. It was concluded that lower operating temperatures, moderate feed compositions (above 50%) and higher space times should be employed in order to maximize the yield of decene. Two final experiments were conducted to test the validity of this conclusion. A temperature of 380°C was chosen, based on the results of run 11. The experiments were also conducted at the highest values of space time attainable on the reactor rig, in order to test the practical limits of the set-up. At 380°C, 100% feed composition and $3200 \text{ g} \cdot \text{min} \cdot \text{mol}^{-1}$, the yield of decene was 5.1%. This was higher than what was achieved in all other experiments (for catalyst B), but did not represent a significant improvement. At 380°C, 55% feed composition and $2875 \text{ g} \cdot \text{min} \cdot \text{mol}^{-1}$, the yield of decene was

12.8%. This final result was almost three times greater than the previous highest yield and did represent a significant improvement. It was concluded that the results of the factorial experimental design were correct in predicting the region of operating conditions that were most conducive to the production of decene via the metathesis of 1-hexene over WO_3/SiO_2 .

The mass balance consistency for each of the experiments in the optimization study was checked using the methods discussed in section 6.2. The results of the calculations are presented in Table 6.19 and Figure 6.44. There was a random scatter of the carbon balance consistency data. For the extended runs, large errors were reported for the experimental data collected during the first hour of operation but this has been ascribed to the fact that the reaction temperature was unstable during this period. The carbon balance consistency was generally within 10% error (absolute). This value again compares favourably with the 10% mass balance error reported in a Sasol patent publication, for a similar study of alkene metathesis (van Schalkwyk et al., 2004).

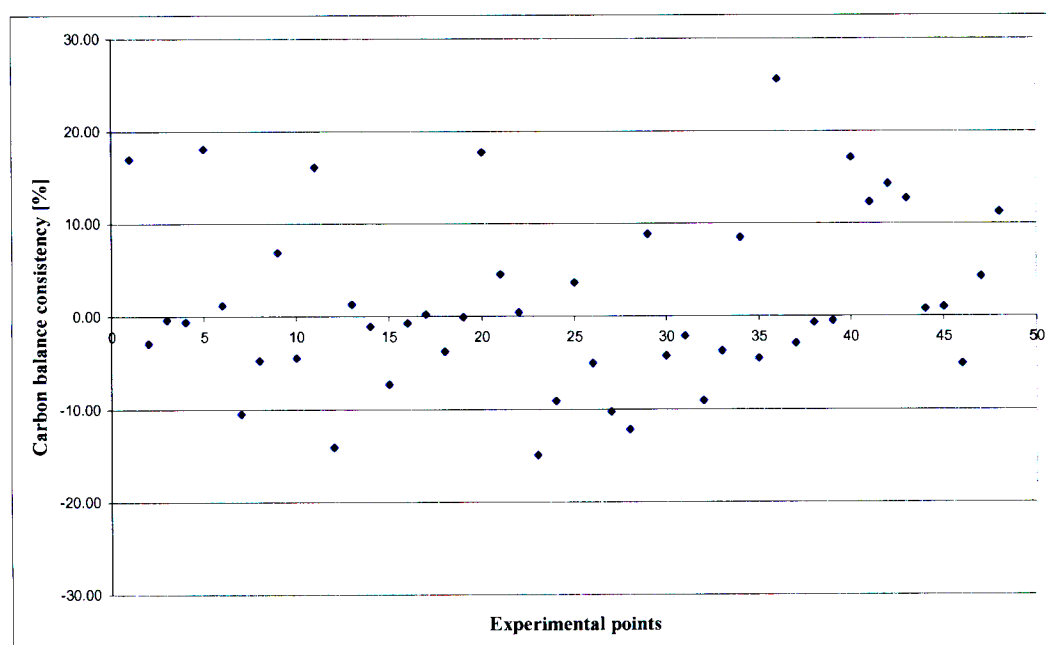


Figure 6.44 Carbon balance consistency plot for the experiments conducted at UKZN

Run No.	Temp [°C]	Feed composition [mol % 1-hexene]	W/F [g.min.mol ⁻¹]	Carbon balance consistency [%]
R1-01	460	96.41	336	16.95
R1-02	460	96.41	336	-2.93
R1-04	460	96.41	336	-0.39
R1-05	460	96.41	336	-0.59
R2-01	460	95.83	334	18.08
R2-02	460	95.83	334	1.19
R2-03	460	95.83	334	-10.45
R2-04	460	95.83	334	-4.73
R2-05	460	95.83	334	6.90
R2-06	460	95.83	334	-4.46
R3-01	460	95.89	334	16.09
R3-02	460	95.89	334	-14.03
R3-03	460	95.89	334	1.32
R3-04	460	95.89	334	-1.08
R3-05	460	95.89	334	-7.30
R3-06	460	95.89	334	-0.70
R4-01	420	63.62	1413	0.23
R4-02	420	54.70	646	-3.78
R4-03	420	54.81	221	-0.06
R5-01	480	54.83	221	17.71
R5-02	500	62.44	1405	4.55
R5-03	460	100.00	869	0.41
R5-04	460	74.53	648	-14.92
R5-05	500	54.36	220	-9.08
R6-01	420	88.94	221	3.67
R6-02	420	90.85	670	-5.05
R6-03	500	90.76	669	-10.22
R6-04	500	89.36	222	-12.16
R7-01	420	27.98	393	8.84
R7-04	420	28.42	399	-4.27
R7-02	420	28.92	196	-2.14
R7-03	420	28.80	142	-9.05
R8-01	420	51.59	661	-3.72
R8-02	460	76.28	403	8.53
R8-03	500	54.49	698	-4.51
R9-01	460	95.99	335	25.67
R9-02	460	95.99	335	-2.93
R9-03	460	95.99	335	-0.67
R9-04	460	95.99	335	-0.49
R10-01	460	94.61	330	17.11
R10-02	460	94.61	330	12.28
R10-03	460	94.61	330	14.26
R10-04	460	94.61	330	12.69
R11-01	380	94.52	200	0.79
R11-02	380	94.09	300	1.00
R11-03	380	94.99	403	-5.07
R12-01	380	100.00	3200	4.34
R13-01	380	55.14	2874	11.24

Table 6.19 Carbon balance consistency data for the experiments conducted at UKZN

Chapter

7

Conclusions and recommendations

The performance of an 8wt% WO_3/SiO_2 metathesis catalyst was investigated for the metathesis of 1-hexene in a laboratory-scale, gas-phase fixed bed tubular reactor. An improved yield of decene (4.37%) was obtained after high temperature oxidative pre-treatment of the catalyst followed by a short period under hydrogen and a nitrogen purge, compared to 4.21%, achieved after a conventional 18 hour N_2 pre-treatment. The conversion level, selectivity and yield of decene (1.45%) dropped appreciably after pre-treatment under hydrogen and nitrogen only. Over-reduction of the tungsten metal centres and the formation of an inactive non-stoichiometric surface phase have been suggested as possible causes for this last result. A combined pre-treatment sequence of 6 hours under air, 1 ½ hours under hydrogen and 18 hours under nitrogen was retained for all subsequent experiments. From a three variable, two level full factorial experimental design it was concluded that lower operating temperatures and feed gas compositions and higher values of space time should be employed in order to maximize the yield of decene. It is unlikely that a temperature much lower than 380°C can be used since very high values of space time have to be employed in this temperature range to keep conversions at acceptable levels (>50%). At very high (>90%) and very low (<30%) feed gas compositions, the selectivity and yield of decene dropped appreciably. At low compositions in particular, cracking reactions appeared to dominate, resulting in excessive amounts of ethylene and propylene in the product gas and the formation of high levels of coke. The optimum feed composition probably lies between 50% and 70% 1-hexene. For the range of space time and particle sizes that were employed in the tests for transport resistance effects, no significant

external or intra-particle mass transfer resistances were observed. To test the results of the optimization study a run was performed at 380°C, 55% feed composition and 2874g.min.mol⁻¹ (10 times the average space time employed for all prior experiments). A decene yield of 12.8% was obtained, which was three times the average yield obtained from previous experiments. At these conditions, a much higher yield of decene was expected, based on the high selectivity obtained in other experiments conducted at 380°C and at lower values of space time. An optimum value of space time may exist, for the low temperature/low feed composition combination, between 600g.min.mol⁻¹ and 3000g.min.mol⁻¹. It is well known that for parallel reactions conducted under isothermal conditions, the selectivity towards the primary product is reduced by the existence of external mass transfer resistance (Smith, 1981). At very low feed flow-rates, attenuated mass transfer effects and a drop in selectivity may account for the lower than expected yield of decene at extremely high values of space time. The 12.8% yield of decene obtained in this final experiment is significantly better than the 4.9% yield of tetradecene (the primary metathesis product) obtained by Sasol for the metathesis of 1-octene in a once-through fixed bed reactor at 460°C, 5.6h⁻¹ LHSV and for 300µm WO₃/SiO₂ catalyst particles (van Schalkwyk et al., 2003 a). The optimization study may be extended for feed composition and space time (at a fixed operating temperature of 380°C) by implementing a simplex search in two-dimensional space with the target function being the yield of decene. The starting point for the simplex search can be the last experimental point considered in this work (12.8% yield of decene). The results of run 11, at 380°C, 95% feed composition and 403g.min.mol⁻¹, suggest a different approach. The selectivity to higher olefins and decene was 65% and 28% respectively, with the low conversion resulting in a low decene yield of 3%. These selectivities are, however, greater than the values reported by van Schalkwyk et al. (2003 a) for primary metathesis and higher olefin products for the metathesis of 1-octene in a once-through fixed bed reactor at 460°C and 16h⁻¹ LHSV. In that study a selectivity of 30% towards C₁₁ – C₁₄ olefins was reported. Since the highest yield of decene was obtained in this work at a very low feed flow-rate of 1-hexene, the once through fixed bed reactor is certainly not the best configuration for the metathesis of 1-hexene over WO₃/SiO₂. Operating the reactor at the conditions of run 11, but with a recycle of the 1-hexene in the product stream, may significantly improve the overall yield of decene. At optimized conditions of 420°C, 22h⁻¹ LHSV and a recycle ratio of 4, a dodecene (primary metathesis product) yield of 40% was obtained in a recycle reactor for the metathesis of 1-heptene over WO₃/SiO₂ (van Schalkwyk et al., 2003 a). The results of this optimization study indicate that a better yield of primary products may possibly be obtained for the metathesis of 1-hexene at similar conditions. Further laboratory-scale work should be carried out in order to assess the commercial viability of this option.

References

1. Aguado, J., Escola, J.M, Castro, M.C. and Paredes, B., "Metathesis of 1-hexene over rhenium oxide supported on ordered mesoporous aluminas: comparison with $\text{Re}_2\text{O}_7/\gamma\text{-Al}_2\text{O}_3$ ", *Applied Catalysis A: General* **284** (2005) 47 - 57
2. Anderson, J.R. and Pratt, K.C., "Introduction to characterization and testing of catalysts", Academic Press, Sydney, 1985
3. Antony, J., "Design of experiments for engineers and scientists", Elsevier, Amsterdam, 2003
4. Aso, I., Nakao, M., Yamazoe, N. and Seiyama, T., "Study of metal oxide catalysts in the olefin oxidation from their reduction behaviour - I. Reduction of various metal oxides with propylene", *Journal of Catalysis* **57** (1979) 287 - 295
5. Banks, R.L. and Bailey, G.C., "Olefin disproportionation - a new catalytic process", *Industrial and Engineering Chemistry Product Research and Development* **3** No. 3 (1964) 170 - 173
6. Bartholomew, C.H., "Mechanisms of catalyst deactivation", *Applied Catalysts A: General* **212** (2001) 17 - 60
7. Barton, D.G., Soled, S.L. and Iglesia, E., "Solid acid catalysts based on supported tungsten oxides", *Topics in Catalysis* **6** (1998) 87 - 99
8. Basrur, A.G., Patwardhan, S.R. and Vyas, S.N., "Propene metathesis over silica-supported tungsten oxide catalyst - catalyst induction mechanism", *Journal of Catalysis* **127** (1991) 86 - 95
9. Beens, J., Boelens, H., Tijssen, R. and Blomberg, J., "Quantitative aspects of comprehensive two-dimensional gas chromatography (GC x GC)", *Journal of High Resolution Chromatography* **21** (1998) 47 - 54
10. Bernholc, J., Horsley, J.A., Murrell, L.L., Sherman, L.G. and Soled, S., "Brønsted acid sites in transition metal oxide catalysts: Modelling of structure, acid strengths and support effects", *Journal of Physical Chemistry* **91** (1987) 1526 - 1530
11. Berty, J.M., "Experiments in catalytic reaction engineering", Elsevier, Amsterdam, 1999
12. Berty, J.M., "Testing commercial catalysts in recycle reactors", *Catalysis Reviews: Science and Engineering* **20** No. 1 (1979) 75 - 96
13. Carberry, J.J., "Designing laboratory catalytic reactors", *Industrial and Engineering Chemistry* **56** No. 11 (1964) 39 - 46
14. Chorkendorff, I. and Neimantsverdriet, J.W., "Concepts of modern catalysis and kinetics", Wiley-VCH, Weinheim, 2003

15. Crynes, B.L., "AIChE modular instruction – Kinetics: Heterogeneous catalysis", AIChE, New York, 1982
16. Cuadros-Rodríguez, L., Bagur-González, M.G., Sánchez-Viñas, M., González-Casado, A. and Gómez-Sáez, A.M., "Principles of analytical calibration/quantification for the separation sciences", *Journal of Chromatography A* **1158** (2007) 33 - 46
17. El - Sawi, M., Iannibello, A., Morelli, F., Catalano, G., Intrieri, F. and Giorandano, G., "A kinetic study of the metathesis of propene on a rhenium - aluminium catalyst", *Journal of Chemical Technology and Biotechnology* **31** (1981), 388 - 394
18. Fogler, H.S., "Elements of chemical reaction engineering", 3rd Edition, Prentice Hall, New Jersey, 1999
19. Fuller, E.N., Schettler, P.D. and Giddings, J.C., "New method for prediction of binary gas-phase diffusion coefficient", *Industrial and Engineering Chemistry* **58** No. 5 (1966) 18-27
20. Gangwal, S.K., Fathi-kalajahi, J. and Wills, G.B., "Break-in behaviour of a tungsten oxide on silica catalyst in propylene disproportionation", *Industrial and Engineering Chemistry Product Research and Development* **16** No. 3 (1977) 237 - 241
21. Gartside, R.J., Greene, M.I., Khonsari, A.M. and Murrell, L.L., International patent WO 02/100535 A1 (2002)
22. Gayubo, A.G., Arandes, J.M., Aguayo, A.T., Olazar, M. and Bilbao, J., "Deactivation and acidity deterioration of a $\text{SiO}_2/\text{Al}_2\text{O}_3$ catalyst in the isomerization of cis-butene", *Industrial and Engineering Chemistry Research* **32** (1993) 588 - 593
23. Gomes, V.G. and Fuller, O.M., "Dynamics of propene metathesis: physisorption and diffusion in heterogeneous catalysis", *AIChE Journal* **42** No. 1 (1996) 204 - 213
24. Grubbs, R.H., "Olefin metathesis", *Tetrahedron* **60** (2004) 7117 - 7140
25. Grubbs, R.H., Carr, D.D., Hoppin, C. and Burk, P.L., "Consideration of the mechanism of the metal catalyzed olefin metathesis reaction", *Journal of the American Chemical Society* **98** No. 12 (1976) 3478 - 3483
26. Guisnet, M. and Magnoux, P., "Organic chemistry of coke formation", *Applied Catalysis A: General* **212** (2001) 83 - 96
27. Hagen, J., "Industrial catalysis - A practical approach", Wiley-VCH, Weinheim, 1999
28. Hattikudur, U.R. and Thodos, G., "Reaction kinetics of the disproportionation of propylene over a tungsten oxide-silica catalyst", in "Chemical Reaction Engineering II", pp. 80-95, Academic Press, New York, 1975
29. Hérisson, J.L. and Chauvin, Y., "Catalysis of transformation of olefins by tungsten complexes", *Makromolekulare Chemie* **141** (1970) 161
30. Horsley, J.A., Wachs, I.E., Brown, J.M., Via, G.H. and Hardcastle F.D., "Structure of surface tungsten oxide species in the $\text{WO}_3/\text{Al}_2\text{O}_3$ supported oxide system from x-ray

- adsorption near-edge spectroscopy and Raman spectroscopy”, *Journal of Physical Chemistry* **91** (1987) 4014 - 4020
31. Huang, S., Chen, F., Liu, S., Zhu, Q., Zhu, X., Xin, W., Feng, Z., Li, C., Wang, Q. and Xu, L., “The influence of preparation procedures and tungsten loading on the metathesis activity of ethene and 2-butene over supported WO_3 catalysts”, *Journal of Molecular Catalysis A: Chemical* **267** (2007) 224 - 233
32. Huang, S., Liu, S., Zhu, Q., Zhu, X., Xin, W., Liu, H., Feng, Z., Li, C., Xie, S., Wang, Q. and Xu, L., “The effect of calcination time on the activity of $\text{WO}_3/\text{Al}_2\text{O}_3/\text{HY}$ catalysts for the metathesis reaction between ethene and 2-butene”, *Applied Catalysis A: General* **323** (2007) 94 - 103
33. Incropera, F.P. and de Witt, D.P., “Fundamentals of heat and mass transfer”, 3rd Edition, Wiley, New York, 1990
34. Kapteijn, F. and Mol, J.C., “Stereochemistry in metathesis of n-alkenes using heterogeneous oxide catalysts”, *Journal of the Chemical Society, Faraday Transactions* **78** No. 1 (1982) 2583 - 2592
35. Kapteijn, F., Bredt, H.L.G., Homsburg, E. and Mol, J.C., “Kinetics of the metathesis of propene over $\text{Re}_2\text{O}_7/\gamma\text{-Al}_2\text{O}_3$ ”, *Industrial and Engineering Chemistry Product Research and Development* **20** No. 3 (1981) 457 - 466
36. Krasnov, V.I., Musaev, K.M. and Atlas, V.V., “Computer - aided analysis of kinetic models for hexene - 1 metathesis reaction”, *Doklady Akademii Nauk Azerbaidzhanskoi SSR* **42** 2 (1986) 33 - 37 (in Russian)
37. Lievenspiel, O., “Chemical reaction engineering”, 3rd Edition, Wiley, New York, 1998
38. Logie, V., Maire, G., Michel, D. and Vignes J.L., “Skeletal isomerization of hexenes on tungsten oxide supported on porous α -Alumina”, *Journal of Catalysis* **188** (1999) 90 – 101
39. Luckner, R.C. and Wills, G.B., “Transient kinetics of the disproportionation of propene over a tungsten oxide on silica catalyst”, *Journal of Catalysis* **28** (1973) 83 - 91
40. Matisova, E., “Quantitative analysis of aromatic hydrocarbons in complex hydrocarbon mixtures by high resolution capillary gas chromatography”, *Chemicke Listy* **92** (1998) 870 – 874
41. Missen, R.W., Mims, C.A. and Saville, B.A., “Chemical reaction engineering and kinetics”, Wiley, New York, 1999
42. Mol, J.C., “Industrial applications of olefin metathesis”, *Journal of Molecular Catalysis A: Chemical* **213** (2004) 39 - 45
43. Mol, J.C., “Olefin metathesis over supported rhenium oxide catalysts”, *Catalysis Today* **51** (1999) 289 - 299

44. Moodley, D.J., van Schalkwyk, C., Spamer, A., Botha, J.M. and Datye, A.K., "Coke formation on WO₃/SiO₂ metathesis catalysts", *Applied Catalysis A: General* **318** (2007) 155 – 159
45. Oakley, G.W., "Solid-state olefin metathesis", PhD Thesis – University of Florida, 2004
46. Raal, J.D. and Mühlbauer, A.L., "Phase equilibria - measurement and computation", Taylor and Francis, Washington, 1998
47. Ramani, N.C., Sullivan, D.L. and Ekerdt, J.G., "Isomerization of 1-butene over silica-supported Mo(VI), W(VI) and Cr(VI)", *Journal of Catalysis* **173** (1998) 105 - 114
48. Rodríguez-Ramos, I., Guerrero-Ruiz, A., Homs, N., Ramírez de la Piscina, P. and Fierro, J.L.G., "Reactions of propene on supported molybdenum and tungsten oxides", *Journal of Molecular Catalysis A: Chemical* **95** (1995) 147 - 154
49. Rouhi, M., "Olefin metathesis: big-deal reaction", *Chemical and Engineering News* **80** No. 51 (2002) 29 - 33
50. Rouhi, M., "Olefin metathesis: the early days", *Chemical and Engineering News* **80** No. 51 (2002) 34 – 38
51. Satterfield, C.N., "Heterogeneous catalysis in industrial practice", 2nd Edition, McGraw-Hill, New York, 1991
52. Seader, J.D. and Henley, E.J., "Separation process principles", Wiley, New Jersey, 1998
53. Schell, D.J., Farmer, J., Newman, M. and McMillan, D., "Dilute sulphuric acid pretreatment of corn stover in pilot-scale reactor", *Applied Biochemistry and Biotechnology* **105** No. 1-3 (2003) 69-85
54. Spamer, A., Dube, T.I., Moodley, D.J., van Schalkwyk, C. and Botha, J.M., "The reduction of isomerization activity on a WO₃/SiO₂ metathesis catalyst", *Applied Catalysis A: General* **225** (2003) 153 – 167
55. Smith, J.C., "Chemical engineering kinetics", 2nd edition, McGraw-Hill, Auckland, 1981
56. Spronk, R., Dekker, F.H.M. and Mol, J.C., "Metathesis of 1-alkenes in the liquid phase over a Re₂O₇/γ-Al₂O₃ catalyst - I. Reactivity of the alkenes", *Applied Catalysis* **70** (1991) 295 - 306
57. Spronk, R., Dekker, F.H.M. and Mol, J.C., "Metathesis of 1-alkenes in the liquid phase over a Re₂O₇/γ-Al₂O₃ catalyst - II. Kinetics of deactivation", *Applied Catalysis A: General* **83** (1992) 213 - 233
58. Tarasov, A.L., Shelimov, B.N., Kazansky, V.B. and Mol, J.C., "Olefin metathesis on supported rhenium catalysts activated by γ-irradiation", *Journal of Molecular Catalysis A: Chemical* **115** (1997) 219 - 228
59. Thomas, J.M., "Principles and practice of heterogeneous catalysis", Wiley - VCH, Weinheim, 1996

60. Truett, W.L., Johnson, D.R., Robinson, I.M. and Montague, B.A., "Polynorbornene by co-ordination polymerization", *Journal of the American Chemical Society* **82** (1960) 2337 - 2340
61. van Roosmalen, A.J. and Mol, J.C., "Active centres for the metathesis and isomerization of alkenes on tungsten - oxide/ silica catalysts", *Journal of Catalysis* **78** (1982) 17 - 23
62. van Roosmalen, A.J. and Mol, J.C., "An infrared study of the silica gel surface - 1. Dry silica gel", *Journal of Physical Chemistry* **82** No. 25 (1978) 2748 - 2751
63. van Roosmalen, A.J., Koster, D. and Mol, J.C., "Infrared spectroscopy of some chemisorbed molecules on tungsten oxide – silica", *Journal of Physical Chemistry* **84** (1980) 3075 - 3079
64. van Schalkwyk, C., Spamer, A., Moodley, D.J., Dube, T., Reynhardt, J. and Botha, J.M., "Application of a WO_3/SiO_2 catalyst in an industrial environment: Part I", *Applied Catalysis A: General* **255** (2003) 121 – 131
65. van Schalkwyk, C., Spamer, A., Moodley, D.J., Dube, T. and Botha, J.M., "Application of a WO_3/SiO_2 catalyst in an industrial environment: Part II", *Applied Catalysis A: General* **255** (2003) 133 - 142
66. van Schalkwyk, C., Spamer, A., Moodley, D.J., Dube, T., Reynhardt, J., Vosloo, H.C.M. and Botha, J.M., "Factors that could influence the activity of an WO_3/SiO_2 catalyst: Part III", *Applied Catalysis A: General* **255** (2003) 143 - 152
67. van Schalkwyk, C., Spamer, A., Moodley, J.M., Dube, T., Reynhardt, J., Botha, J.M., International patent WO 2004/016351 A1 (2004)
68. Venables, D.S. and Brown, M.E., "Reduction of tungsten oxides with carbon monoxide", *Thermochimica Acta* **291** No. 1-2 (1997) 131
69. Verpoort, F., Bossuyt, A.R. and Verdonck, L., "Olefin metathesis catalyst. Part II. Activation and characteristics of a 'molecular' tungsten unit on silica", *Journal of Molecular Catalysis A: Chemical* **95** (1995) 75 - 82
70. Wang, Y., Chen, Q., Yang, W., Xie, Z., Xu, W. and Huang, D., "Effect of support nature on WO_3/SiO_2 structure and butene-1 metathesis", *Applied Catalysis A: General* **250** (2003) 25 - 37
71. Westhoff, R. and Moulijn, J.A., "Reduction and activity of the metathesis catalyst WO_3/SiO_2 ", *Journal of Catalysis* **46** (1977) 414 - 416
72. Wojciechowski, B.W. and Rice, N.M., "Experimental methods in kinetic studies", 2nd Edition, Elsevier, Amsterdam, 2003
73. Xia, X., Jin, R., He, Y., Deng, J. and Li, H., "Surface properties and catalytic behaviours of WO_3/SiO_2 in selective oxidation of cyclopentene to glutaraldehyde", *Applied Surface Science* **165** (2000) 255 - 259

Appendix

A

Equipment calibration data

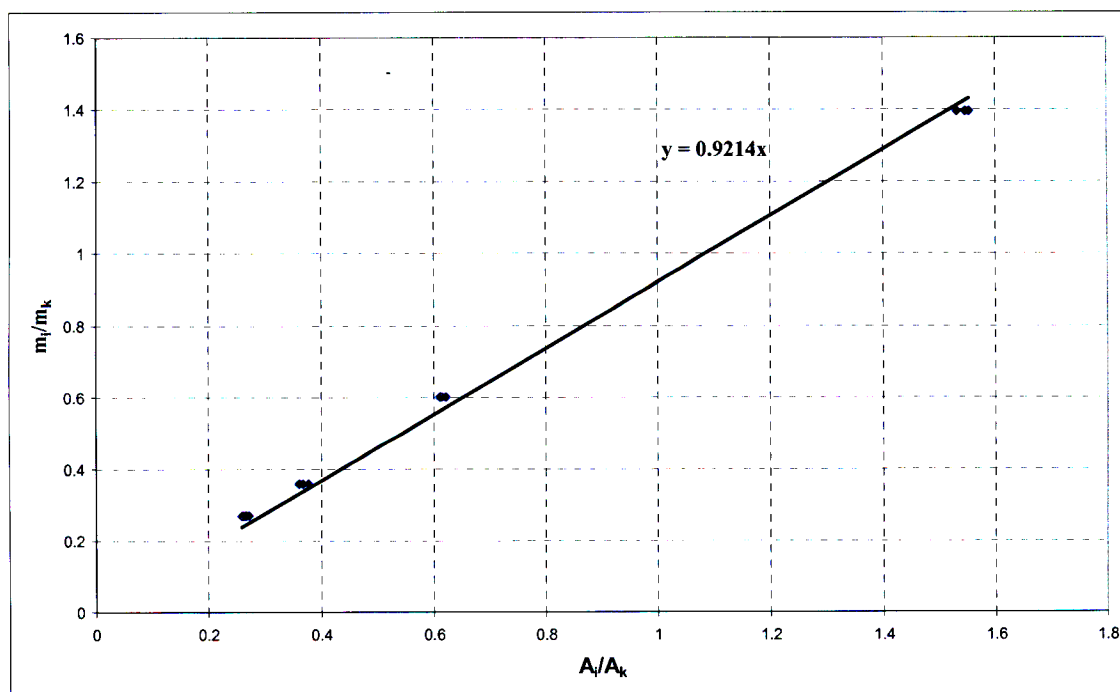


Figure A.1 G.C detector calibration curve, 1-decene (reference component: 1-hexene)

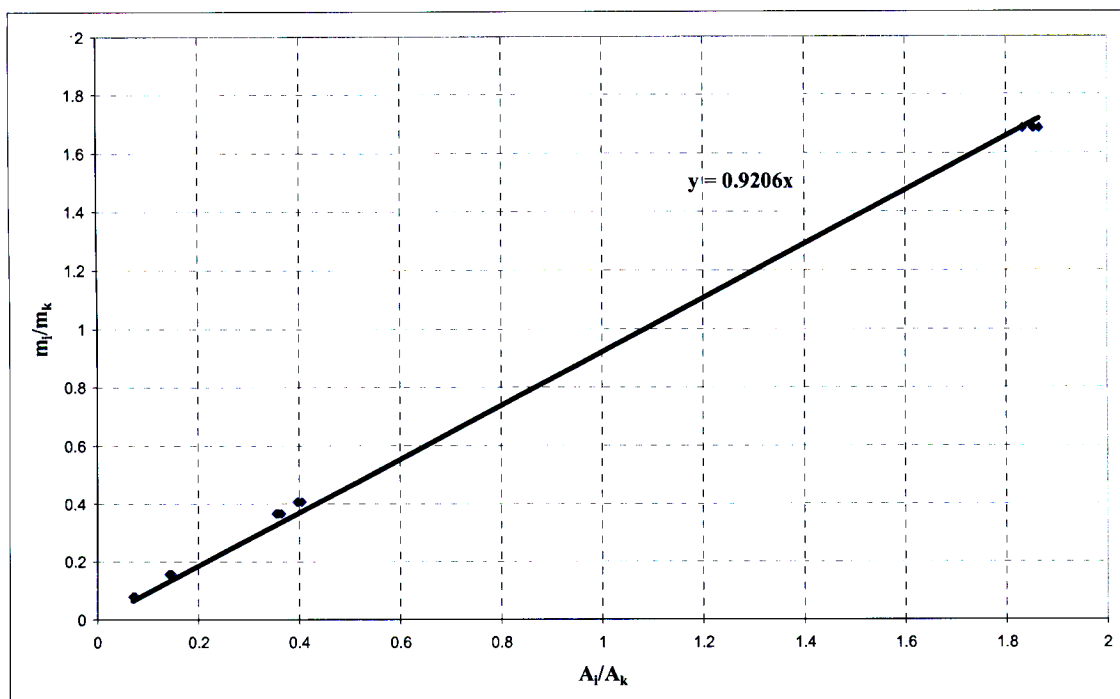


Figure A.2 G.C detector calibration curve, 1-nonene (reference component: 1-hexene)

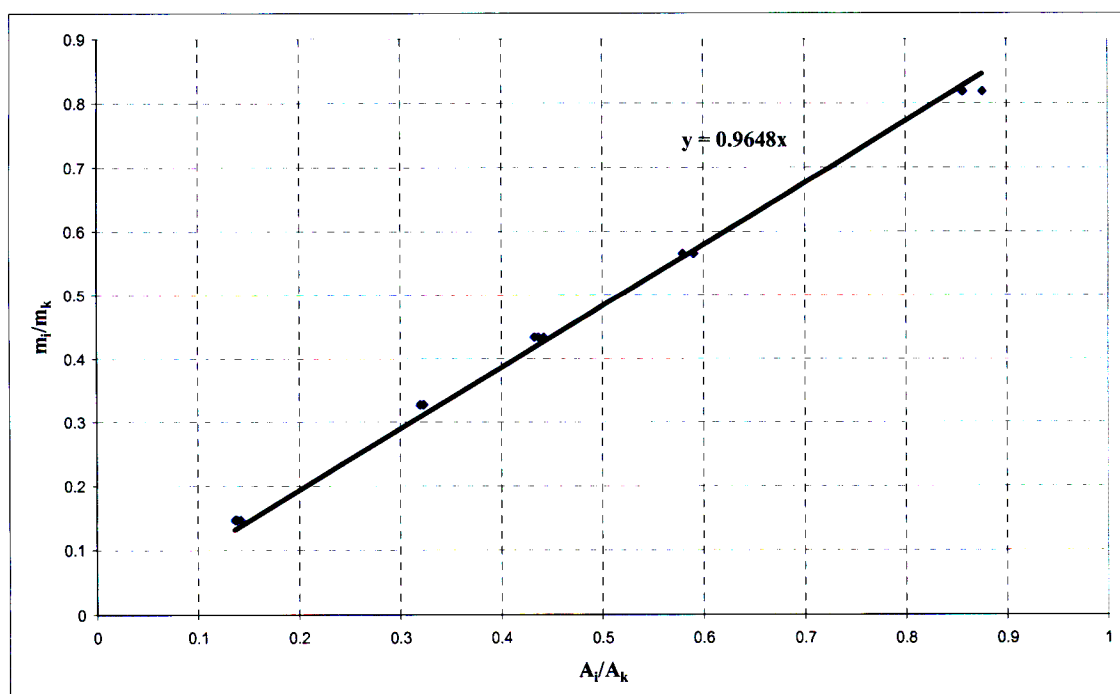


Figure A.3 G.C detector calibration curve, 1-octene (reference component: 1-hexene)

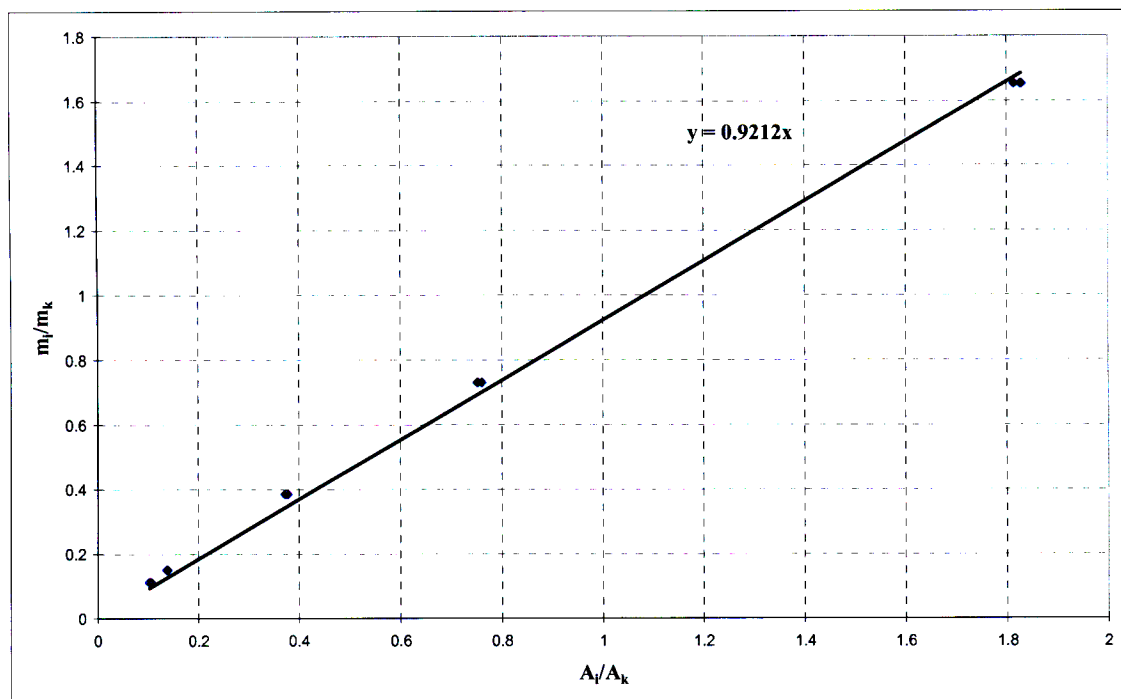


Figure A.4 G.C detector calibration curve, 1-heptene (reference component: 1-hexene)

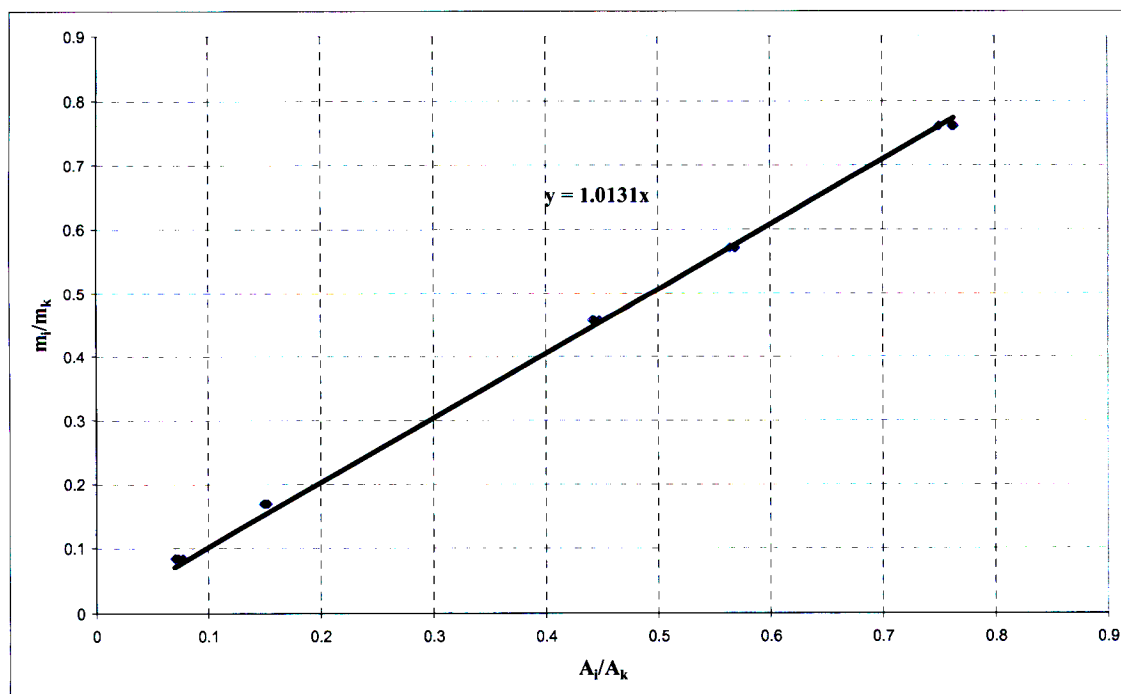


Figure A.5 G.C detector calibration curve, 1-pentene (reference component: 1-hexene)

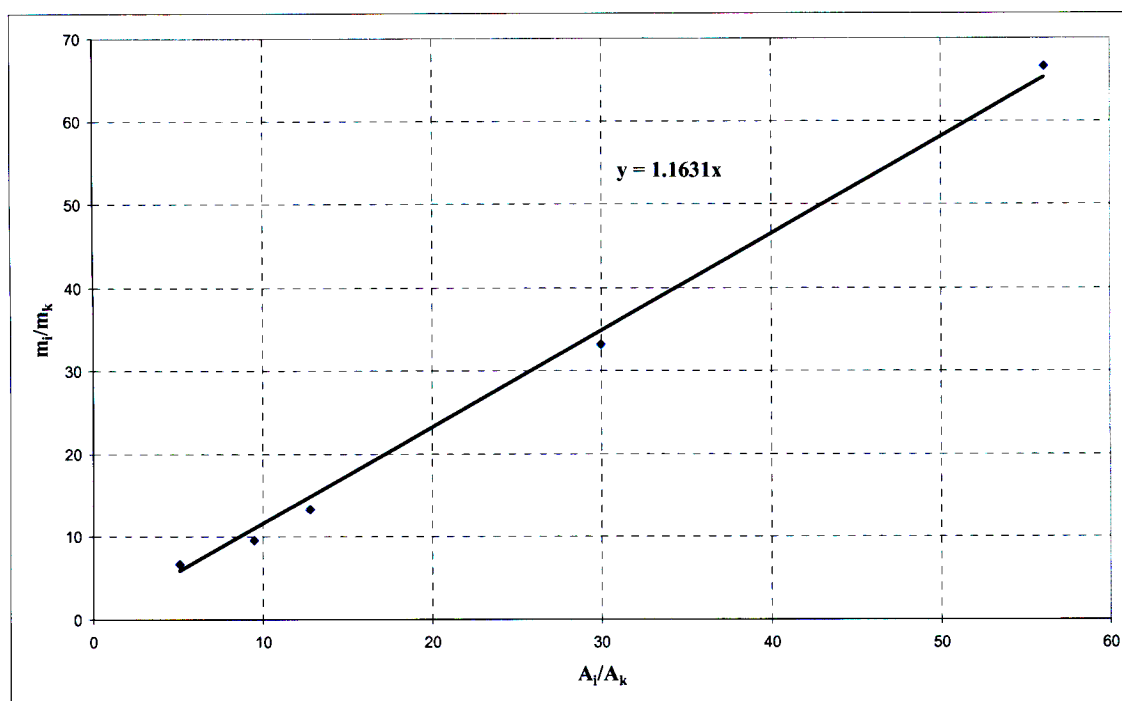


Figure A.6 G.C detector calibration curve, 1-butene (reference component: 1-hexene)

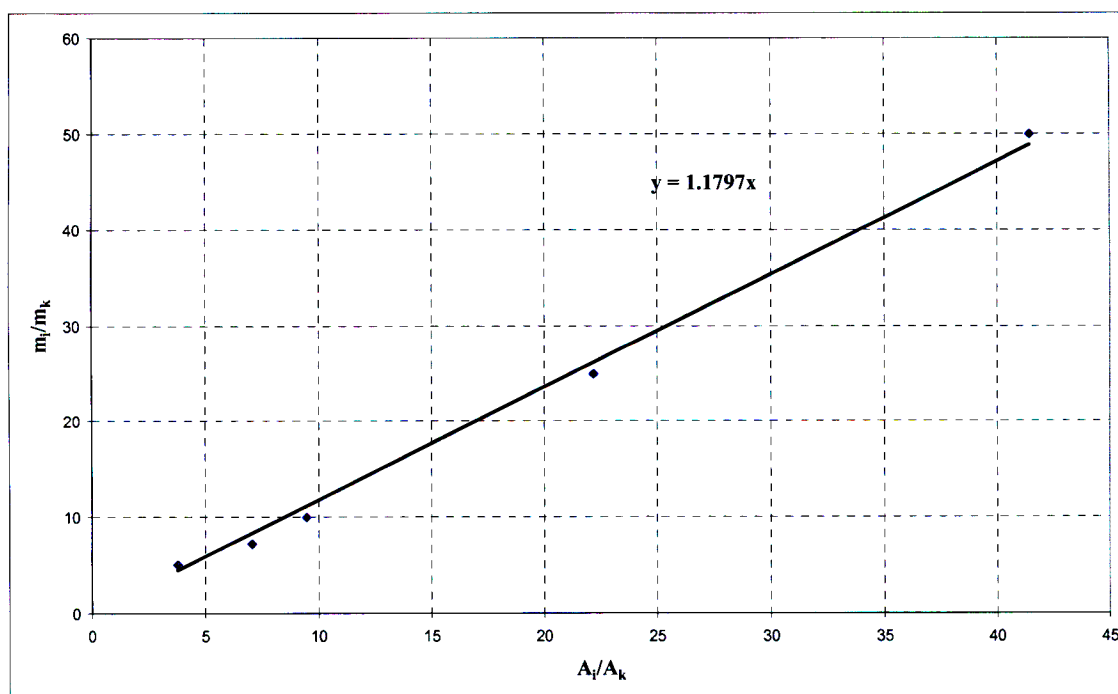


Figure A.7 G.C detector calibration curve, propylene (reference component: 1-hexene)

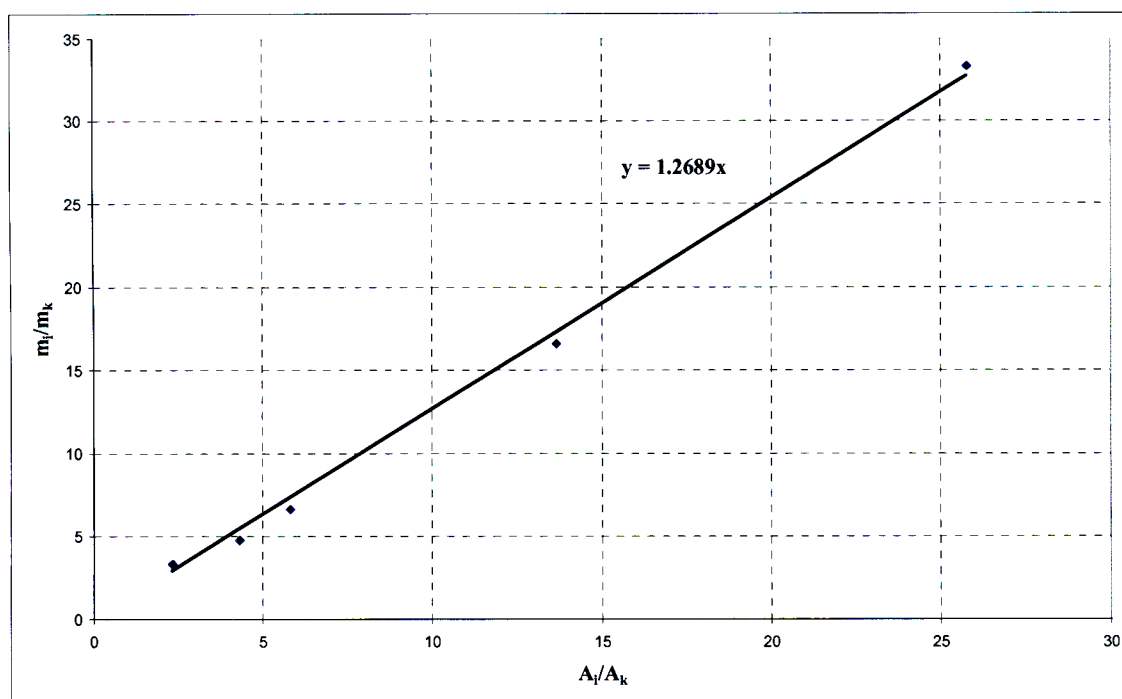


Figure A.8 G.C detector calibration curve, ethylene (reference component: 1-hexene)

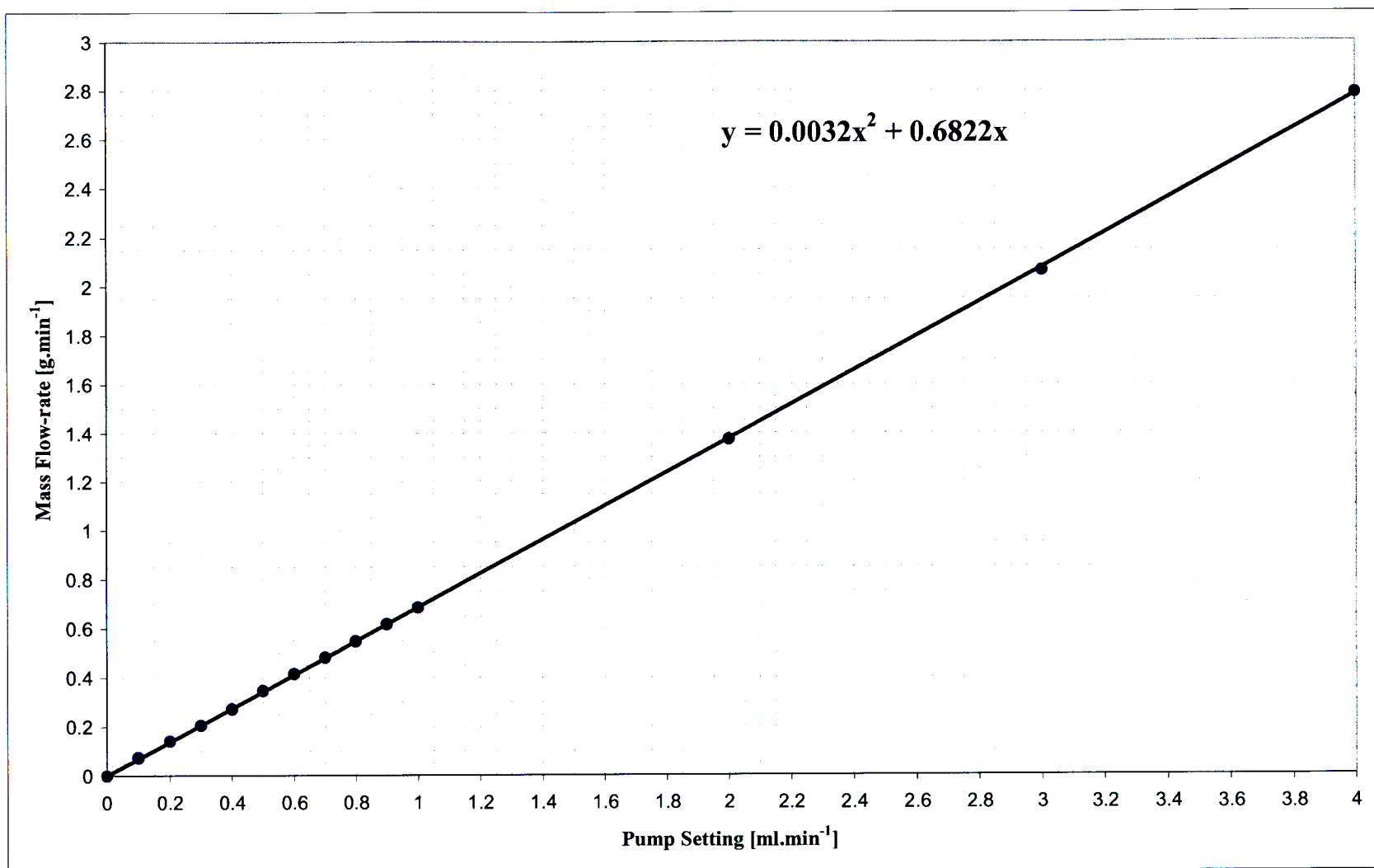


Figure A.9 Spectrochrom P100 isocratic pump calibration curve (1-hexene at 30°C)

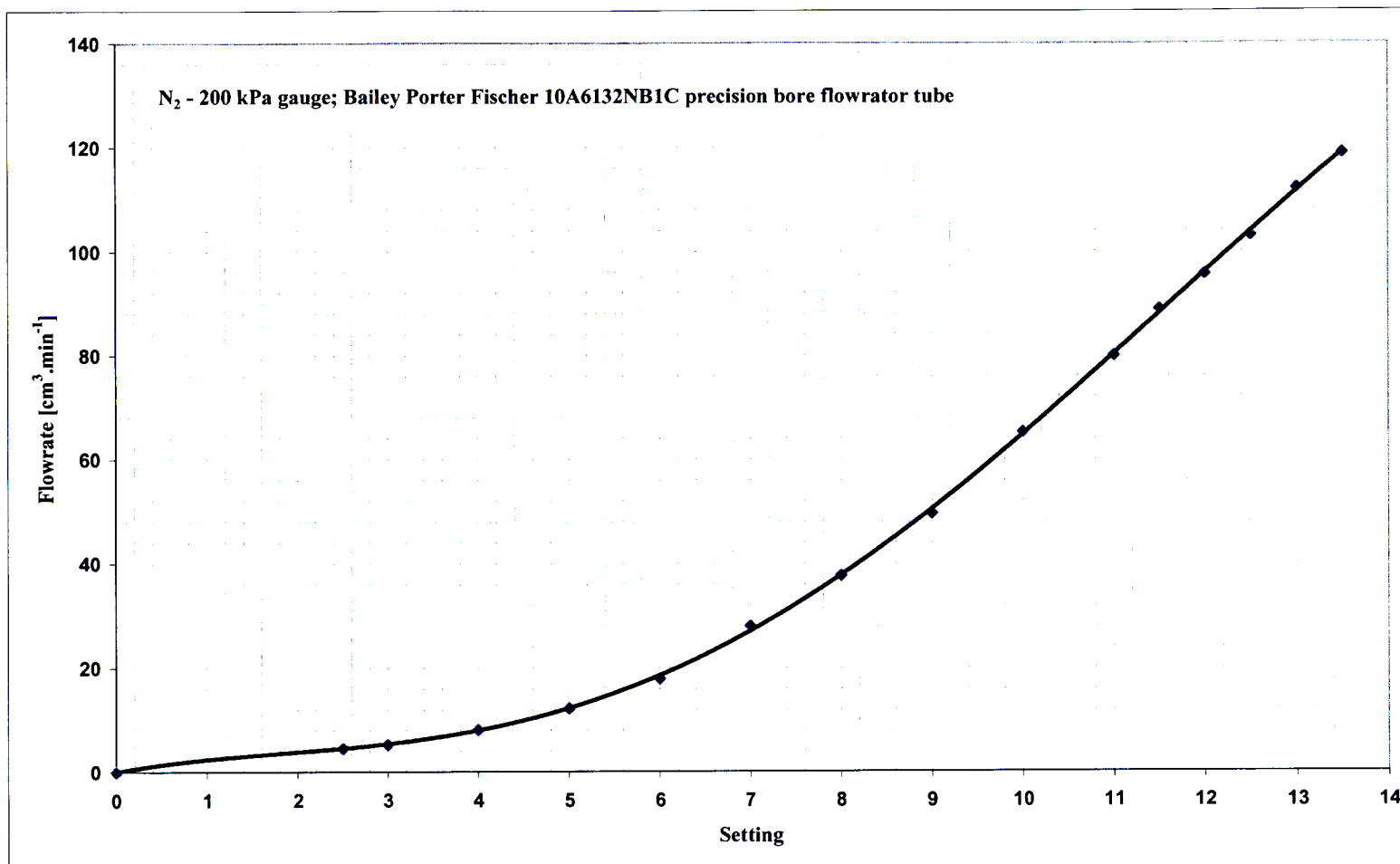


Figure A.10 R102 rotameter calibration curve – Nitrogen (2barg supply)

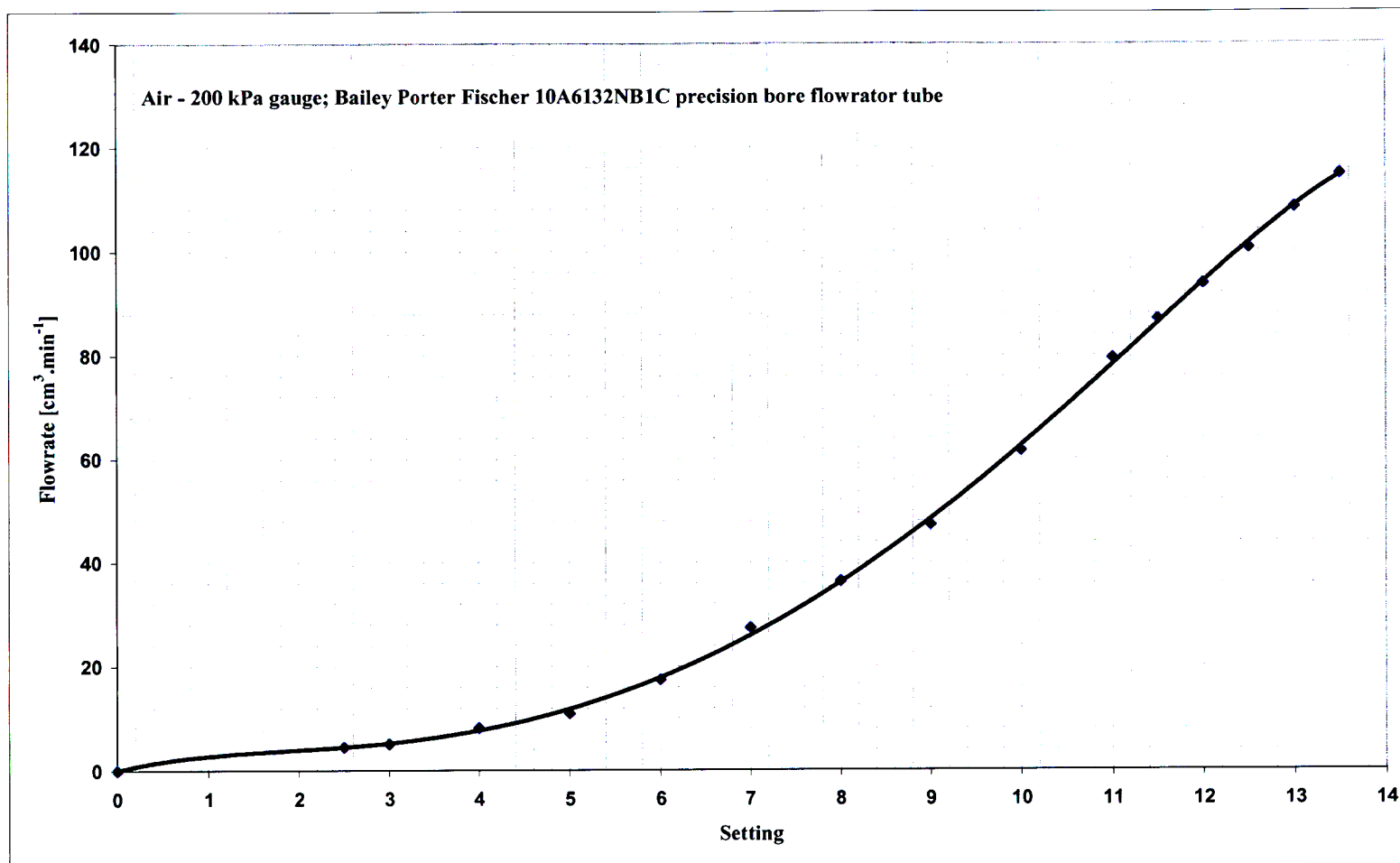


Figure A.11 R102 rotameter calibration curve – Air (2barg supply)

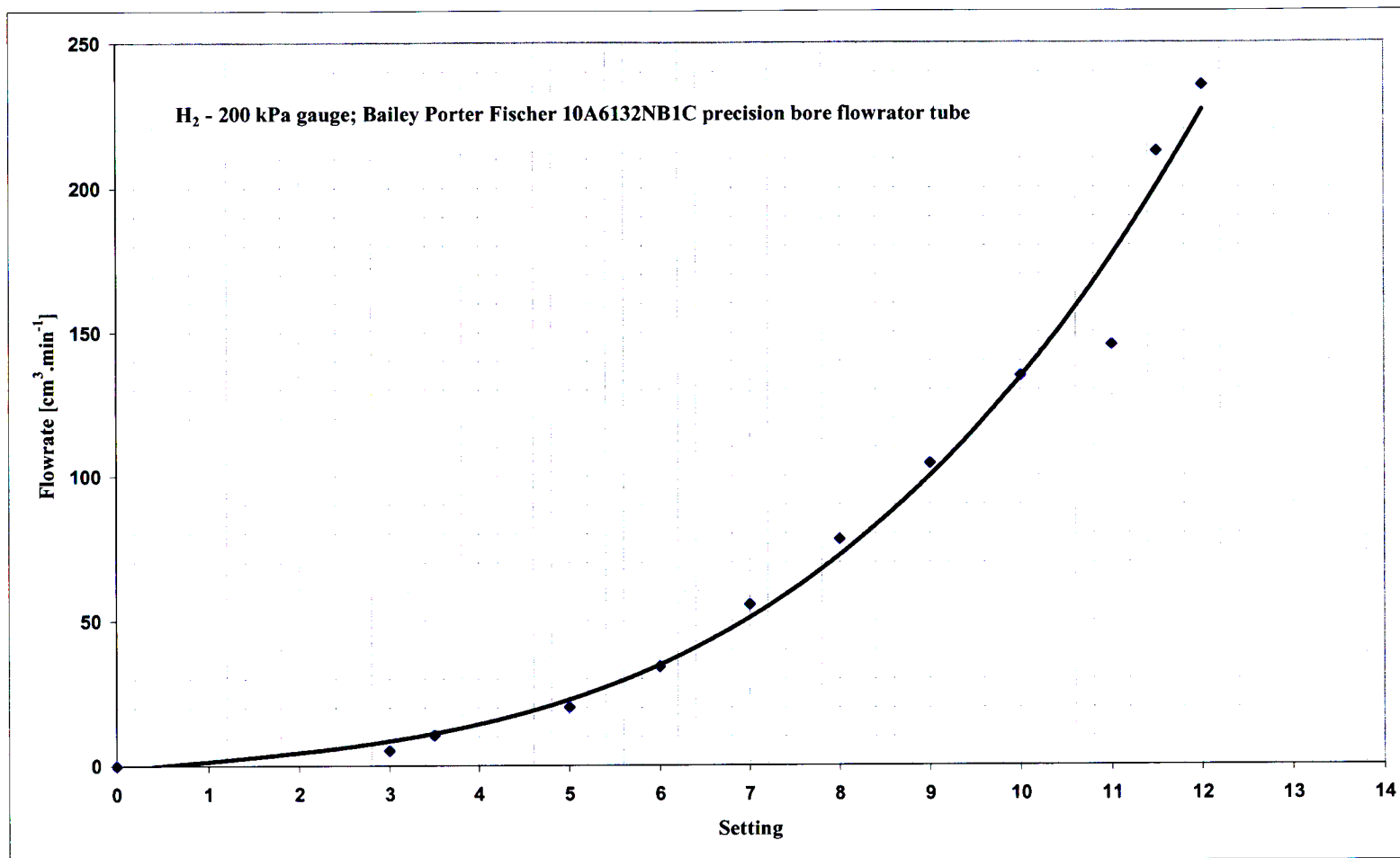


Figure A.12 R102 rotameter calibration curve – Hydrogen (2barg supply)

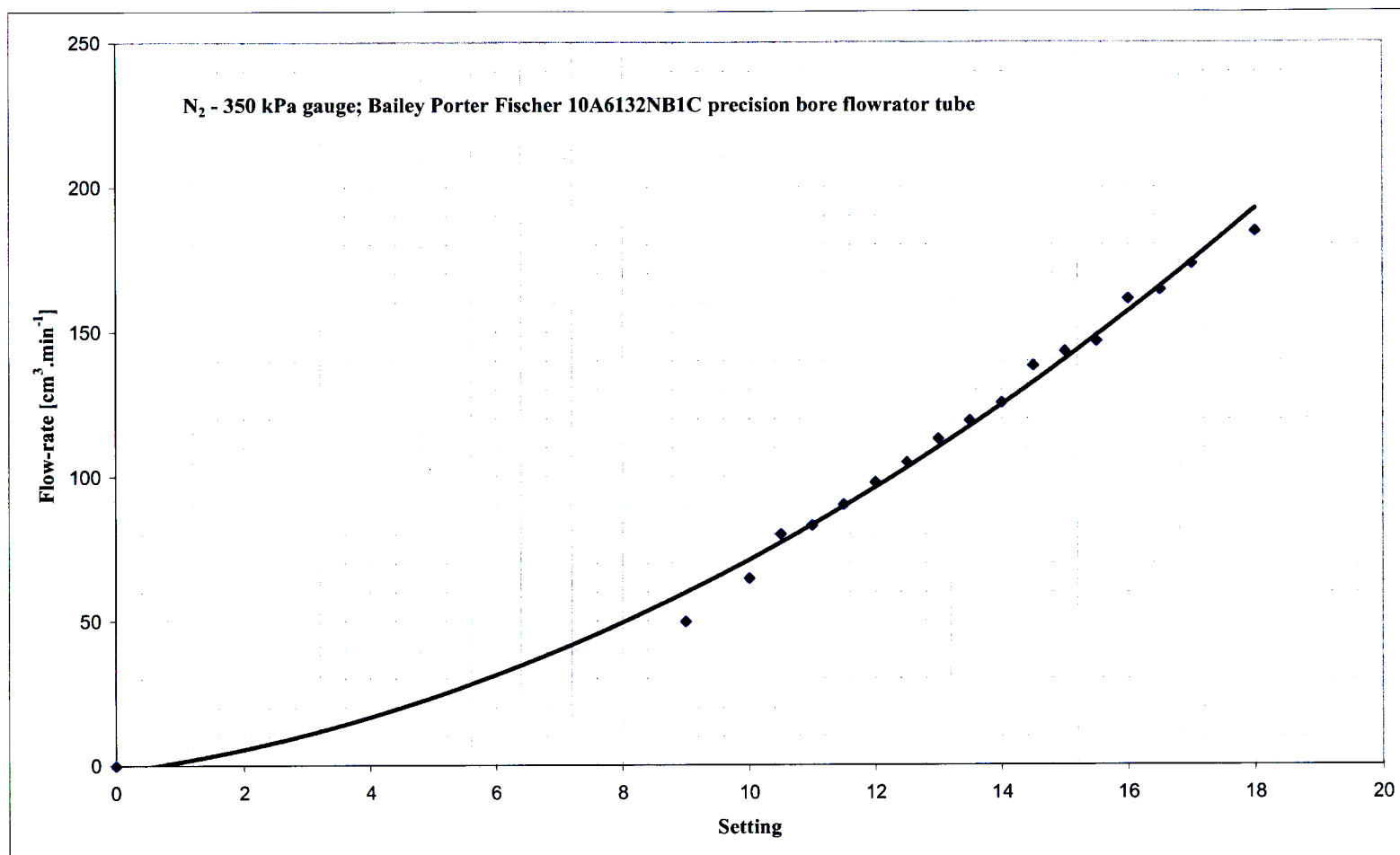


Figure A.13 R102 rotameter calibration curve – Nitrogen (3.5barg supply)

Appendix

B

MATLAB® computer simulation and process calculation script files

B.1.1 Polish program experimental calculations script file

```
% Evaluation of the rate of metathesis reaction from experimental
data

clear all
close all

if exist('marek_results_2006.txt'),
    delete marek_results_2006.txt
end
datafile = dir('marek_*.m');
N = size(datafile,1);
for i=1:N,
    Samples(i,:) = datafile(i).name;
end
Samples = sortrows(Samples);

sG = ['Nitrogen      '
      'Ethene        '
      'Propene        '
      'Butene         '
      'Pentene        '
      'Hexene         '
      'Heptene        '
      'Octene         '
      'Nonene         '
      'Decene         '
      'Undecene       '
      'Dodecene       ']
```

```

        'Tridecene '
        'Tetradecene'];

R = 8.314;                % universal gas constant, J/mol.K

% Molecular weights, g/mol
MW = [ 28.0341, 28.054,   42.810,   56.108,   70.135,   84.162,
98.189, ...
      112.216, 126.243, 140.270, 154.297, 168.324, 182.351,
196.378];

% Crystalline density of catalyst, g/cm³
percent_WO3 = 8;
rhos_WO3 = 7.16;
rhos_SiO2 = 2.22;
rhos = 100/(percent_WO3/rhos_WO3+(100-percent_WO3)/rhos_SiO2);
% Particle density, g/cm³
rhop = 1.0364;
% Particle porosity
ep = 1-rhop/rhos;
% Bed porosity (voidage)
eb = 0.655;
% Bed bulk density, g/cm³
rhob = 1-rhop*eb;

% Internal pipe diameter (flowmeter-reactor line), mm
dpipe = 3;
% Total length of piping (flowmeter-reactor line), m
Lpipe = 1.75;

% Nitrogen flowmeter equation constants
AA = 11.51353;
BB = -14.77262;

diary marek_results_2006.txt
J = 2:14;                % indices of alkenes
for i=1:N,
    eval(Samples(i,1:end-2))

% Bed height, m
H = W/(rhob*pi*(D/10)^2/4)/100;
% Mean particle size, m
dp = 0.001*sqrt(dim(1)*dim(2));

% Pressure drop through the bed, kPa
[rho, mu] = props(tC_in, P_out);
u0 = (1e-6*V_in/60)/(pi*(D/1000)^2/4);
DP_bed = 0.001*rho*H*(150*(1-eb)^2*mu*u0*H/(eb^3*dp^2*rho)+ ...
    1.75*(1-eb)*u0^2/(eb^3*dp));
% Pressure at the reactor inlet, kPa
P_in = P_out+DP_bed;

% Volumetric flow rate of nitrogen at the flow temperature,
cm3/min
V_N2 = (AA*MF+BB)*(tC_MF+273.15)/298.15;

% Pressure drop between the nitrogen flowmeter and the reactor,
kPa
[rho, mu] = props(tC_MF, P_in);
epsilon = 0.045/dpipe; % commercial steel
u1 = (1e-6*V_N2/60)/(pi*(dpipe/1000)^2/4);

```

```

Re = (dpipe/1000)*u1*rho/mu;
A = (-2.457*log((7/Re)^0.9+0.27*epsilon))^16;
B = (37530/Re)^16;
f = 2*((8/Re)^12+(A+B)^(-1.5))^(1/12);
K1 = 1000;
Ki = 0.69;
Kd = 4;
Kf = K1/Re+Ki*(1+Kd/(dpipe/25.4));
DP_pipe = 0.001*(4*f*Lpipe/(dpipe/1000)+12*Kf)*u1^2/2*rho;
% Pressure in the nitrogen flowmeter, kPa
P_N2 = P_in+DP_pipe;

% Total molar inlet concentration of gas at temperature tC_in,
mol/m3
Ctot_in = 1000*P_in/(R*(tC_in+273.15));

% Total molar inlet flow rate of gas, mol/h
Ftot_in = Ctot_in*(60*1e-6*V_in);

% Molar inlet flow rate of nitrogen, mol/h
F_in(1) = 1000*P_N2*(60*1e-6*V_N2)/(R*(tC_MF+273.15));

% Molar inlet flow rate of gas - organic "phase", mol/h
Forg_in = Ftot_in-F_in(1);

% Molar inlet flow rates of alkenes in gas, mol/h
F_in(J) = yorg_in(J-1)*Forg_in;

% Molar composition of reactor inlet stream, mole fraction
y_in = F_in/Ftot_in;

% Inlet molar gas-phase concentrations at temperature tC_in,
mol/m3
C_in = y_in*Ctot_in;

% Total molar outlet concentration of gas at temperature tC_out,
mol/m3
Ctot_out = 1000*P_out/(R*(tC_out+273.15));

% Molar outlet flow rate of nitrogen, mol/h
FG_out(1) = F_in(1);

% Total molar outlet flow rate of non-condensed gas, mol/h
FGtot_out = 1000*P_out*(60*1e-6*V_out)/(R*(tC_out+273.15));

% Molar outlet flow rate of non-condensed gas - organic "phase",
mol/h
FGorg_out = FGtot_out-FG_out(1);

% Molar outlet flow rates of alkenes in non-condensed gas, mol/h
FG_out(J) = yorg_out(J-1)*FGorg_out;

% Total mass outlet flow rate of condensate, g/h
WLtot_out = 60*mass/tau;

% Mean molecular weight of condensate, g/mol
ML_out = xorg_out*MW(2:end)';

% Total molar outlet flow rate of condensate, mol/h
FLtot_out = WLtot_out/ML_out;

```



```

%      Molar outlet flow rates of alkenes in condensate, mol/h
FL_out(J) = xorg_out(J-1)*FLtot_out;

%      Total molar outlet flow rate (non-condensed gas + condensate),
mol/h
Ftot_out = FGtot_out+FLtot_out;

%      Molar outlet flow rates (non-condensed gas + condensate), mol/h
F_out = FG_out+FL_out;

%      Molar composition of reactor outlet stream, mole fraction
y_out = F_out/Ftot_out;

%      Outlet molar gas-phase concentrations at temperature tC_out,
mol/m3
C_out = y_out*Ctot_out;

%      Mean pressure in the reactor, Pa
P = 1000*(P_in+P_out)/2;

%      Mean molar flow rates through the reactor, mol/h
F = (F_in+F_out)/2;

%      Mean total molar flow rate through the reactor, mol/h
Ftot = sum(F);

%      Mean molar composition of gas in the reactor, mole fraction
y = (y_in+y_out)/2;

%      Mean total volumetric flow rate of gas through the reactor,
cm3/min
Vtot = 1e6*Ftot/60*R*(tC+273.15)/P;

%      Mean residence time, s
MRT = 60*W*(1/rhob-1/rhop)/Vtot;

%      Total molar gas concentration in the reactor at temperature tC,
mol/m3
Ctot = P/(R*(tC+273.15));

%      Mean molar gas concentrations in the reactor at temperature tC,
mol/m3
C = y*Ctot;

%      Entrance molar flowrate of carbon, mol/h
Carbon_in = J*F_in(J)';

%      Exit molar flowrate of carbon, mol/h
Carbon_out = J*F_out(J)';

%      Consumption rate of hexene, mol/kg cat/h
r_HEX = (F_in(6)-F_out(6))/(0.001*W);

%      Consumption rate of hexene towards olefins higher than hexene,
mol/kg cat/h
r_HOlef = 0;
for j=7:14,
    r_HOlef = r_HOlef+(F_out(j)-F_in(j))/(0.001*W);
end

%      Conversion of hexene, %

```

```

X = (F_in(6)-F_out(6))/F_in(6)*100;

% Yield of decene, %
Y = 100*(F_out(10)-F_in(10))/(F_in(6));

% Selectivity towards higher olefins, %
for u=7:14;
    Hi_Olefin(u-6)= F_out(u)-F_in(u);
end

Hi_olefin_total = sum(Hi_Olefin);

Sel = (Hi_olefin_total/(F_in(6)-F_out(6)))*100;

% Yield of higher olefins, %
Yel = (Hi_olefin_total/F_in(6))*100;

% Selectivity towards Decene, %
Sel_Dec = 100*(F_out(10)-F_in(10))/(F_in(6)-F_out(6));

% Space time (W/F), g.min/mol
ST=W/(Ftot_in/60);

% Results
if i>9,
    rr = num2str(i);
else
    rr = ['0', num2str(i)];
end
disp([' ====='])
disp([' RUN #', rr])
disp([' ====='])
disp(' ')
disp([' Particle size: ', decform(dim(1), 1, 1), ' x ',
decform(dim(2), 1, 1), ' mm'])
disp([' Amount of catalyst: ', decform(W, 1, 4), ' g'])
disp([' Nitrogen/Inlet/Exit pressure: ', decform(P_N2, 1,
3), ...
' ', decform(P_in, 1, 3), ' ', decform(P_out, 1, 3), '
kPa'])
disp([' Nitrogen/Saturation/Inlet/Exit temperature: ',
decform(tC_MF, 3, 1), ...
' ', decform(tC_sat, 3, 1), ' ', decform(tC_in, 3, 1),
' ', decform(tC_out, 3, 1), ' °C'])
disp([' Reactor operating temperature: ', decform(tC, 3, 1),
' °C'])
disp([' Nitrogen(', decform(tC_MF, 2, 1), ' °C)/Inlet(',
decform(tC_in, 2, 1), ' °C)/Exit(', ...
decform(tC_out, 2, 1), ' °C) vol. flowrate: ',
decform(V_N2, 3, 2), ' ', decform(V_in, 3, 2), ...
' ', decform(V_out, 3, 2), ' cm³/min'])
disp([' Mean residence time of gas in the reactor (per bulk
void space): ', decform(MRT, 2, 3), ' s'])
disp([' Inlet(', decform(tC_in, 2, 1), ' °C)/Exit(',
decform(tC_out, 2, 1), ' °C)/Reactor(', ...

```

```

        decform(tC, 3, 1), '°C) hexene concentration: ',
decform(C_in(6), 2, 4), ' ', ...
        decform(C_out(6), 2, 4), ' ', decform(C(6), 2, 4), '
mol/m³']])
    disp(' ')

    disp(['      Inlet:          Total molar gas flowrate: ',
decform(1000*Ftot_in, 4, 2), ' mmol/h'])
    disp(' ')
    disp(['                                Mole fraction      Flow rate
(mmol/h)'])
    for j=1:length(sG),
        disp([' ', sG(j,:), ' ', decform(y_in(j), 2,
4), ' ', decform(1000*F_in(j), 4, 2)])
    end
    disp(' ')
    disp(['      Outlet:          Total molar gas flowrate: ',
decform(1000*Ftot_out, 4, 2), ' mmol/h'])
    disp(' ')
    disp(['                                Mole fraction      Flow rate
(mmol/h)'])
    for j=1:length(sG),
        sz = ' ';
        if y_out(j)<0,
            sz = '-';
        end
        disp([' ', sG(j,:), ' ', sz, decform(y_out(j),
1, 4), ' ', sz, decform(1000*F_out(j), 4, 2)])
    end

    disp(' ')
    disp(['      Reactor (mean values):      Total molar gas flowrate:
', decform(1000*Ftot, 4, 2), ' mmol/h'])
    disp(' ')
    disp(['                                Mole fraction      Flow rate
(mmol/h)      Concentration (mol/m³)'])
    for j=1:length(sG),
        disp([' ', sG(j,:), ' ', decform(y(j), 1, 4),
...
        ' ', decform(1000*F(j), 4, 2), '
', decform(C(j), 2, 4)])
    end

    disp(' ')
    disp(['      Space time: ', decform(ST, 3, 1), 'g.min/mol'])
    disp(['      Conversion of hexene: ', decform(X, 2, 1), ' %'])
    disp(['      Yield of decene: ', decform(Y, 2, 4), ' %'])
    disp(['      Yield of higher olefins: ', decform(Yel, 2, 4), '
%'])
    disp(['      Hexene consumption rate: ', decform(r_HEX, 2, 2), '
mol/(kg cat.h)'])
    disp(['      Higher olefins production rate: ', decform(r_HOlef,
2, 3), ' mol/(kg cat.h)'])
    disp(['      Selectivity towards higher olefins: ', decform(Sel,
2, 1), ' %'])
    disp(['      Selectivity towards decene: ', decform(Sel_Dec, 2,
1), ' %'])
    disp(['      Carbon in/out: ', decform(1000*Carbon_in, 3, 1), '
', decform(1000*Carbon_out, 3, 1), ' mmol/h'])
    disp(['      Carbon balance consistency: ',
decform(100*(Carbon_out-Carbon_in)/Carbon_in, 2, 2), ' %'])

```

```

disp(' ')

cat(i) = W; % g
rate(i) = r_HEX; % mol/(kg cat.h)
rate1(i) = r_HOlef; % mol/(kg cat.h)
temperature(i) = tC; % °C
psize1(i) = dim(1); % mm
psize2(i) = dim(2); % mm
VN2(i) = V_N2; % cm³/min
Xhex(i) = X; % percent
Chex(i) = C(6); % mol/m³
end
diary off
save marek_rates.mat cat temperature psize1 psize2 VN2 Xhex Chex
rate rate1

```

B.1.2 Pressure function m-file

```

clear all

z = 187; % m n.p.m, Lodz-Lublinek

% Pressure reduced to the sea level, kPa
RP = [1021.5, 1022.5, 1021.0, 1017.5, 1019.0, 1017.3, 1019.0, ...
      1018.3, 1017.0, 1017.0, 1015.5, 1014.3]/10;

% Temperature, °C
tC = [33.0, 30.0, 30.3, 32.0, 29.5, 30.8, 26.0, 29.0, 27.0, ...
      29.3, 26.0, 28.3];

M = 28.96;
g0 = 9.806;

cor = exp(-M/1000*g0*z./(8.314*(tC+273.15)));
P = RP.*cor;
PmmHg = 760*P/101.325

cor = 10.^(-z/18400./(1+tC/273));
P = RP.*cor;
PmmHg = 760*P/101.325

```

B.1.2 Physical property function m-file

```

function [rho, mu] = props(tC, P)

M = 28.0135; % molecular mass of
nitrogen gas, kg/kmol
rho = P*1e-03*M/(8314*(tC+273.15)); % density of nitrogen
gas, kg/m3
mu25 = 1.772E-05; % viscosity of nitrogen
gas at 25°C, kg/(m.s)
Tc = 126.24; % critical temperature of
nitrogen gas, K
Tr25 = (25+273.15)/Tc;
f25 = 1.058*Tr25^0.645-0.261/(1.9*Tr25)^(0.9*log10(1.9*Tr25));
Tr = (tC+273.15)/Tc;
f = 1.058*Tr^0.645-0.261/(1.9*Tr)^(0.9*log10(1.9*Tr));
mu = mu25*f/f25;

```

B.1.3 Number formats function m-file

```
function out = decform(x, m, n)
% decform.m converts fixed-point formatted (long or short) numbers
to
% (m,n)-numbers with an appropriate number of blanks in front of the
% number. Note: (4,5)-number has a format 2222.22222

    if nargin<2,
        disp('Sorry, format must be specified!');
        pause
    end
    if nargin<3,
        n = 0;
    end

    minus = x<0;
    if (nargin>2 & n<0),
        s = sprintf(['%',int2str(1),'.',int2str(m),'E'], abs(x));
    else
        s = sprintf(['%',int2str(m),'.',int2str(n),'f'], abs(x));
    end
    out = blanks(m+n+1-length(s)-minus);
    if x<0,
        out = [out, '-'];
    end
    out = [out, s];
```

B.1.4 Sample data file

```
% =====
% MAREK: Data file for Run # 01
% =====

% ID w117: 11.07.2006, Stelmachowski/Slowinski/Lokhat

% Mass of catalyst, g
W = 1.406;
% Catalyst size [height, diameter], mm
dim = [0.35, 0.30];
% Bed diameter, mm
D = 10;

% Nitrogen stream: Brooks flowmeter reading, %
MF = 15;
% Nitrogen stream: temperature, °C
tC_MF = 35;

% Reactor operating temperature, °C
tC = 469.7;

% Outlet pressure, kPa
P_out = 100.04;

% Saturation temperature, °C
tC_sat = 44;

% Total inlet gas stream: flowrate, cm3/min
V_in = 201.5;
```

B.2.1 Optimization program experimental calculations script file¹

¹ The number format function m-file is shared between programs

```

        'Decene      '
        'Undecene    '
        'Dodecene    '
        'Tridecene   '
        'Tetradecene'];

R = 8.314;           % universal gas constant, J/mol.K

% Molecular weights, g/mol
MW = [ 28.0341, 28.054, 42.810, 56.108, 70.135, 84.162,
98.189, ...
      112.216, 126.243, 140.270, 154.297, 168.324, 182.351,
196.378];

% Crystalline density of catalyst, g/cm³
percent_WO3 = 8;
rhos_WO3 = 7.16;
rhos_SiO2 = 2.22;
rhos = 100/(percent_WO3/rhos_WO3+(100-percent_WO3)/rhos_SiO2);
% Particle density, g/cm³
rhop = 1.0364;
% Particle porosity
ep = 1-rhop/rhos;
% Bed porosity (voidage)
eb = 0.642;
% Bed bulk density, g/cm³
rhob = 1-rhop*eb;

diary david_results_2007.txt
J = 2:14;           % indices of alkenes
for i=1:N,
    eval(Samples(i,1:end-2))

% Bed height, m
H = W/(rhob*pi*(D/10)^2/4)/100;
% Mean particle size, m
dp1=dp_cat          % mm
dp = 0.001*dp1;      % m

% Molar inlet flow rate of nitrogen, mol/h
F_in(1)=1000*P_N2*(60*1e-06*V_N2)/(R*(TC_N2+273.15));

% Mean molecular weight of liquid feed, g/mol
ML_in=xorg_in*MW(2:end)';

% Molar inlet flow rate of gas - organic "phase", mol/h
Forg_in=morg/ML_in;

% Molar inlet flow rates of alkenes, mol/h
F_in(J)=xorg_in(J-1)*Forg_in;

% Total molar inlet flow rate, mol/h
Ftot_in=sum(F_in);

% Molar composition of reactor inlet stream, mole fraction
y_in = F_in/Ftot_in;

% Total molar inlet concentration of gas at temperature TC_in,
mol/m3
Ctot_in=1000*P_in/(R*(TC_in+273.15));

```

```

%      Inlet molar gas-phase concentrations at temperature TC_in,
mol/m³
    C_in = y_in*Ctot_in;

%      Total volumetric flow-rate of inlet gas, cm³/min
    V_in=Ftot_in/(Ctot_in*60*1e-6);

%      Pressure drop through the bed, kPa
    [rho, mu] = props(TC_in, P_in);
    u0 = (1e-6*V_in/60)/(pi*(D/1000)^2/4); %m/s
    DP_bed = 0.001*rho*H*(150*(1-eb)^2*mu*u0*H/(eb^3*dp^2*rho)+ ...
        1.75*(1-eb)*u0^2/(eb^3*dp));

    Reynolds= dp*u0*rho/mu;

%      Pressure at the reactor exit, kPa
    P_out=P_in-DP_bed;

%      Outlet molar gas-phase concentrations at temperature TC_out,
mol/m³
    Ctot_out=1000*P_out/(R*(TC_out+273.15));

%      Molar outlet flow rate of nitrogen, mol/h
    FG_out(1) = F_in(1);

%      Total molar outlet flow rate of non-condensed gas, mol/h
    FGtot_out = 1000*P_prod*(60*1e-6*V_prod)/(R*(TC_prod+273.15));

%      Molar outlet flow rate of non-condensed gas - organic "phase",
mol/h
    FGorg_out = FGtot_out-FG_out(1);

%      Molar outlet flow rates of alkenes in non-condensed gas, mol/h
    FG_out(J) = yorg_out(J-1)*FGorg_out;

%      Total mass outlet flow rate of condensate, g/h
    WLtot_out = 60*mass/tau;

%      Mean molecular weight of condensate, g/mol
    ML_out = xorg_out*MW(2:end)';

%      Total molar outlet flow rate of condensate, mol/h
    FLtot_out = WLtot_out/ML_out;

%      Molar outlet flow rates of alkenes in condensate, mol/h
    FL_out(J) = xorg_out(J-1)*FLtot_out;

%      Total molar outlet flow rate (non-condensed gas + condensate),
mol/h
    Ftot_out = FGtot_out+FLtot_out;

%      Molar outlet flow rates (non-condensed gas + condensate), mol/h
    F_out = FG_out+FL_out;

%      Molar composition of reactor outlet stream, mole fraction
    y_out = F_out/Ftot_out;

%      Outlet molar gas-phase concentrations at temperature TC_out,
mol/m³
    C_out = y_out*Ctot_out;

```

```

% Total volumetric flow-rate of outlet gas, cm3/min
V_out=Ftot_out/(Ctot_out*60*1e-06);

% Mean pressure in the reactor, Pa
P = 1000*(P_in+P_out)/2;

% Mean molar flow rates through the reactor, mol/h
F = (F_in+F_out)/2;

% Mean total molar flow rate through the reactor, mol/h
Ftot = sum(F);

% Mean molar composition of gas in the reactor, mole fraction
y = (y_in+y_out)/2;

% Mean total volumetric flow rate of gas through the reactor,
cm3/min
Vtot = 1e6*Ftot/60*R*(TC+273.15)/P;

% Mean residence time, s
MRT = 60*W*(1/rhob-1/rhop)/Vtot;

% Total molar gas concentration in the reactor at temperature TC,
mol/m3
Ctot = P/(R*(TC+273.15));

% Mean molar gas concentrations in the reactor at temperature TC,
mol/m3
C = y*Ctot;

% Entrance molar flowrate of carbon, mol/h
Carbon_in = J*F_in(J)';

% Exit molar flowrate of carbon, mol/h
Carbon_out = J*F_out(J)';

% Consumption rate of hexene, mol/kg cat/h
r_HEX = (F_in(6)-F_out(6))/(0.001*W);

% Consumption rate of hexene towards olefins higher than hexene,
mol/kg cat/h
r_HOlef = 0;
for j=7:14,
    r_HOlef = r_HOlef+(F_out(j)-F_in(j))/(0.001*W);
end

% Conversion of hexene, %
X = (F_in(6)-F_out(6))/F_in(6)*100;

% Yield of decene, %]]
Y = 100*(F_out(10)-F_in(10))/(F_in(6));

% Selectivity towards higher olefins, %
for u=7:14;
    Hi_Olefin(u-6)= F_out(u)-F_in(u);
end

Hi_olefin_total = sum(Hi_Olefin);

Sel = (Hi_olefin_total/(F_in(6)-F_out(6)))*100;

```

```

%      Selectivity towards Decene, %

      Sel_Dec = 100*(F_out(10)-F_in(10))/(F_in(6)-F_out(6));

%      Space time (W/F), g.min/mol

      ST=W/(Ftot_in/60);

%      Results
      if i>9,
          rr = num2str(i);
      else
          rr = ['0', num2str(i)];
      end

      disp(['      ====='])
      disp(['      RUN #', rr])
      disp(['      ====='])
      disp(' ')
      disp(['      Time since the reactor startup: ', decform(hour, 1,
1), ' h'])
      disp(['      Particle size: ', decform(dp1, 1, 3), ' mm '])
      disp(['      Amount of catalyst: ', decform(W, 1, 4), ' g'])
      disp(['      Nitrogen/Inlet/Product/Exit pressure: ',
decform(P_N2, 1, 3), ...
      ' ', decform(P_in, 1, 3), ' ', decform(P_prod, 1, 3),
      ' ', decform(P_out, 1, 3), ' kPa'])
      disp(['      Nitrogen/Inlet/Product/Exit temperature: ',
decform(TC_N2, 3, 1), ...
      ' ', decform(TC_in, 3, 1), ' ', decform(TC_prod, 3,
1), ' ', decform(TC_out, 3, 1), ' °C'])
      disp(['      Reactor operating temperature: ', decform(TC, 3, 1),
      ' °C'])

      disp(['      Nitrogen(', decform(TC_N2, 2, 1), ' °C)/Inlet(',
decform(TC_in, 2, 1), ' °C)/Product(', decform(TC_prod, 2, 1),
      ' °C)/Exit(', ...
      decform(TC_out, 2, 1), ' °C) vol. flowrate: ',
decform(V_N2, 3, 2), ' ', decform(V_in, 3, 2), ...
      ' ', decform(V_prod, 3, 2), decform(V_out, 3, 2), '
cm³/min'])

      disp(['      Mean residence time of gas in the reactor (per bulk
void space): ', decform(MRT, 2, 3), ' s'])

      disp(['      Inlet(', decform(TC_in, 2, 1), ' °C)/Exit(',
decform(TC_out, 2, 1), ' °C)/Reactor(', ...
      decform(tC, 3, 1), ' °C) hexene concentration: ',
decform(C_in(6), 2, 4), ' ', ...
      decform(C_out(6), 2, 4), ' ', decform(C(6), 2, 4), '
mol/m³'])

      disp(' ')

      disp(['      Inlet:      Total molar gas flowrate: ',
decform(1000*Ftot_in, 4, 2), ' mmol/h'])
      disp(' ')
      disp(['      Mole fraction      Flow rate
(mmol/h)'])
      for j=1:length(sG),

```

```

disp([' ', sG(j,:), ' ', decform(y_in(j), 2,
4), ' ', decform(1000*F_in(j), 4, 2)])
end
disp(' ')
disp([' Outlet: Total molar gas flowrate: ',
decform(1000*Ftot_out, 4, 2), ' mmol/h'])
disp(' ')
disp([' Mole fraction Flow rate
(mmol/h)'])
for j=1:length(sG),
sz = ' ';
if y_out(j)<0,
sz = '';
end
disp([' ', sG(j,:), ' ', sz, decform(y_out(j),
1, 4), ' ', sz, decform(1000*F_out(j), 4, 2)])
end

disp(' ')
disp([' Reactor (mean values): Total molar gas flowrate:
', decform(1000*Ftot, 4, 2), ' mmol/h'])
disp(' ')
disp([' Mole fraction Flow rate
(mmol/h) Concentration (mol/m³)'])
for j=1:length(sG),
disp([' ', sG(j,:), ' ', decform(y(j), 1, 4),
...
', decform(1000*F(j), 4, 2), '
', decform(C(j), 2, 4)])
end

disp(' ')
disp([' Space time: ', decform(ST, 3, 1), 'g.min/mol'])
disp([' Superficial velocity at reaction temperature: ',
decform(uo, 1, 4), ' m/s'])
disp([' Reynolds number at reaction conditions: ',
decform(Reynolds, 3, 2), ' dimensionless'])
disp([' Conversion of hexene: ', decform(X, 2, 1), ' %'])
disp([' Yield of decene: ', decform(Y, 1, 4), ' %'])
disp([' Hexene consumption rate: ', decform(r_HEX, 2, 2), '
mol/(kg cat.h)'])
disp([' Higher olefines production rate: ', decform(r_HOlef,
2, 3), ' mol/(kg cat.h)'])
disp([' Selectivity towards higher olefins: ', decform(Sel,
2, 1), ' %'])
disp([' Selectivity towards decene: ', decform(Sel_Dec, 2,
1), ' %'])
disp([' Carbon in/out: ', decform(1000*Carbon_in, 3, 1), '
', decform(1000*Carbon_out, 3, 1), ' mmol/h'])
disp([' Carbon balance consistency: ',
decform(100*(Carbon_out-Carbon_in)/Carbon_in, 2, 2), ' %'])
disp(' ')

cat(i) = W; % g
rate(i) = r_HEX; % mol/(kg cat.h)
ratel(i) = r_HOlef; % mol/(kg cat.h)
temperature(i) = TC; % °C
psize1(i) = dp1; % mm
Finlet(i)=Fin; % mol/h
Foutlet(i)=Fout; % mol/h

```

```

        Xhex(i) = X;                                %    percent

    end
    diary off
    save david_rates.mat cat temperature psize1 Finlet Foutlet Xhex
    Chex rate ratel

```

B.2.2 Physical property function m-file

```

function [rho, mu] = props(TC, P_in)

    M = 84.141;                                     %    molecular mass of hexene
    gas, kg/kmol
    rho = P_in*M/(1000*8.314*(TC+273.15));          %    density of hexene gas,
    kg/m3

    mu = -7.7434 +(0.258*TC)+(-4.7e-05*TC^2); %viscosity of hexene gas,
    micropoise

    mu=mu/1000;                                     %viscosity of hexene gas,
    Pa.s

```

B.2.3 Sample data file

```

%    =====

%    David:      Data file for Run #    1
%    =====

%    ID    T0801:      08.01.2008, Lokhat

%    Reaction time

        hour=1

%    Mass of catalyst, g
    W      =      2
%    Catalyst size, mm
    dp_cat =      0.180
%    Bed diameter, mm
    D      =      9.52

%    Nitrogen stream: temperature, °C
    TC_N2 =      24.7

%    Nitrogen stream: pressure, Kpa
    P_N2  =      100

%    Nitrogen stream: volumetric flow, cm3/min
    V_N2  =      0.0881

%    Product gas stream: temperature, °C
    TC_prod =      24.7

%    Product gas stream: pressure, Kpa
    P_prod =      100

%    Product gas stream: volumetric flow, cm3/min

```

```

V_prod      =      2.0297

%      Reactor      operating      temperature,      °C
TC      =      460

%      Reactor      inlet      temperature,      °C
TC_in =      460

%      Reactor      outlet      temperature,      °C
TC_out      =      460

%      Inlet pressure,      kPa
P_in      =      104

%      Mass flow-rate of liquid feed, g/h
morg      =      28.966

%      Mass of the collected liquid sample,      g

mass      =      16.4073
%      Collection time, min
tau      =      74.283

%      Inlet liquid      stream      organic      composition,      mole
fraction
xorg_in      =      0      0      0      0      1      0      ...
0.0000,      0.0000,      0      0      0      0      0

%      Outlet      gas      stream      organic      composition,      mole
fraction
yorg_out      =      [0.41835,      0.31040,      0.12850,      0.04647,
0.08027,      0.01599,      ...
0.00000,      0.00000,      0.00000,      0.00000,      0.00000,
0.00000,      0.00000];

%      Outlet      liquid      stream      organic      composition,
mole fraction
xorg_out      =      [0.00000,      0.00000,      0.03625,      0.058413,
0.53475,      0.14607,      ...
0.07206,      0.04718,      0.08488,      0.00687,      0.00715,
0.00402,      0.00235];

```

B.3 Feed-tank open-loop process simulation script file

```

close all
clear all

period=17000; % seconds
dT=1; % seconds
m=(period/dT)+1;
time=0:period;

hL=zeros(1,m);
TL=zeros(1,m);
Tm=zeros(1,m);
TJA=zeros(1,m);
TJexit=zeros(1,m);

TJo=40; %degrees Celsius

```

```

hL(1,1)= 0.3;           % metres
TL(1,1)=25;            % degrees Celcius
Tm(1,1)=25;            % degrees Celsius

TJo=TJo + 273.15;
TL(1,1)=TL(1,1) + 273.15;
Tm(1,1)=Tm(1,1) + 273.15;
TJA(1,1)=TJo;
TJexit(1,1)=TJo;

FL= 1.0145e-08;         % m^3/s
R= 8.314;              % J/mol.K
Mhex=84.161;           % kg/kmol
MN2=28;                % kg/kmol
TN2=21;                % degrees Celcius
TN2=TN2 + 273.15;
Dt=0.15;               % metres
FN2=4.167e-07;         % m^3/s
rhoL=690;              % kg/m^3
CL=2198 ;              % J/kg.K
kL=0.116 ;             % W/m^2.K
muL=0.51e-03 ;         % Pa.s

hdatum=0.12;           % metres
Dcoil=9.52e-03;        % metres
Ucoil=1850;            % W/m.K
FJ=4e-06;              % m^3/s
rhoJ=1000;             % kg/m^3
VJ=3.345e-05;          % m^3
CJ=4194;               % J/kg.K
hfg=3.648e+05;         % J/kg
n_impeller=180;        % rpm
n_speed=n_impeller/60; % 1/s
rhom=8238;              % kg/m^3
Vm=5.631e-04;          % m^3
Cm=468;                % J/kg.K
Tair=25;               % degrees Celcius
Tair= Tair + 273.15;
g=9.81;                % m^2/s
ht=0.47;               % metres
Dot=0.155;             % metres
Ao1=ht*pi*Dot;
Ao2=(pi*(Dot^2))/4;
Act=1.767e-02;         % m^2
Lcoil1=1.53;           % metres
Dimp=4/100; % metres

% average fluid properties Nitrogen

rhoN2=1;               % kg/m^3
CN2=1041;              % J/kg.K
muN2=190e-07;          % Pa.s
vN2=18e-06;            % m^2/s
kN2=27e-03;            % W/m.K
alphaN2=26e-06;        % m^2/s
PrN2=0.714;

% average fluid properties Air

rhoAir=1;              % kg/m^3

```

```

CAir=1008; % J/kg.K
muAir=196e-07; % Pa.s
vAir=18e-06; % m^2/s
kAir=28.1e-03; % W/m.K
alphaAir=26.2e-06; % m^2/s
PrAir=0.704;

counter1=1;
counter2=m/2;

% liquid mass balance

VL(1,1)=hL(1,1)*Act;

for k=2:m;

    c1=k-1;

    nLPsat=15.8089-(2654.89/(TL(1,c1)-47.3));
    Psat=(exp(nLPsat))*133.3224; % Pa

    rho_sat=(Mhex*Psat)/(1000*R*TL(1,c1)); % kg/m^3

    Tf=(TN2+TL(1,c1))/2;

    Mab=2/(1/Mhex+1/MN2);

    A= 18.5;
    B=123.12;

    Dab=(0.00143*(Tf^1.75))/(1*(Mab^0.5)*(A^(1/3)+B^(1/3))^2); %
    cm^2/s
    Dab=Dab/1e+04; % m^2/s

    uN2=FN2/Act;

    hm=0.664*((uN2*Dt/vN2)^0.5)*((vN2/Dab)^(1/3))*(Dab/Dt); % m/s

    VL(1,k)=(-1*FL-(hm*rho_sat*Act/rhoL))*dT + VL(1,c1); % m^3

    hL(1,k)=VL(1,k)/Act; % m

%-----

% Jacket energy balance

Acoil=Lcoil1*pi*Dcoil + 2*(hL(1,c1)-hdatum)*pi*Dcoil; % m^2

Qcoil=Ucoil*Acoil*(TJA(1,c1)-TL(1,c1));

TJA(1,k)=TJA(1,c1)+dT*(FJ*CJ*rhoJ*(TJo-TJexit(1,c1))-
Ucoil*Acoil*(TJA(1,c1)-TL(1,c1)))/(rhoJ*VJ*CJ);

TJexit(1,k)=2*TJA(1,k)-TJo;

%-----

hh= 0.664*((uN2*Dt/vN2)^0.5)*((PrN2)^(1/3))*(kN2/Dt);

QN2=hh*Act*(TL(1,c1)-TN2)-hm*rho_sat*Act*hfg;

```

```

%-----

Ai=hL(1,c1)*pi*Dt + (pi*Dt^2)/4;

hi=
0.36*((Dimp^2)*n_speed*rhoL/muL)^0.67)*((CL*muL/kL)^(1/3))*(kL/Dt);

Qout_total=hi*Ai*(TL(1,c1)-Tm(1,c1));

Tf2=(Tm(1,c1)+Tair)/2;

beta=1/Tf2;

Gr_air=(g*beta*(Tm(1,c1)-Tair)*(ht^3))/(vAir^2);

ho1=0.138*(Gr_air^0.36)*(PrAir^0.175 - 0.55)*(kAir/ht);

Ra_air=(g*beta*(Tm(1,c1)-Tair)*(Dot^3))/(vAir*alphaAir);

ho2=(0.27*(Ra_air^0.25)*kAir)/(Dot);

Tm(1,k)=Tm(1,c1) + dT*(hi*Ai*(TL(1,c1)-Tm(1,c1))-ho1*Ao1*(Tm(1,c1)-
Tair)-ho2*Ao2*(Tm(1,c1)-Tair))/(rhoL*Vm*Cm);

%-----

% liquid energy balance

dVLTL_dt=(-1*rhoL*CL*FL*TL(1,c1)+Qcoil-Qout_total-QN2)/(rhoL*CL);

VLTL=dVLTL_dt*dT + VL(1,c1)*TL(1,c1);

TL(1,k)=VLTL/VL(1,k);

counter1=counter1+1;

if counter1>counter2
    FJ=2.577096e-007;    % m^3/s
end

end

plot(time,TL)

```

B.4 Particle size distribution script file

```

% Particle Size Distribution

clear all

F0 = 'TIF';
F0 = upper(F0);
F = ['*.', F0];

[imfile, impath] = uigetfile(F);
disp(imfile)
BW0 = imread(imfile);
info = imfinfo(imfile);
RESinch = info.XResolution;
RESmm = RESinch/25.4;

```



```

MB = info.FileSize/1000000;
D = 2; % MBytes
NS = max([1, round(MB/D)]);
[M0, N] = size(BW0);
m = round(M0/NS);
for i=1:NS,
    disp(['Section no. ', num2str(i)])
    i1 = (i-1)*m+1;
    if i<NS,
        i2 = i*m;
    else
        i2 = M0;
    end
    BW = BW0(i1:i2,:);
    imwrite(BW, [imfile(1:end-4), '_', num2str(i), '.TIF'], 'TIF',
'Resolution', RESinch)
end
save psd.mat imfile NS RESinch

load psd.mat
PixArea = [];
lut = [-1, 0, 1];
for i=1:NS,
    disp(['Section no. ', num2str(i)])
    BW = imread([imfile(1:end-4), '_', num2str(i), '.TIF']);
    [M, N] = size(BW);
    L(M+2, N+2) = uint8(0);
    L(2:M+1, 2:N+1) = BW(1:M, 1:N);
    clear BW
    M = M+2;
    N = N+2;
    L = bwlabel(L, 4);
    idx1 = find(L);
    elementValues = L(idx1);
    S = sparse(idx1, elementValues, 1);
    % Loop over each column of the sparse matrix. Finding the
    % row indices of the nonzero entries in S(:,P) is equivalent
    % to finding the linear indices of pixels in L that equal P.
    % Convert the linear indices to row-column indices and store
    % the results in the pixel list.
    R = max(L(:));
    area = zeros(R,1);
    for k = 1:R,
        idx2 = find(S(:,k))-1;
        c = floor(idx2/M)+1;
        r = rem(idx2,M)+1;
        K = length(r);
        area(k,1) = length(idx2);
    end
    PixArea = [PixArea; area];
end

Area_mm2 = PixArea/RESmm^2;
D_mm = sqrt(4*Area_mm2/pi);
D_micron = D_mm*1000;
Dmax = ceil(max(D_micron));
for D=1:Dmax,
    j = find(D_micron<=D);
    V(D) = sum(pi*D_micron(j).^3/6);
end
Vtot = sum(pi*D_micron.^3/6);

```

```

w_mass = V/Vtot;
D_mean = sum([1:Dmax-1].*(w_mass(2:Dmax)-w_mass(1:Dmax-1)));

figure(1)
clf
plot(1:Dmax, w_mass);
xlabel('Particle diameter')
ylabel('Mass fraction')
title('Particle size distribution - cumulative curve')
axis([0,800, 0,1])

```

B.5 Analysis of results of the experiments conducted in Poland – calculation script file

```

clear all
close all

tC = [470, 480.1, 490.3, 469.6, 480, 490, 470, 479.8, 470, 480.4,
489.9, 480];
dp = [300, 300, 300, 346, 346, 346, 346, 346, 447, 447, 447, 447];
y0 = [19.63, 21.54, 20.88, 19.24, 21.46, 22.27, 19.13, 21.49, 19.02,
21.70, 18.20, 18.92]/100;
WF = [176.1, 125.8, 100.2, 214.2, 152.3, 1191, 214.3, 152.3, 270.5,
191.4, 158.3, 199.0];
X = [12.84, 22.05, 34.3, 4.42, 12.06, 23.79, 6.34, 14.51, 17.55,
27.66, 32.92, 36.62]/100;

r0 = X./WF; % zero-th order; also a differential bed,
any order
r1 = -log(1-X); % 1st order
r2 = X./(1-X)./WF; % 2nd order
r3 = 2*(1-(1-X).^0.5); % 1/2-th order

C0 = ones(1,12);

for counter=1:12

    C0(1,counter)=(y0(1,counter)*101325)/(8.314*(tC(1,counter)+273.15));

end

k0 = r0./C0.^2; % differential bed, 2nd order
k1 = r1./C0;
k2 = r2./C0.^2;
k3 = r3./C0.^0.5;

s1 = [1:3];
s2 = [4,5,7,8];
s3 = [9:12];

F = [];
X = 1./(tC(s1)+273.15)';
Y = log(k0(s1))';
n = length(s1);
F(:,1) = X;
F(:,2) = ones(n,1);
p = (F'*F)\(F'*Y);
Y_pred = F*p;
E0_1 = -8.314*p(1)/1000; % kJ/mol

```

```

F = [];
X = 1./(tC(s2)+273.15)';
Y = log(k0(s2))';
n = length(s2);
F(:,1) = X;
F(:,2) = ones(n,1);
p = (F'*F)\(F'*Y);
Y_pred = F*p;
E0_2 = -8.314*p(1)/1000;    % kJ/mol

```

```

F = [];
X = 1./(tC(s3)+273.15)';
Y = log(k0(s3))';
n = length(s3);
F(:,1) = X;
F(:,2) = ones(n,1);
p = (F'*F)\(F'*Y);
Y_pred = F*p;
E0_3 = -8.314*p(1)/1000;    % kJ/mol

```

```

F = [];
X = 1./(tC(s1)+273.15)';
Y = log(k1(s1))';
n = length(s1);
F(:,1) = X;
F(:,2) = ones(n,1);
p = (F'*F)\(F'*Y);
Y_pred = F*p;
E1_1 = -8.314*p(1)/1000;    % kJ/mol

```

```

F = [];
X = 1./(tC(s2)+273.15)';
Y = log(k1(s2))';
n = length(s2);
F(:,1) = X;
F(:,2) = ones(n,1);
p = (F'*F)\(F'*Y);
Y_pred = F*p;
E1_2 = -8.314*p(1)/1000;    % kJ/mol

```

```

F = [];
X = 1./(tC(s3)+273.15)';
Y = log(k1(s3))';
n = length(s3);
F(:,1) = X;
F(:,2) = ones(n,1);
p = (F'*F)\(F'*Y);
Y_pred = F*p;
E1_3 = -8.314*p(1)/1000;    % kJ/mol

```

```

F = [];
X = 1./(tC(s1)+273.15)';
Y = log(k2(s1))';
n = length(s1);
F(:,1) = X;
F(:,2) = ones(n,1);
p = (F'*F)\(F'*Y);
Y_pred = F*p;
E2_1 = -8.314*p(1)/1000;    % kJ/mol

```

```

F = [];
X = 1./(tC(s2)+273.15)';
Y = log(k2(s2))';
n = length(s2);
F(:,1) = X;
F(:,2) = ones(n,1);
p = (F'*F)\(F'*Y);
Y_pred = F*p;
E2_2 = -8.314*p(1)/1000;    % kJ/mol

F = [];
X = 1./(tC(s3)+273.15)';
Y = log(k2(s3))';
n = length(s3);
F(:,1) = X;
F(:,2) = ones(n,1);
p = (F'*F)\(F'*Y);
Y_pred = F*p;
E2_3 = -8.314*p(1)/1000;    % kJ/mol

F = [];
X = 1./(tC(s1)+273.15)';
Y = log(k3(s1))';
n = length(s1);
F(:,1) = X;
F(:,2) = ones(n,1);
p = (F'*F)\(F'*Y);
Y_pred = F*p;
E3_1 = -8.314*p(1)/1000;    % kJ/mol

F = [];
X = 1./(tC(s2)+273.15)';
Y = log(k3(s2))';
n = length(s2);
F(:,1) = X;
F(:,2) = ones(n,1);
p = (F'*F)\(F'*Y);
Y_pred = F*p;
E3_2 = -8.314*p(1)/1000;    % kJ/mol

F = [];
X = 1./(tC(s3)+273.15)';
Y = log(k3(s3))';
n = length(s3);
F(:,1) = X;
F(:,2) = ones(n,1);
p = (F'*F)\(F'*Y);
Y_pred = F*p;
E3_3 = -8.314*p(1)/1000;    % kJ/mol

E0 = [E0_1, E0_2, E0_3]
E1 = [E1_1, E1_2, E1_3]
E2 = [E2_1, E2_2, E2_3]
E3 = [E3_1, E3_2, E3_3]

figure(1)
plot(tC(s1), r0(s1), 'b.', 'MarkerSize', 16)
hold on
plot(tC(s2), r0(s2), 'g.', 'MarkerSize', 16)

```

```
plot(tC(s3), r0(s3), 'r.', 'MarkerSize', 16)
xlabel('Temperature [K]')
ylabel('reaction rate [mol/g.min]')
legend('300 \mum', '346 \mum', '447 \mum')

figure(2)
plot(tC(s1), r1(s1), 'b.', 'MarkerSize', 16)
hold on
plot(tC(s2), r1(s2), 'g.', 'MarkerSize', 16)
plot(tC(s3), r1(s3), 'r.', 'MarkerSize', 16)
xlabel('Temperature [K]')
ylabel('reaction rate [mol/g.min]')
legend('300 \mum', '346 \mum', '447 \mum')

figure(3)
plot(tC(s1), r2(s1), 'b.', 'MarkerSize', 16)
hold on
plot(tC(s2), r2(s2), 'g.', 'MarkerSize', 16)
plot(tC(s3), r2(s3), 'r.', 'MarkerSize', 16)
xlabel('Temperature [K]')
ylabel('reaction rate [mol/g.min]')
legend('300 \mum', '346 \mum', '447 \mum')

figure(4)
plot(tC(s1), r3(s1), 'b.', 'MarkerSize', 16)
hold on
plot(tC(s2), r3(s2), 'g.', 'MarkerSize', 16)
plot(tC(s3), r3(s3), 'r.', 'MarkerSize', 16)
xlabel('Temperature [K]')
ylabel('reaction rate [mol/g.min]')
legend('300 \mum', '346 \mum', '447 \mum')

figure(5)
plot(1./(tC(s1)+273.15), log(k0(s1)), 'b.', 'MarkerSize', 16)
hold on
plot(1./(tC(s2)+273.15), log(k0(s2)), 'g.', 'MarkerSize', 16)
plot(1./(tC(s3)+273.15), log(k0(s3)), 'r.', 'MarkerSize', 16)
xlabel('1/T [K^{-1}]')
ylabel('ln k_{0}')
legend('300 \mum', '346 \mum', '447 \mum')

figure(6)
plot(1./(tC(s1)+273.15), log(k1(s1)), 'b.', 'MarkerSize', 16)
hold on
plot(1./(tC(s2)+273.15), log(k1(s2)), 'g.', 'MarkerSize', 16)
plot(1./(tC(s3)+273.15), log(k1(s3)), 'r.', 'MarkerSize', 16)
xlabel('1/T [K^{-1}]')
ylabel('ln k_{1}')
legend('300 \mum', '346 \mum', '447 \mum')

figure(7)
plot(1./(tC(s1)+273.15), log(k2(s1)), 'b.', 'MarkerSize', 16)
hold on
plot(1./(tC(s2)+273.15), log(k2(s2)), 'g.', 'MarkerSize', 16)
plot(1./(tC(s3)+273.15), log(k2(s3)), 'r.', 'MarkerSize', 16)
xlabel('1/T [K^{-1}]')
ylabel('ln k_{2}')
legend('300 \mum', '346 \mum', '447 \mum')
```

```
figure(8)
plot(1./(tC(s1)+273.15), log(k3(s1)), 'b.', 'MarkerSize', 16)
hold on
plot(1./(tC(s2)+273.15), log(k3(s2)), 'g.', 'MarkerSize', 16)
plot(1./(tC(s3)+273.15), log(k3(s3)), 'r.', 'MarkerSize', 16)
xlabel('1/T [K^{-1}]')
ylabel('ln k_{1/2}')
legend('300 \mum', '346 \mum', '447 \mum')
```

Appendix

C

Sample process calculations

Sample calculations for Run 1 – subset 1:

$$F_{N_2} = \frac{P_{N_2} \dot{V}_{N_2}}{RT_{N_2}} = \frac{100 \text{ kPa} \times 1000 \times \left(\frac{5 \text{ cm}^3}{56.750 \text{ s}} \right) \times 1 \times 10^{-6}}{8.314 \text{ J} \cdot \text{mol}^{-1} \cdot \text{K}^{-1} \times (24.7^\circ \text{C} + 273.15)} = 3.558 \times 10^{-6} \text{ mol} \cdot \text{s}^{-1}$$

$$F_{hex} = \frac{\dot{m}_{hex}}{60 \times M_{hex}} = \frac{0.483 \text{ g} \cdot \text{min}^{-1}}{60 \times 84.161 \text{ g} \cdot \text{mol}^{-1}} = 9.561 \times 10^{-5} \text{ mol} \cdot \text{s}^{-1}$$

$$F_{gas \text{ product}} = \frac{P_{prod} \dot{V}_{prod}}{RT_{prod}} = \frac{100 \text{ kPa} \times 1000 \times \left(\frac{15 \text{ cm}^3}{7.390 \text{ s}} \right) \times 1 \times 10^{-6}}{8.314 \text{ J} \cdot \text{mol}^{-1} \cdot \text{K}^{-1} \times (24.7^\circ \text{C} + 273.15)} = 8.197 \times 10^{-5} \text{ mol} \cdot \text{s}^{-1}$$

$$F_{org \text{ gas product}} = F_{gas \text{ product}} - F_{N_2} = 8.197 \times 10^{-5} \text{ mol} \cdot \text{s}^{-1} - 3.558 \times 10^{-6} \text{ mol} \cdot \text{s}^{-1} = 7.841 \times 10^{-5} \text{ mol} \cdot \text{s}^{-1}$$

$$\dot{m}_{liquid \text{ product}} = \frac{\text{mass collected}}{\text{collection time}} = \frac{16.4073 \text{ g}}{74.28 \text{ min}} = 0.221 \text{ g} \cdot \text{min}^{-1}$$

$$M_{avg, liquid \text{ product}} = \sum x_{i, liquid} \times M_i = 91.379 \text{ g} \cdot \text{mol}^{-1}$$

$$F_{\text{liquid product}} = \frac{\dot{m}_{\text{liquid product}}}{M_{\text{avg, liquid product}} \times 60} = \frac{0.221 \text{ g} \cdot \text{min}^{-1}}{91.379 \text{ g} \cdot \text{mol}^{-1} \times 60} = 4.029 \times 10^{-5} \text{ mol} \cdot \text{s}^{-1}$$

$$F_{i, \text{org gas product}} = y_{i, \text{org gas product}} \times F_{\text{org gas product}}$$

e.g.:

$$\begin{aligned} F_{\text{ethene, org gas product}} &= y_{\text{ethene, org gas product}} \times F_{\text{org gas product}} = 0.554 \times 7.841 \times 10^{-5} \text{ mol} \cdot \text{s}^{-1} \\ &= 4.345 \times 10^{-5} \text{ mol} \cdot \text{s}^{-1} \end{aligned}$$

$$F_{i, \text{liquid product}} = x_{i, \text{liquid product}} \times F_{\text{liquid product}}$$

e.g.:

$$\begin{aligned} F_{\text{decene, liquid product}} &= x_{\text{decene, liquid product}} \times F_{\text{liquid product}} = 0.083 \times 4.029 \times 10^{-5} \text{ mol} \cdot \text{s}^{-1} \\ &= 3.332 \times 10^{-6} \text{ mol} \cdot \text{s}^{-1} \end{aligned}$$

$$F_{i, \text{product}} = F_{i, \text{org gas product}} + F_{i, \text{liquid product}}$$

e.g.:

$$\begin{aligned} F_{\text{decene, product}} &= F_{\text{decene, org gas product}} + F_{\text{decene, liquid product}} = 3.471 \times 10^{-7} \text{ mol} \cdot \text{s}^{-1} + 3.332 \times 10^{-6} \text{ mol} \cdot \text{s}^{-1} \\ &= 3.679 \times 10^{-6} \text{ mol} \cdot \text{s}^{-1} \end{aligned}$$

$$\frac{W}{F_{\text{hex, in}}} = \frac{2 \text{ g} \times 60}{9.561 \times 10^{-5} \text{ mol} \cdot \text{s}^{-1}} = 336.14 \text{ g} \cdot \text{min} \cdot \text{mol}^{-1}$$

$$X = \left(\frac{F_{\text{hex, in}} - F_{\text{hex, product}}}{F_{\text{hex, in}}} \right) \times 100 = \left(\frac{9.561 \times 10^{-5} \text{ mol} \cdot \text{s}^{-1} - 2.378 \times 10^{-5} \text{ mol} \cdot \text{s}^{-1}}{9.561 \times 10^{-5} \text{ mol} \cdot \text{s}^{-1}} \right) \times 100 = 75.13\%$$

$$\text{Selectivity (C}_7\text{ - C}_{16}\text{)} = \frac{\sum_{C_7}^{C_{16}} F_{i, \text{product}}}{F_{\text{hex, in}} - F_{\text{hex, product}}} \times 100 = \left(\frac{1.412 \times 10^{-5} \text{ mol.s}^{-1}}{9.561 \times 10^{-5} \text{ mol.s}^{-1} - 2.378 \times 10^{-5} \text{ mol.s}^{-1}} \right) \times 100$$

$$= 19.65\%$$

$$\text{Selectivity (C}_{10}\text{)} = \frac{F_{\text{decene, product}}}{F_{\text{hex, in}} - F_{\text{hex, product}}} \times 100 = \left(\frac{3.697 \times 10^{-6} \text{ mol.s}^{-1}}{9.561 \times 10^{-5} \text{ mol.s}^{-1} - 2.378 \times 10^{-5} \text{ mol.s}^{-1}} \right) \times 100$$

$$= 5.12\%$$

$$\text{Yield (C}_7\text{ - C}_{16}\text{)} = \frac{\sum_{C_7}^{C_{16}} F_{i, \text{product}}}{F_{\text{hex, in}}} \times 100 = \left(\frac{1.412 \times 10^{-5} \text{ mol.s}^{-1}}{9.561 \times 10^{-5} \text{ mol.s}^{-1}} \right) \times 100 = 14.76\%$$

$$\text{Yield (C}_{10}\text{)} = \frac{F_{\text{decene, product}}}{F_{\text{hex, in}}} \times 100 = \left(\frac{3.697 \times 10^{-6} \text{ mol.s}^{-1}}{9.561 \times 10^{-5} \text{ mol.s}^{-1}} \right) \times 100 = 3.848\%$$

Appendix

D

Catalyst characterization data

Sample weight	0.0541	g
Evacuation rate	500	mmHg.min ⁻¹
Measured free space	-0.649	cm ³ STP
Analysis mode	Equilibration	
Evacuation time	5	min
Saturation Press.	771.13	mmHg
Equilibration time	10	s
Surface area	181.0062	m ² .g ⁻¹
Slope	0.023919	
Y-intercept	0.000131	
C	182.965118	
V _m	41.580048	

Relative pressure	Pressure	V adsorbed	Time
	[mmHg]	[cm ³ .g ⁻¹]	[h:m]
0.0503	38.75	38.117	00:32
0.0754	58.15	41.292	00:37
0.1005	77.53	43.847	00:42
0.1256	96.82	46.005	00:47
0.1507	116.24	48.003	00:52
0.1759	135.63	49.809	00:56
0.2009	154.89	51.582	01:01
0.2262	174.41	53.249	01:05
0.2513	193.76	54.812	01:10
0.2762	213.00	56.375	01:14
0.3012	232.27	57.958	01:19

Table D.1 BET Multipoint surface area report (Micrometrics Gemini) – Fresh catalyst A

Sample weight	0.0448	g
Evacuation rate	500	mmHg.min ⁻¹
Measured free space	-0.663	cm ³ STP
Analysis mode	Equilibration	
Evacuation time	5	min
Saturation Press.	771.13	mmHg
Equil. time	10	s
Surface area	275.7106	m ² .g ⁻¹
Slope	0.01564	
Y-intercept	0.000149	
C	106.254974	
V _m	63.335163	

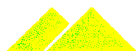
Relative pressure	Pressure	V adsorbed	Time
	[mmHg]	[cm ³ .g ⁻¹]	[h:m]
0.0502	38.72	55.731	00:31
0.0753	58.08	60.592	00:36
0.1004	77.43	64.557	00:42
0.1255	96.79	68.032	00:47
0.1506	116.14	71.176	00:52
0.1756	135.44	74.136	00:56
0.2007	154.8	76.988	01:01
0.2259	174.16	79.742	01:06
0.2509	193.48	82.472	01:11
0.2760	212.82	85.204	01:16
0.3010	232.13	87.85	01:20

Table D.2 BET Multipoint surface area report (Micrometrics Gemini) – Fresh catalyst B

Sample weight	0.0611	g
Evacuation rate	500	mmHg.min ⁻¹
Measured free space	-0.739	cm ³ STP
Analysis mode	Equilibration	
Evacuation time	5	min
Saturation Press.	771.13	mmHg
Equil. time	10	s
Surface area	147.8248	m ² .g ⁻¹
Slope	0.02906	
Y-intercept	0.000388	
C	75.860008	
V _m	33.957737	

Relative pressure	Pressure	V adsorbed	Time
	[mmHg]	[cm ³ .g ⁻¹]	[h:m]
0.0501	38.63	28.467	00:35
0.0752	57.96	31.207	00:41
0.1003	77.31	33.48	00:46
0.1254	96.67	35.484	00:51
0.1505	116.06	37.328	00:56
0.1757	135.46	39.055	01:01
0.2007	154.80	40.692	01:06
0.2259	174.21	42.223	01:10
0.2509	193.49	43.752	01:16
0.2762	213.01	45.313	01:20
0.3013	232.37	46.728	01:25

Table D.3 BET Multipoint surface area report (Micrometrics Gemini) – Spent catalyst B (460°C, 96.41% 1-hexene, 336 g.min.mol⁻¹, 6 hours on-stream)



MASTERSIZER



Result Analysis Report

Sample Name:

A_av

SOP Name:

silt_fine_sand

Measured:

19 February 2008 11:39:23

Sample Source & type:

Measured by:

Mark

Analysed:

19 February 2008 11:39:24

Sample bulk lot ref:

Result Source:

Averaged

Particle Name:

Silica 0.1

Accessory Name:

Hydro 2000MU (A)

Analysis model:

General purpose

Sensitivity:

Enhanced

Particle RI:

1.544

Absorption:

0.1

Size range:

0.020 to 2000.0... um

Obscuration:

14.87 %

Dispersant Name:

Water

Dispersant RI:

1.330

Weighted Residual:

0.320 %

Result Emulation:

Off

Concentration:

0.0554 %Vol

Span :

3.566

Uniformity:

1.25

Result units:

Volume

Specific Surface Area:

0.232 m²/g

Surface Weighted Mean D[3.2]:

25.829 um

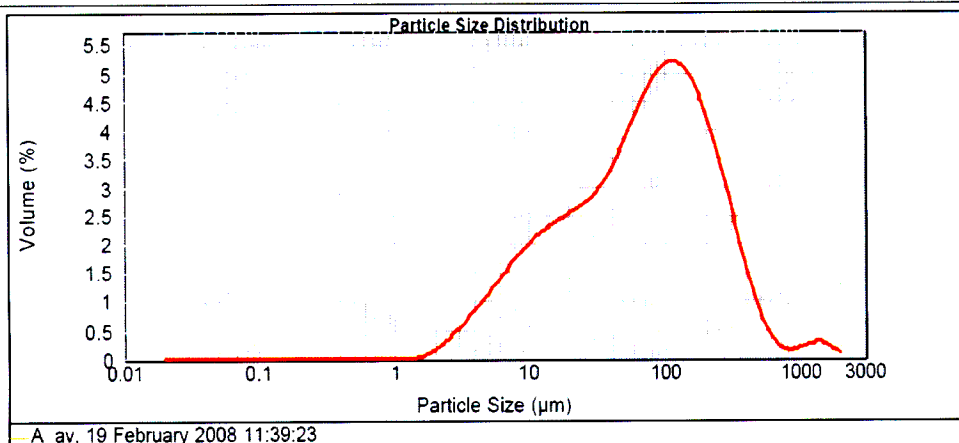
Vol. Weighted Mean D[4.3]:

123.274 um

d(0.1): 9.461 um

d(0.5): 74.351 um

d(0.9): 274.618 um



Size (µm)	Volume In %	Size (µm)	Volume In %	Size (µm)	Volume In %	Size (µm)	Volume In %	Size (µm)	Volume In %	Size (µm)	Volume In %
0.020	0.00	0.142	0.00	1.002	0.00	7.096	1.25	50.238	2.95	355.656	1.40
0.022	0.00	0.159	0.00	1.125	0.00	7.962	1.36	56.368	3.16	399.052	1.06
0.025	0.00	0.178	0.00	1.262	0.00	8.934	1.46	63.246	3.36	447.744	0.75
0.028	0.00	0.200	0.00	1.416	0.00	10.024	1.55	70.963	3.56	502.377	0.51
0.032	0.00	0.224	0.00	1.589	0.03	11.247	1.63	79.621	3.72	563.677	0.31
0.036	0.00	0.252	0.00	1.783	0.07	12.619	1.71	89.337	3.84	632.456	0.19
0.040	0.00	0.283	0.00	2.000	0.07	14.159	1.77	100.237	3.91	709.627	0.12
0.045	0.00	0.317	0.00	2.244	0.14	15.887	1.82	112.468	3.92	796.214	0.10
0.050	0.00	0.366	0.00	2.518	0.20	17.825	1.87	126.191	3.88	893.367	0.12
0.056	0.00	0.399	0.00	2.825	0.37	20.000	1.92	141.589	3.76	1002.374	0.15
0.063	0.00	0.448	0.00	3.170	0.47	22.440	1.96	158.866	3.60	1124.683	0.18
0.071	0.00	0.502	0.00	3.557	0.57	25.179	2.05	178.250	3.38	1261.915	0.20
0.080	0.00	0.564	0.00	3.991	0.68	28.251	2.14	200.000	3.12	1415.852	0.19
0.089	0.00	0.632	0.00	4.477	0.79	31.698	2.25	224.404	2.82	1568.656	0.14
0.100	0.00	0.710	0.00	5.024	0.91	35.966	2.39	251.786	2.48	1762.502	0.09
0.112	0.00	0.796	0.00	5.637	1.02	39.905	2.55	282.506	2.19	2000.000	0.09
0.126	0.00	0.890	0.00	6.325	1.14	44.774	2.74	316.579	1.76		
0.142	0.00	1.002	0.00	7.096	1.25	50.238	2.95	355.656			

Operator notes: Average of 3 measurements from DLokhat_ChemEng

Figure D.1 Malvern® Mastersizer™ 2000 results analysis report – catalyst B crushed (Run 10)



MASTERSIZER



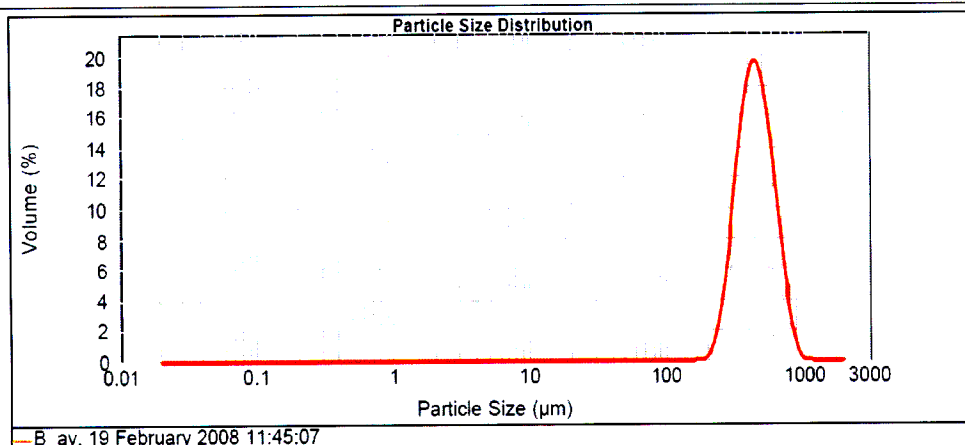
Result Analysis Report

Sample Name: B_av	SOP Name: silt_fine_sand	Measured: 19 February 2008 11:45:07
Sample Source & type:	Measured by: Mark	Analysed: 19 February 2008 11:45:08
Sample bulk lot ref:	Result Source: Averaged	

Particle Name: Silica 0.1	Accessory Name: Hydro 2000MU (A)	Analysis model: General purpose	Sensitivity: Enhanced
Particle RI: 1.544	Absorption: 0.1	Size range: 0.020 to 2000.000 um	Obscuration: 12.61 %
Dispersant Name: Water	Dispersant RI: 1.330	Weighted Residual: 1.355 %	Result Emulation: Off

Concentration: 0.8082 %Vol	Span : 0.786	Uniformity: 0.248	Result units: Volume
Specific Surface Area: 0.0142 m ² /g	Surface Weighted Mean D[3.2]: 422.155 um	Vol. Weighted Mean D[4.3]: 460.178 um	

d(0.1): 300.024 um d(0.5): 441.280 um d(0.9): 646.846 um



Size (µm)	Volume In %	Size (µm)	Volume In %	Size (µm)	Volume In %	Size (µm)	Volume In %	Size (µm)	Volume In %	Size (µm)	Volume In %
0.020	0.00	0.142	0.00	1.002	0.00	7.096	0.00	50.238	0.00	356.666	13.09
0.022	0.00	0.159	0.00	1.125	0.00	7.962	0.00	56.368	0.00	399.052	14.62
0.025	0.00	0.178	0.00	1.262	0.00	8.834	0.00	63.246	0.00	447.744	14.43
0.028	0.00	0.200	0.00	1.416	0.00	10.024	0.00	70.963	0.00	502.377	12.58
0.032	0.00	0.224	0.00	1.589	0.00	11.247	0.00	79.621	0.00	563.677	9.62
0.036	0.00	0.252	0.00	1.783	0.00	12.619	0.00	89.337	0.00	632.496	6.36
0.040	0.00	0.283	0.00	2.000	0.00	14.159	0.00	100.237	0.00	709.627	3.43
0.045	0.00	0.317	0.00	2.244	0.00	15.887	0.00	112.468	0.00	796.214	1.45
0.050	0.00	0.356	0.00	2.518	0.00	17.825	0.00	126.191	0.00	893.367	0.25
0.056	0.00	0.399	0.00	2.825	0.00	20.000	0.00	141.589	0.00	1002.374	0.02
0.063	0.00	0.448	0.00	3.170	0.00	22.440	0.00	158.866	0.00	1124.683	0.00
0.071	0.00	0.502	0.00	3.557	0.00	25.179	0.00	178.250	0.00	1261.915	0.00
0.080	0.00	0.564	0.00	3.991	0.00	28.251	0.00	200.000	0.00	1415.892	0.00
0.089	0.00	0.632	0.00	4.477	0.00	31.696	0.00	224.404	0.00	1588.666	0.00
0.100	0.00	0.710	0.00	5.024	0.00	36.566	0.00	251.785	0.00	1782.502	0.00
0.112	0.00	0.796	0.00	5.637	0.00	39.905	0.00	282.508	0.00	2000.000	0.00
0.126	0.00	0.893	0.00	6.325	0.00	44.774	0.00	316.979	0.00		
0.142	0.00	1.002	0.00	7.096	0.00	50.238	0.00	356.666	10.38		

Operator notes: Average of 3 measurements from DLokhat_ChemEng

Figure D.2 Malvern® Mastersizer™ 2000 results analysis report – catalyst B normal (Runs 1-8 and 11-12)

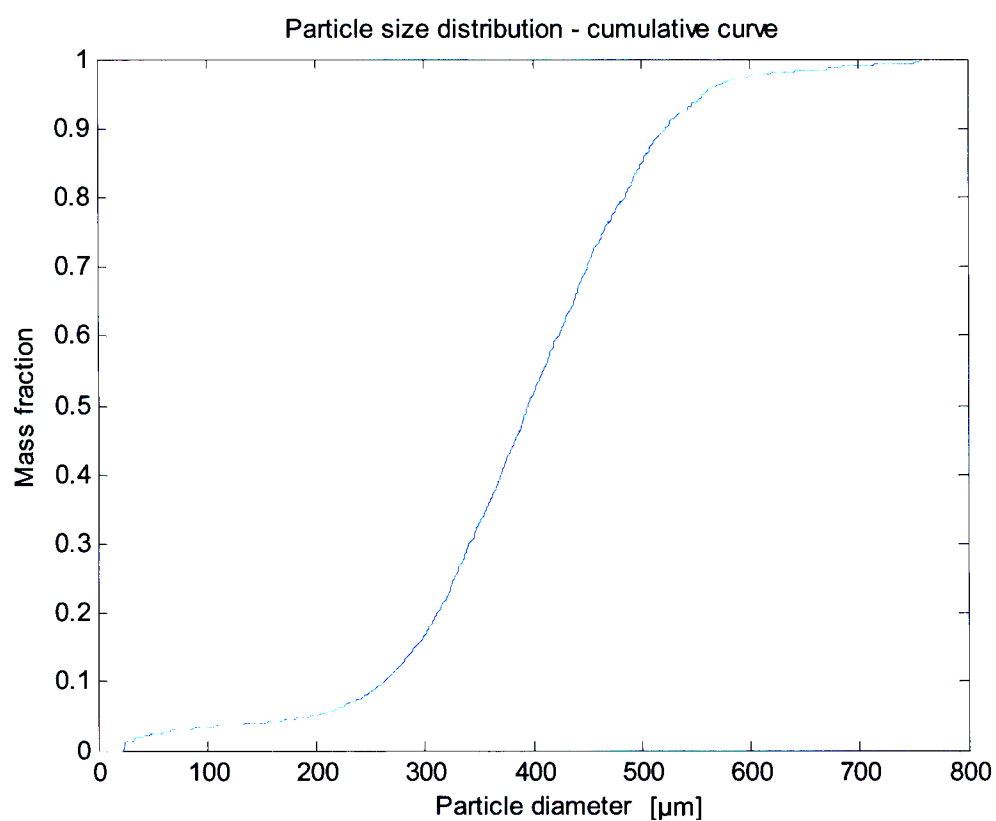


Figure D.3 Cumulative size distribution curve (image analysis) for catalyst pellets – catalyst B normal (Runs 1-8 and 11-12)

Appendix

E

Solution of the unsteady state material balance for saturation of nitrogen gas with 1-hexene

The residence time, for bubbles of an average $R = 1\text{mm}$ radius, required to reach 99% of the saturated vapour concentration at the bubble centre, was calculated using the theory of transient diffusion. Assuming a constant binary diffusion coefficient and one dimensional mass transfer in the radial direction, the model of transient diffusion of species A (1-hexene) in a stagnant medium reduces to:

$$D_{AB} \frac{\partial C_A}{\partial r^2} = \frac{\partial C_A}{\partial t} \quad (\text{E.1})$$

with an initial zero concentration within the entire bubble,

$$C_A(0, r) = C_{A,i} = 0 \quad (\text{E.2})$$

and two generally established boundary conditions,

$$\left. \frac{\partial C_A}{\partial r} \right|_{r=0} = 0 \quad (\text{E.3})$$

$$C_A(t, R) = C_{A,S} \quad (\text{E.4})$$

The second boundary condition is valid only if there is no mass transfer resistance on the liquid side. This is true since 1-hexene is assumed to be a pure liquid.

For 99% saturated vapour, the dimensionless concentration of 1-hexene at the bubble centre is:

$$\gamma_A^* = \frac{C_{A,S} - C_A(t^*, 0)}{C_{A,S} - C_{A,i}} = 0.01 \quad (\text{E.5})$$

where t^* is the time instant at which 99% saturation is achieved.

Assuming an infinitely large mass transfer coefficient (no resistance to mass transfer on the liquid side), the mass transfer Biot number,

$$Bi_m = \frac{k_c R}{D_{AB}} \quad (\text{E.6})$$

approaches infinity, or $Bi_m^{-1} \rightarrow 0$. The Fourier number for mass transfer in a sphere is:

$$Fo_m = \frac{D_{AB} t^*}{R^2} \quad (\text{E.7})$$

The dimensionless concentration plotted against the Fourier number for mass transfer (Heisler chart), enables one to estimate the diffusion time t^* for bubbles of diameter $2R$.

D_{AB} may be estimated from the following empirical equation of Fuller, Schettler and Giddings (1966):

$$D_{AB} = \frac{0.00143 T^{1.75}}{PM_{AB}^{0.5} \left[\left(\sum \nu \right)_A^{1/3} + \left(\sum \nu \right)_B^{1/3} \right]^2} \quad (\text{E.8})$$

where D_{AB} is in $\text{cm}^2 \cdot \text{s}^{-1}$, P is in atmospheres, T is in Kelvin,

$$M_{AB} = \frac{2}{\left(\frac{1}{M_A} \right) + \left(\frac{1}{M_B} \right)} \quad (\text{E.9})$$

M_i is the molar mass and $\sum v$ = summation of atomic and structural diffusion volumes. For the binary system concerned, $\sum v_{N_2} = 18.5$ and $\sum v_{C_6H_{12}} = 123.12$.

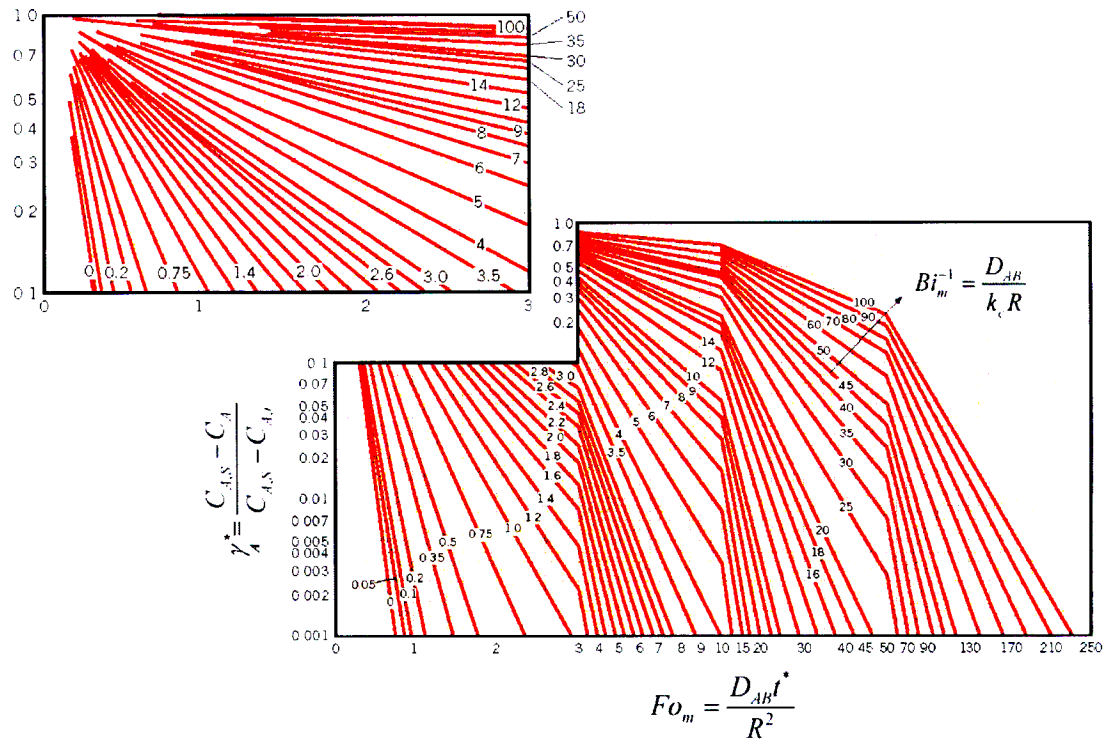


Figure E.1 Centre-line dimensionless concentration as a function of time for a sphere of radius R - Heisler chart (modified after Incropera and de Witt, 1990, p. 250)

From Figure E.1, with $\gamma_A^* = 0.01$ and $Bi_m^{-1} = 0$, $Fo_m = 0.52$. The average time required to reach 99% of the saturated vapour concentration at the bubble centre (2mm diameter bubbles in a vessel of 1-hexene maintained at 57°C) was found to be 0.21 seconds.

Appendix

F

Mass and energy balances for the 1-hexene feed tank

The development of the mass and energy balances around the feed tank were based on the following set of assumptions:

- Constant average properties
- Clean heat transfer surfaces
- Contents of the tank well mixed (lumped parameter system)
- Heat loss to the vapour space above the liquid from the copper coil was not considered.

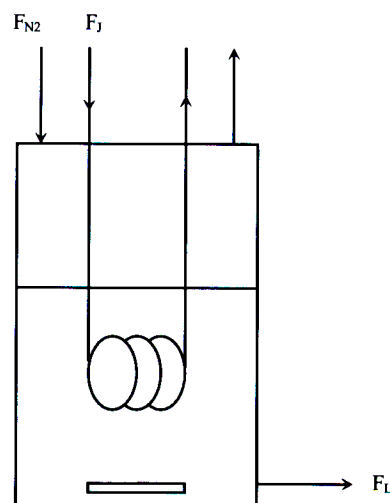


Figure F.1 Flow model of the feed tank assembly

The following set of balance equations was used (Incropera and de Witt, 1990):

1. Liquid phase

Mass:

$$\rho_L \frac{dV_L}{dt} = -\rho_L F_L - n_A'' A_c \quad (\text{F.1})$$

$$n_A'' = h_m \rho_{sat}(T_L) \quad (\text{F.2})$$

$$\frac{h_m D_t}{D_{AB}} = 0.664 \text{Re}^{0.5} \text{Sc}^{1/3} \quad (\text{F.3})$$

Energy:

$$\rho_L \frac{d(V_L H_L)}{dt} = 0 - \rho_L F_L H_L + Q_{coil} - Q_{out} - Q_{N_2} \quad (\text{F.4})$$

$$H_L = C_L T_L \quad (\text{F.5})$$

$$Q_{coil} = U_{coil} A_{coil} \Delta T_{coil} \quad (\text{F.6})$$

$$\Delta T_{coil} = T_L - T_{JA} \quad (\text{F.7})$$

$$T_{JA} = \frac{T_{J0} + T_{Jexit}}{2} \quad (\text{F.8})$$

$$Q_{N_2} = h_{N_2} (T_{N_2} - T_L) - n_A'' h_{fg} \quad (\text{F.9})$$

$$\frac{h_{N_2} D_t}{k_{N_2}} = 0.644 \text{Re}^{0.5} \text{Pr}^{1/3} \quad (\text{F.10})$$

$$Q_{out} = h_i A_i (T_L - T_m) \quad (\text{F.11})$$

$$\frac{h_i D_t}{k_L} = 0.36 \left(\frac{D_{imp}^2 n_{imp} \rho_L}{\mu_L} \right)^{0.67} \left(\frac{C_L \mu_L}{k_L} \right)^{1/3} \quad (F.12)$$

Coil:

$$\rho_J V_J C_J \frac{dT_{JA}}{dt} = F_J \rho_J C_J (T_{J0} - T_{Jexit}) + U_{coil} A_{coil} (T_L - T_{JA}) \quad (F.13)$$

Metal wall (lumped capacitance model):

$$\rho_m V_m C_m \frac{dT_m}{dt} = h_i A_i (T_L - T_m) - h_o A_o (T_m - T_\infty) \quad (F.14)$$

$$h_o = h_o^1 + h_o^2 \quad (F.15)$$

$$\frac{h_o^1 L_t}{k_\infty} = 0.138 Gr^{0.36} [Pr^{0.175} - 0.5] \quad (F.16)$$

$$Gr = \frac{g \beta (T_m - T_\infty) L_t}{\nu_\infty^2} \quad (F.17)$$

$$\frac{h_o^2 D_{t,out}}{k_\infty} = 0.27 Ra^{0.25} \quad (F.18)$$

$$Ra = \frac{g \beta (T_m - T_\infty) D_{t,out}^3}{\nu_\infty \alpha_\infty} \quad (F.19)$$

Appendices G and H may be found on the CD on the inside back cover of this dissertation.